Universität Hamburg

Dissertation with the aim of achieving a doctoral degree at the Faculty of Mathematics, Informatics and Natural Sciences

Departement of Physics

Microstructures in Fiber-Reinforced Materials

Maximilian Witte

Beiersdorf AG
Institut für Nanostruktur- und Festkörperphysik

2020

Declaration of Authorship

I hereby declare on oath that I have written the present dissertation by my own and have not used other than the acknowledged resources and aids.

Signature:

_____

Date:

_____

Gutachter der Dissertation:	Prof. Dr. Michael Rübhausen Dr. Frank Fischer
Zusammensetzung der Prüfungskommission:	Prof. Dr. Michael Rübhausen Dr. Frank Fischer Prof. Dr. Arwen Pearson Prof. Dr. Nils Huse Prof. Dr. Daniela Pfannkuche
Vorsitzende der Prüfungskommission:	Prof. Dr. Daniela Pfannkuche
Datum der Disputation:	14.08.2020
Vorsitzender Fach-Promotionsausschusses PHYSIK:	Prof. Dr. Günter H. W. Sigl
Leiter des Fachbereichs PHYSIK:	Prof. Dr. Wolfgang Hansen
Dekan der Fakultät MIN:	Prof. Dr. Heinrich Graener

Abstract

The macroscopic behavior of fiber-reinforced materials is determined by the properties of embedded fibers, especially their orientation. For example, in biological tissue like skin, aligned collagen fibers are responsible for its anisotropic, non-linear mechanical behavior. In this thesis, novel methods are introduced to investigate the orientation of fiber networks in materials.

The adaptive filter method (AF method) was developed to determine the angular orientation distribution without any assumptions on the fiber network. The AF method showed a significantly increased accuracy in determining the dispersion of the fiber network compared to a state-of-the art band-pass method. Its applicability to experimental data was demonstrated by the analysis of in-vivo second harmonic generation (SHG) images of dermal collagen.

Collagen fiber networks are reported to consist of multiple fiber families. The Fiber Image Network Evaluation (FINE) algorithm was developed to quantify the number of fiber families and their properties based on the cumulative orientation distribution. Greyscale images with multiple fiber families were simulated using a Monte-Carlo method to benchmark the algorithm. The FINE algorithm was found to reliably determine the number of aligned fiber families and the ratio of anisotropic fibers. Furthermore, morphological changes of the collagen network across skin depth were identified by applying the FINE algorithm to in-vivo SHG images of dermal collagen.

Various viscoleastic properties of biological tissue such as creep, strain-rate and strain history-dependence are believed to be related to the collagen fiber network. A multiphoton microscope stretching device was developed to apply mechanical deformations to skin samples, while capturing SHG images of the collagen network at the same time. The FINE algorithm was applied at every state of deformation to track the evolution of the collagen fiber network due to external forces. Cyclic sequences of stretching and relaxation revealed permanent as well as periodical variations of the collagen fiber network of pig skin. A permanent alignment of collagen fibers was associated with the presence of an isotropic fiber family. Furthermore, large differences across the mechanical behavior of samples were successfully related to the initial orientation of their collagen fiber network prior to deformation.

The electrical line resistance of novel silver-nanowire photopolymer composites strongly increases with mechanical stretch. To observe changes of the nanowire network during stretching, the FINE algorithm was applied to light microscopy images of these nanowire networks. Nanowires were found to exhibit one isotropic fiber family, that slightly aligns in the stretching direction in case of a low nanowire concentration. However, it was found that the increase in line resistance is dominated by breaking nanowire junctions rather than by their alignment.

Zusammenfassung

Das makroskopische Verhalten von faserverstärkten Materialien wird maßgeblich durch die Eigenschaften enthaltener Fasern, insbesondere deren Orientierung, bestimmt. In biologischen Geweben, wie der Haut, sind ausgerichtete Kollagenfasern ausschlaggebend für ein anisotropes, nicht-lineares mechanisches Verhalten. In dieser Arbeit werden Methoden vorgestellt, die die Orientierung von Fasern in Materialien quantifizieren. Die adaptive Filtermethode (AF method) wurde entwickelt, um die Winkelverteilung eines Fasernetzwerkes zu bestimmen, ohne dabei Annahmen über das Netzwerk zu treffen. Die AF-Methode wies im Vergleich zu einer state-of-the-art Methode eine signifikant erhöhte Genauigkeit bei der Bestimmung der Dispersion des Fasernetzwerks auf. Die Anwendbarkeit auf experimentelle Daten wurde durch die Analyse von in-vivo Bildern von dermalen Kollagenfasern, die mittels Frequenzverdopplung (SHG) gemessen wurden, belegt.

Kollagenfasernetzwerke bestehen im Allgemeinen aus mehreren Faserfamilien. Der FINE-Algorithmus (Fiber Image Network Evaluation algorithm) wurde entwickelt, um die Anzahl der Faserfamilien und ihre Eigenschaften basierend auf der kumulativen Orientierungsverteilung zu bestimmen. Die Performance des Algorithmus wurde mittels simulierter Faserbilder gemessen. Der FINE-Algorithmus ist dabei in der Lage sowohl die Zahl mehrerer ausgerichteter Faserfamilien als auch den anisotropen Anteil des Fasernetzwerkes präzise zu quantifizieren. Außerdem konnten mit dem FINE-Algorithmus detaillierte morphologische Unterschiede des dermalen Kollagennetzwerkes über die Hauttiefe in-vivo identifiziert werden.

Es wird angenommen, dass verschiedene viskoelastische Eigenschaften von biologischem Gewebe mit dessen Mikrostruktur zusammenhängen. Ein spezielles Dehnungsgerät für den Einsatz am Multiphotonenmikroskop wurde entwickelt, um Veränderungen des Kollagennetzwerkes bei gleichzeitiger Verformung von Haut zu untersuchen. Durch die Anwendung des FINE Algorithmus zu jedem Zeitpunkt einer zyklischen Verformung konnten permanente und reversible Veränderungen des Kollagennetzwerkes von Schweinehaut identifiziert werden. Eine permanente, Ausrichtung wurde mit der Existenz einer isotrop verteilten Faserfamilie assoziiert. Außerdem konnten große Unterschiede in dem mechanischen Verhalten verschiedener Proben erfolgreich bestimmt und mit der Orientierung ihres Kollagennetzwerkes vor Verformung korreliert werden.

Der elektrische Linienwiderstand von neuartigen Photopolymer-Verbundwerkstoffen mit Silber-Nanodrähten nimmt bei mechanischer Dehnung stark zu. Um Veränderungen des Nanodrahtnetzwerkes bei mechanischer Belastung zu untersuchen, wurde der FINE-Algorithmus auf lichtmikroskopische Bilder des Materials angewandt. Es wurde festgestellt, dass Nanodrähte eine isotrope Faserfamilie ausbilden, die sich bei einer niedrigen Nanodrahtkonzentration leicht in Richtung der anliegenden Kraft ausrichtet. Allerdings zeigten Simulationen, dass die Erhöhung des Linienwiderstandes von brechenden Nanodrahtverbindungen dominiert wird.

Contents

List of Figures

List of Tables

Chapter 1

Introduction

Fiber-reinforced materials occur in a large variety of fields. For example, fibers are embedded in construction materials, like reinforced concrete [1] and carbon fiber composites [2], to enhance their mechanical properties. In biological tissue, like skin, collagen fibers represent the main load bearing constituent and allow for its ability to sustain large deformations [3]. Besides their mechanical functionality, fibers can also be the key factor for the electrical properties of materials, like silver-nanowires in photopolymer composites [4].
An important factor determining the properties of fiber-reinforced materials, is the orientation of its fiber network [5, 6]. Due to its complex micro-structure and high anisotropy, the investigation of collagen fibers in biological tissue was extensively studied in the past [3, 7, 8]. The orientation of collagen in skin was analyzed relative to the so-called Langer lines in various ex-vivo experiments [9–13]. The Langer lines, also known as cleavage lines or main tension lines, were discovered in 1861 by Karl Langer [14]. He observed that circular wounds, that he made in the skin of a cadaver, turned into an elliptical shape. Based on the long axes of the ellipsoid, he could identify the main tension lines of skin. Lapeer *et al.* measured a ratio of 2.21:1 of the skin's tensile strength parallel to the Langer lines compared to a perpendicular tension [15] . The main tension lines were related to a preferred orientation of collagen in ex-vivo experiments using histology [13, 16]. However, some ex-vivo experiments failed to support this model [11, 17–19]. Used image processing methods to quantify the orientation of the collagen fiber network are found to rely on assumptions about the material including the diameter of fibers and the number of main orientations [20, 21].
In this thesis objective methods for quantifying and classifying the orientation of fibers in grayscale images are introduced. These methods are applied to collagen fibers of skin and to silver-nanowires of photopolymer composites to investigate their micro-structure and its contribution to the macroscopic behavior of the material.

In chapter 3 of this thesis, the adaptive filter method (AF method) is introduced allowing for an objective and reliable quantification of the orientation of the fiber network in

greyscale images. It is compared to a state-of-the-art method to measure its accuracy. The AF method is applied to in-vivo images of dermal collagen, that are obtained by second harmonic generation (SHG) imaging.

In general, collagen fiber networks are reported to consist of multiple fiber families [8]. Thus, the Fiber Image Network Algorithm (FINE algorithm), which quantifies the number of families in fiber networks and their properties in greyscale image based on the AF method, is developed. The FINE algorithm is presented in chapter 4 of this work. In-vivo SHG imaging in combination with the FINE algorithm is used to objectively quantify the main orientations of collagen fiber families with respect to the Langer lines. Various quantities of the FINE algorithm are employed to resolve differences in the fiber network across different skin layers.

In addition to its high deformation ability, skin exhibits diverse viscoelastic properties such as creep, stress relaxation, history dependence, and strain-rate dependence, which are believed to depend on the collagen fiber network [22–27]. However, a clear micro-structural interpretation is still missing. In chapter 5, a special device is presented, which allows for controlled deformations of skin samples, while capturing their collagen fiber network using SHG imaging. By applying the FINE algorithm of chapter 4 to every state of deformation, changes of the collagen fiber network are related to the macroscopic mechanical behavior of skin.

In chapter 6 the FINE algorithm of chapter 4 is applied to silver-nanowire (Ag:NW) photopolymer composites. The functional printing of this material was proposed recently [4] and provides tunable optical and electronic properties for various applications. The electrical line resistance of this material strongly increases upon mechanical stretch. Similar to chapter 5, the FINE algorithm is used to investigate micro-structural changes of the fiber network in relation to the macroscopic properties of the material.

Chapter 2

Materials and Methods

Collagen fibers of skin play a central role in this work. Thus, the structure and properties of collagen are briefly described in this chapter. In addition, the physical background of the imaging of collagen fibers by second harmonic generation (SHG) is given.

2.1 Collagen Fibers in Skin

Collagen fibers are contained in the dermal skin layer, the *dermis*, which has a thickness of about 0.6 mm in the eyelids up to 3 mm in the back [28]. It is located underneath the epidermal layer, which covers $(85 \pm 15)\,\mu$m of depth [29]. The dermis can be subdivided into papillary dermis and reticular dermis [28]. The papillary dermis features the papillae, which are protrusions into the epidermis and part of the dermal-epidermal junction (DEJ), as well as thin collagen fibers, blood capillaries, sensory nerve endings, and cytoplasm. The papillary dermis has a thickness of $(65 - 175)\,\mu$m and can be distinguished from the reticular dermis by a different organization of collagen fibers, mainly observed in histology images [30].
In total, collagen amounts to 70 % of the dry weight of the dermis and plays a major role for the mechanical behavior of skin [10, 12, 31]. Depending on their structure, different types of collagen are identified [32]. Collagen type I covers 80% of the skins collagen, while collagen type III accounts for 15%. Type II collagen is mainly located in cartilage. Type IV collagen is found in the basement membrane, while type V occurs in, for example, cell surfaces and hair [32]. Collagen type I and III have a hierarchical structure, schematically represented in figure 2.1. Collagen fibers, shown in figure 2.1 (a), are undulated and consist of bundles of collagen fibrils (figure 2.1 (b)). Collagen fibrils have a thickness of $50 - 100$ nm. They express a cross striation pattern with a $60-70$ nm periodicity, which is formed by overlapping 300 nm $\times$ 1.5 nm triple-superhelix tropocollagen molecules (figure 2.1(c)).
The reticular dermis contains thick collagen fibers, which are organized in densely distributed bundles. Its hierarchical substructure, results in a high tensile strength, especially in the large strain domain [3]. In the small strain region, the load is mainly

carried by elastic fibers, which are much more elastic than collagen fibers and have the ability to fully recover from strains of up to 100 % [33]. Their mechanical entanglement with the collagen network of the dermis gives the skin its resilience and recoil ability [34]. Elastic fibers as well as collagen fibers are continuously created by fibroblasts, which are the most abundant cell linage in the human dermis.

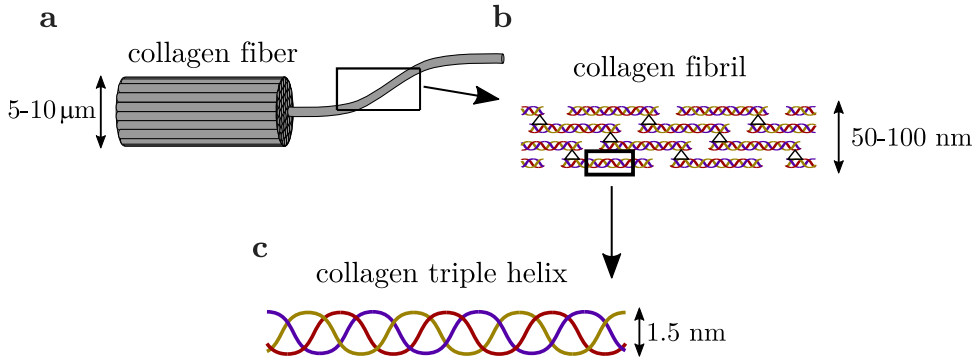

Figure 2.1: Hierarchical structure of collagen type I and III. (**a**) Collagen fibers form the dermal collagen network and consist of collagen fibrils. (**b**) Collagen fibrils, which in turn consist of periodically overlapping tropocollagen molecules. (**c**) Collagen triple helix molecule, also known as tropocollagen. Note that collagen type I and type III only differ in the molecular composition of the tropocollagen.

A widely used technique for measuring the fiber arrangement in-vivo and ex-vivo is multiphoton microscopy [24, 35–44]. Since it represents the most important image modality in this work, its physical fundamentals are briefly described.

2.2 Multiphoton Microscopy

While near physiological conditions can be conserved during imaging, modern confocal laser scanning microscopes (CLSM) provide the link between micro-structure and the function of biological systems [45–47]. Confocal microscopy that makes use of non-linear excitation, called multiphoton microscopy, enables an extensive *in-vivo* examination of skin [48]. In this work, a sophisticated multiphoton microscope, *DermaInspect*, is used for resolving the structure of the collagen fiber network. This microscope was developed in-house in collaboration with JenLab GmbH (Jena, Germany) [49] and was used in diverse skin-related research topics [50–54]. The physical basis of non-linear excitation as well as the generation of second harmonics produced by collagen fibers is explained in the following.

2.2.1 Non-Linear Excitation

Light in general has two natures, which are responsible for its diverse properties. Light is an electromagnetic wave described by the wave equations:

$$\frac{1}{c_0^2}\frac{\partial^2 \mathbf{E}}{\partial t^2} - \nabla^2 \mathbf{E} = 0 \tag{2.1}$$

$$\frac{1}{c_0^2}\frac{\partial^2 \mathbf{B}}{\partial t^2} - \nabla^2 \mathbf{B} = 0, \tag{2.2}$$

where $\mathbf{E}$ and $\mathbf{B}$ describe the electric and the magnetic field, respectively. c_0 denotes the speed of light in vacuum. Equation (2.1) and (2.2) follow from Maxwell's equations that form the foundation of electromagnetism [55]:

$$\nabla \cdot \mathbf{E} = \frac{\rho}{\epsilon_0}, \tag{2.3}$$

$$\nabla \cdot \mathbf{B} = 0, \tag{2.4}$$

$$\nabla \times \mathbf{E} = \frac{\partial \mathbf{B}}{\partial t}, \tag{2.5}$$

$$\nabla \times \mathbf{B} = (\mu_0 \mathbf{j} + \mu_0 \epsilon_0 \frac{\partial \mathbf{E}}{\partial t}), \tag{2.6}$$

where $\mathbf{E}$ and $\mathbf{B}$ describe the electric and the magnetic field, respectively. ρ indicates the total electrical charge density, while ϵ_0, and μ_0, indicate the permittivity and the permeability of the vacuum, respectively. Both quantities are linked to the speed of light by:

$$c_0 = \frac{1}{\sqrt{\epsilon_0 \mu_0}} = 2.99792458 \cdot 10^8 \, \frac{\mathrm{m}}{\mathrm{s}}. \tag{2.7}$$

In addition to its wave-like properties, light behaves like a particle. For example, the Compton effect describes the inelastic scattering of light with a free charged particle. The observation of this phenomenon at low intensity of light leads to the consideration that light can also be treated as a steam of particle-like objects. These particles are called photons, which energy E is proportional to the frequency of light ν:

$$E = \frac{\hbar c}{\lambda} = \hbar\omega = h\nu, \tag{2.8}$$

where $h = 6.626 \cdot 10^{-34}\,\mathrm{Js}$ is the Planck constant, the quantum of the electromagnetic action. It is related to the reduced Planck constant $\hbar$ by $\hbar = \frac{h}{2\pi}$. $\omega = 2\pi\nu$ denotes the angular frequency. Besides the Compton effect, photons can interact with matter via the photoelectric effect and the pair production. The effective cross-section of each of these processes strongly depends on the photon's energy. While pair production becomes relevant only for high photon energies, the photoelectric effect is dominant at lower photon energies, as in the visible light range.

The photo effect includes the excitation and emission of electrons as a consequence of

photon absorption. The energy that is required to excite electrons within atoms or molecules to a higher energy level is characteristic for each material. Excited electrons are able to spontaneously fall back to their ground state. The difference in energy is compromised by emitting a photon with the respective energy. This process is called fluorescence. Let E_0 denote the energy level of an electron in the ground state, that is excited due to the absorption of a photon with an energy of $E_{\text{ex}} = \hbar\omega_{\text{ex}}$. The energy of the emitted photon $E_{\text{emit}} = \hbar\omega_{\text{emit}}$ is given by:

$$E_{\text{emit}} = \hbar\omega_{\text{emit}} = \hbar\omega_{\text{ex}} - E_{\text{loss}}, \tag{2.9}$$

where E_{loss} denotes non-radiative, internal energy losses, leading to the emittance of a photon, which has a longer wavelength compared to the absorbed photon:

$$\lambda_{\text{emit}} > \lambda_{\text{ex}}. \tag{2.10}$$

The respective Jablonski diagram of one-photon fluorescence is shown in figure 2.2 (a). Fluorescing chemical compound are called fluorophores. As a fluorophore is hit by a photon with angular frequency ω, the probability of excitation is measured by the cross-section $\sigma_{1\text{P}} = \sigma_{1\text{P}}(\omega)$. The rate at which such a transition is induced, is given by the intensity I of the incident light:

$$R_{1\text{P}} = \sigma_{1\text{P}}(\omega) \cdot I, \tag{2.11}$$

where the intensity I of light gives the number of photons n in units of $\frac{\text{photons}}{m^2 s}$:

$$I = \frac{nc}{2\pi\hbar\omega}|\mathbf{E}|^2. \tag{2.12}$$

In general, a transition to an excitation state is not limited by the absorption of a single photon, but can also be induced by multiphoton absorption. The angular frequency $\omega_{2\text{P}}$ of each photon being involved in a two-photon excitation is halved, compared to a single photon excitation:

$$\omega_{\text{ex,2P}} = \frac{\hbar\omega_{\text{ex}}}{2}. \tag{2.13}$$

The corresponding Jablonski diagram is shown in figure 2.2 (b). Considering light with intensity I, the two-photon excitation occurs with an excitation rate of:

$$R_{2\text{P}} = \sigma_{2\text{P}}(\omega) \cdot I^2. \tag{2.14}$$

Since the excitation rate (equation (2.14)) of a two-photon process depends on the squared light intensity, it is called non-linear excitation. Contrary, one-photon excitation, equation (2.11), is related to as linear excitation.[56]

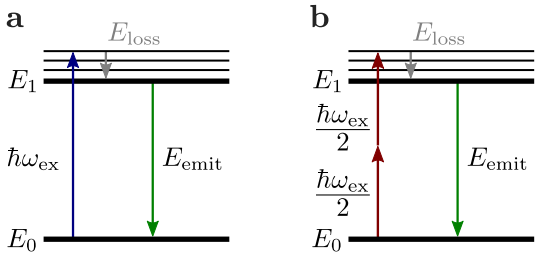

Figure 2.2: Jablonski diagram for one- and two-photon fluorescence. (**a**) Jablonski diagram for one-photon fluorescence. (**b**) Jablonski diagram for two-photon fluorescence. Thick lines represent stable states, whereas thin lines are vibrational and rotational states.

2.2.2 Higher Harmonic Generation

The interactions of light with matter are summarized by the non-linear susceptibility tensor describing the relationship between the electric field of the light and the induced polarization **P**, which is the dipole moment per unit volume. The induced polarization **P** of a material as a consequence of an electric field **E** is generally expressed by:

$$\mathbf{P}(t) = \epsilon_0 \left[\chi^{(1)}\mathbf{E}^1(t) + \chi^{(2)}\mathbf{E}^2(t) + \chi^{(3)}\mathbf{E}^3(t) + \dots \right], \tag{2.15}$$

where $\chi^{(n)}$ denotes the n-th order non-linear susceptibility tensor with rank $n+1$. Each term of equation (2.15) is associated with different orders of electromagnetic interactions including linear and non-linear effects [56]. $\chi^{(1)}$ describes linear excitation like absorption and reflection, while higher orders cover non-linear effects. The generation of second harmonics (SHG), sum and difference frequency generation, occurs as a result of second order effects described by $\chi^{(2)}$. $\chi^{(3)}$ describes the generation of third harmonics (THG), multiphoton absorption, and coherent anti-Stokes Raman scattering. For simplicity, $P(t)$, $\chi^{(n)}$, and $E(t)$ are treated as scalar quantities.

The time-varying polarization of non-linear media can act as a source of new components of the electromagnetic field. Accelerated, charged particles generate electromagnetic radiation, which leads to a modification of the wave equation in non-linear optical media:

$$\nabla^2 E - \frac{n^2}{c^2}\frac{\partial^2 E}{\partial t^2} = \frac{1}{\epsilon_0 c^2}\frac{\partial^2 P_{\text{NL}}}{\partial t^2}, \tag{2.16}$$

where the polarization P_{NL} describes the non-linear response. Equation (2.16) can be understood as an inhomogeneous wave equation, where P_{NL} acts as a driver of the electric field.[56]

Since the principle of second harmonic generation (SHG) is mainly used in this work, the second order polarization:

$$P^{(2)}(t) = \epsilon_0 \chi^{(2)} E^2(t) \tag{2.17}$$

plays a major role. $P^{(2)}$ can only occur in non-centrosymmetric crystals. This can be shown by considering a centrosymmetric crystal that displays inversion symmetry,

which is the case for materials like liquids, gases, or amorphous solids. In these materials, an inversion of the sign of E must also inverse the sign of the polarization:

$$-P^{(2)} = \epsilon_0 \chi^{(2)} (-E)^2(t), \tag{2.18}$$

which only holds for a vanishing second order susceptibility $\chi^{(2)} = 0$. Non-centrosymmetric crystals, like collagen, do not display inversion symmetry and are therefore able to produce second harmonics. Considering the electric field of a coherent light source, e.g. a laser beam:

$$E(t) = Ee^{(-i\omega t)} + E^* e^{(i\omega t)}, \tag{2.19}$$

which incidents upon a crystal with a non-vanishing second order susceptibility $\chi^{(2)}$. The respective second order polarization follows from inserting the wave equation (2.19) in equation (2.17):

$$P^{(2)}(t) = \epsilon_0 \chi^{(2)} \left(Ee^{(-i\omega t)} + E^* e^{(i\omega t)} \right)^2 \tag{2.20}$$

$$= 2\epsilon_0 \chi^{(2)} EE^* + (\underbrace{\epsilon_0 \chi^{(2)} E^2 e^{-i2\omega t}}_{\text{SHG}} + \underbrace{\epsilon_0 \chi^{(2)} E^{*2} e^{i2\omega t}}_{\text{complex conjugate}}) \tag{2.21}$$

The first term does not lead to the creation of electromagnetic radiation since its time derivative vanishes. It is known as optical rectification, which describes the creation of a static electric field across the non-linear crystal.[56] The second term describes the generation of electromagnetic radiation at frequency 2ω, the second harmonic frequency ω_{SHG}:

$$\omega_{\text{SHG}} = 2\omega \tag{2.22}$$

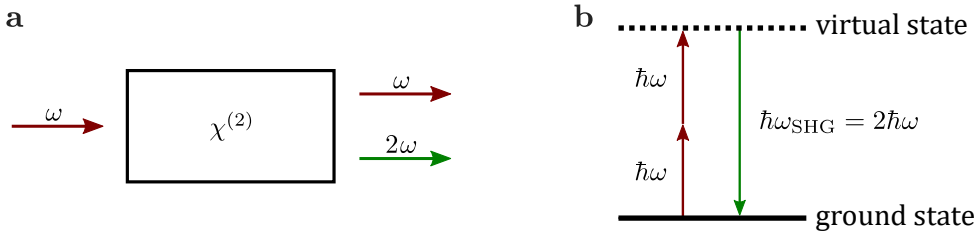

Figure 2.3: Second harmonic generation. (**a**) Process diagram of second harmonic generation. (**b**) Energy level diagram of second harmonic generation

The process diagram of the second harmonic generation is shown in figure 2.3 (a), the corresponding energy level diagram in figure 2.3 (b). Also note that the energy levels which are involved in the generation of second harmonics (SHG) are virtual. Contrary to the two photon fluorescence (TPF) (figure 2.2), no energy is deposited in the medium. As a consequence, the frequency of the SHG signal ω_{SHG} is higher than the frequency of the two-photon fluorescence ω_{TPF} if both processes are induced by the same frequency ω:

$$2\omega = \omega_{\text{SHG}} > \omega_{\text{TPF}} \qquad \frac{\lambda}{2} = \lambda_{\text{SHG}} < \lambda_{\text{TPF}}. \tag{2.23}$$

Since the deposited energy E_{loss} is continuous, the frequency spectrum of TPF is broad, whereas the frequency spectrum of SHG has a sharp peak at 2ω. Since both phenomena occur at a similar excitation frequency, they are often included in the same imaging modality, such as multiphoton microscopy. In addition, since the SHG wavelength is shorter than the TPF wavelength, the SHG can be separated from the TPF, allowing for a simultaneous measurement of both processes.
In the slowly varying envelope approximation (SVEA) the envelope of a forward traveling electromagnetic wave wave is assumed to vary slowly in time and space compared to its wavelength [57]. This is fulfilled for a narrow-banded spectrum of the source of the electromagnetic wave. In this approximation the intensity of the SHG signal caused by an electromagnetic wave with amplitude $E(\omega)$ that incidents on a non-linear crystal with refraction index n reads as:

$$I_{2\omega}(z) \propto I_\omega^2 z^2 \left(\frac{\sin\left(\frac{1}{2}\Delta k z\right)}{\frac{1}{2}\Delta k z} \right)^2 \qquad \text{with} \qquad I_\omega = \frac{1}{2} n \sqrt{\epsilon_0 \mu_0} |E|^2 \tag{2.24}$$

where z defines the length of the interaction of the incident wave and the non-linear crystal. Δk denotes the phase difference between the incident wave with wave vector $k(\omega)$ and the second harmonic wave with wave vector $k(2\omega)$:

$$\Delta k = 2k_\omega - k_{2\omega} \tag{2.25}$$

The term $\sin\left(\frac{1}{2}\Delta k z\right)/\frac{1}{2}\Delta k z$ has a maximum at $\Delta k = 0$. Thus, the intensity of the SHG is maximized for the phase matching condition $2k_\omega = k_{2\omega}$ [58]. The phase mismatch Δk is related to a coherence length l_c at which the conversion of the signal decreases:

$$l_c = \frac{2\pi}{\Delta k} \tag{2.26}$$

Other than TPF, SHG conversion is not emitted isotropically. Since it is a coherent process, the majority of the SHG signal keeps the direction of the incident light, $\mathbf{k}$. However, depending on the phase matching condition, it can also be emitted in backward direction, $\mathbf{k}_{2\omega} = -2\mathbf{k}_\omega$. It was shown that the signal ratio of forward to backward (F/B) emitted SHG depends on the axial size of the objects [59]. Objects, that exhibit a size in the order of the second harmonic wavelength λ_{SHG}, mainly produce forward directed SHG. Small objects with a size less than $\lambda_{\text{SHG}}/10$ will equally produce forward and backward directed SHG [59–61]. As dermal collagen mainly consists of collagen fibrils with diameters ranging from 40 nm to 100 nm, a substantial amount of the SHG signal is emitted in backward direction, allowing for the in-vivo measurement of dermal collagen [62–64].

2.2.3 Multiphoton Microscope *DermaInspect*

The DermaInspect is a confocal microscope, which allows for the measurement of the TPF as well as the SHG [65]. Confocal microscopes focus the excitation laser beam on

a small spot within the $x-y-z$ coordinates of the measurement sample. As SHG and TPF are emitted from the focal spot, the intensity of the emitted signal is captured by photo-multiplier tubes. Depending on the intensity of the detected signal, the pixel, which corresponds to the location of the excited volume, is given a grayvalue.
Scattering processes of the focused laser beam cause a loss of penetration depth and a broadening of the excitation spot, inducing a decreased spatial resolution. The probability that a photon with wavelength λ is scattered, depends on the parametrized size x of a scatterer with radius r:

$$x = \frac{2\pi r}{\lambda} \tag{2.27}$$

In skin, the size of the scattering particles is small compared to the wavelength, and $x \ll 1$. Thus, Rayleigh scattering is the dominant scattering process, which cross section σ_s reads as:

$$\sigma_s = \frac{2\pi^5}{3}\frac{d^6}{\lambda^4}\left(\frac{n^2-1}{n^2+2}\right)^2, \tag{2.28}$$

where n denotes the refractive index and d the diameter of the scatterers. Equation (2.28) indicates that the cross-section of Rayleigh scattering is heavily reduced if the wavelength of the scattering photon is increased. As non-linear processes like TPF and SHG both work at roughly half the wavelength of linear excitation, a comparably deep imaging depth with a high planar spatial resolution $(x-y)$ is achieved.
To simultaneously cover the excitation wavelength of the fluorophores that are contained in skin, as well as the wavelength at which dermal collagen produces second harmonics, a femtosecond Titanium:Sapphire laser (*Mai Tai*, Spectra-Physics, California, USA) with a tunable wavelength in the range of 710 nm to 920 nm is used. As the laser emits short laser pulses, high peak intensities are achieved. High photon intensities are beneficial for both, TPF as well SHG, since their intensity increases with the square of the intensity of the incident laser beam. In addition, due to the extremely short pulse durations, physical processes that occur on the time scale of the pulse duration such as fluorescence lifetime imaging (FLIM) can be resolved [66].
The schematic representation of the DermaInspect is shown in figure 2.4. Laser scanning mirrors enable a scan of the focal spot in the focal plane $(x-y)$. The depth of the focal plane is set by a piezo stage, which moves the objective lens in the z-direction. The SHG/TPF signal is directed to the detector by means of a beam splitter. To separate both signals from each other, different band-pass filters are included in the filter set of the microscope. According to equation (2.23), the wavelength of the SHG signal, λ_{SHG} amounts to half of the excitation wavelength, which is shorter than the wavelength of the TPF. As the SHG of collagen is excited at 820 nm, a narrow band-pass filter at (410 ± 10) nm is used for capturing the SHG signal. Since the spectrum of the TPF signal is broad and shifted to higher wavelengths, a broad-banded filter at (548 ± 150) nm is used for an excitation wavelength of 750 nm. The filtered signal is

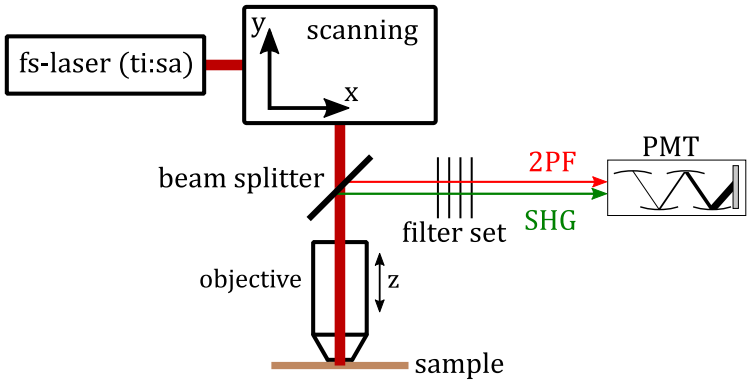

Figure 2.4: Schematic setup of the DermaInspect multiphoton microscope. The filter set contains different band-pass filters to switch between the detection of the TPF signal and the SHG signal.

amplified and measured by a photomultiplier tube (PMT). The final intensity is then passed to a personal computer, which collects the signal for each measured volume and assigns it to the corresponding pixel.[65]

In order to capture the three-dimensional distribution of SHG/TPF planar multiple $x-y$ slices with a predefined slice spacing in z-direction are measured. The image quality in terms of the signal-to-noise ratio depends on the defined scan-time and the image dimension. Potential output image dimensions are 128×128 pixels, 256×256 pixels, 512×512 pixels, 1024×1024 pixels, and 2048×2048 pixels. The maximum spatial resolution of the DermaInspect microscope is $0.4\,\mu$m in lateral $(x-y)$, and $1.3\,\mu$m in vertical (z) direction [67]. Due to scattering-induced signal loss, the maximum measurement depth amounts to $\sim 150\,\mu$m in skin. The spatial dimension of the measured image slices is given by the magnification of the objective lens. The spatial dimension using a $40\times$ magnification objective lens (Zeiss, Oberkochen, Germany) is $(220 \times 220)\,\mu$m, while it is doubled using an objective lens with a $20\times$ magnification (*XLUMPlanFI*, Olympus, Shinjuku, Tokio, Japan).

Chapter 3

Fiber Orientations in Greyscale Images

3.1 Monte-Carlo Simulation of Greyscale Fiber Images

To benchmark the method presented in this chapter, artificial fiber images with defined properties are used. A Monte-Carlo simulation is developed to create images with a predefined fiber geometry in terms of width and length, as well as a predefined angular orientation distribution and image quality. Contrary to approaches published in literature, non-binary images with a continuous greyscale are simulated [20, 21]. Rectangles with a predefined width and length serve as fibers. The orientation of the fibers is sampled from a π-periodic von-Mises distribution:

$$P_{\mathrm{vm}}(\theta) = \frac{1}{\pi I_0(k)} e^{k \cdot \cos\left(2(\theta - \bar{\theta})\right)}, \tag{3.1}$$

where $I_0(k)$ is the modified Bessel function of order zero. The von-Mises function has a maximum at $\theta = \bar{\theta}$, while its width is given by the dispersion parameter k. The dispersion parameter can be understood as a reciprocal standard deviation.
The Monte-Carlo procedure is exemplary shown in figure 3.1. In figure 3.1 (a), the simulation starts with placing a fiber with predefined orientation, width and length randomly within the image such that the entire fiber fits into the image boundaries. This process is repeated in figure 3.1 (b) for a second fiber. If fibers are overlapping as shown in figure 3.1 (c), grey values are summed to mimic a high signal intensity. This process is repeated until the number of iterations of the Monte-Carlo simulation, N_f, is reached (figure 3.1 (d)). In the final step of the procedure, random noise is added to the image, as shown in figure 3.1 (e). A noise factor is introduced defining the maximum intensity of added speckle noise. A vanishing noise factor indicates the absence of speckle noise, while a noise factor of 1 indicates added speckle noise with a maximum intensity equal to half the maximum image intensity. Note that the geometry of artificial fibers is alternatively defined by their width and aspect ratio [21, 68].

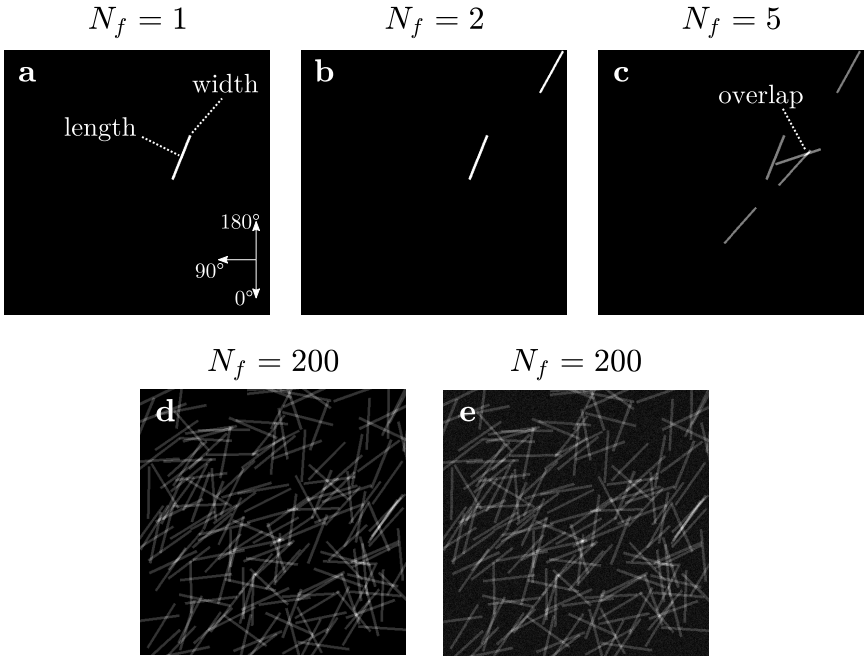

Figure 3.1: Monte-Carlo simulation of an artificial greyscale fiber image. (**a**) First iteration ($N_f = 1$) of the Monte-Carlo simulation of a greyscale fiber image with a fiber distribution with mean orientation $\bar{\theta} = 45°$ and dispersion $k = 1$. A single fiber with a width of 5 pixels and a length of 100 pixels is randomly placed into a 512×512 pixels image. (**b**) Next iteration of the Monte-Carlo simulation ($N_f = 2$). (**c**) Iteration $N_f = 5$ of the Monte-Carlo simulation. Note that the maximum intensity of the image is now given by the overlap of two fibers. (**d**) Final iteration ($N_f = 200$) of the Monte-Carlo simulation. (**e**) Random speckle noise with a noise factor of 0.375 is added to the image in the final step of the Monte-Carlo procedure.

3.2 Angular Orientation Distribution in the Frequency Domain

Various methods for quantifying fiber orientations in scientific images have been published in the past. In magnetic resonance imaging, fiber tracking methods allow for the reconstruction of white matter tracts of the central nervous system by exploiting directional anisotropy, measured by diffusion tensor imaging [69].

Pixel values of microscopy images obtained by histology staining or non-invasive optical methods, such as SHG or TPF, lack information about the directionality of fibers. In order to quantify the angular orientation distribution of fibers in these images, different approaches that are either based on the spatial domain or on the frequency domain have been introduced.

Spatial domain methods are dominated by fiber tracking algorithms [70–73]. A minor role is played by ellipsoidal fitting [6]. The major drawback of these methods is the need for various, parameter-dependent image filters to highlight fibers in greyscale images, for example in [70]. Frequency domain based methods quantify the entire directional

information that is present in the image and are therefore more stable against variations of image quality [74].
The angular information of an image is summarized in the angular orientation distribution, which is denoted by $\mathcal{I}(\theta)$. The angular orientation distribution quantifies the contribution of each direction to the image. In this section, the computation of $\mathcal{I}(\theta)$ in the frequency domain is derived.

3.2.1 The Fourier Transform

The Fourier transform $\hat{f} = \mathcal{F}[f(x)]$ of an integrable function $f : \mathbb{R} \to \mathbb{C}$ is defined as [75]:

$$\hat{f}(\nu) = \int_{-\infty}^{\infty} f(x) e^{-2\pi \mathrm{i} \nu x} \mathrm{d}x, \tag{3.2}$$

where ν has the inverse unit of x. In case of x being the time in seconds, ν is a frequency measured in $1/s$. Analogous to equation (3.2), the inverse Fourier transform $\mathcal{F}^{-1}[\hat{f}(x)]$ reads as:

$$f(x) = \int_{-\infty}^{\infty} \hat{f}(\nu) e^{2\pi \mathrm{i} x \nu} \mathrm{d}\nu. \tag{3.3}$$

In an experimental setting, a signal is recorded in a finite interval with a sequence of N values $\{f_n\} = f_0, f_1, \ldots, f_{N-1}$. In that case, equation (3.2) and (3.3) reduce to finite sums:

$$\hat{f}_\nu = \sum_{n=0}^{N-1} f_n \cdot e^{-\frac{2\pi \mathrm{i} \nu n}{N}} \quad \text{with} \quad \nu = 0, 1, \ldots, N \tag{3.4}$$

$$f_n = \frac{1}{N} \sum_{\nu=0}^{N-1} \hat{f}_\nu \cdot e^{\frac{2\pi \mathrm{i} \nu n}{N}}, \tag{3.5}$$

which are referred to as discrete Fourier transform (DFT) and inverse DFT. The DFT $\hat{f}_n$ is N-periodic:

$$\hat{f}_{\nu+N} = \sum_{n=0}^{N-1} f_n \cdot e^{-\frac{2\pi \mathrm{i} \nu (n+N)}{N}} = \sum_{n=0}^{N-1} f_n \cdot e^{-\frac{2\pi \mathrm{i} \nu n}{N}} \cdot \underbrace{e^{-\frac{2\pi \mathrm{i} \nu N}{N}}}_{1} = \hat{f}_\nu. \tag{3.6}$$

The transformation of an image $I : \Omega \to \mathbb{R}$ defined on $\Omega = \{0, \ldots, X-1\} \times \{0, \ldots, Y-1\}$, to the frequency domain, is achieved from applying a two-dimensional DFT (2D-DFT). The 2D-DFT $I(x, y) \to \mathcal{F}[I(x, y)] = \hat{I}(u, v)$ is given by:

$$\hat{I}(u, v) = \sum_{y=0}^{Y-1} \sum_{x=0}^{X-1} I(x, y) \cdot e^{-2\pi \mathrm{i} \left(\frac{x}{X} u + \frac{y}{Y} v \right)}, \tag{3.7}$$

with the respective inverse 2D-DFT:

$$I(x, y) = \sum_{u=0}^{Y-1} \sum_{v=0}^{X-1} \hat{I}(u, v) \cdot e^{2\pi \mathrm{i} \left(\frac{x}{X} u + \frac{y}{Y} v \right)}. \tag{3.8}$$

Thus, the image $I(x, y)$ can be represented by a linear combination of complex exponentials $e^{2\pi \mathrm{i}\left(\frac{x}{X}u+\frac{y}{Y}v\right)}$ with complex weights $\hat{I}(u, v)$. Complex weights can also be represented in terms of their real and imaginary parts:

$$\hat{I}(u, v) = \mathrm{Re}[\hat{I}(u, v)] + \mathrm{i}\,\mathrm{Im}[\hat{I}(u, v)], \tag{3.9}$$

with:

$$\mathrm{Re}[\hat{I}(u, v)] = \sum_{y=0}^{Y-1}\sum_{x=0}^{X-1} I(x, y) \cos\left(2\pi\left(\frac{x}{X}u + \frac{y}{Y}v\right)\right), \tag{3.10}$$

$$\text{and} \quad \mathrm{Im}[\hat{I}(u, v)] = -\sum_{y=0}^{Y-1}\sum_{x=0}^{X-1} I(x, y) \sin\left(2\pi\left(\frac{x}{X}u + \frac{y}{Y}v\right)\right). \tag{3.11}$$

3.2.2 Angular Orientation Distribution

To derive the angular orientation distribution $\mathcal{I}(\theta)$ of an image, the relationship between the orientations of structures in the spatial domain and the 2D-DFT has to be derived. For this purpose, complex weights $\hat{I}(u, v)$ are expressed in the polar form using the amplitude $|\hat{I}(u, v)|$ and the phase ϕ:

$$\hat{I}(u, v) = |\hat{I}(u, v)| \cdot e^{\mathrm{i}\phi} \quad \text{with} \quad \phi = \tan^{-1}\left(\mathrm{Im}[\hat{I}(u, v)]/\,\mathrm{Re}[\hat{I}(u, v)]\right), \tag{3.12}$$

The square of the amplitude is also known as the power spectrum $P(u, v)$:

$$\mathcal{P}(u, v) = |\mathcal{F}[I(x, y)]|^2 = \mathrm{Re}[\hat{I}]^2 + \mathrm{Im}[\hat{I}]^2. \tag{3.13}$$

Assuming a quadratic image with $X = Y$, the complex exponential $e^{\frac{2\pi \mathrm{i}}{X}(xu+yv)}$ can be expressed in terms of a scalar product of two vectors $\vec{r} = (x, y)$ and $\vec{v} = (u/w, v/w)$ with $w = \sqrt{u^2 + v^2}$:

$$e^{\frac{2\pi \mathrm{i}}{X}(xu+yv)} = e^{\frac{2\pi \mathrm{i}w}{X}\left(\frac{x}{w}u+\frac{y}{w}v\right)} = e^{\frac{2\pi \mathrm{i}w}{X}(\vec{r}\vec{v})}. \tag{3.14}$$

$\vec{r}$ is a vector in the direction of (x, y), while $\vec{v}$ is a normalized vector in the direction of (u, v). Since all points (x, y) on a straight line perpendicular to the direction of $\vec{v}$ exhibit the same projection $\vec{r}\vec{v}$, the exponential $e^{\frac{2\pi \mathrm{i}w}{X}(\vec{r}\vec{v})}$ describes a planar sinusoidal in the $x-y$ plane along the direction:

$$\theta = \tan^{-1}\left(\frac{v}{u}\right) \quad \text{with frequency} \quad w = \sqrt{u^2 + v^2}. \tag{3.15}$$

As a consequence, the contribution of structures that are aligned in a certain direction θ' to the angular orientation distribution is quantified by the summed amplitude of all weights:

$$\mathcal{I}(\theta') = \sum_{u,v} |\hat{I}(u, v)|^2 = \sum_{u,v} \mathcal{P}(u, v) \quad \text{with} \quad \tan^{-1}\left(\frac{v}{u}\right) = \theta' + 90°. \tag{3.16}$$

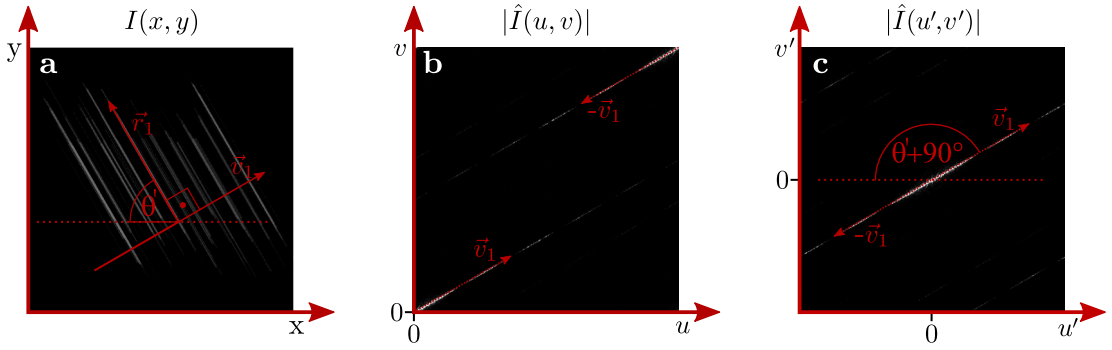

Figure 3.2: Relation between the direction of structures in the spatial and the frequency domain. (**a**) Exemplary image with aligned structures in the direction of $\vec{r}$, i.e. θ. (**b**) Amplitude of the 2D-DFT of (a). (**c**) Coordinate shift $(u, v) \rightarrow (u', v')$ such that low frequencies appear in the center.

Note that instead of the amplitude, the squared amplitude (power spectrum, equation (3.13)) is used for measuring the intensity of each contribution. Figure 3.2 illustrates the relation between the direction of aligned structures in the images and the weights of the Fourier transform. In figure 3.2 (a), multiple lines are aligned in the direction of $\vec{r}_1$, i.e. with angle θ' measured against the negative x-axis. The respective amplitude of the complex weights is given in figure 3.2 (b). The aligned structure of the image is represented by the linear combination of multiple planar sinusoidal in the direction of $\vec{v}_1$, perpendicular to $\vec{r}_1$ with weights $\hat{I}(u, v)$. A coordinate shift $(u, v) \rightarrow (u', v')$ is performed, such that low frequencies are appearing the image center, for example shown in figure 3.2 (c). For now, the coordinate shift is implicitly applied, while coordinates are indicated using u and v.
Since image pixels have a finite size, an angular width $\delta\theta$ is introduced and the expression (3.16) reads as:

$$\mathcal{I}(\theta) = \sum_{u,v} \mathcal{P}(u, v) \quad \text{with} \quad \tan^{-1}\left(\frac{v}{u}\right) \in [\theta - \delta\theta, \theta + \delta\theta), \tag{3.17}$$

where $\theta = \theta' + 90$ denotes the angle between the vertical and the horizontal coordinate in the frequency domain. To ensure a continuous angular orientation spectrum, the contribution of each pixel is weighted by its areal fraction within the angular interval $[\theta - \delta\theta, \theta + \delta\theta)$ by a factor $w_{\text{int}}(u, v, \theta)$. The angular orientation distribution follows as:

$$\mathcal{I}(\theta) = \sum_{u,v} \mathcal{P}(u, v) \cdot w_{\text{int}}(u, v, \theta) \quad \text{with} \quad \tan^{-1}\left(\frac{v}{u}\right) \in [\theta - \delta\theta, \theta + \delta\theta). \tag{3.18}$$

The weighting factors are exemplary shown for $\theta = 45°$ in figure 3.3. If a pixel is fully contained in the angular interval $[\theta - \delta\theta, \theta + \delta\theta)$, $w_{\text{int}}(u, v, \theta)$ is equal to one. Note that the sum over all weighting factors is equal to the number of pixels $\sum_{u,v,\theta} w_{\text{int}}(u, v, \theta) = X \cdot Y$.

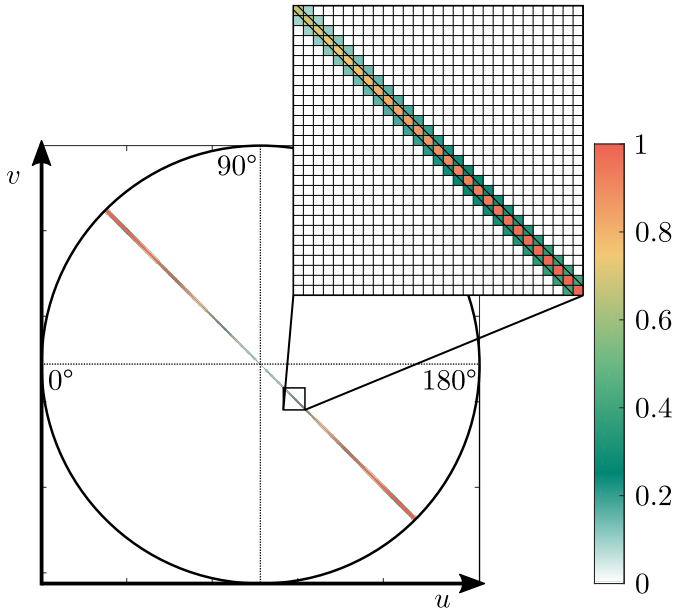

Figure 3.3: Weighting factors of the radial sum for $\theta = 45°$. Weighting factors are calculated based on the fraction of area that is enclosed within an angular interval, which is chosen here as $[45° - 0.5°, 45° + 0.5°)$. Note that the evaluated region is always circular.

3.3 Implicit Periodization Artifact

Analogous to the symmetry condition of equation (3.6) in the one-dimensional case, the 2D-DFT $\hat{I}(u, v)$ is $[X, Y]$ periodic. Thus, the DFT can be interpreted as the continuous Fourier transform (equation (3.2)) of a periodic distribution [76]. The consideration of an image to be periodic causes cross-like grey value discontinuities in the Fourier domain, which are referred to as periodization artifact [76]. As an example, the vertical borders of the test image *Boat*, which is shown in figure 3.4 (a), do not express similar grey values. As a consequence, the corresponding power spectrum exhibits vertical discontinuities through its center, which are illustrated in figure 3.4(b). These discontinuities cause a known artifact in the angular orientation distribution. A popular approach used within the scope of quantifying the angular orientation distribution is the application of window functions, that gradually reduce the grey values towards the image borders [20, 68, 74, 78, 79]. A Hamming window, for example, gradually reduces the grey values of the image $I(x, y)$ towards the image border using a cosine function:

$$H\left[I(x, y)\right] = I(x, y) \cdot h_x(x) h_y(y) \tag{3.19}$$

with:

$$h_x(x) = 0.54 - 0.46 \cdot \cos\left(\frac{2\pi x}{X - 1}\right) \quad \text{and} \tag{3.20}$$

$$h_y(y) = 0.54 - 0.46 \cdot \cos\left(\frac{2\pi y}{Y - 1}\right). \tag{3.21}$$

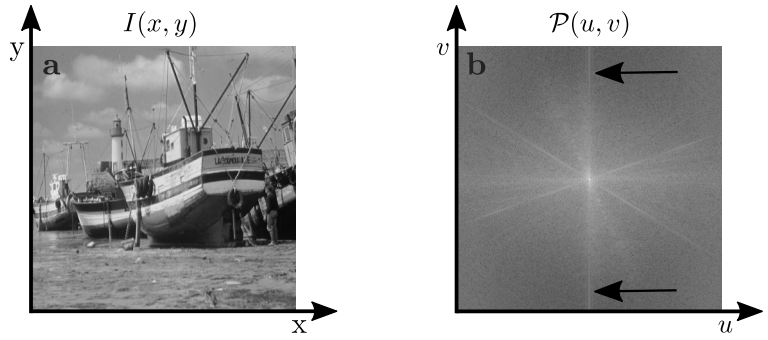

Figure 3.4: Grey value discontinuities due to the implicit periodization of the 2D-DFT. (**a**) Example image in which opposite grey values at the border are not similar. This image was obtained from [77]. (**b**) Power spectrum $\mathcal{P}(u,v) = |\hat{I}(u,v)|^2$ shown in logarithmic scale for a better visibility. Discontinuities are marked with arrows. Note that they are appearing in the center due to the coordinate shift (figure 3.2).

Since grey values are reduced to zero at the image border, the grey value discontinuities are removed. In this work, the periodic plus smooth decomposition of Moisan *et al.* [76] is used, since it is reported to have little effects on the image. Consider an image $I \in \mathbb{R}$ defined on $\Omega = \{0,\dots,X-1\} \times \{0,\dots,Y-1\}$. The periodic component of the image in the frequency domain, $\widehat{\mathrm{per}}(u,v)$, is defined as [76]:

$$\forall (x,y) \in \Omega \setminus (0,0), \quad \widehat{\mathrm{per}}(x,y) = \hat{I}(x,y) - \frac{\hat{v}(x,y)}{4 - 2\cos\left(\frac{2\pi x}{X}\right) - 2\cos\left(\frac{2\pi y}{Y}\right)}, \tag{3.22}$$

and $\widehat{\mathrm{per}}(0,0) = \hat{u}(0,0)$, where $v = v_1 + v_2$ and:

$$\forall (x,y) \in \Omega, \quad v_1(x,y) = \begin{cases} u(x,y) - u(X-1-x,y) & \text{if } x = 0 \text{ or } x = X-1, \\ 0 & \text{else,} \end{cases} \tag{3.23}$$

$$\forall (x,y) \in \Omega, \quad v_2(x,y) = \begin{cases} u(x,y) - u(x,Y-1-y) & \text{if } y = 0 \text{ or } y = Y-1, \\ 0 & \text{else.} \end{cases} \tag{3.24}$$

The periodic component of the image $I(x,y)$ simply follows from an inverse 2D-DFT, $\mathrm{per}(x,y) = \mathcal{F}^{-1}[\widehat{\mathrm{per}}(u,v)]$.

The removal of the grey value discontinuities by the periodic component and the Hamming window is shown in figure 3.5 for the example image *Boat*. Its periodic component is shown in figure 3.5 (a). The difference between the original image and its periodic component in figure 3.5 (b) exhibits minor deviations from zero near the image border. Hence, almost the entire information of the image in the spatial domain is conserved. The periodization artifacts in the power spectrum of figure 3.4 (b) are missing in figure 3.5 (c). Hence, the corrected artifacts are pronounced in the difference between both power spectra in figure 3.5 (d). The windowed image image is shown in figure 3.5 (e). The difference to the original image in figure 3.5 (f) indicates a severe loss of image

information in the spatial domain. As a consequence, features in the power spectrum of the windowed image in figure 3.5 (g) are less pronounced, and are therefore appearing in the difference between both power spectra, shown in figure 3.5 (h).
The periodic decomposition therefore represents an approach to effectively remove the periodization artifact without loss of image information, neither in the spatial nor in the frequency domain.

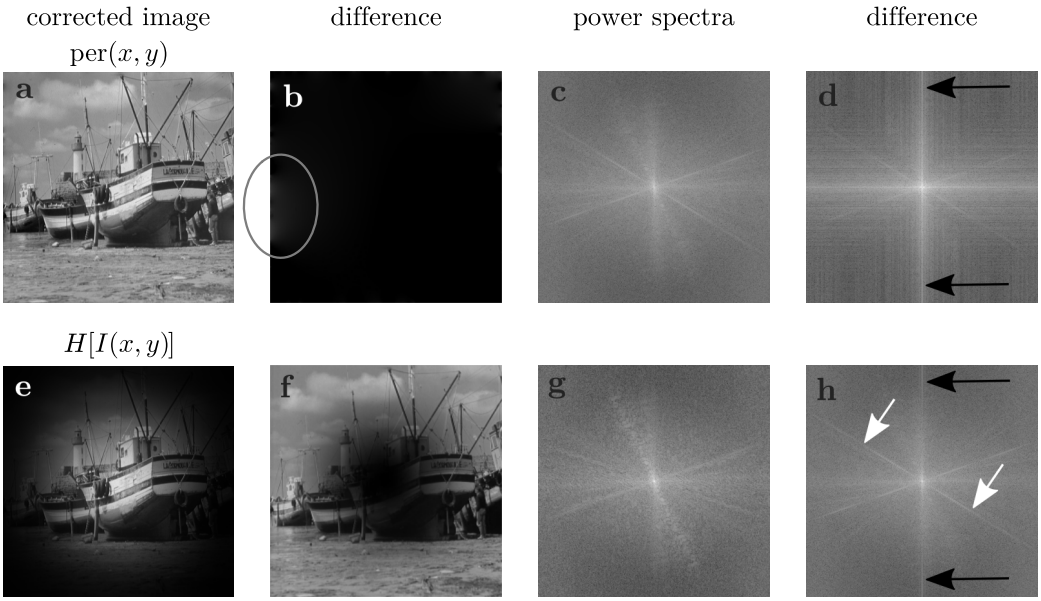

Figure 3.5: Periodization artifcat removal: Hamming window vs. periodic component. (**a**) Periodic component of the image *boat* (figure 3.4 (a)). (**b**) Difference between the original image and the periodic component of the image. Highest differences are marked by a circle. (**c**) Power spectrum $|\widehat{\text{per}}(u, v)|^2$ of (a). (**d**) Difference between the power spectrum of the original image (figure 3.4 (b)) and the power spectrum of the periodic component. The periodization artifact is removed as indicated by black arrows. (**e**) Hamming window applied on the image *Boat*. (**f**) Difference between the original image and the windowed image. (**g**) Power spectrum of the windowed image (e) . (**h**) Difference between the power spectrum of the original image and the power spectrum of the windowed image. The periodization artifact is removed as indicated by black arrows. In addition, features of the original power spectrum are removed, indicated by white arrows.

3.4 Fourier Filtering

3.4.1 Band-Pass Filtering

Equation (3.18) was derived to calculate the angular orientation spectrum of an image $I(x, y)$ using its power spectrum $\mathcal{P}(u, v)$. However, it was found in literature that small frequencies located around the center of the power spectrum as well as high frequencies decrease the accuracy of Fourier based methods [21, 78, 80, 81]. Centered Frequencies have high intensities but provide insufficient information about the directional depen-

dence of the signal. In contrast, frequencies far from the image center exhibit a high angular resolution but suffer from a low intensity. Band-pass filtering, for example used by Morrill *et al.* [21], aims on radially excluding low and high frequencies by a band-pass filter:

$$\hat{I}_{w_l,w_h}(u,v) = \hat{I}(u,v) \cdot m_{w_l,w_h}(u,v) \quad \text{with} \quad m_{w_l,w_h} = \begin{cases} 1 & \text{if } w_l < \sqrt{u^2+v^2} < w_h, \\ 0 & \text{else,} \end{cases} \tag{3.25}$$

where w_l and w_h denote the low cut-off frequency and the high cut-off frequency, respectively.

The frequency ν_{fiber} of a fiber with diameter t, that is located in a quadratic image with dimension X is given by [74]:

$$\nu_{\text{fiber}} = \frac{X}{2t}. \tag{3.26}$$

Morrill *et al.* [21] determined an optimum for each cut-off frequency at $t = 32$ and $t = 2$ for images containing collagen fibers. Using equation (3.26), the corresponding frequencies for a 512×512 amount to $w_l = 8$ and $w_h = 128$. Thus, band-pass filter parameters are defined as a function of the fiber width, which has to be known prior evaluation.

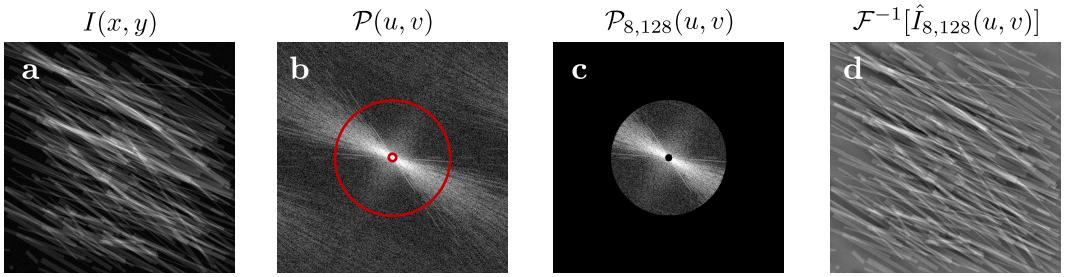

Figure 3.6: Exemplary application of a band-pass filter. (**a**) Exemplary 512×512 Monte-Carlo simulated fiber image with $N_f = 300$ highly aligned fibers ($k = 10$). (**b**) Power spectrum of (a) with circles whose radii correspond to the cut-off frequencies $w_l = 8$ and $w_h = 128$, shown in red. (**c**) Band-pass filtered power spectrum of (a) using $w_l = 8$ and $w_h = 128$ (equation (3.25)). (**d**) Inverse 2D-DFT of the band-pass filtered Fourier transform of $I(x,y)$.

Furthermore, the signal of the power spectrum might exhibit a high anisotropy, like exemplary shown in figure 3.6 (a). In this case, isotropic band-pass filtering negates the anisotropic nature of the signal. This is shown in figure 3.6 (b) and figure 3.6 (c). The inverse 2D-DFT of the band-pass filtered fourier transform, shown in figure 3.6 (d) indicates a loss of sharpness and image contrast.

3.4.2 Adaptive Filtering

To account equally for isotropic and anisotropic fiber distributions, an adaptive filter is derived. The pixel intensity of each image originating from optical imaging is pro-

portional to the number of counted photons (see section 2.2.2). Assuming Poissonian light, the probability of detecting n_{ph} photons in each pixel over a fixed time interval is described by the Poisson distribution:

$$P(n) = \frac{e^{-\langle n \rangle} \langle n \rangle^n}{n!}, \tag{3.27}$$

where $\langle n \rangle$ denotes the average number of counted photons in a single pixel. The uncertainty of photon counting is defined by the variance of equation (3.27) and follows as $\sigma_{\mathrm{ph}} = \sqrt{\langle n \rangle}$. Thus, the pixel-wise uncertainty of an image with intensity $I(x, y)$ can be assumed as $\Delta I(x, y) = \sqrt{I(x, y)}$. Note that the Poisson distribution transforms into a Gaussian for a large number of counted photons. $\Delta I(x, y)$ is propagated to the frequency domain to obtain the uncertainty of the power spectrum $\Delta \mathcal{P}(u, v)$.

3.4.2.1 Uncertainty propagation

The Taylor series expansion of a function $f(a, b)$ depending on two variables a and b in the first order is given by:

$$f(a, b) \approx f_0 + \frac{\partial f}{\partial a} a + \frac{\partial f}{\partial b} b. \tag{3.28}$$

The uncertainty follows directly:

$$\Delta f(a, b)^2 \approx \left| \frac{\partial f}{\partial a} \right|^2 \Delta a^2 + \left| \frac{\partial f}{\partial b} \right|^2 \Delta b^2 + 2 \frac{\partial f}{\partial a} \frac{\partial f}{\partial b} \Delta_{ab}, \tag{3.29}$$

where Δa and Δb are the uncertainties of a and b, respectively. $\Delta_{a,b}$ denotes the covariance between a and b. Applying 3.29 to equation (3.13), the uncertainty of the power spectrum $\Delta P(u, v)$ follows as:

$$\Delta \mathcal{P} \approx 2 \sqrt{\left(\mathrm{Re}[\hat{I}] \Delta \,\mathrm{Re}[\hat{I}] \right)^2 + \left(\mathrm{Im}[\hat{I}] \Delta \,\mathrm{Im}[\hat{I}] \right)^2 + 2 \,\mathrm{Re}[\hat{I}] \,\mathrm{Im}[\hat{I}] \Delta \hat{I}^2_{\mathrm{Re\,Im}}}. \tag{3.30}$$

Similarly, the uncertainties of the real and imaginary parts, $\Delta \,\mathrm{Re}[\hat{I}]$ and $\Delta \,\mathrm{Im}[\hat{I}]$, respectively, are calculated:

$$\Delta \,\mathrm{Re}[\hat{I}(u, v)] = \sqrt{\sum_{y=0}^{Y-1} \sum_{x=0}^{X-1} \Delta I^2(x, y) \cos^2 \left(2\pi \left(\frac{x}{X} u + \frac{y}{Y} v \right) \right)}, \tag{3.31}$$

$$\Delta \,\mathrm{Im}[\hat{I}(u, v)] = \sqrt{\sum_{y=0}^{Y-1} \sum_{x=0}^{X-1} \Delta I^2(x, y) \sin^2 \left(2\pi \left(\frac{x}{X} u + \frac{y}{Y} v \right) \right)}. \tag{3.32}$$

Since $\Delta \,\mathrm{Re}[\hat{I}]$ and $\Delta \,\mathrm{Im}[\hat{I}]$ both depend on $\Delta I(x, y)$, the covariance $\Delta \hat{I}_{\mathrm{Re\,Im}}$ needs to be considered [82, 83]:

$$\Delta \hat{I}_{\mathrm{Re\,Im}}(u, v) = \sqrt{\sum_{y=0}^{Y-1} \sum_{x=0}^{X-1} \Delta I^2(x, y) \sin \left(2\pi \left(\frac{x}{X} u + \frac{y}{Y} v \right) \right) \cos \left(2\pi \left(\frac{x}{X} u + \frac{y}{Y} v \right) \right)}. \tag{3.33}$$

Note that the uncertainty propagation equations (3.31)-(3.33) represent transformations that differ from the 2D-DFT (equation (3.7)). An efficient implementation of each transformation is presented in the appendix B.
Equation (3.30) directly leads to the formulation of a criterion for the maximum relative error of the power spectrum $\frac{\Delta\mathcal{P}(u,v)}{\mathcal{P}(u,v)}$ to define an adaptive filter mask $m_{\delta_{\text{cut}}}$:

$$m_{\delta_{\text{cut}}}(u,v) = \begin{cases} 1 & \text{if } \frac{\Delta\mathcal{P}(u,v)}{\mathcal{P}(u,v)} \leq \delta_{\text{cut}}, \\ 0 & \text{else.} \end{cases}, \tag{3.34}$$

where δ_{cut} defines the maximum relative error. Note that a similar criterion could have been formulated by using a relative error constraint on another quantity, e.g. $\Delta\,\mathrm{Re}[\hat{I}]$. $\Delta\mathcal{P}$ is chosen since it contains the information of the real and imaginary part of $\hat{I}(u,v)$. In a recent publication a scaling factor was introduced to increase the accuracy of determining the angular orientation distribution [68]. This factor empowers the entire angular orientation distribution. Here, a factor α is introduced, which takes advantage of the anisotropic nature of the adaptive filter (equation (3.34)). The angular orientation distribution including the adaptive filter $m_{\delta_{\text{cut}}}$ of equation (3.34) and the factor α then reads as:

$$\mathcal{I}(\theta) = \frac{n(\theta)^{\alpha}}{N_{\mathcal{I}}} \sum_{u,v} \mathcal{P}(u,v) \cdot w_{\text{int}}(u,v,\theta) \cdot m_{\delta_{\text{cut}}}(u,v) \quad \text{with} \quad \tan^{-1}\left(\frac{v}{u}\right) \in [\theta - \delta\theta, \theta + \delta\theta) \tag{3.35}$$

$$\text{and} \quad n(\theta) = \sum_{u,v} w_{\text{int}}(u,v,\theta) \cdot m_{\delta_{\text{cut}}}(u,v), \tag{3.36}$$

where $N_{\mathcal{I}}$ represents a normalization factor such that $\mathcal{I}(\theta)$ is normalized over the interval $[0°, 180°]$: $\sum_{\theta'=0°}^{180°} \mathcal{I}(\theta') = 1$. The term $\sum_{u,v} w_{\text{int}}(u,v,\theta) \cdot m_{\delta_{\text{cut}}}(u,v)$ can be understood as the weighted number of pixels within the angular interval $[\theta - \delta\theta, \theta + \delta\theta)$ of the filtered power spectrum. The empowerment by α therefore amplifies a potential signal anisotropy. The uncertainty of the angular orientation directly follows from the propagation of equation (3.35):

$$\Delta\mathcal{I}(\theta) = \sqrt{\frac{n(\theta)^{2\alpha}}{N_{\mathcal{I}}^2} \sum_{u,v} \left(\Delta\mathcal{P}(u,v) \cdot w_{\text{int}}(u,v,\theta) \cdot m_{\delta_{\text{cut}}}(u,v)\right)^2 + \left(\Delta N_{\mathcal{I}} \frac{\mathcal{I}(\theta)}{N_{\mathcal{I}}}\right)^2} \tag{3.37}$$

$$\text{with} \quad \tan^{-1}\left(\frac{v}{u}\right) \in [\theta - \delta\theta, \theta + \delta\theta). \tag{3.38}$$

From now, adaptive filtering in combination with the amplification by the factor α is referred to as the *AF method* (equation (3.35) and (3.37)). Prior to estimate the optimal parameter set $(\delta_{\text{cut}}, \alpha)$, the validity of the error propagation, equation (3.30)-(3.33), is verified by a Monte-Carlo based noise simulation.

3.4.2.2 Noise Simulation

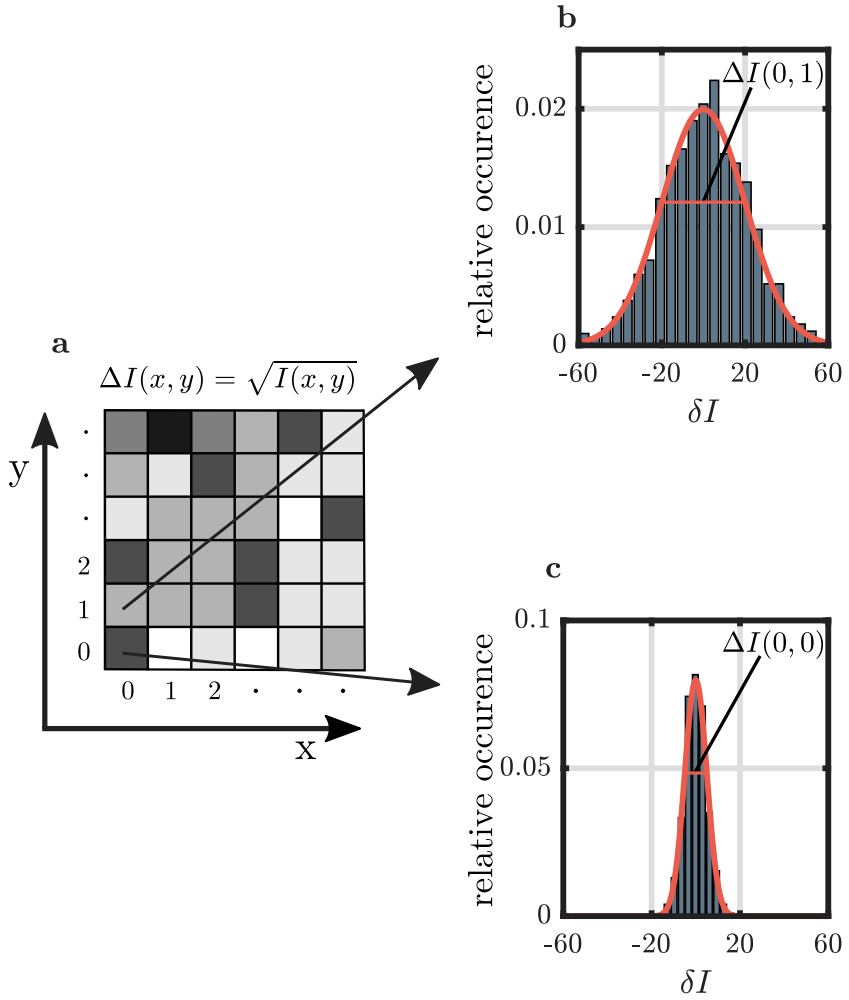

Figure 3.7: Principle of the Monte-Carlo noise simulation. (**a**) Image uncertainty $\Delta I(x,y) = \sqrt{I(x,y)}$. (**b**) Exemplary sampling of uncertainties for the pixel located at $(0,1)$. (**c**) Exemplary sampling of uncertainties for the pixel located at $(0,0)$. This figure was adapted from [54].

The number of photons n is assumed to be large, that the fluctuation of the number of counted photons around its mean value is Gaussian distributed with a standard deviation of $\Delta I(x,y)$. Figure 3.7 (a) illustrates the pixel-wise image uncertainty. In the noise simulation, a perturbed image $I'(x,y) = I(x,y) + \delta I(x,y)$ is computed from sampling random image noise within each pixel according to its uncertainty. Figure 3.7 (b) and (c) illustrate exemplary Gaussian-shaped distributions of sampled noise values. The investigated transformation, i.e. $P(u,v) = |\mathcal{F}[I(x,y)]|^2$, is then applied to the image with added random noise, denoted as $C[I'(x,y)]$. The transformed, simulated uncertainty, ΔC_{MC}, follows from the standard deviation of N_{MC} iterations of noise

sampling:

$$\Delta C_{\mathrm{MC}} = \sqrt{\frac{1}{N_{\mathrm{MC}}} \sum_{k=0}^{N_{\mathrm{MC}}-1} \left(C[I(x,y)] - C[I'_k(x,y)]\right)^2} \tag{3.39}$$

$$= \sqrt{\frac{1}{N_{\mathrm{MC}}} \sum_{k=0}^{N_{\mathrm{MC}}-1} \left(C[I(x,y)] - C[I(x,y) + \delta I_k(x,y)]\right)^2}. \tag{3.40}$$

A rejection sampling algorithm is used for the generation of the pixel-wise image noise. To save computational effort, the interval, where random numbers are sampled from, is constrained to $5\sigma = 5\Delta I$. To quantify the averaged error between numerical and theoretical uncertainty, the relative error Δ_{MC} is evaluated:

$$\Delta_{\mathrm{MC}} = \frac{1}{XY} \left(\sum_{y=0}^{Y-1} \sum_{x=0}^{X-1} \frac{|\Delta C(x,y) - \Delta C_{\mathrm{MC}}(x,y)|}{\Delta C_{\mathrm{MC}}(x,y)} \right). \tag{3.41}$$

Note that the relative error is averaged over the domain of the transformed image, which could be either the spatial or the frequency domain. The Monte-Carlo noise simulation is applied to the periodic decomposition (equation (3.22)) and to the power spectrum (equation (3.13)). Since the periodic decomposition only has minor effects on the image (figure 3.5), its numerical uncertainty is compared to the original image error $\Delta I(x,y)$. A high number of iterations N_{MC} is crucial to minimize effects that are induced by random sampling. In order to investigate the influence of the number of iterations N_{MC} on the sampling error, a simple noise simulation using the identity transformation $C[I(x,y)] = I(x,y)$ with a variable number of iterations is performed. For each number of iterations, the mean relative error (equation (3.40)) with $\Delta C = \Delta I(x,y) = \sqrt{I(x,y)}$ is calculated. The result is shown in figure 3.8 for the test image *Boat*. Note that the image is scaled to 16 bit to ensure high pixel intensities to represent sufficiently high photon counts. The theoretical image uncertainty of the test image is shown in figure 3.8 (a). At a low number of iterations, the sampled image noise fluctuates strongly, as shown in figure 3.8 (b) for $N = 6$. As visualized in figure 3.8 (c) and (d), fluctuations reduce with an increasing number of iterations. This is also reflected by a reduction of the mean relative error, Δ_{MC}, as a function of the number of iterations, plotted in figure 3.8 (d). At $N_{\mathrm{MC}} = 10^4$, the mean relative error amounts to $(0.6 \pm 0.4)\,\%$, which is considered as sufficiently low. Hence, $N_{\mathrm{MC}} = 10^4$ is chosen as the number of iterations for the noise simulation of the periodic decomposition and the power spectrum.

The results of both simulations, using the test images *Goldhill*, *Barbara*, *Cameraman*, and *Boat*, are summarized in table 3.1. All test images were obtained from [77]. As expected, the periodic decomposition has minor effects on the image error expressed by a maximum mean relative error of $(1.0 \pm 3.0)\,\%$. These errors are related to effects of the periodic decomposition on the image boundary. This is confirmed by a decrease of the mean relative error to a maximum of $(0.7 \pm 0.7)\,\%$, if the boundary is excluded from statistical analysis. Hence, it is reasonable to assume an image uncertainty of

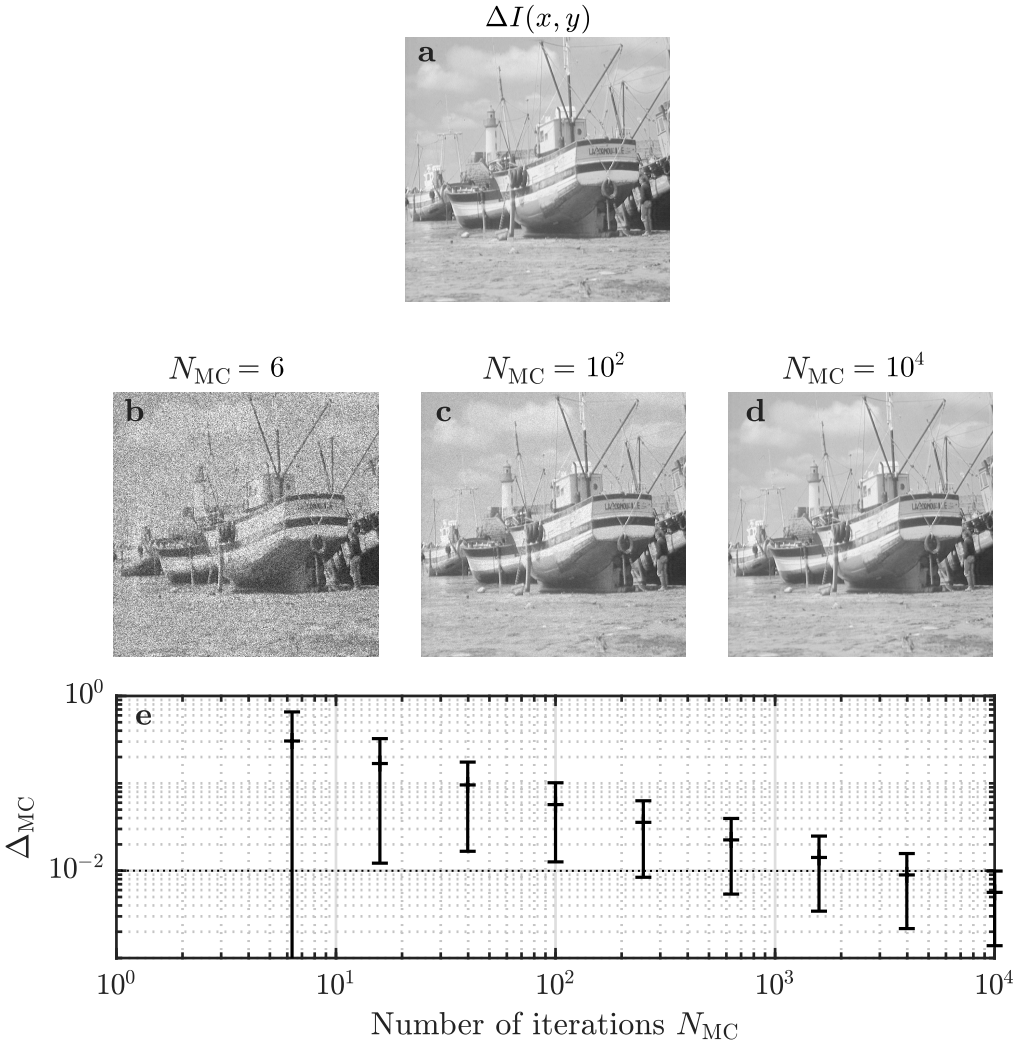

Figure 3.8: Effect of the number of iterations on the Monte-Carlo sampling error. (**a**) theoretical image uncertainty $\Delta I(x, y) = \sqrt{I(x, y)}$ of the test image *Boat*. (**b**) Numerical uncertainty ΔC_{MC} for $N = 6$ iterations. (**c**) Numerical uncertainty ΔC_{MC} for $N = 10^2$ iterations. (**d**) Numerical uncertainty ΔC_{MC} for $N = 10^4$ iterations. (**e**) Relative error between the theoretical and the numerical uncertainty Δ_{MC} (equation (3.41)). Both axis are in logarithmic scale.

$\Delta I(x, y)$ for the periodic component $\mathrm{per}(x, y)$.

The noise simulation reveals a non-vanishing relative error between the theoretical and numerical uncertainty of the power spectrum with a maximum of $(5.4 \pm 12.9)\,\%$. However, the relative uncertainty of the unfiltered power spectra exhibits enormous values, as shown in figure 3.9 (a) for the test image *Boat*. Filtering its power spectrum, which is shown for different values of δ_{cut} in figure 3.9 (b)-(e), effectively removes noisy pixels. At the same time, the anisotropy of the signal is maintained. The corresponding inverse Fourier transforms in figure 3.9 (f)-(i) keep the main features of the original image, although the majority of pixels in the frequency domain are removed due to δ_{cut}. Adaptive filtering dramatically reduces the relative error between theoretical

and numerical uncertainty to $(0.6 \pm 0.4)\,\%$ at $\delta_{\text{cut}} = 0.1$ for all test images (see table 3.1). This error is similar to the Monte-Carlo sampling error for the number of chosen iterations (figure 3.8). As a consequence, the theoretical uncertainty of the power spectrum (equation (3.30)) represents an accurate estimation.

Table 3.1: Result of the Monte-Carlo noise simulation of different test images. Ω_{bnd} defines the image boundary $\Omega_{\text{bnd}} = \{0, X-1\} \times \{0, Y-1\}$. $\Delta\mathcal{P}_{\delta_{\text{cut}}}(u,v)$ denotes the filtered power spectrum (equation (3.34)).

	Goldhill	*Barbara*	*Cameraman*	*Boat*
$\Delta_{\text{MC}}[\%]$ for $\Delta\text{per}(x,y)\,\forall\,(x,y) \in \Omega$	0.8 ± 2.1	0.8 ± 2.1	1.0 ± 3.0	0.8 ± 2.2
$\Delta_{\text{MC}}[\%]$ for $\Delta\text{per}(x,y)\,\forall\,(x,y) \in \Omega \backslash \Omega_{\text{bnd}}$	0.6 ± 0.5	0.6 ± 0.6	0.7 ± 0.7	0.6 ± 0.8
$\Delta_{\text{MC}}[\%]$ for $\Delta\mathcal{P}(u,v)$	3.2 ± 7.2	5.4 ± 12.9	1.6 ± 4.3	4.2 ± 8.8
$\Delta_{\text{MC}}[\%]$ for $\Delta\mathcal{P}_{\delta_{\text{cut}}=0.1}(u,v)$	0.6 ± 0.4	0.6 ± 0.4	0.6 ± 0.4	0.6 ± 0.4

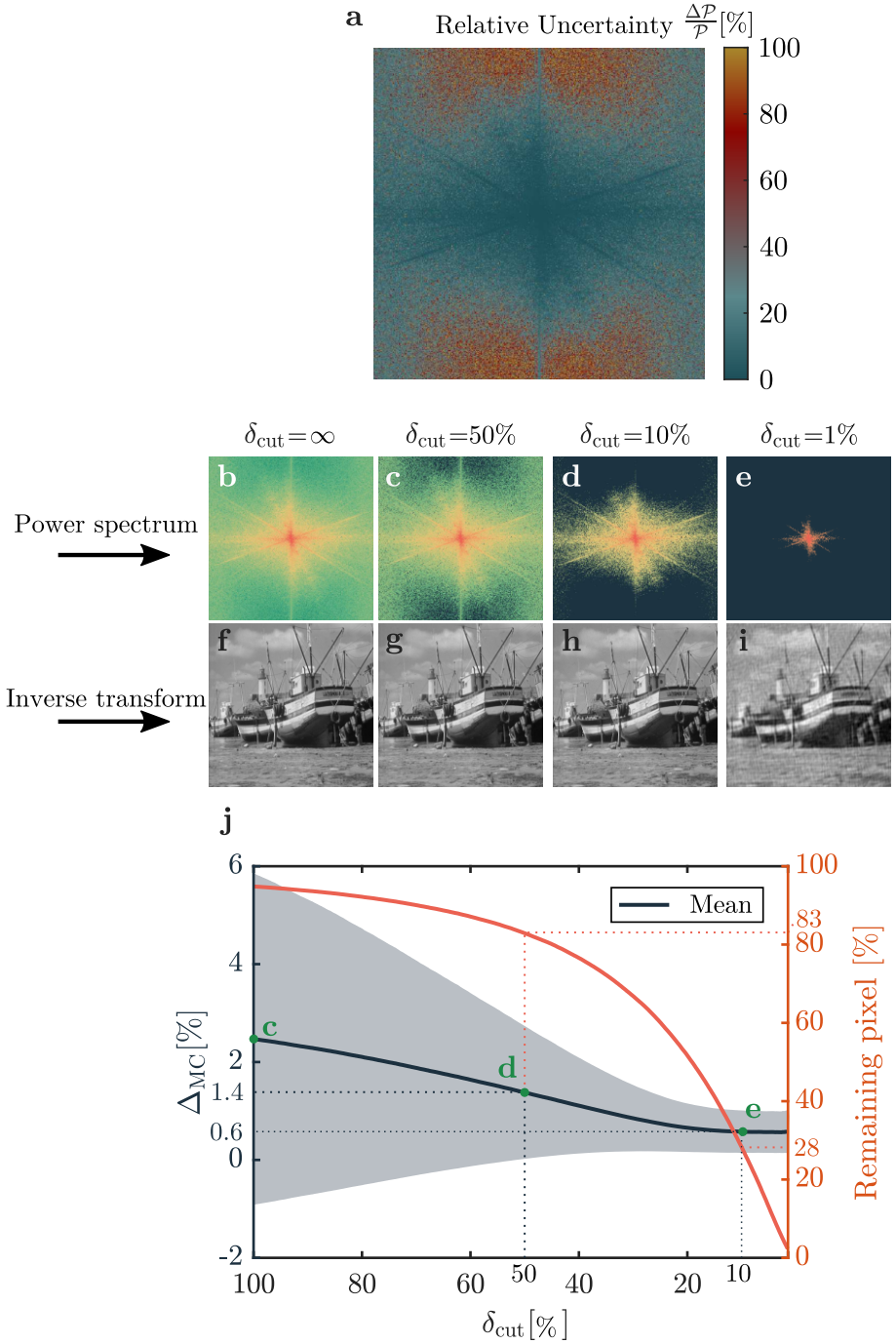

Figure 3.9: Relative uncertainty of the power spectrum and the effect of adaptive filtering. (**a**) Relative uncertainty of the unfiltered power spectrum of the test image *Boat* in false colors. (**b**) Unfiltered power spectrum of the test image *Boat*, which is similar to a filtered power spectrum with $\delta_{\text{cut}} = \infty$. (**c**)-(**e**) Filtered power spectra $\mathcal{P}_{\delta_{\text{cut}}}$ for different values of $\delta_{\text{cut}} = \{50\,\%, 10\,\%, 1\,\%\}$. (**f**)-(**i**) Corresponding inverse Fourier transforms of the filtered 2D-DFT $\mathcal{F}[\hat{I}_{\delta_{\text{cut}}}(u, v)]$. (**j**) Error of the noise simulation, Δ_{MC}, and the percentage of remaining pixel after filtering as a function of δ_{cut}. Note that a similar figure was created in [54], but with the 8 bit version of the test image.

3.5 Quantification of the Angular Orientation Distribution

The angular orientation distribution $\mathcal{I}(\theta)$ is now used to quantify parameters of the fiber network. The common approach studied in literature uses the semi-circular von-Mises distribution (equation (3.1)) to quantify the angular orientation distribution by means of the mean orientation $\bar{\theta}$ and the dispersion parameter k [16, 20, 21, 68, 74, 84–86]. This approach is exemplary shown for a Monte-Carlo image (figure 3.10 (a)) in figure 3.10 (b). Since the method, however, exhibits large errors in the limit of a highly dispersed fiber network [21], a sigmoidal approach based on the cumulative orientation distribution $\mathcal{C}(\theta)$ is introduced here.
The cumulative orientation distribution (COD) follows directly from $\mathcal{I}(\theta)$:

$$\mathcal{C}(\theta) = \sum_{\theta'=0°}^{\theta} \mathcal{I}(\theta') \quad \text{with} \quad \theta \in [0°, 180°]. \tag{3.42}$$

Propagating equation (3.42) gives its uncertainty:

$$\Delta\mathcal{C}(\theta) = \sqrt{\sum_{\theta'=0°}^{\theta} \Delta\mathcal{I}(\theta')^2} \quad \text{with} \quad \theta \in [0°, 180°]. \tag{3.43}$$

Since the choice of the starting angle of the summation in equation is arbitrarily chosen to be at $\theta' = 0°$, the uncertainty $\Delta\mathcal{C}(\theta)$ must be independent from θ. Thus, the maximum of equation (3.43) is considered as uncertainty $\Delta\mathcal{C}$:

$$\Delta\mathcal{C} := \max\left[\sqrt{\sum_{\theta'=0°}^{\theta} \Delta\mathcal{I}(\theta')^2}\right] \quad \text{with} \quad \theta \in [0°, 180°]. \tag{3.44}$$

A peak in the angular orientation distribution is represented by a step in the COD. Thus, a sigmoid function is used to model the COD to obtain the mean orientation $\bar{\theta}$ and the dispersion parameter b:

$$S(\theta; b, \bar{\theta}) = \frac{1}{1 + e^{-b\cdot(\theta-\bar{\theta})}}. \tag{3.45}$$

The dispersion parameter b indicates the steepness of the step, which is measure for the anisotropy of the fiber network. The angular orientation is semi-circular, i.e. $\mathcal{I}(\theta) = \mathcal{I}(\theta + 180°) = \mathcal{I}(\theta - 180°)$, which is fulfilled by the von-Mises function ($P_{\mathrm{vm}}(\theta) = P_{\mathrm{vm}}(\theta + 180°) = P_{\mathrm{vm}}(\theta - 180°)$). A similar condition for the cumulative orientation distribution reads as:

$$\mathcal{C}(\theta) = \mathcal{C}(\theta + 180°) - 1 = \mathcal{C}(\theta - 180°) + 1 \quad \text{with} \quad \mathcal{C}(0°) = 0 \quad \text{and} \quad \mathcal{C}(180°) = 1. \tag{3.46}$$

To meet the conditions of 3.46, the sigmoid function is defined as:

$$\forall \quad \theta \in [0°, 180°] : \tag{3.47}$$

$$S_{\text{circ}}(\theta) = A\left[S(\theta) + S(\theta + 180°) - S(180°) + S(\theta - 180°) - S(-180°) + B\right], \tag{3.48}$$

where the quantities A and B are chosen such that $S_{\text{circ}}(0°) = 0$ and $S_{\text{circ}}(180°) = 1$:

$$0 \stackrel{!}{=} S_{\text{circ}}(0°) = A\left[S(0°) + B\right] \Rightarrow B = -S(0°) \quad \text{with} \quad A \neq 0 \tag{3.49}$$

and: (3.50)

$$1 \stackrel{!}{=} S_{\text{circ}}(180°) = A\left[S(360°) - S(-180°)\right] \Rightarrow A = \frac{1}{S(360°) - S(-180°)}. \tag{3.51}$$

The sigmoid function of equation (3.48) is exemplary shown in figure 3.10 (c).

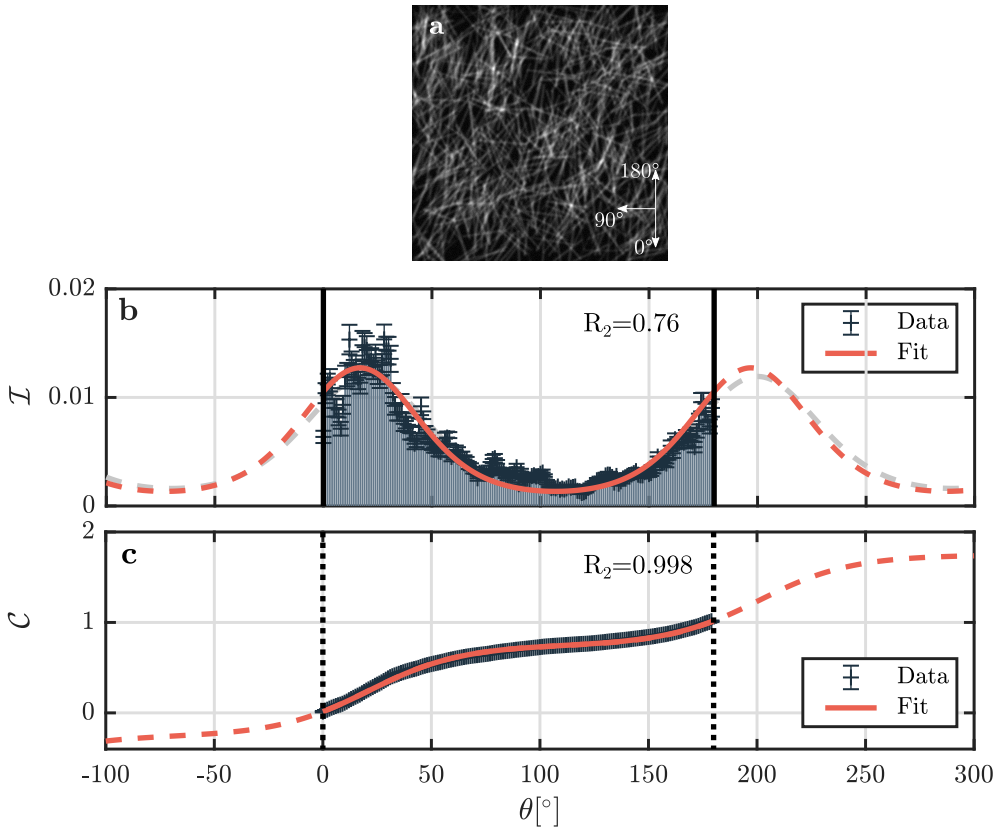

Figure 3.10: Von-Mises approach vs. sigmoidal approach. (**a**) Monte-Carlo simulated greyscale image with 1000 fibers, a mean orientation of $\bar{\theta} = 20°$ and a dispersion of $k = 1$ ($b = 0.047$). (**b**) Von-Mises approach: Angular orientation distribution with the von-Mises fit with parameter $\bar{\theta} = (20.0 \pm 1.2)°$ and $k = 1.3 \pm 0.1$ shown in red. The reference von-Mises function, from which fiber angles of (a) are sampled, is plotted in grey. (**c**) Sigmoidal approach: Cumulative orientation distribution with sigmoid fit with parameter $\bar{\theta} = (20.1 \pm 0.3)°$ and $b = 0.054 \pm 0.000$. Note that the reference sigmoid function overlaps perfectly with the fitted sigmoid and is therefore not visible.

In order to correlate the dispersion parameter of the von-Mises approach to the dispersion parameter of the sigmoidal approach, a numerical transfer function is calculated.

This is done by sampling values from a von-Mises function with predefined dispersion k to obtain an angular orientation distribution. The respective COD (equation (3.42)) is then modeled using the sigmoid function of equation (3.48) to obtain the dispersion parameter b. A total of ten values of the dispersion b are averaged for each value of k. In total $2 \cdot 10^4$ different values of k are processed. The resulting dataset $b(k)$ is modeled using the following function:

$$b(k) = \begin{cases} c_1 \cdot k^{c_2} + c_3 & \text{if } k < 2, \\ c_4 \cdot k^{c_5} + c_6 & \text{if } k \geq 2. \end{cases} \tag{3.52}$$

A least square fit yields the coefficients $\{c_1, \ldots, c_6\}$:

$$b(k) = \begin{cases} (0.031 \pm 0) \cdot k^{0.837 \pm 0.006} + (0.016 \pm 0) & \text{if } k < 2, \\ (0.068 \pm 0) \cdot k^{0.477 \pm 0.001} - (0.019 \pm 0.001) & \text{if } k \geq 2. \end{cases} \tag{3.53}$$

Data points, as well as the fitted function of equation (3.52) are shown in figure 3.11.

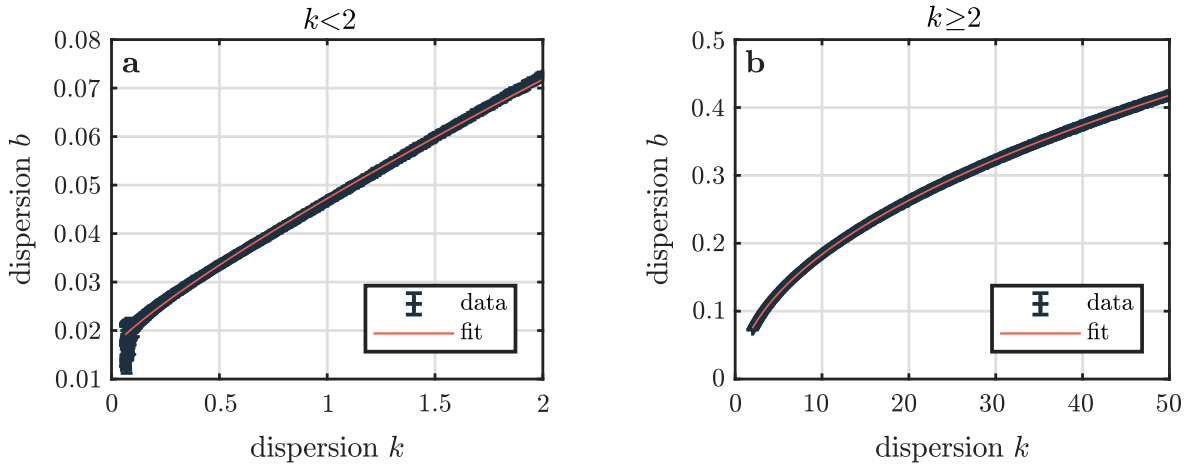

Figure 3.11: Numerical transfer function b(k). (**a**) Transfer function and data points for $k < 2$. (**b**) Transfer function and data points for $k \geq 2$

3.6 Monte-Carlo Simulations

Monte-Carlo simulated greyscale images (section 3.1) are used to, first, find optimal values of the evaluation parameter $(\delta_{\text{cut}}, \alpha)$ of the AF method and, second, to compare the AF method in combination with the sigmoid approach against the state-of-the-art band-pass filtering method of Morrill *et al.*[21]. This method was proven to be more accurate than other methods and was successfully applied to experimental data [86].

3.6.1 Parameter optimization of the AF method

The AF method is parametrized by δ_{cut} and α, which define the strength of the filter as well as the weighting of the anisotropy of the signal. The optimization approach of

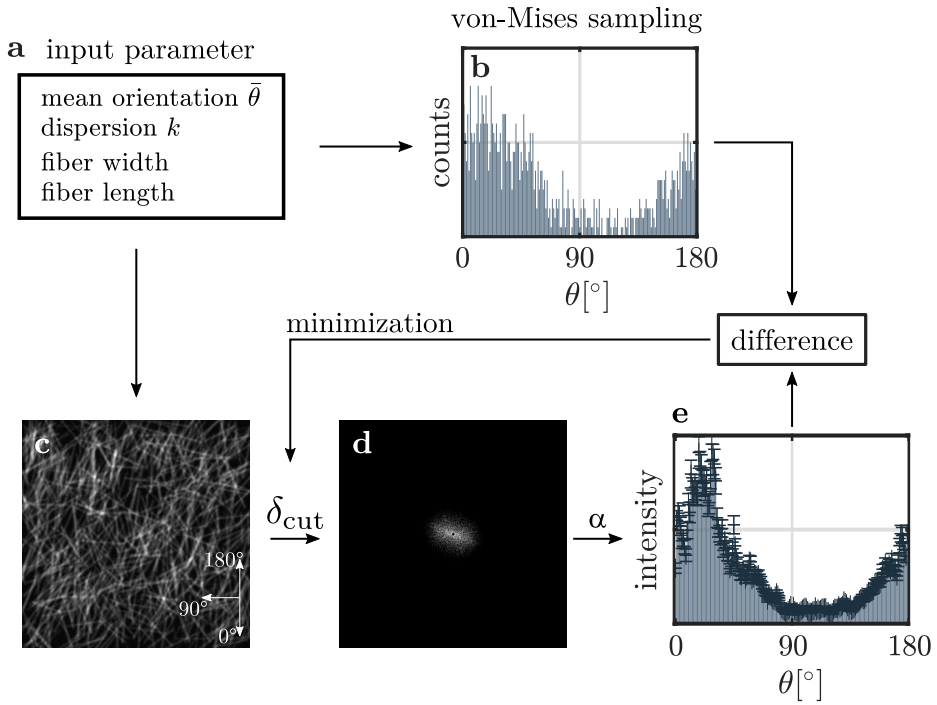

Figure 3.12: Approach to optimize the evaluation parameters of the AF method. (**a**) Input parameters defining the distribution of fiber angles. (**b**) Histogram of fiber angles that are sampled from a von-Mises described by the input parameters k and $\bar{\theta}$. The histogram serves as ground truth for optimizing δ_{cut} and α. A total of $N_f = 1000$ fiber angles are sampled in this example. (**c**) Monte-Carlo test image defined by input parameters of (a). (**d**) Filtered power spectrum (equation (3.34)) using a specific value for δ_{cut}. (**e**) Angular orientation distribution of (d) using equation (3.35) for a specific value of α. δ_{cut} and α are optimized until the squared difference between the histogram of sampled angles and the angular orientation distribution calculated by the AF method (equation (3.54)) reaches a minimum.

δ_{cut} and α is shown in figure 3.12. The input parameter set (figure 3.12 (a)) defines the distribution of fiber angles as well as their width and length. The distribution of sampled fiber angles (figure 3.12 (b)) serves as reference angular orientation distribution $\mathcal{I}_{\text{ref}}(\theta)$. The fiber image in figure 3.12 (c) is generated from the input parameter set and evaluated using the AF method for specific values of δ_{cut} and α to obtain the angular orientation distribution $\mathcal{I}(\theta)$ (figure 3.12 (d) and (e)). Evaluation parameter δ_{cut} and α are modified until the squared difference between the reference and the calculated angular orientation distribution reaches a minimum:

$$\text{SD} = \sum_{\theta} \left(\mathcal{I}_{\text{ref}}(\theta) - \mathcal{I}(\theta) \right). \tag{3.54}$$

This two-parameter optimization is realized by using the *Nelder-Meat simplex* method, which is implemented in MATLAB (*fminsearch*) [87]. A difference smaller than 10^{-3} between the values of δ_{cut} and α of consecutive iterations is employed as termination criterion. Since MATLAB uses the same termination criterion for both parameters,

α is scaled by a factor of 0.1 to match the magnitude of δ_{cut}. This optimization is repeated for a total of $N = 10^4$ Monte-Carlo simulated greyscale images. The input parameters of the Monte-Carlo simulation are randomly chosen to account for different fiber angle distributions and fiber geometries. They are summarized in table 3.2.

Table 3.2: Input parameter ranges of the Monte-Carlo simulation of greyscale fiber images that are used to find optimal parameters of the AF method.

input parameter	values
dispersion k	$[0.01, 20]$
mean orientation $\bar{\theta}$	$[0°, 180°]$
fiber width	$[1, 10]$
fiber length	$[150, 450]$
noise factor	$[0, 1]$

3.6.2 Comparison to the Band-pass Method

Table 3.3: Input parameters of the Monte-Carlo simulation for the comparison of the AF method with the band-pass method.

input parameter	values
dispersion k	$\{0.01, 0.025, \ldots 5\}$
mean orientation $\bar{\theta}$	$[0°, 180°]$
fiber width [pixels]	$\{1, 5, 10\}$
aspect ratio	$\{15, 30, 45\}$
noise factor	$\{0, 0.5, 1\}$

The approach to compare the AF method to the band-pass method is illustrated in figure 3.13. Based on the input parameter of the Monte-Carlo simulation (figure 3.13 (a)), fiber angles are sampled (figure 3.13 (b)) to determine reference parameter b_{ref}, k_{ref} and $\bar{\theta}$ (figure 3.13 (c) and (d)). This approach automatically accounts for sampling errors, which are particularly large for a small number of sampled values (figure 3.8). Simultaneously, sampled fiber angles are used to simulate an artificial fiber image (figure 3.13 (e)). This image is evaluated using the band-pass method (figure 3.13 (f) and (g)) as well as the AF method (figure 3.13 (h) and (i)). The band-pass method is applied using the software *FiberFit* provided by Morrill *et al.* [21]. Following [21], $w_l = 8\,\text{pixels}$ and $w_h = 128\,\text{pixels}$ are chosen as low and high cut-off radius. Parameters of the AF method, δ_{cut} and α, are chosen according to the optimization of the previous section. Calculated parameters of both methods are then compared to the corresponding reference parameters. To analyze the effects of fiber properties such as fiber width, length and angle distribution on the accuracy of both methods, Monte-Carlo images with diverse input parameter are created in a controlled fashion. The input parame-

ters are shown in table 3.3. The result of 20 Monte-Carlo images is averaged for every parameter combination, such that a total of $N_{\mathrm{MC}} = 11340$ images are generated.

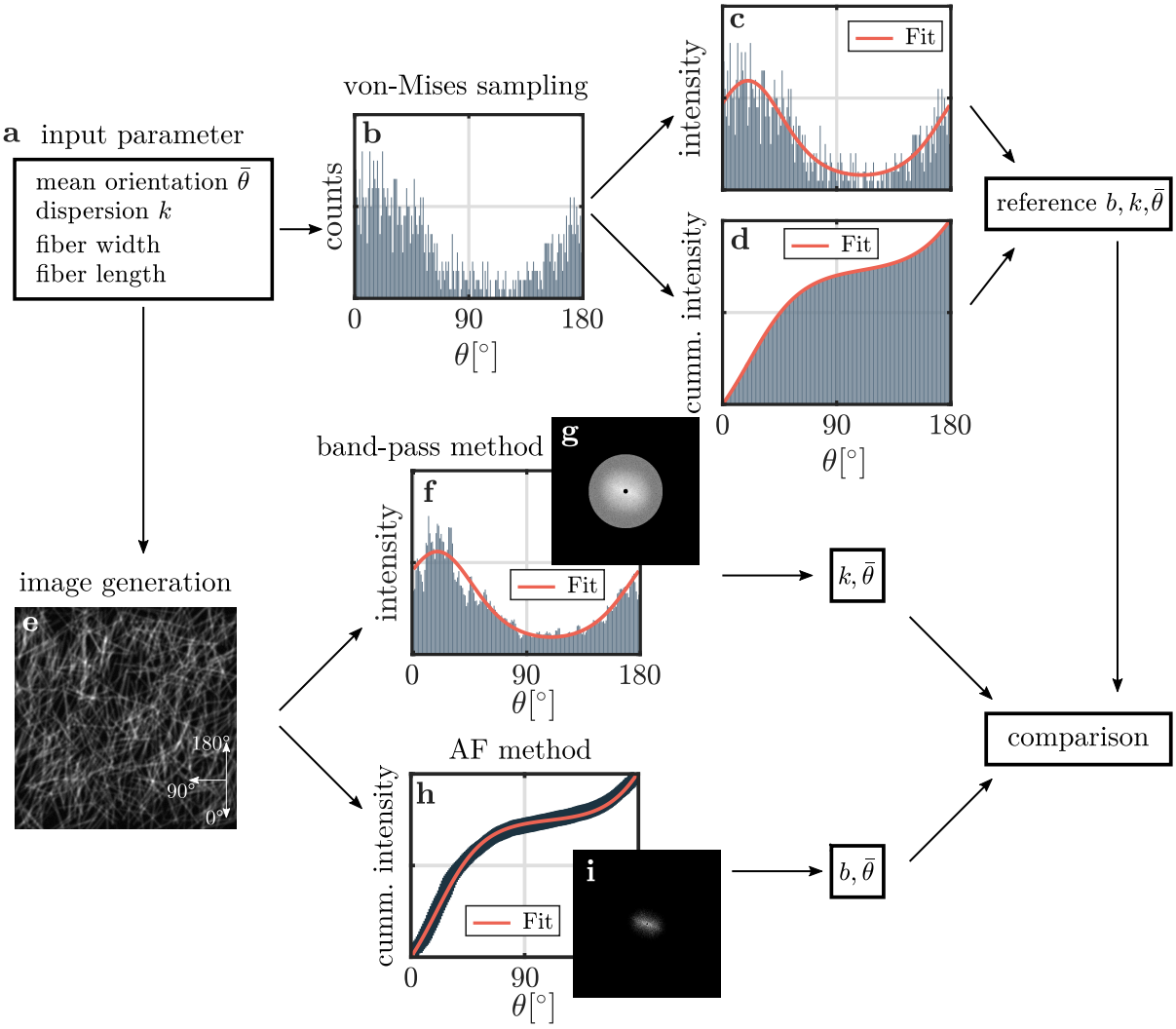

Figure 3.13: Approach to compare the AF method with the band-pass method. (**a**) Input parameters defining the distribution of fiber angles (b) as well as the fiber geometry of the simulated greyscale image in (e). Here, the following parameter are used: $k = 1$, $\bar{\theta} = 20°$, fiber width = 5 pixels, fiber length = 100 pixels. (**b**) Histogram of fiber angles that are sampled from a von-Mises described by the input parameter k and $\bar{\theta}$. A total of $N_f = 1000$ fiber angles are sampled in this example. (**c**) Generation of reference parameters $(k, \bar{\theta})$ by fitting the distribution of sampled angles using a von-Mises function. (**d**) Generation of reference parameters $(b, \bar{\theta})$ by fitting the cumulative distribution of sampled angles using the sigmoid function, defined in equation (3.48). (**e**) Monte-Carlo simulated greyscale images with parameters defined in (a). (**f**) Von-Mises fit of the angular orientation distribution of the band-pass method. (**g**) Band-pass filtered power spectrum of (e). Resulting parameter of the band-pass method are compared to the reference parameters. (**h**) Sigmoid fit of the cumulative angular orientation distribution of the AF method. (**i**) Power spectrum after application of the adaptive filter. Resulting parameter of the AF method are compared to the reference parameters.

3.7 Application to Experimental Data

To demonstrate the applicability of the AF method to experimental data, in-vivo SHG images showing dermal collagen are evaluated [41]. The images were recorded at the multiphoton microscope DermaInspect (section 2.2.3) with a scan time of 13 s and image dimensions of 512×512 pixels. A total of ten images from ten different volunteers are used. Images were recorded at a depth of 30 μm underneath the basal membrane located at the cheek.

To measure the accuracy of the AF method in this setting, ground truth parameters $(b_{\text{ref}}, \bar{\theta}_{\text{ref}})$ need to be determined. This is realized by means of a graphical user interface (GUI), written in MATLAB, to manually trace the fibers with line segments within each image. The GUI is shown in the appendix C.2. The reference angular orientation distribution is calculated from the sum of the length of all line segments that are oriented along a direction $\theta \in [\theta - \delta\theta, \theta + \delta\theta)$:

$$\mathcal{I}_{\text{man}}(\theta) = \frac{1}{\sum_{i=1}^{N_l} \sum_{\theta'=0^\circ}^{180^\circ} l_i(\theta')} \left(\sum_{i=1}^{N_l} \sum_{\theta'=\theta-\delta\theta}^{\theta+\delta\theta} l_i(\theta') \right), \tag{3.55}$$

where $l_i(\theta)$ denotes the orientation distribution of the i-th line segment and N_l the total number of line segments. Consider a line segment, which has a length of L and an orientation in the direction of θ^*. $l(\theta)$ is then defined as:

$$l(\theta) = \begin{cases} L & \text{if } \theta = \theta^*, \\ 0 & \text{else.} \end{cases} \tag{3.56}$$

To increase the number of line segments, the images are each evaluated five times in random order. A smooth orientation distribution is achieved by filtering $\mathcal{I}_{\text{man}}(\theta)$ using a Gaussian kernel with a standard deviation of 1°. Reference parameter $\bar{\theta}_{\text{ref}}$ and b_{ref} are obtained by fitting the corresponding cumulative orientation distribution $\mathcal{C}_{\text{man}}(\theta)$ using the sigmoid function of equation (3.48).

3.8 Results

The results of the Monte-Carlo simulations and the application to in-vivo data are presented and discussed in a paper published in *PLOS ONE* [54]. The publication is shown in 3.10. However, a brief summary of the main findings is given here.

Parameter optimization of the AF method. Optimal parameters of the AF method are successfully identified as $\delta_{\text{cut}} = 2.1\,\%$ and α. Thereby, termination of the optimization is achieved in 99.8 % of the processed images. Explicitly evaluating the deviation to the reference distribution (equation (3.54)) on a defined grid of values $(\delta_{\text{cut}}, \alpha)$, verifies that the global optimum of evaluation parameters is found.

Calculations also revealed that the optimum of both parameters is stable against variations of noise, fiber geometry (width, length) and angular orientation in terms of k and $\bar{\theta}$.

Comparison to the Band-Pass Method. Overall, both methods are found to accurately measure the mean orientation $\bar{\theta}$ with a mean error of $(2.2 \pm 1.8)^\circ$ and $(1.8 \pm 1.4)^\circ$ for the band-pass and the AF method, respectively. The accuracy of measuring $\bar{\theta}$ is found to neither depend on the characteristics of the fiber network nor on the image quality. In contrast, the error of the calculated dispersion of the fiber network is significantly reduced with the AF method. While the mean relative error of the dispersion parameters using the band-pass method is $(33.9 \pm 26.5)\,\%$, it is reduced to $(13.2 \pm 12.7)\,\%$ using the AF method. Increasing the alignment of the fiber network is found to increase the dispersion error of the band-pass method, while the dispersion error of the AF method even decreases to $\sim 5\,\%$. Moreover, both dispersion errors are significantly dependent on the fiber geometry. The band-pass method is not capable of capturing the dispersion of very thin fibers (fiber width = 1 pixel) as errors of $> 50\,\%$ are measured. In turn, the AF method only fails in case of thin and short fibers. The image quality, which is controlled by means of a noise factor, increases the dispersion error of both methods predominantly in aligned fiber networks. However, the quantification of the dispersion of fiber networks with large fibers (width = 10 pixels, length = 450 pixels) is not effected by image noise using either method.

Application to Experimental Data. The AF method is applied to ten images of dermal collagen. The error of the mean orientation $\bar{\theta}$ with respect to the manual tracing of fibers amounts to $(6.0 \pm 4.0)^\circ$, whereas the mean relative error of the dispersion parameter is $(9.3 \pm 12.2)\,\%$.

3.9 Discussion

In this chapter, the AF method was introduced as a Fourier-based method to measure the angular orientation distribution of fibers in scientific images. A major advantage of the AF method over other methods, that measure the angular orientation distribution is the consideration of measurement uncertainties [20, 21, 31, 40, 70–73, 79, 81].
Best results are achieved if the parameter of the adaptive filter is chosen as $\delta_{\text{cut}} = 2.1\,\%$. This indicates that neither a large number of erroneous data points nor a small number of accurate data points provide a good estimate of the angular orientation distribution. In contrast to Polzer *et al.* [68], which used a similar amplification factor, α of the AF method is found to be independent from the characteristics of the fiber network. The generalized character of the AF method by using a relative error constraint allows a reliable application to isotropic and anisotropic fiber networks. In contrast, the band-pass method uses an isotropic filter neglecting the anisotropic characteristic of

the signal, particularly pronounced in aligned fiber networks. As a consequence, the error of the dispersion k of the fiber network using the band-pass method of [21] increases constantly towards a high fiber alignment. In addition, cut-off frequencies of the band-pass method depend on the fiber geometry, which is generally not constant within a fiber image.

Remarkably, a significantly lower performance of the band-pass method compared to the original study of Morrill *et al.* [21] is observed. This is mainly related to the fact, that binary Monte-Carlo images were used to benchmark their method. Superimposing fibers to generate greyscale images might lead to a mismatch between the distribution of sampled fiber angles and the corresponding intensities in the power spectrum, which would decrease the performance of both methods.

A good agreement of the AF method with a manual evaluation was found for dermal collagen fibers in SHG images. The AF method is found to be capable of processing raw data. Existing Fourier based methods rely on contrast enhancement or even on binarizing the images [21, 86].

It has to be emphasized, that quantifying the angular orientation distribution or its cumulative distribution with either a von-Mises function or a sigmoid function, respectively, is reasonable when only a single main orientation is present in the image. In case of multiple main orientations, or a mixture of isotropic and anisotropic contributions, both approaches are not suitable. In these cases, multiple von-Mises functions, or sigmoid functions need to be considered.

3.10 Publication

PLOS ONE

RESEARCH ARTICLE

Noise reduction and quantification of fiber orientations in greyscale images

Maximilian Witte[1,2], **Sören Jaspers**[2], **Horst Wenck**[2], **Michael Rübhausen**[1], **Frank Fischer**[2]*

1 Center for Free-Electron Laser Science (CFEL), University of Hamburg, Hamburg, Germany, **2** Beiersdorf AG, Hamburg, Germany

* frank.fischer@beiersdorf.com

OPEN ACCESS

Citation: Witte M, Jaspers S, Wenck H, Rübhausen M, Fischer F (2020) Noise reduction and quantification of fiber orientations in greyscale images. PLoS ONE 15(1): e0227534. https://doi.org/10.1371/journal.pone.0227534

Editor: William Speier, University of California Los Angeles, UNITED STATES

Received: September 25, 2019

Accepted: December 21, 2019

Published: January 16, 2020

Peer Review History: PLOS recognizes the benefits of transparency in the peer review process; therefore, we enable the publication of all of the content of peer review and author responses alongside final, published articles. The editorial history of this article is available here: https://doi.org/10.1371/journal.pone.0227534

Data Availability Statement: All relevant data are within the manuscript and its Supporting Information files. All images are available from the figshare database (DOI: 10.6084/m9.figshare.10529879).

Abstract

Quantification of the angular orientation distribution of fibrous tissue structures in scientific images benefits from the Fourier image analysis to obtain quantitative information. Measurement uncertainties represent a major challenge and need to be considered by propagating them in order to determine an adaptive anisotropic Fourier filter. Our adaptive filter method (AF) is based on the maximum relative uncertainty δ_{cut} of the power spectrum as well as a weighted radial sum with weighting factor α. We use a Monte-Carlo simulation to obtain realistic greyscale images that include defined variations in fiber thickness, length, and angular dispersion as well as variations in noise. From this simulation the best agreement between predefined and derived angular orientation distribution is found for evaluation parameters $\delta_{cut} = 2.1\%$ and $\alpha = 1.5$. The resulting cumulative orientation distribution was modeled by a sigmoid function to obtain the mean angle and the fiber dispersion. A comparison to a state-of-the-art band-pass method revealed that the AF method is more suitable for the application on greyscale fiber images, since the error of the fiber dispersion significantly decreased from (33.9 ± 26.5)% to (13.2 ± 12.7)%. Both methods were found to accurately quantify the mean fiber orientation with an error of (1.9 ± 1.5)° and (2.3 ± 2.1)° in case of the AF and the band-pass method, respectively. We demonstrate that the AF method is able to accurately quantify the fiber orientation distribution in in vivo second-harmonic generation images of dermal collagen with a mean fiber orientation error of (6.0 ± 4.0)° and a dispersion error of (9.3 ± 12.1)%.

Introduction

The evaluation of the angular distribution of structures in scientific greyscale images is of major importance for various applications like in the analysis of soft tissue fibers e.g. in [1–15], textiles [16, 17], electrospun scaffolds [18–20] or even reinforced concrete [21]. Knowing the angular distribution in fiber reinforced materials gives meaningful insights into their mechanical functionality [22]. For example, in case of biological tissue, the orientation distribution of collagen fibers can be directly inserted into biomechanical material models for finite element simulations [23, 24].

Funding: Beiersdorf AG provided support in the form of salaries for authors MW, SJ, HW and FF, but did not have any additional role in the study design, data collection and analysis, decision to publish, or preparation of the manuscript. The specific roles of these authors are articulated in the 'authors contribution' section.

Competing interests: We have the following interests: MW, SJ, HW and FF are employed by Beiersdorf AG. There are no patents, products in development or marketed products to declare. This does not alter our adherence to all the PLOS ONE policies on sharing data and materials, as detailed online in the guide for authors.

Fiber images from different image modalities such as scanning electron microscopy [25], histology [1], and laser scanning microscopy as e.g. in [2, 3, 7, 8, 10, 15, 22, 26–29] provide diverse image properties in terms of sharpness, contrast and fiber appearance. Thus, a variety of automated image processing techniques were developed including ellipsoidal fitting in the spatial domain [30], fiber tracking [31], the structure tensor method [10] and Fourier domain image processing [7, 9, 12, 32–34].

Looking into the Fourier method in more detail, it can be split into four major steps: image preprocessing, Fourier transform and filtering, calculation of the angular distribution and its quantification.

In the Fourier domain it is of key importance to reduce noise as it was shown that rotationally symmetric band-pass filtering significantly improve the accuracy of the method [6, 33, 34]. In mechanical experiments, (e.g. stretching of fiber reinforced material), fiber properties such as angular distribution and diameter get modified [2, 35]. Accordingly, isotropic as well as anisotropic signal responses in the Fourier domain has to be accounted for, which requires an adaptive anisotropic filtering. Quantification of the angular orientation distribution in terms of mean angle and fiber dispersion is commonly realized by fitting a semi-circular von-Mises distribution to the angular orientation distribution [6, 10, 12, 22, 30, 34, 36, 37].

Here, we investigate the Fourier method by exploiting objective approaches at any of the four mentioned steps. To approach the requirement of adaptive anisotropic filtering we introduce an image filter, which is based on the propagation of measurement uncertainties through the discrete Fourier transform. And finally, in terms of an improved quantification of the angular orientation distribution, we test a sigmoid function to model the cumulative orientation distribution.

To capture the performance of our method, we quantitatively compare it to a band-pass method, introduced by Morrill et. al [34], which was proven to provide an accurate quantification of the angular orientation distribution. Based on realistic Monte-Carlo simulated greyscale fiber images we observe the evolution of accuracy with respect to fiber width, fiber aspect ratio, degree of alignment and image quality.

To validate the applicability of our method on real images, we quantify the mean fiber orientations and dispersions in vivo second-harmonic generation (SHG) images of collagen fibers of human skin [38].

Material and methods

Any calculations were performed using MATLAB [39]. The *Image Processing Toolbox* [40] as well as the *Curve Fitting Toolbox* [41] were applied.

Note that in the following the term *uncertainty* is used for statistical measurement errors, whereas the term *error* is associated with the deviation of a value to its reference.

Fourier transform and uncertainty propagation

Let $I(x, y)$ be an image with $x \in [0, X]$ and $y \in [0, Y]$. The discrete Fourier transform $I(x, y) \rightarrow \mathcal{F}[I(x, y)] = \hat{I}(u, v)$ is given by:

$$\hat{I}(u, v) = \sum_{y=0}^{Y-1} \sum_{x=0}^{X-1} I(x, y) \cdot e^{-2\pi i \left(\frac{x}{X}u + \frac{y}{Y}v\right)} \quad , \tag{1}$$

where the real and imaginary parts read as

$$\Re[\hat{I}(u, v)] = \sum_{y=0}^{Y-1} \sum_{x=0}^{X-1} I(x, y) \cos\left(2\pi \mathrm{i}\left(\frac{x}{X}u + \frac{y}{Y}v\right)\right) \tag{2}$$

$$\Im[\hat{I}(u,v)] = -\sum_{y=0}^{Y-1}\sum_{x=0}^{X-1} I(x,y)\sin\left(2\pi\mathrm{i}\left(\frac{x}{X}u+\frac{y}{Y}v\right)\right) \tag{3}$$

The intensities of the angular distribution are calculated by evaluating the centered power spectrum of $I(x, y)$, which is defined as the squared magnitude of $\hat{I}$:

$$\mathcal{P}(u,v) = |\mathcal{F}[I(x,y)]|^2 = \Re[\hat{I}]^2 + \Im[\hat{I}]^2 \tag{4}$$

Any intensity image exhibits a specific intensity uncertainty $\Delta I(x, y)$, which is at least equal to the photon counting uncertainty $\Delta I(x,y) = \sqrt{I(x,y)}$ assuming Poissonian statistics [42]. The uncertainty of the real and imaginary part, $\Delta\Re$ and $\Delta\Im$ are given by propagating Eqs 2 and 3:

$$\Delta\Re[\hat{I}(u,v)] = \sqrt{\sum_{y=0}^{Y-1}\sum_{x=0}^{X-1}\Delta I^2(x,y)\cos^2\left(2\pi\mathrm{i}\left(\frac{x}{X}u+\frac{y}{Y}v\right)\right)} \tag{5}$$

$$\Delta\Im[\hat{I}(u,v)] = \sqrt{\sum_{y=0}^{Y-1}\sum_{x=0}^{X-1}\Delta I^2(x,y)\sin^2\left(2\pi\mathrm{i}\left(\frac{x}{X}u+\frac{y}{Y}v\right)\right)} \tag{6}$$

Since $\Delta\Re[\hat{I}]$ and $\Delta\Im[\hat{I}]$ both depend on the image uncertainty ΔI, the covariance $\Delta\hat{I}_{\Re\Im}$ has to be taken into account [43, 44]:

$$\Delta\hat{I}_{\Re\Im}(u,v) = \sqrt{\sum_{y=0}^{Y-1}\sum_{x=0}^{X-1}\Delta I^2(x,y)\sin\left(2\pi\mathrm{i}\left(\frac{x}{X}u+\frac{y}{Y}v\right)\right)\cos\left(2\pi\mathrm{i}\left(\frac{x}{X}u+\frac{y}{Y}v\right)\right)} \tag{7}$$

The calculation of $\Delta\mathcal{P}(u, v)$ is straight forward:

$$\Delta\mathcal{P} \quad = 2\sqrt{(\Re[\hat{I}]\cdot\Delta\Re[\hat{I}])^2 + (\Im[\hat{I}]\cdot\Delta\Im[\hat{I}])^2 + 2\cdot\Re[\hat{I}]\Im[\hat{I}]\cdot\Delta\hat{I}^2_{\Re\Im}} \tag{8}$$

Noise simulation

To verify the validity of our image transformations and uncertainty calculations, a Monte-Carlo based noise simulation with different test images was carried out.

The uncertainty of each pixel, $\Delta I(x,y) = \sqrt{I(x,y)}$, is assumed as a normal-distributed fluctuation of a repeated measurement $I_k(x, y)$ around the measured intensity $I(x,y) = \frac{1}{N}\sum_{k=0}^{N} I_k(x,y) = \frac{1}{N}\sum_{k=0}^{N}(I(x,y)+\delta I_k(x,y))$ with $\frac{1}{N}\sum_{k=0}^{N}\delta I_k(x,y) = 0$. N is the number of measurements (Fig 1).

The propagation of the image uncertainty $\Delta I(x, y)$ through an arbitrary image operation $I(x, y) \rightarrow C(I(x, y))$, $\Delta I(x, y) \rightarrow \Delta C(I(x, y))$ is compared to the standard deviation of the Monte-Carlo simulated images ΔC_{MC}:

$$\Delta C_{\mathrm{MC}} = \sqrt{\frac{1}{N-1}\sum_{k=0}^{N}[C(I(x,y)+\delta I(x,y)) - C(I(x,y))]^2} \tag{9}$$

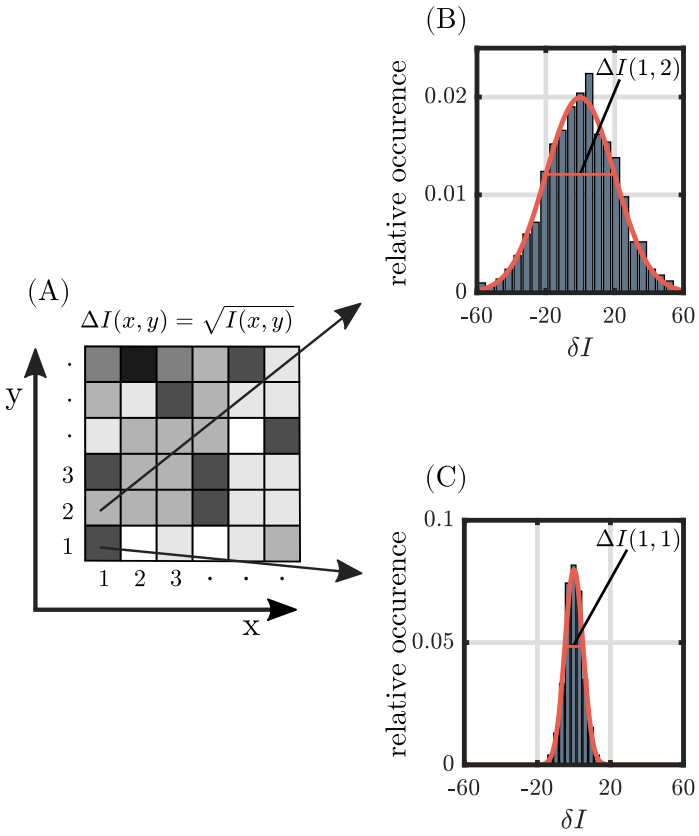

Fig 1. Schematic outline of the pixel-wise noise simulation. (A) The photon counting noise results in the standard deviation of each image pixel. In the pixel-wise uncertainty simulation, normal distributions are used to sample the intensity deviation $\delta I(x, y)$ in each pixel, as exemplary shown in (B) and (C) for pixels (1, 2) and (1, 1), respectively. Thereby, high intensity pixels are associated with a large absolute deviation of potential intensity values (B).

https://doi.org/10.1371/journal.pone.0227534.g001

The result of Eq 9 is then compared to the calculated uncertainty ΔC by computing the relative deviation as:

$$\Delta_{\mathrm{MC}} = (\Delta C - \Delta C_{\mathrm{MC}})/\Delta C_{\mathrm{MC}} \tag{10}$$

Preprocessing and filtering

Artifact removal. The computation of the discrete Fourier transform (Eq 1) intrinsically assumes a periodical continuation of the image causing cross-like artifacts to appear in the Fourier domain mainly along the major axis (Fig 2). The magnitude of these artifacts depends on the image intensities near the boundary. Weighting functions in the spatial domain such as the Hamming or Welch window, which gradually reduce the image intensity towards the boundary, are able to remove these artifacts [6, 12, 16, 32, 36, 45]. However, applying window functions is a trade-off between reducing the image content and removing the artifacts in the Fourier domain. To overcome the drawback of weighting functions in the spatial domain, the

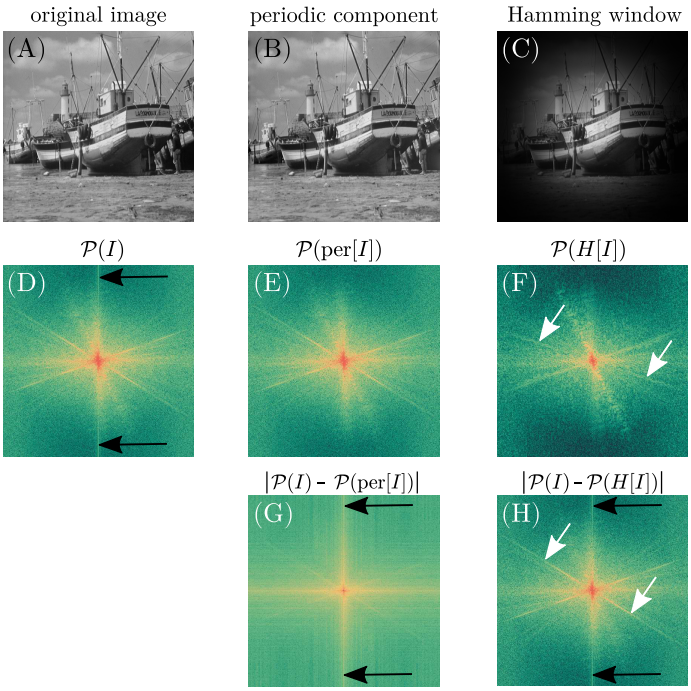

Fig 2. Effect of spatial domain image filters on the power spectrum. Images in the spatial domain are shown in greyscale (A-C), whereas the respective power spectra are shown in false colors as well as in logarithmic scale for a better visibility (D-H). Power spectrum values are shifted, such that low frequencies are located in the center. (A) shows the original image *boat* [46]. (B) shows the periodic component of the periodic plus smooth decomposition of Moisan et. al [45]. Apart from small areas near the image boundary, the entire image information of the original image is conserved. However, as shown in (C), the Hamming window reduces the image information gradually towards the image boundary. (D), the discrete Fourier transform of images causes cross-like artifacts (black arrows) to appear in the power spectrum as the image is assumed to be periodical. (E-F), these artifacts disappear in the power spectra if firstly either the periodic decomposition or the Hamming window are applied. Note that the artifacts reappear in (G) and (H) where the absolute difference of the power spectra of the filtered images with respect to the power spectrum of the original image are shown. (G) also reveals that mostly non-directional information is removed from the power spectrum of the original image as only cross-like shapes are pronounced. Other than in (F), where the reduction of image information by the Hamming window also affects the power spectrum, which appears less sharp (white arrows) compared to (D) and (E).

https://doi.org/10.1371/journal.pone.0227534.g002

linear decomposition of the image $I(x, y) \rightarrow \mathrm{per}[I(x, y)]$ into a smooth component $s(x, y)$ and a periodic component $p(x, y) = \mathrm{per}[I(x, y)]$ with $I(x, y) = p(x, y) + s(x, y)$ as proposed by Moisan [45] is used here (Fig 2). Since the periodic component per(I) differs only slightly from I (Fig 2), the effect of the periodic mapping on ΔI is believed to be negligible. Verification of the effect of the periodic mapping on the image uncertainty is carried out by applying the Monte-Carlo noise simulation and evaluating Eq 9 to three different test images. Classic image processing greyscale test images including the *Lena*, *Cameraman* and *Boat* image were chosen [46]. The *Boat* image serves as example in several figures. The image uncertainty ΔI is assumed as $\Delta I = \sqrt{I}$, which is indeed an arbitrary choice but since the focus here is on validation only the assumption is reasonable.

The overall mean deviation (Eq 10, $N = 10^5$ iterations) averaged over all images and the entire image range amounts for $\Delta_{\mathrm{MC}} = (0.01 \pm 2.21)\%$. The image uncertainty exceeds the Monte-

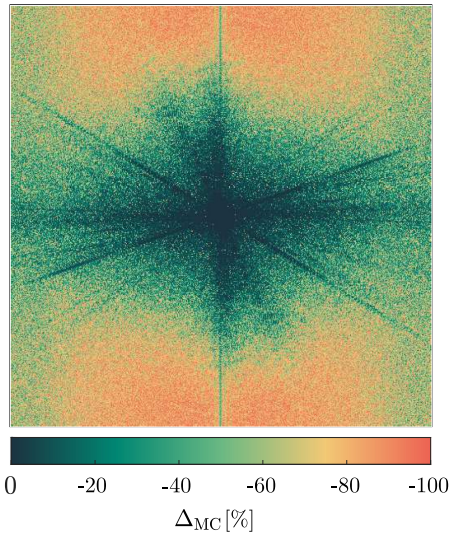

Fig 3. Relative uncertainty between calculated and simulated uncertainty of the power spectrum. The relative deviation between the theoretical uncertainty $\Delta\mathcal{P}$ and the Monte-Carlo simulated uncertainty $\Delta\mathcal{P}_{MC}$, $\Delta_{MC} = (\Delta\mathcal{P} - \Delta\mathcal{P}_{MC})/\Delta\mathcal{P}_{MC}$ of the *Boat* image (Fig 4). Note that the spectrum values are shifted such that low frequencies are located in the origin and that the original image was used here.

https://doi.org/10.1371/journal.pone.0227534.g003

Carlo calculated uncertainty at the boundary by (23 ± 6)%. Thus, the original image uncertainty is slightly underestimated due to the uncertainty of the remaining pixels by −(0.23 ± 0.61)%. This deviation is considered as sufficiently low to reasonably assume $\Delta(\mathrm{per}(I)) = \Delta I$. Detailed results for every test image are listed in the supplementary (S1 Table).

Power spectrum filtering. The same set of test images is used for validating the calculated uncertainty of the real and imaginary parts (Eqs 5 and 6). The averaged relative deviation (Eq 10) amounts for (0.00 ± 0.22)% for the real and imaginary parts of all images.

Lastly, the Monte-Carlo method was applied on Eq 8 for the same images and same number of iterations. Averaging the relative deviation Δ_{MC} over the entire image yields a maximum deviation of −(59.32 ± 26.48)% (S2 Table). However, Δ_{MC} correlates well with the relative uncertainty of the power spectrum $\Delta\mathcal{P}/\mathcal{P}$ (Fig 3), which ranges from minor values up to relative uncertainties above 800%. Restricting the area of evaluation to pixels which exhibit a maximum relative uncertainty of 100% increases the accuracy of the uncertainty calculation to −(8.09 ± 5.46)% at maximum (S2 Table, Fig 4). Excluding values with a high relative uncertainty naturally filters the power spectrum, while leaving the back-transformed image relatively unaffected.

In order to find the optimal cut-off value δ_{cut}, images with known ground truth have to be used. Since fibrous images are in the scope of this work, Monte-Carlo generated greyscale fiber images serve as test images for determining the optimal cut-off value.

Monte-Carlo image generation

Besides the Monte-Carlo simulation for noise simulation, another Monte-Carlo routine was implemented for the generation of images containing fibers with a known angular distribution.

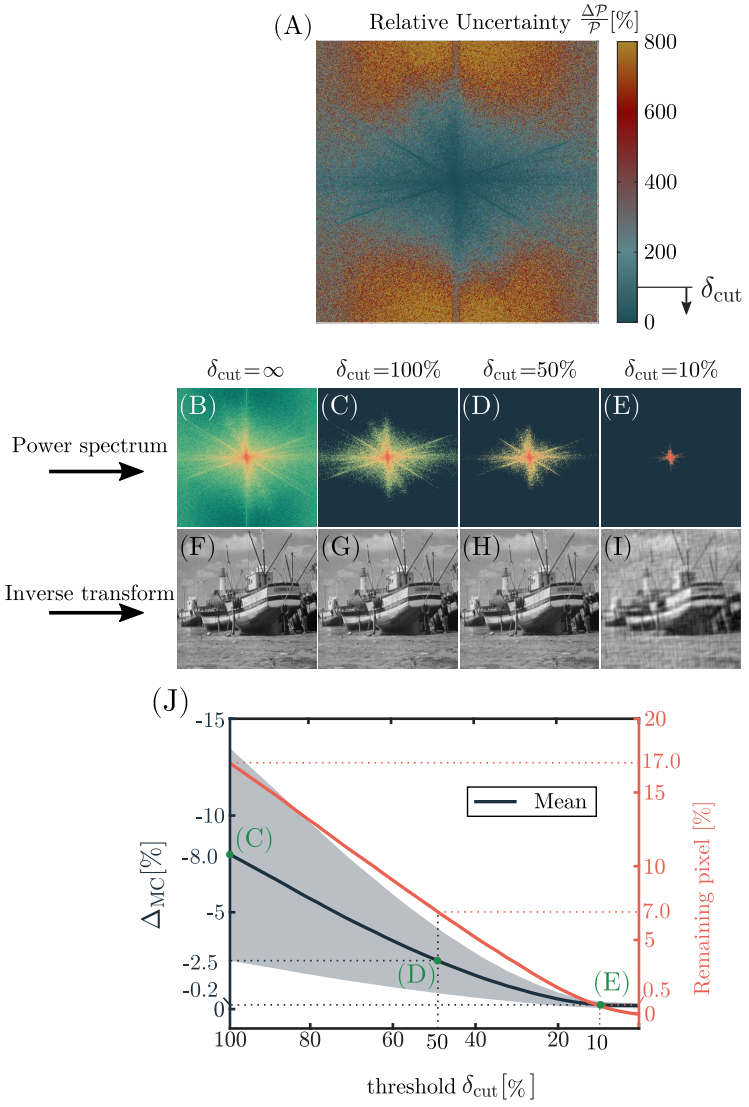

Fig 4. Relative uncertainty and filtering of the power spectrum. The relative uncertainty (A) of the power spectrum increases with distance from the origin to values above 800%. A filter mask for the power spectrum is achieved from excluding relative uncertainties above δ_{cut}. (B-E) show the filtered power spectra for different δ_{cut} with the respective inverse Fourier transformations in (F-I). The number of remaining pixels after filtering as well as the error of the uncertainty calculation compared to the Monte-Carlo simulation Δ_{MC} is shown in (J). The mean error, its standard deviation (*grey* shaded areas) as well as the number of remaining pixels gradually decrease towards a lower threshold δ_{cut}. Note that even if 99.5% of the pixels are excluded, the contours of the major image components are still visible (E).

https://doi.org/10.1371/journal.pone.0227534.g004

A single fiber is defined by its width, length, orientation and location. While several publications dealt with the generation of binary fiber images [12, 34] we focus on the generation of random greyscale intensity images including noise knowing that the contrast of the fibers influence their contribution within the power spectrum [36]. Since our goal here is to find the

optimal evaluation parameters for a large variety of realistic images similar to the SHG images of dermal collagen that are used later on, the usage of binary images is not reasonable. In addition, our approach aims on evaluating images without any preprocessing, thus the test images should cover different image qualities.

The orientation of the fibers is sampled from a semi-circular π-periodic von-Mises distribution:

$$P(\theta;\bar{\theta},k) = \frac{1}{\pi I_0(k)} e^{k\cdot\cos(2(\theta-\bar{\theta}))} \tag{11}$$

with the dispersion parameters k and $\bar{\theta}$ defining the width and the center of the distribution. $I_0(k)$ is the modified zero order bessel function $I_0(k) = \frac{0}{\pi}\int_0^{\pi} \cos(x)\mathrm{d}x$. A rejection sampling algorithm is used to sample fiber angles. The intensity of each sampled fiber with certain width and aspect ratio is added to the existing image to obtain a greyscale image. The image is then smoothed using a gaussian kernel with standard deviation of two to slightly dissolve sharp edges. After that, intensities are scaled such that the maximum intensity is equal to the maximum intensity of a 16-bit intensity image. Width, aspect ratio and dispersion k of the fibers affect the accuracy of the image processing algorithm [34]. The minimum fiber width amounts for one pixel as the maximum fiber width is confined by the image size and the maximum allowed aspect ratio. As images at 512 × 512 pixels are generated, a maximum aspect ratio of 45 and a maximum fiber width of 10 are chosen to still allow for an effective placement of the fibers within the image boundaries. A minimum aspect ratio of 10 was proposed by Marquez et. al [6] to allow for a reasonable evaluation of orientation. As we are generating greyscale fiber images with overlapping fibers we choose a minimum aspect ratio of 15. Dispersed as well as aligned fiber networks are achieved by sampling k within [0.01, 5].

To enforce different image qualities, we introduce a noise factor. The noise factor ranges from a minimum of 0, which corresponds to a completely denoised image up to a maximum of 1 which corresponds to random speckle noise which can value up to half of the maximum intensity of the image.

Angular distribution generation

Quantifying the angular orientation of the fibers by means of mean angle and fiber dispersion requires the calculation of the total intensity of each angle of the filtered power spectrum. This is realized by using a radial summation. The total intensity of a certain angle is given by the sum over all pixels of the power spectrum, that are included within the angular range $[-\delta\theta, +\delta\theta]$. The contribution of each pixel is weighted by the percentage of area, which is included in $[-\delta\theta, +\delta\theta]$.

$$\mathcal{I}(\theta) = \sum_{\theta\in[-\delta\theta,\delta\theta]}\sum_{r}\mathcal{P}'(\theta,r)\cdot w_\theta(\theta,r) \qquad \text{with} \qquad \frac{1}{X\cdot Y}\sum_{\theta}\sum_{r} w_\theta(\theta,r) = 1 \tag{12}$$

The uncertainty propagates as:

$$\Delta\mathcal{I}(\theta) = \sqrt{\sum_{\theta\in[-\delta\theta,\delta\theta]}\sum_{r}(\mathcal{P}'(\theta,r)\cdot w_\theta(\theta,r))^2} \tag{13}$$

The calculated intensity is normalized such that $\sum_\theta \mathcal{I}(\theta) = 1$. An issue that is faced here are high intensity pixels close to the center of the power spectrum, which do not provide any directional information. The intensity of these pixels is several magnitudes higher than the intensities of interest, which causes artifacts in the angular distribution. A sensitivity analysis

of a set of test images showed that zeroing pixel with a distance smaller than 3 pixels from the center is sufficient to remove these artifacts (S1 Fig).

Additionally, a modified intensity is defined, which exploits the anisotropy of the introduced filter. Let $N_{\Delta\theta}$ be the number of non-zero pixels within the angular range $\Delta\theta$ of the filtered power spectrum $\mathcal{P}'$. The modified intensity then reads as:

$$\mathcal{I}(\theta) = N_{\Delta\theta}^{\alpha} \cdot \sum_{\theta\in[-\delta\theta,\delta\theta]} \sum_{r} \mathcal{P}'(\theta, r) \cdot w_{\theta}(\theta, r), \tag{14}$$

with the uncertainty given by:

$$\Delta\mathcal{I}(\theta) = N_{\Delta\theta}^{\alpha} \cdot \sqrt{\sum_{\theta\in[-\delta\theta,\delta\theta]} \sum_{r} (\mathcal{P}'(\theta, r) \cdot w_{\theta}(\theta, r))^2}, \tag{15}$$

where α defines the impact of $N_{\Delta\theta}$. A value of $\alpha = -1$ corresponds to an averaged intensity, whereas $\alpha > 0$ amplifies the number of remaining pixels within the given angular range. The ideal choice of α strongly depends on the chosen cut-off value δ_{cut} for the power spectrum. For example in case of a low cut-off value, the filtered power spectrum $\mathcal{P}'$ might exhibit a high anisotropy, where $\alpha > 1$ might lead to a more accurate result compared to the unweighted sum. Considering a very high cut-off value, $\mathcal{P}' = \mathcal{P}$ holds and the number of summed pixels should not have any influence. Thus $\alpha = -1$ might be the value of choice. A somewhat similar approach was used by Polzer et. al [36], which used a factor to empower the entire intensity distribution $\mathcal{I}(\theta)$.

To find the optimal parameter set $[\theta_{\text{cut}}, \alpha]$, a two parameters optimization algorithm is applied on $N = 10^4$ Monte-Carlo generated images. For this purpose we use the MATLAB-implemented Nelder-Mead simplex method (*fminsearch*) [47]. To account for different types of images, fiber properties, namely width, aspect ratio and dispersion as well as the noise factor are randomly sampled from the respective interval specified before. We use the mean squared difference (MSD) between the calculated orientation distribution $\mathcal{I}_{\text{MC}}(\theta)$ and the prescribed orientation distribution $\mathcal{I}(\theta)$ as objective function, which is minimized:

$$\text{MSD} = \frac{1}{N-1} \sum_{i=0}^{N} \text{SD}_i \qquad \text{with} \qquad \text{SD}_i = \sum_{\theta} (\mathcal{I}_i(\theta) - \mathcal{I}_{i,\text{MC}}(\theta))^2 \tag{16}$$

Termination was enforced as soon as the difference between consecutive iterations of both parameters was smaller than 10^{-3}. MATLAB uses the same termination criterion for both parameters. Therefore, we scaled α by a factor of 0.1 to match the magnitude of δ_{cut}. A subset of 10^3 images was evaluated prior optimization on a 10×10 grid with $\alpha \in [-1, 8]$ and with $\delta_{\text{cut}} \in [1, 100]$% to ensure that the calculated minimum is global and to get an estimate for the starting values of each parameter. We estimated that $\alpha = 2$ and $\delta_{\text{cut}} = 2\%$ provide a suitable set of starting values.

Angular distribution quantification

Conventional approach. The common approach for quantifying the mean orientation and dispersion is to fit a semi-circular von-Mises function (Eq 11) to the distribution $\mathcal{I}(\theta)$. This approach provides accurate results in case of aligned fibers but looses accuracy in case of isotropic distributions [34]. Additionally, the use of an arbitrary averaging range to smooth the angular orientation distribution prevents a meaningful and objective interpretation of the data in terms of e.g. the number of dominant fiber directions.

New fitting approach. To find an objective evaluation procedure which reliably can deal with unprocessed data, fitting the cumulative distribution function (CDF) $\mathcal{C}(\theta)$ is quite appealing, since the data are naturally smoothed:

$$\mathcal{C}(\theta) = \sum_{\theta'=-90^\circ}^{\theta} \mathcal{I}(\theta') \tag{17}$$

The uncertainty of $\Delta\mathcal{C}$ is given by a quadratic summation:

$$\Delta\mathcal{C}(\theta) = \sqrt{\sum_{\theta'=-90^\circ}^{\theta} (\Delta\mathcal{I}(\theta'))^2} \tag{18}$$

Since the choice of the starting angle of the summation (Eq 17) is arbitrary, the uncertainty $\Delta\mathcal{C}$ must be independent from θ. Thus, the maximum uncertainty of $\mathcal{C}(\theta)$ is set as uncertainty for all angles. A peak in the angular distribution corresponds to a step in the cumulative distribution, which approaches a first order polynomial for isotropic distributions. To model the cumulative orientation distribution a sigmoid function is chosen:

$$S(\theta; b, \bar{\theta}) = \frac{1}{1 + e^{-b\cdot(\theta-\bar{\theta})}} \tag{19}$$

The advantage of fitting a von-Mises distribution is its semi-circularity, namely $P_{\mathrm{VM}}(\theta) = P_{\mathrm{VM}}(\theta + 180^\circ)$. Since the cumulative distribution function is monotonically increasing, the corresponding condition reads as $\mathcal{C}(\theta) = \mathcal{C}(\theta - 180^\circ) + 1 = \mathcal{C}(\theta + 180^\circ) - 1$. In order to meet this condition, Eq 19 is modified by adding neighboured sigmoid functions accounting for the added offsets:

$$S_{\mathrm{circ}}(\theta; b, \bar{\theta}) = S(\theta; b, \bar{\theta}) + S(\theta + 180^\circ; b, \bar{\theta}) - S(180^\circ; b, \bar{\theta}) + S(\theta - 180^\circ; b, \bar{\theta}) - S(-180^\circ; b, \bar{\theta}) \tag{20}$$

Validation

Comparison to band-pass filtering. In the following we refer to our method as AF method (adaptive filtering method) for convenience. To capture the performance of the implemented procedure we compare the AF method to the state of the band-pass method, which has been proven to provide more accurate results than other methods [34]. In order to observe the influence of fiber and image properties on the accuracy of both methods, we created a dataset, where each property is altered separately using the introduced Monte-Carlo method for generating greyscale images. The following sets of values were used for creating the image dataset:

$$\text{width} = \{1, 5, 10\}, \qquad \text{AR} = \{15, 30, 45\}, \qquad \text{noise factor} = \{0, 0.5, 1\} \tag{21}$$

$$\text{and} \quad k = \{0.01, 0.25, ..., 5\} \tag{22}$$

In order to enable a reasonable statistical evaluation, 20 images with random mean fiber orientation $\bar{\theta}$ are created for each category, which adds up to a total of $N = 3^3 \cdot 21 \cdot 20 = 11,340$ images. Each image is evaluated using the AF method using the optimal evaluation parameters $\delta_{\mathrm{cut}} = 2.1\%$ and $\alpha = 1.5$ and using the band-pass method of Morrill et. al by applying their provided software *FiberFit*. We follow their recommendations of the upper and lower cutoff

parameter $t = 2$ and $t = 32$ yielding a lower cutoff frequency of 8 and an upper cutoff frequency of 128. The resulting evaluation parameters, mean orientation $\bar{\theta}$ and dispersion coefficients b and k are compared to the reference parameters. To account for Monte-Carlo sampling errors, reference mean orientation and distribution parameter k are obtained from fitting the frequency distribution of sampled fiber angles. The reference dispersion parameter b is obtained from fitting the cumulative frequency distribution of sampled fiber angles using the modified sigmoid function (Eq 20). Mean orientations $\bar{\theta}_{FF}$ of the FiberFit software were inverted and shifted to match our coordinate system $\bar{\theta}'_{FF} = 180^{\circ} - \bar{\theta}_{FF}$. Additionally, angles exceeding the interval $[0^{\circ}, 180^{\circ}]$ were shifted by 180°. Comparisons to the reference parameters are performed by considering the absolute error of the mean orientation angle angle $\Delta\bar{\theta}$ and the absolute relative error of the dispersion parameters Δb_{rel} and Δk_{rel}. A small fraction of images were found to exhibit large relative errors Δb_{rel} and Δk_{rel}. Those are classified as outliers if they are exceeding three times the interquartile range of the respective distribution.

Statistics. A paired t-test is used to calculate the level of significance (p-value) between the error of both evaluation methods for the same subset of images in terms of width, aspect ratio, dispersion and noise. If a value is classified as outlier, the corresponding value of the pair is excluded for p-value calculation. An unpaired t-test is used for p-value calculations among groups with different noise factor. Significance levels of 0.05, 0.01 and 0.001 are marked as $(^{*}, ^{**}, ^{***})$, respectively.

Application on experimental data. Finally, we checked the applicability of the AF method on in vivo experimental data. We use SHG-images of dermal collagen that were recorded using a CE-certified multi-photon microscope (DermaInspect) for in vivo applications, which was developed in collaboration with Jenlab GmbH (Jena, Germany). The SHG signal was captured using an excitation wavelength of 820 nm together with a specific bandpass filter (410 ± 10 nm, AQ 410/20m-2P, Chroma Technology Corp., Bellows Falls, VT). A scan time of 13 s and image dimensions of 512 × 512 pixels with a $220 \times 220\ \mu m$ field of view were chosen as image acquisition parameters. For a detailed description of the microscope refer to [48–50]. In total, ten SHG images of dermal collagen were taken from ten different volunteers at a depth of $30\ \mu m$ under the basal membrane located at the cheek.

This study was conducted according to the recommendations of the current version of the Declaration of Helsinki and the Guideline of the International Conference on Harmonization Good Clinical Practice, (ICH GCP). In addition, this study was approved and cleared by the institutional ethics review board (Beiersdorf AG, Hamburg, Germany). Written informed consent was obtained from each volunteer.

To get the reference angular distribution we manually trace the collagen fibers. Statistical variance is achieved by tracing each image three times in random order. The angular orientation distribution is achieved from adding up the length of each fiber being oriented along a certain angle in 1° steps. A smooth distribution is obtained by filtering the data using a Gaussian kernel with a standard deviation of 1°. Reference parameters $\bar{\theta}_m$ and b_m are obtained by fitting the modified sigmoid function (Eq 20).

Results

Angular distribution generation

Fig 5 shows the result of the optimization procedure of the evaluation parameters δ_{cut} and α. Apart from a minor fraction of outliers, data points of minimal difference spread within $\delta_{\mathrm{cut}} < 4\%$ and $0 < \alpha < 3$. Since the frequency distributions $p(\delta_{\mathrm{cut}})$ and $p(\alpha)$ are not normally distributed, the median value of both parameters is considered as estimation of the overall minimum

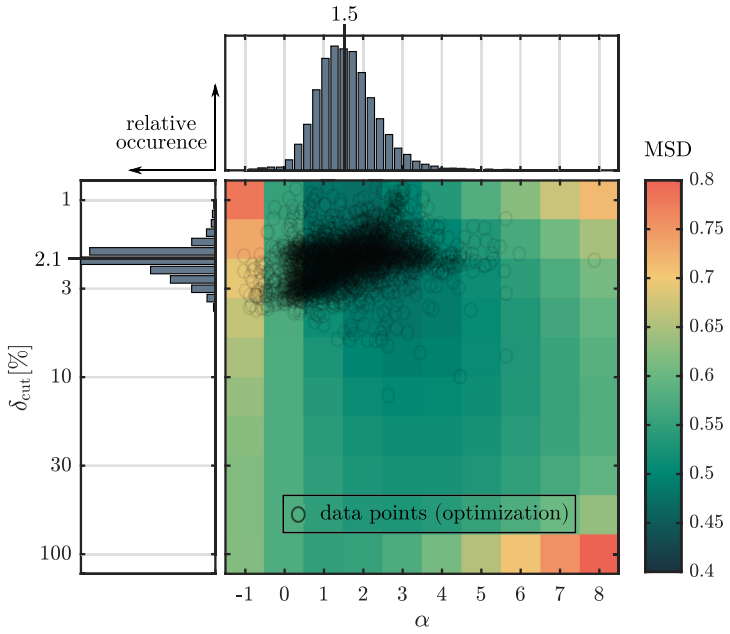

Fig 5. Effect of evaluation parameters δ_{cut} and α on the error. False colours indicate the mean squared difference MSD between the computed angular distributions and their reference on a subset of $N = 10^3$ images for a discrete set of 10×10 parameter values. Data points represent the optimal parameter set for each image ($N = 10^4$) based on the exploited two parameters Nelder-Mead optimization algorithm which used the squared difference between reference and calculated orientation distribution as objective function. Histograms show the frequency distribution of parameter δ_{cut} and α. The median values of both distributions($\delta_{cut} = 2.1\%$, $\alpha = 1.5$) were identified as optimal evaluation parameters. The mean number of iterations, until the termination criterion was met, is 23 ± 9. Only 0.2% of the images reached the maximum number of iterations, which was set to 100.

https://doi.org/10.1371/journal.pone.0227534.g005

($\delta_{cut} = 2.1\%$, $\alpha = 1.5$). The mean squared difference minimizes for α in [1, 3] and for $\delta_{cut} < 10\%$ indicating that a global minimum is considered. Subsequent calculations using the AF method are performed with $\delta_{cut} = 2.1\%$ and $\alpha = 1.5$. Median values of the mean squared difference as a function of fiber dispersion k, image quality (NF) and fiber geometry (width, aspect ratio) are provided in the supplement (S2 Fig).

Validation

Comparison to band-pass filtering. The overall error of the mean fiber orientation, $\Delta\bar{\theta}$ amounts for $(2.2 \pm 1.8)^\circ$ and $(1.8 \pm 1.4)^\circ$ ($p < 0.001$) for the band-pass and the AF method, respectively (Table 1). Note that for calculating the overall error $\Delta\bar{\theta}$ highly dispersed fiber

Table 1. Overall error of mean orientation and dispersion determined by the band-pass method and by the AF method. Note that f indicates the percentage of data points that were classified as outlier.

	$\Delta\bar{\theta}[^\circ](k > 1)$	$\Delta b_{rel}\|\Delta k_{rel}[\%]$	$f_{\Delta b\|\Delta k}[\%]$	R^2
band-pass method	2.3 ± 2.1	33.9 ± 26.5	0.73	0.78 ± 0.24
AF method	1.9 ± 1.5	13.2 ± 12.7	0.76	0.99 ± 0.00
p-value	< 0.001	< 0.001		< 0.001

https://doi.org/10.1371/journal.pone.0227534.t001

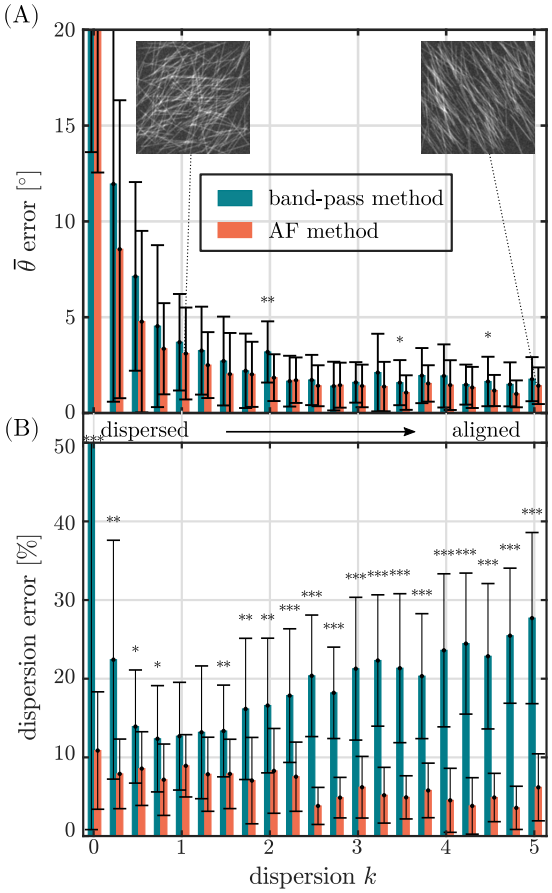

Fig 6. Error of the band-pass method and the AF method vs. the dispersion *k* of the fiber network. Fibers with a width of 5, aspect ratio of 30 and an image noise factor of 1 were considered here. (A) shows the error of the mean fiber orientation $\Delta\bar{\theta}$. Inlets show exemplary Monte-Carlo generated greyscale fiber images from respective distributions. (B) shows the relative error of the fiber dispersion parameters Δk_{rel}, Δb_{rel}. Sample greyscale images, that were simulated by the implemented Monte-Carlo method are shown for $k = 0.01$ and $k = 5$. ($^{*}p < 0.05$, $^{**}p < 0.01$, $^{***}p < 0.001$).

https://doi.org/10.1371/journal.pone.0227534.g006

networks ($k < 1$) were excluded from statistical analysis since they do not feature a mean orientation. The overall mean error of the dispersion parameters Δk_{rel}, Δb_{rel} amounts for (33.9 ± 26.5)% and (13.2 ± 12.7)% ($p < 0.001$) using the band-pass and the AF method, respectively. It was found that for both methods the error of the mean fiber orientation $\Delta\bar{\theta}$ mainly depends on the degree of the alignment of the fiber network (Fig 6A) and is rather independent from the fiber geometry or image quality (not shown). The error of both methods reduces towards an increasing degree of fiber alignment.

The error of the dispersion parameters Δb_{rel} and Δk_{rel} is found to strongly depend on the degree of alignment, fiber geometry and image noise (Figs 6B and 7). With increasing the degree of alignment, the fiber dispersion error of the AF method, Δb_{rel}, continuously decreases from a maximum error of 10.9% at $k = 0.01$ to a plateau of ∼5% for $k > 2.2$. The

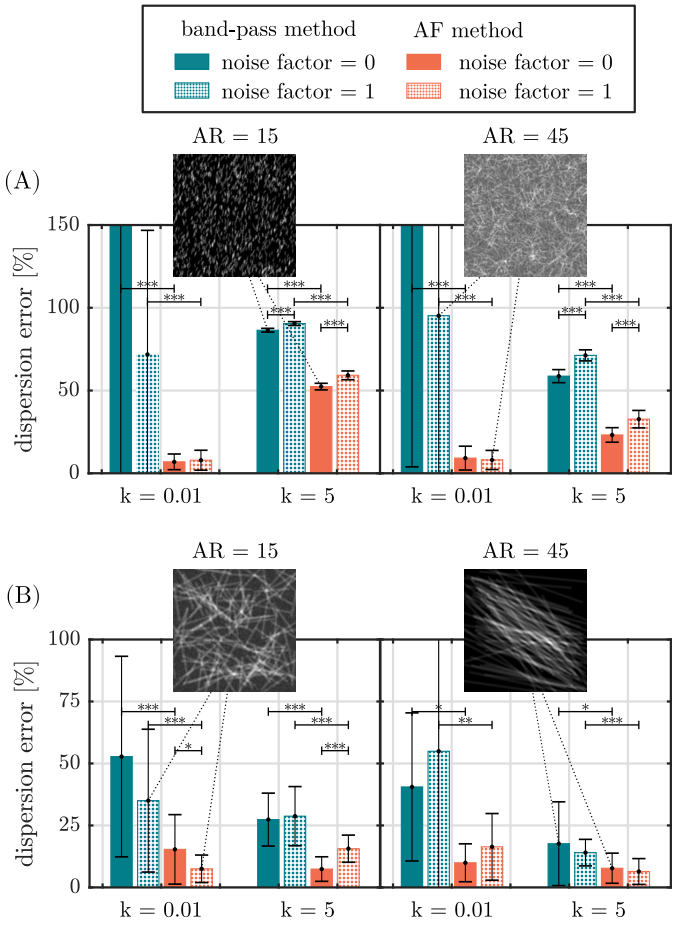

Fig 7. Error of the dispersion parameter of the band-pass method and the AF method for different fiber geometries, dispersions and noise factors. (A) shows the error of the dispersion parameter for fibers with a width of 1 pixel for aspect ratios 15 and 45 as well as noise factors 0 and 1. (B) shows the same as in (A) but for fibers with a width of 10 pixels. Each error is given for a dispersed ($k = 0.01$) and an aligned fiber network ($k = 5$). Inlets show exemplary Monte-Carlo generated greyscale fiber images from respective distributions. ($^{*}p < 0.05$, $^{**}p < 0.01$, $^{***}p < 0.001$).

https://doi.org/10.1371/journal.pone.0227534.g007

fiber dispersion error of the band-pass method, Δk_{rel}, exhibits a large error at $k = 0.01$ $\Delta k_{rel} = 101.4\%$, which is first reduced to a minimum error of $\Delta k_{rel} \sim 12\%$ around $k \sim 1$ but then is increased again towards aligned fiber networks to an error of 27.7% at $k = 5$ (Fig 6B). Except for $k = 1$ and $k = 1.25$ the error of both methods shows a significant ($p < 0.05$), for most values of k even highly significant ($p < 0.001$) difference.

Other than the error of the mean fiber orientation, the error of the dispersion parameter strongly depends on the fiber geometry, image noise and choice of evaluation method (Fig 7). An at least significant decrease ($p < 0.05$) in error was found for every group if the image was evaluated with the AF method.

A decreased fiber width strongly increases Δk_{rel} for every combination of aspect ratio, dispersion and noise. In case Δb_{rel}, the increase in error can be noted for aligned networks only.

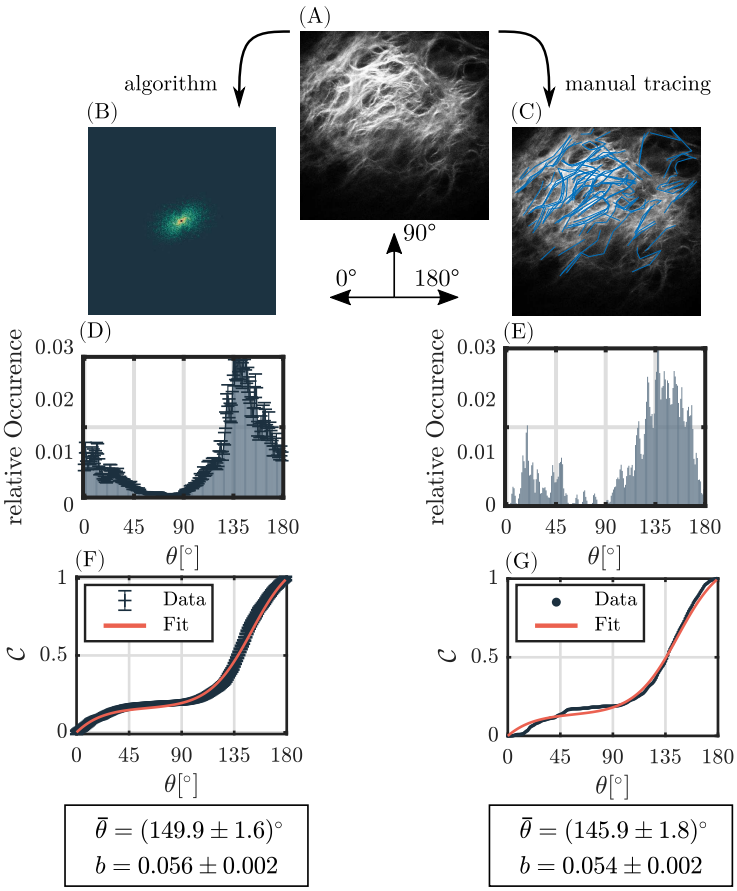

Fig 8. Evaluation example of an in vivo SHG-image of dermal collagen. Left column ((B),(D),(F)): Evaluation steps of the implemented image processing algorithm. Right column ((C),(E),(G)): Manual fiber tracing of fibers, which serves as ground truth. (A) shows the original SHG-image as measured with the multi-photon microscope. (B), the filtered power spectrum for $\delta_{cut} = 2.1\%$. (C), manually traced fibers. (D) and (E) show the resulting angular orientation distributions. For (D), $\alpha = 1.5$ was used. (F) and (G) show the respective cumulative orientation distributions and the fit parameters obtained from sigmoid fitting.

https://doi.org/10.1371/journal.pone.0227534.g008

A raised noise factor significantly ($p < 0.001$) increases Δk_{rel} and Δb_{rel} for aligned networks of fibers with a width of 1. Additionally, a significant ($p < 0.05$) decrease and a highly significant increase ($p < 0.001$) in Δb_{rel} was found for thick, short fibers (width = 10, AR = 15).

Application on experimental data. Our implemented algorithm was applied on an exemplary set of ten in vivo recorded SHG images of dermal collagen. Parameters of the cumulative angular distribution $\bar{\theta}$ and b were calculated using the AF method and compared to reference parameters $\bar{\theta}$ and b achieved from manual fiber tracing (Fig 8, S1 Dataset). The absolute mean error between calculation and manual segmentation for the mean orientation amounts for $\Delta\bar{\theta} = (6.0 \pm 4.0)^\circ$, whereas the mean relative error of the fiber dispersion is Δb_{rel} = (9.3 ± 12.1)%. The mean coefficient of determination was $R^2 = 0.99 \pm 0.01$.

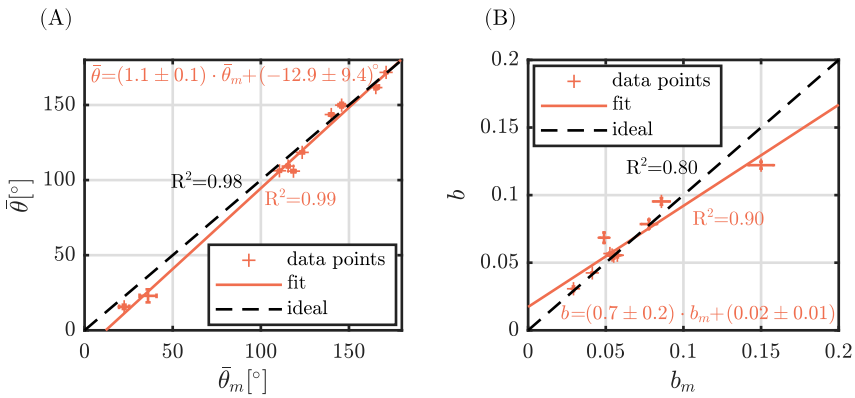

Fig 9. Calculated angular distribution parameters vs. reference distribution parameters for the experimental data. (A) Mean fiber orientation $\bar{\theta}$ vs. mean fiber orientation $\bar{\theta}_m$ achieved from manual segmentation. (B) Fiber dispersion b vs. fiber dispersion b_m achieved from manual segmentation. R^2 values are given for the fitted curve (solid, orange) as well as for the ideal curve (dashed, black) with a slope of one. Errorbars represent 95% confidence bounds of fitted parameters.

https://doi.org/10.1371/journal.pone.0227534.g009

Value pairs of calculated and reference parameter were fitted using a first order polynomial (Fig 9). High Pearson correlations were found for both parameters, namely $R^2 = 0.99$ and $R^2 = 0.90$ for the mean orientation angle and dispersion, respectively. Calculated Pearson correlations with respect to an ideal calculation (slope equal to one) amount for $R^2 = 0.98$ and $R^2 = 0.8$.

Discussion

We report on a robust method to quantify the angular distribution of fibers in noisy greyscale fiber image. The whole image processing procedure covers: the application of the periodic decomposition to remove cross-like artifacts in the Fourier domain, Fourier filtering by only permitting values below a certain relative uncertainty δ_{cut}, computation of the angular distribution by weighting the number of pixels with N^α and quantification of the mean angle and dispersion by fitting a modified sigmoid function to the cumulative orientation distribution.

In comparison to conventionally used window functions like in [12, 16, 32, 36], the periodic decomposition has the advantage of conserving almost the entire image information while completely removing artifacts in the Fourier domain, as shown in Fig 2. Therefore, we omit a quantitative analysis. The Monte-Carlo noise simulation revealed that the effect on the uncertainty can be neglected since the periodic mapping only has significant effects on the image boundary only.

Filtering the power spectrum by excluding values above a predefined relative uncertainty allows for the definition of an adaptive filter. Optimal evaluation parameters were identified by applying a two parameter Nelder-Mead optimization, which succeeded for 99.8% of the images. A maximum cut-off error of $\delta_{cut} = 2.1\%$ and a weighting factor of $\alpha = 1.5$ was calculated, while the non-locality of the optimum was ensured. Polzer et. al introduced a similar weighting factor which raises the entire intensity distribution $I(\theta)$ [36]. However, the optimum value of their weighting factor seems to suffer from large fluctuations, whereas the optimal value of α is stable throughout the degree of alignment of fiber networks and throughout different fiber properties and image noise (S2 Fig).

Previously used filtering methods like the bandpass method [6, 34, 36] work with rotationally symmetric filters, which disregard the anisotropy of the signal. The derivation of optimal band-pass range is based on the fiber diameter [6]. With the AF method we apply a relative uncertainty criterion without any assumptions on the underlying fiber properties. The optimal value of δ_{cut} is found to be completely independent from the chosen fiber geometries, fiber disperion and image noise (S2A, S2C, S2E and S2G Fig). As a consequence, the fiber dispersion can be quantified with a significantly lower error for completely dispersed and highly aligned fiber networks in comparison to the band-pass method (Fig 6B). Especially the quantification of highly dispersed fiber networks ($k < 1$) is much more reliable using the AF method, whereas the dispersion calculated by the band-pass method suffers from large errors ($\Delta k_{rel} > 100\%$) (Figs 6B and 7). This is in accordance with the observations of Morrill et. al [34], who measured an error of $\sim 30\%$ for $k \sim 0.2$ using binary Monte-Carlo images.

If we use the AF method in conjunction with a von-Mises fit of the angular orientation distribution, large errors of the dispersion coefficient can be noted towards dispersed fiber networks (S3 Fig). Contrary to the band-pass method, Δk_{rel} rapidly decreases towards aligned networks to a level of $\sim 10\%$. This effect is solely related to the adaptive filter and the weighted radial summation of the AF method, whereas the sigmoid fit ensures a reliable dispersion parameter estimation for dispersed networks.

Fibers with a width of 1 somehow represent an exception in comparison to the images containing fibers with width > 1 pixel. Regarding the result of the optimization of α with respect to different image and fiber properties (S2 Fig), it can be seen that α is quite stable throughout the dispersion k, noise factor and different fiber geometries. α fluctuates within the interval [1, 2] except for fibers with a width of 1 pixel, where the median value α amounts for $\alpha_{width=1} = 2.4$. The application of the gauss-filter to dissolve sharp edges might even reduce the true fiber dimension down to a size which is near the resolution limit of power spectrum based methods resulting in large deviations of the dispersion for highly aligned fiber networks.

Using the Monte-Carlo approach to create artificial fibrous images for validation purposes is a common tool. However, it is rather difficult to draw a comparison to the accuracy of other methods found in the literature since mostly a low quantity of binary images was investigated [12, 34]. For example, Morrill et. al measured an overall error of $(0.71 \pm 0.43)^\circ$ for the mean orientation and $(7.4 \pm 3.0)\%$ for the fiber dispersion using binary fiber images, whereas we measured errors of $(2.3 \pm 2.1)^\circ$ and $(33.9 \pm 26.5)\%$ [34]. The use of greyscale images will generally result in a lower accuracy compared to the evaluation of binary images, since the superimposition of fibers might generate intensity deviations in the power spectrum.

The AF method was applied to in vivo SHG images of dermal collagen. The multi-photon images that were used provide a sufficiently high image intensity $I(x, y)$ (16-bit), which comes along with a sufficiently low relative intensity error $\Delta I/I = 1/\sqrt{I}$. Therefore, $\delta_{cut} = 2.1\%$ provides a reasonable filtering value, which results in an accurate quantification of the angular orientation distribution in terms of mean fiber orientation and fiber dispersion.

Conclusion

The proposed adaptive filter method modifies common Fourier methods at different stages, namely artifact removal in the Fourier domain, filtering of the power spectrum and quantification of the angular signal.

The adaptive filter conserves the anisotropy of the angular signal in the Fourier domain, which ensures a stable error for disordered as well as highly aligned fiber networks. Using the cumulative distribution naturally averages the data, which spares out any averaging of the angular distribution. The high mean goodness of the fit $R^2 = 0.99$ which was measured for

both, Monte-Carlo images and SHG-images, indicates that the modified sigmoid function provides a perfect model of the cumulative distribution function.

The adaptive filtering method was found to be a reliable and accurate tool for quantifying the angular orientation distribution in fibrous SHG images of dermal collagen, even for images suffering from a low image quality. Aside from its benefits concerning accuracy and reliability, the AF method considers measurement uncertainties, which are of key importance in any kind of scientific experiment.

Supporting information

S1 Table. Periodic decomposition: Relative deviation of the error propagation simulated by Monte-Carlo and the basic image error ΔI for $N = 10^5$ iterations.
(PDF)

S2 Table. Power spectrum: Relative deviation between calculated and Monte-Carlo simulated uncertainty for $N = 10^5$ iterations.
(PDF)

S1 Fig. Sensitivity analysis of the central cut-off radius. (A) Squared difference between calculated angular orientation distribution and sampled fiber angle distribution on $N = 10^4$ images (Monte-Carlo generated). The same dataset was also used for evaluation parameter optimization. Unfiltered power spectra are used to isolate the effect of the cut-off radius. (B-D) Evaluation example for cut-off radii (0,3,6). The artifact dramatically reduces from a 0 pixel cut-off to a radial cut-off of 3 pixels. Cut-off radii above 3 pixels barely influence the angular distribution. In order to save angular information, we choose a cut-off radius of 3 pixels.
(EPS)

S2 Fig. Optimal evaluation parameters vs. fiber properties and image noise. Plotted are median values and errorbars represent the interquartile range (25, 75). (A,C,E,G) represent plots of δ_{cut} vs. dispersion k, noise factor NF, aspect ratio (AR) and width. (B,D,F,H) are plots of the weighting factor α vs. dispersion k, noise factor NF, aspect ratio (AR) and width.
(EPS)

S3 Fig. Error of the dispersion parameter k and b of the von-Mises fit and the sigmoid fit of the AF method for fibrous Monte-Carlo images (width = 5, AR = 30). The von-Mises fit was applied to the angular orientation distribution as calculated by the AF method, whereas the sigmoid fit was applied to the respective cumulative orientation distribution.
(EPS)

S1 Dataset. The .csv file provides the reference parameter as well as the parameter calculated by the AF method for each image.
(CSV)

Author Contributions

Conceptualization: Maximilian Witte, Michael Rübhausen, Frank Fischer.

Data curation: Frank Fischer.

Software: Maximilian Witte.

Supervision: Sören Jaspers, Horst Wenck, Michael Rübhausen, Frank Fischer.

Validation: Maximilian Witte.

Visualization: Maximilian Witte.

Writing – original draft: Maximilian Witte.

Writing – review & editing: Maximilian Witte, Michael Rübhausen, Frank Fischer.

References

1. Ní Annaidh A, Bruyère K, Destrade M, Gilchrist MD, Otténio M. Characterization of the anisotropic mechanical properties of excised human skin. J Mech Behav Biomed Mater. 2012; 5(1):139–148. https://doi.org/10.1016/j.jmbbm.2011.08.016 PMID: 22100088
2. Bancelin S, Lynch B, Bonod-Bidaud C, Ducourthial G, Psilodimitrakopoulos S, Dokládal P, et al. Ex vivo multiscale quantitation of skin biomechanics in wild-type and genetically-modified mice using multiphoton microscopy. Sci Rep. 2015; 5(December):1–14.
3. Chen X, Nadiarynkh O, Plotnikov S, Campagnola PJ. Second harmonic generation microscopy for quantitative analysis of collagen fibrillar structure. Nat Protoc. 2012; 7(4):654–669. https://doi.org/10.1038/nprot.2012.009 PMID: 22402635
4. Frisch KE, Duenwald-Kuehl SE, Kobayashi H, Chamberlain CS, Lakes RS, Vanderby R. Quantification of collagen organization using fractal dimensions and Fourier transforms. Acta Histochem. 2012; 114 (2):140–144. https://doi.org/10.1016/j.acthis.2011.03.010 PMID: 21529898
5. Levillain A, Orhant M, Turquier F, Hoc T. Contribution of collagen and elastin fibers to the mechanical behavior of an abdominal connective tissue. J Mech Behav Biomed Mater. 2016; 61:308–317. https://doi.org/10.1016/j.jmbbm.2016.04.006 PMID: 27100469
6. Marquez JP. Fourier analysis and automated measurement of cell and fiber angular orientation distributions. Int J Solids Struct. 2006; 43(21):6413–6423. https://doi.org/10.1016/j.ijsolstr.2005.11.003
7. Mega Y, Robitaille M, Zareian R, McLean J, Ruberti J, DiMarzio C. Quantification of lamellar orientation in corneal collagen using second harmonic generation images. Opt Lett. 2012; 37(16):3312–4. https://doi.org/10.1364/OL.37.003312 PMID: 23381241
8. Mercatelli R, Ratto F, Rossi F, Tatini F, Menabuoni L, Malandrini A, et al. Three-dimensional mapping of the orientation of collagen corneal lamellae in healthy and keratoconic human corneas using SHG microscopy. J Biophotonics. 2017; 10(1):75–83. https://doi.org/10.1002/jbio.201600122 PMID: 27472438
9. Nesbitt S, Scott W, Macione J, Kotha S. Collagen Fibrils in Skin Orient in the Direction of Applied Uniaxial Load in Proportion to Stress while Exhibiting Differential Strains around Hair Follicles. Materials (Basel). 2015; 8(4):1841–1857. https://doi.org/10.3390/ma8041841
10. Rezakhaniha R, Agianniotis A, Schrauwen JTC, Griffa A, Sage D, Bouten CVC, et al. Experimental investigation of collagen waviness and orientation in the arterial adventitia using confocal laser scanning microscopy. Biomech Model Mechanobiol. 2012; 11(3-4):461–473. https://doi.org/10.1007/s10237-011-0325-z PMID: 21744269
11. Ribeiro JF, dos Anjos EHM, Mello MLS, de Campos Vidal B. Skin Collagen Fiber Molecular Order: A Pattern of Distributional Fiber Orientation as Assessed by Optical Anisotropy and Image Analysis. PLoS One. 2013; 8(1):5–7. https://doi.org/10.1371/journal.pone.0054724
12. Schriefl AJ, Reinisch AJ, Sankaran S, Pierce DM, Holzapfel GA. Quantitative assessment of collagen fibre orientations from two-dimensional images of soft biological tissues. J R Soc Interface. 2012; 9 (76):3081–3093. https://doi.org/10.1098/rsif.2012.0339 PMID: 22764133
13. Stender CJ, Rust E, Martin PT, Neumann EE, Brown RJ, Lujan TJ. Modeling the effect of collagen fibril alignment on ligament mechanical behavior. Biomech Model Mechanobiol. 2018; 17(2):543–557. https://doi.org/10.1007/s10237-017-0977-4 PMID: 29177933
14. Van Zuijlen PPM, Ruurda JJB, Van Veen HA, Van Marle J, Van Trier AJM, Groenevelt F, et al. Collagen morphology in human skin and scar tissue: No adaptations in response to mechanical loading at joints. Burns. 2003. https://doi.org/10.1016/s0305-4179(03)00052-4 PMID: 12880721
15. Wu S, Li H, Yang H, Zhang X, Li Z, Xu S. Quantitative analysis on collagen morphology in aging skin based on multiphoton microscopy. J Biomed Opt. 2011. https://doi.org/10.1117/1.3565439
16. Pourdeyhimi B, Dent R, Davis H. Measuring Fiber Orientation in Nonwovens Part III: Fourier Transform. Text Res J. 1997; 67(2):143–151. https://doi.org/10.1177/004051759706700211
17. Ghassemieh E, Acar M, Versteeg H. Microstructural analysis of non-woven fabrics using scanning electron microscopy and image processing. Part 1: Development and verification of the methods. Proc Inst Mech Eng Part L J Mater Des Appl. 2002; 216(3):199–207.

18. Ayres CE, Jha BS, Meredith H, Bowman JR, Bowlin GL, Henderson SC, et al. Measuring fiber alignment in electrospun scaffolds: A user's guide to the 2D fast Fourier transform approach. J Biomater Sci Polym Ed. 2008; 19(5):603–621. https://doi.org/10.1163/156856208784089643 PMID: 18419940

19. D'Amore A, Stella JA, Wagner WR, Sacks MS. Characterization of the complete fiber network topology of planar fibrous tissues and scaffolds. Biomaterials. 2010; 31(20):5345–54. https://doi.org/10.1016/j.biomaterials.2010.03.052 PMID: 20398930

20. Liu C, Zhu C, Li J, Zhou P, Chen M, Yang H, et al. The effect of the fibre orientation of electrospun scaffolds on the matrix production of rabbit annulus fibrosus-derived stem cells. Bone Res. 2015; 3 (January).

21. Redon C, Chermant L, Chermant JL, Coster M. Assessment of fibre orientation in reinforced concrete using Fourier image transform. J Microsc. 1998; 191(3):258–265. https://doi.org/10.1046/j.1365-2818.1998.00393.x PMID: 9767490

22. Stender CJ, Rust E, Martin PT, Neumann EE, Brown RJ, Lujan TJ. Modeling the effect of collagen fibril alignment on ligament mechanical behavior. Biomech Model Mechanobiol. 2018; 17(2):543–557. https://doi.org/10.1007/s10237-017-0977-4 PMID: 29177933

23. Gasser TC, Ogden RW, Holzapfel GA. Hyperelastic modelling of arterial layers with distributed collagen fibre orientations. J R Soc Interface. 2006; 3(6):15–35. https://doi.org/10.1098/rsif.2005.0073 PMID: 16849214

24. Fan R, Sacks MS. Simulation of planar soft tissues using a structural constitutive model: Finite element implementation and validation. J Biomech. 2014. https://doi.org/10.1016/j.jbiomech.2014.03.014 PMID: 24746842

25. Wu H, Fan J, Chu CC, Wu J. Electrospinning of small diameter 3-D nanofibrous tubular scaffolds with controllable nanofiber orientations for vascular grafts. J Mater Sci Mater Med. 2010; 21(12):3207–3215. https://doi.org/10.1007/s10856-010-4164-8 PMID: 20890639

26. Frahs SM, Oxford JT, Neumann EE, Brown RJ, Keller-Peck CR, Pu X, et al. Extracellular Matrix Expression and Production in Fibroblast-Collagen Gels: Towards an In Vitro Model for Ligament Wound Healing. Ann Biomed Eng. 2018; 46(11):1882–1895. https://doi.org/10.1007/s10439-018-2064-0 PMID: 29873012

27. Lau TY, Ambekar R, Toussaint KC. Quantification of collagen fiber organization using three-dimensional Fourier transform-second-harmonic generation imaging. Opt Express. 2012; 20(19):21821. https://doi.org/10.1364/OE.20.021821 PMID: 23037302

28. Lutz V, Sattler M, Gallinat S, Wenck H, Poertner R, Fischer F. Impact of collagen crosslinking on the second harmonic generation signal and the fluorescence lifetime of collagen autofluorescence. Ski Res Technol. 2012; 18(2):168–179. https://doi.org/10.1111/j.1600-0846.2011.00549.x

29. Lutz V, Sattler M, Gallinat S, Wenck H, Poertner R, Fischer F. Characterization of fibrillar collagen types using multi-dimensional multiphoton laser scanning microscopy. Int J Cosmet Sci. 2012; 34(2):209–215. https://doi.org/10.1111/j.1468-2494.2012.00705.x PMID: 22235828

30. Annaidh AN, Karine Bruyère, Destrade M, Gilchrist MD, Maurini C, Otténio M, et al. Automated estimation of collagen fibre dispersion in the dermis and its contribution to the anisotropic behaviour of skin. Ann Biomed Eng. 2012; 40(8):1666–1678. https://doi.org/10.1007/s10439-012-0542-3

31. Bredfeldt JS, Liu Y, Pehlke CA, Conklin MW, Szulczewski JM, Inman DR, et al. Computational segmentation of collagen fibers from second-harmonic generation images of breast cancer. J Biomed Opt. 2014; 19(1):016007. https://doi.org/10.1117/1.JBO.19.1.016007

32. Kim A, Lakshman N, Petroll WM. Quantitative assessment of local collagen matrix remodeling in 3-D Culture: The role of Rho kinase. Exp Cell Res. 2006. https://doi.org/10.1016/j.yexcr.2006.08.009

33. Sander EA, Barocas VH. Comparison of 2D fiber network orientation measurement methods. J Biomed Mater Res—Part A. 2009; 88(2):322–331. https://doi.org/10.1002/jbm.a.31847

34. Morrill EE, Tulepbergenov AN, Stender CJ, Lamichhane R, Brown RJ, Lujan TJ. A validated software application to measure fiber organization in soft tissue. Biomech Model Mechanobiol. 2016; 15 (6):1467–1478. https://doi.org/10.1007/s10237-016-0776-3 PMID: 26946162

35. Yang W, Sherman VR, Gludovatz B, Schaible E, Stewart P, Ritchie RO, et al. On the tear resistance of skin. Nat Commun. 2015; 6:6649. https://doi.org/10.1038/ncomms7649 PMID: 25812485

36. Polzer S, Gasser TC, Forsell C, Druckmüllerova H, Tichy M, Staffa R, et al. Automatic identification and validation of planar collagen organization in the aorta wall with application to abdominal aortic aneurysm. Microsc Microanal. 2013; 19(6):1395–1404. https://doi.org/10.1017/S1431927613013251 PMID: 24016340

37. Schriefl AJ, Wolinski H, Regitnig P, Kohlwein SD, Holzapfel GA. An automated approach for three-dimensional quantification of fibrillar structures in optically cleared soft biological tissues. J R Soc Interface. 2012.

38. Puschmann S, Rahn CD, Wenck H, Gallinat S, Fischer F. In vivo quantification of human dermal skin aging using SHG and autofluorescence. Multimodal Biomed Imaging VII. 2012; 8216:821608. https://doi.org/10.1117/12.906460
39. MATLAB. version 9.4.0.813654 (R2018a). The MathWorks Inc.; 2018.
40. MATLAB. Image Processing Toolbox (version 10.2). The MathWorks Inc.; 2018.
41. MATLAB. Curve Fitting Toolbox (version 3.5.7). The MathWorks Inc.; 2018.
42. Paul H, Jex I, Paul H, Jex I. Photon statistics. Introd to Quantum Opt. 2010; p. 127–154.
43. Becker RI, Morrison N. The errors in FFT estimation. IEEE Trans Signal Process. 2002; 44(8):133–135.
44. Withayachumnankul W, Fischer BM, Lin H, Abbott D. Uncertainty in terahertz time-domain spectroscopy measurement. J Opt Soc Am B. 2008; 25(6):1059. https://doi.org/10.1364/JOSAB.25.001059
45. Moisan L. Periodic plus smooth image decomposition. J Math Imaging Vis. 2011; 39(2):161–179. https://doi.org/10.1007/s10851-010-0227-1
46. University of Wisconsin. Public-Domain Test Images for Homeworks and Projects;. Available from: https://homepages.cae.wisc.edu/~ece533/images/.
47. Lagarias C J, Reeds A J, Wright H M, Wright E P. Convergence Properties of the Nelder-Mead Simplex Method in Low Dimensions. SIAM J Optim. 1998; 9(1):112–147. https://doi.org/10.1137/S1052623496303470
48. Koenig K, Riemann I. High-resolution multiphoton tomography of human skin with subcellular spatial resolution and picosecond time resolution. J Biomed Opt. 2003; 8(3):432. https://doi.org/10.1117/1.1577349
49. Rahn CD, Meine H, Gallinat S, Wenck H, Wittern KP, Fischer F. Fully automated data acquisition and fast data interpretation in a customized multimodal multiphoton microscope. In: Three-Dimensional Multidimens. Microsc. Image Acquis. Process. XVII; 2010.
50. Schwarz M, Riemann I, Stracke F, Huck V, Gorzelanny C, Schneider SW, et al. A comparative study of different instrumental concepts for spectrally and lifetime-resolved multiphoton intravital tomography (5D-IVT) in dermatological applications. In: Imaging, Manip. Anal. Biomol. Cells, Tissues VIII; 2010.

Chapter 4

Classification of Fiber Families

Biological soft tissue, like aorta and skin, is reported to exhibit multiple, so-called fiber families [6, 88]. In this chapter, a general approach to determine the number of fiber families and their angular properties is presented.

4.1 Monte-Carlo Simulation of Multiple Fiber Families

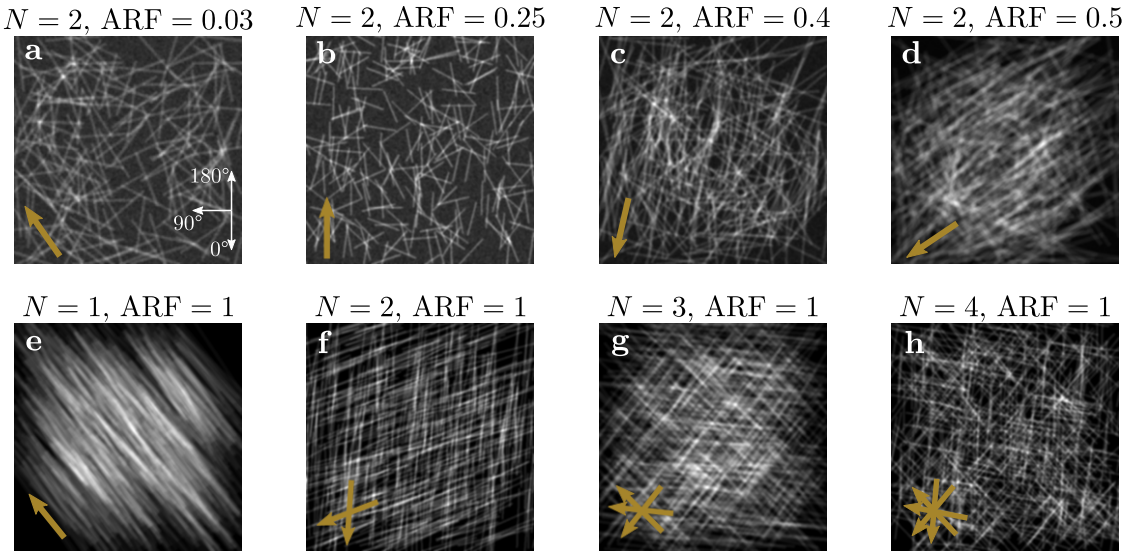

Figure 4.1: Example Monte-Carlo simulated fiber images with multiple fiber families. Arrows indicate the mean orientation $\bar{\theta}$ of each aligned fiber family. N denotes the number of fiber families in each image. (**a**) $N_f = 200$ isotropically distributed fibers and $N_f = 6$ aligned fiber famlies ($k = 10$). (**b**) $N_f = 200$ isotropically distributed fibers and $N_f = 50$ aligned fiber famlies ($k = 10$). (**c**) $N_f = 200$ isotropically distributed fibers and $N_f = 80$ aligned fiber famlies ($k = 10$). (**d**) $N_f = 200$ isotropically distributed fibers and $N_f = 100$ aligned fiber famlies ($k = 10$). (**e**) One aligned fiber family with $N_f = 350$ fibers ($k = 10$). (**f**) Two aligned fiber families with $N_f = 175$ fibers each ($k = 10$). (**g**) Three aligned fiber families with $N_f = 115$ fibers each ($k = 10$). (**h**) Four aligned fiber families with $N_f = 90$ fibers each ($k = 10$).

The Monte-Carlo procedure described in section 3.1, is extended for the simulation of artificial fiber images with multiple fiber families. The angular orientation distribution of the i-th fiber family is described by the von-Mises function (equation (3.1)) with corresponding parameters $\bar{\theta}_i$ and k_i. The number of sampled fibers $N_{f,i}$ for each fiber families is used to control its amplitude. To simulate an isotropically distributed fiber family, angles are uniformly sampled from the entire angular range $[0°, 180°]$. The anisotropic ratio of fibers (ARF) is introduced to quantify the ratio of aligned fibers with respect to the total number of sampled fibers. In case of one isotropic and one aligned fiber family with an equal number of sampled fibers, the ARF amounts to 0.5. Figure 4.1 shows exemplary Monte-Carlo images with multiple fiber families. In figure 4.1 (a-d), an isotropic and an aligned fiber family with a variation of the ARF are shown. The ARF is controlled by keeping a constant number of isotropic fibers ($N_f = 200$), while modifying the number of aligned fibers from $N_f = 6$ (ARF = 0.03) to $N_f = 200$ (ARF = 0.5). Images with a varying number of highly aligned fiber families are shown in figure 4.1 (e-h). Since only aligned fiber families are created, the ARF amounts to 1.

4.2 Fiber Image Network Evaluation Algorithm (FINE Algorithm)

The Fiber Image Network Algorithm (FINE algorithm) is introduced to analyze the angular properties of images considering multiple fiber families. In chapter 3, section 3.5, the sigmoid function S_{circ} (equation (3.48)) was introduced to quantify the cumulative orientation distribution (COD). This approach was found to provide reliable results if a single fiber family is present in the image. To account for multiple fiber families as well as their angular properties, equation (3.48) is generalized to N fiber families:

$$S_N(\theta) = \begin{cases} S_{\text{circ}} & \text{if } N = 1, \\ \sum_{i=1}^{N} a_i S_{\text{circ},i}(\theta) & \text{if } N > 1, \end{cases} \tag{4.1}$$

where a_i denotes the amplitude of the i-th fiber family. Note that the i-th sigmoid function $S_{\text{circ},i}$ contains the mean orientation of each fiber family, $\bar{\theta}_i$, and its dispersion b_i.

Within the FINE algorithm, S_N (equation (4.1)) is fitted to the COD with an iterative increase of the number of fiber families. Even though S_N accounts for isotropic as well as anisotropic fiber families, the first step of the FINE algorithm consists of evaluating the isotropy of the entire cumulative distribution by an isotropy criterion.

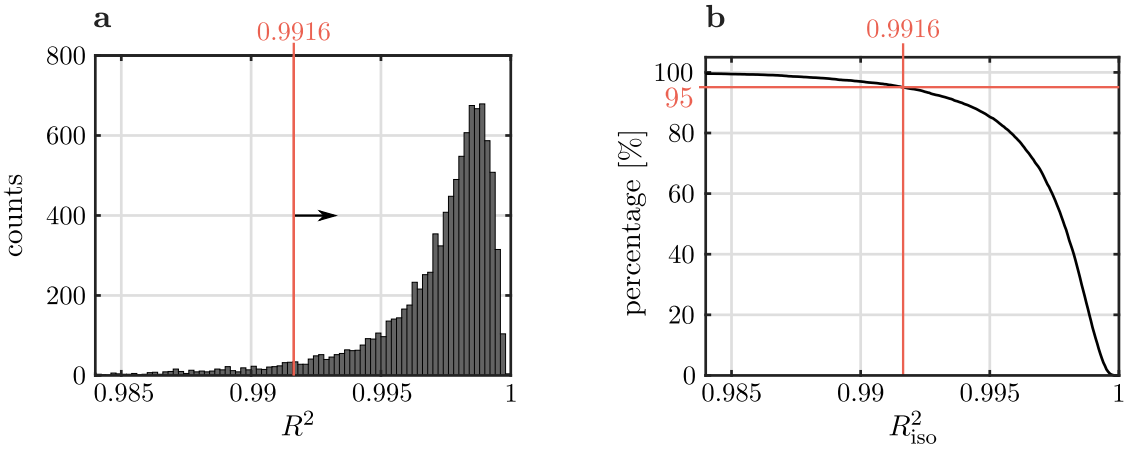

Figure 4.2: Evaluation of the isotropy criterion of the FINE algorithm. (**a**) Distribution of R^2 of the cumulative orientation distribution of 10^4 isotropic Monte-Carlo simulated images with respect to an ideal isotropic distribution. Sampling errors, as well as random fiber overlaps cause the calculated cumulative orientation distribution to deviate from an ideally isotropic distribution. (**b**) Percentage of the images that are included in the isotropy criterion $R^2 \geq R^2_{\text{iso}}$ as a function of the threshold value R^2_{iso}.

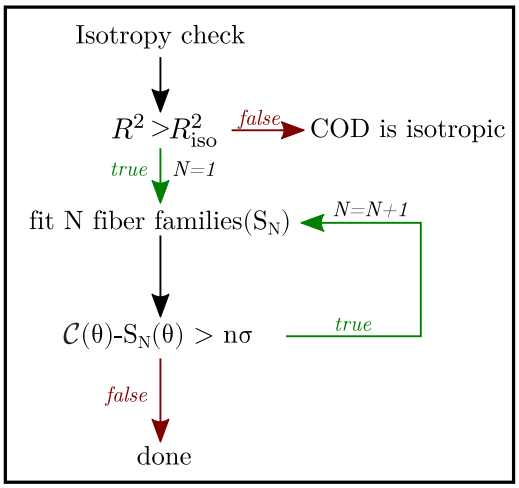

Figure 4.3: Schematic illustration of the FINE algorithm. COD denotes the cumulative orientation distribution $\mathcal{C}(\theta)$. R^2_{iso} denotes the threshold at which the entire COD is assumed to be isotropic. After considering the presence of at least one fiber family, the sigmoid function S_N of equation (4.1) is iteratively fitted to the COD. N denotes the number of fiber families, that is increased at every iteration of the FINE algorithm. The algorithm terminates, if the difference between COD and fitted model is smaller than $n\sigma$. σ denotes the uncertainty of the COD, $\Delta\mathcal{C}(\theta)$, while n gives the level of significance. Parameters R^2_{iso} and n are determined numerically by using Monte-Carlo simulated greyscale images.

A completely isotropic distribution has a cumulative distribution that follows a straight line with slope $1/180°$. With increasing anisotropy of the fiber network, the deviation

from the straight line grows [84]. This deviation is quantified using Pearson's R^2 as measure, where $R^2 = 1$ indicates a completely isotropic distribution. To determine a suitable threshold $R^2 \geq R^2_{\text{iso}}$ at which the COD is classified as isotropic, the Monte-Carlo procedure is used to simulate 10^4 images with an isotropic distribution of fibers. R^2 is calculated for each simulated image using the cumulative orientation distribution (equation (3.42)) of each simulated image. Figure 4.2 (a) shows the distribution of R^2, which has a peak between 0.995 and 1. In figure 4.2 (b), the percentage of images meeting the isotropy criterion $R^2 \geq R^2_{\text{iso}}$ are shown as a function of R^2_{iso}. A 95 % certainty is given for a threshold value of $R^2_{\text{iso}} = 0.9916$. The FINE algorithm is schematically outlined in figure 4.3. After a fiber network is classified to be anisotropic, $S_{N=1}$ (equation (4.1)) is fitted to the COD $\mathcal{C}(\theta)$. If the difference between fit and data, $\mathcal{C}(\theta) - S_1(\theta)$, is larger than the confidence interval $n\sigma = n\Delta\mathcal{C}$, another fiber family is considered by fitting two fiber families to the cumulative orientation distribution (S_2). This procedure is iteratively repeated until the difference $\mathcal{C}(\theta) - S_N(\theta)$ is smaller than $n\sigma$ for all angles θ.

The termination criterion, determined by n, defines the sensitivity of the FINE algorithm to find an additional fiber family. At the same time, n controls the robustness of the algorithm to fluctuations in the COD. To calculate the optimal value of n, Monte-Carlo simulated fiber images with multiple fiber families are created. Images are allowed to contain up to three highly aligned fiber families ($k = 10$, $b = 0.18$). To ensure that neighboured fiber families are not overlapping, the following constraint is applied to their mean orientations:

$$\cos\left(2 \cdot |\bar{\theta}_i - \bar{\theta}_j|\right) \leq \cos\left(2 \cdot 30^\circ\right) = \frac{1}{2} \quad ,\forall (i,j) \in \{1, \ldots, N\} \text{ with } i \neq j. \tag{4.2}$$

If n is chosen too small, the number of fiber families calculated by the FINE algorithm will exceed the number of defined fiber families. In contrast, a large value of n might suppress features of the COD, which in general will lead to an underestimation of the defined number fiber families. Hence, there is an interval $n \in [n_{\min}, n_{\max}]$ for each simulated Monte-Carlo image, to find the correct number of fiber families. Limits $n_{\min}, n_{\max}$ are determined by the variation of n using a bisection algorithm [89]. Note that the algorithm is applied separately to both limits. Termination is enforced if the difference between subsequent iterations is smaller than 10^{-4}. Figure 4.4 shows the percentage of Monte-Carlo images for which the correct number of fiber families is found as a function of n. The highest percentage of 99.8 % is found at $n = 3$.

An application example of the FINE algorithm is shown in figure 4.5 for a Monte-Carlo simulated fiber image in figure 4.5 (a) with one isotropic fiber family ($N_f = 100$) and one aligned fiber family ($N_f = 200$). Since R^2 of the cumulative orientation distribution with respect to the ideal isotropic distribution is smaller than the isotropy criterion $R^2_{\text{iso}} = 0.9916$ (figure 4.5 (b)), the first fiber family is fitted to the COD (S_1) in figure 4.5 (c). As the difference between fit and COD is larger than 3σ in figure 4.5 (d), an additional fiber family is considered by fitting S_2 to the COD in figure 4.5 (e).

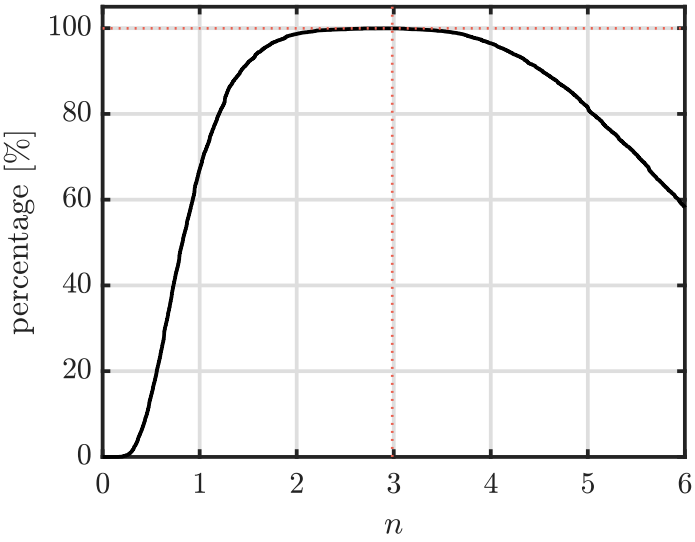

Figure 4.4: Evaluation of the uncertainty criterion of the FINE algorithm. The percentage of simulated Monte-Carlo images, for which the FINE algorithm identified the predefined number of fiber families, is shown as a function of n. n indicates the confidence interval to identify additional fiber families within the FINE algorithm.

Note that for a good fit convergence, the location of the highest difference between fit and COD is considered as starting value for the new fiber family (75° in this example). Since the difference between S_2 and the COD in figure 4.5 (f) fluctuates around zero with an amplitude smaller than 3σ, the algorithm is terminated. Thus, the FINE algorithm identified two fiber families. The fit quality of $R^2 = 0.999$ indicates that S_2 provides an excellent representation of the COD. The dispersion parameters, $b_1 = 0.027 \pm 0.003$ and $b_2 = 0.170 \pm 0.006$, indicate the presence of an isotropic and an aligned fiber family. This is in line with the input parameters of the Monte-Carlo simulation, which include one isotropic fiber family and one aligned fiber family with a dispersion parameter of $b = 0.18$. The respective calculated amplitudes amount to $a_1 = 0.36 \pm 0.02$ and $a_2 = 0.64 \pm 0.02$, which matches the ratio of anisotropic fibers of ARF $= 200/300 = 0.67$. The mean orientation of the simulated, aligned fiber family of $\bar{\theta} = 45°$, is accurately calculated by the FINE algorithm as $\bar{\theta}_2 = (46.9 \pm 0.2)°$. The sigmoid function S_N of the FINE algorithm is independent from $\bar{\theta}$ in the isotropic limit ($b \to 0$). As a consequence, fitting an isotropic fiber family might lead to a high fit uncertainty of the mean orientation $\bar{\theta}$. In this example, this is expressed by an error of $\Delta\bar{\theta}_1 = 3.6°$ of the mean orientation of fiber family 1.

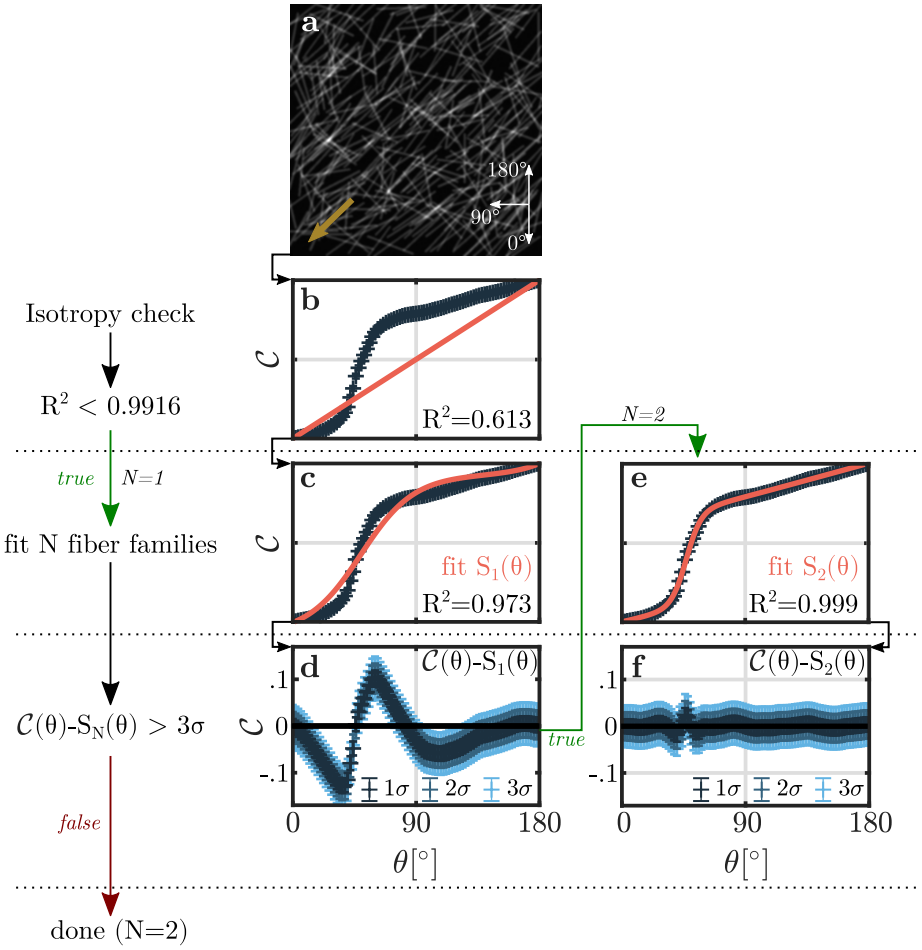

Figure 4.5: Application example of the FINE algorithm. (**a**) Monte-Carlo simulated greyscale image with $N_f = 100$ isotropically distributed fibers and $N_f = 200$ aligned fibers ($\bar{\theta} = 45°$, $b = 0.18$). (**b**) The COD of (a) is checked for isotropy as its R^2 with respect to a straight line is compared to the threshold value $R^2_{\text{iso}} = 0.9916$. (**c**) The first fiber family is fitted to the COD using S_1. (**d**) Difference between fit and COD. Errorbars indicate the levels of significance. The difference at $\sim 75°$ indicates the presence of an additional fiber family. (**e**) Two fiber families are fitted to the COD using $S_2(\theta)$. (**f**) The minor difference between fit and COD terminates the FINE algorithm with fit parameters: ($a_1 = 0.36 \pm 0.02$, $a_2 = 0.64 \pm 0.02$, $\bar{\theta}_1 = (131.6 \pm 3.6)°$, $\bar{\theta}_2 = (46.9 \pm 0.2)°$, $b_1 = 0.027 \pm 0.003$, $b_2 = 0.170 \pm 0.006$)

4.3 Derived Quantities

Besides the number of fiber families and their properties, two quantities are defined that are measures of the overall orientation properties of the fiber network.

The first quantity is called the orientation index (OI) and is commonly used in literature [12, 90, 91]. It quantifies the alignment of the fiber network with respect to its mean orientation $\bar{\theta}$:

$$\text{OI} = 2\frac{\sum_{\theta=0°}^{180°} \mathcal{I}(\theta)\cos^2(\theta - \bar{\theta})}{\sum_{\theta=0°}^{180°} \mathcal{I}(\theta)} - 1. \tag{4.3}$$

Note that this quantity is based on the angular orientation distribution $\mathcal{I}(\theta)$. The mean orientation $\bar{\theta}$ is determined from fitting S_1 the COD. If the fiber network is fully aligned, the OI is equal to unity. Contrary, it vanishes in case of an isotropic distribution. However, the OI is not able to reasonably quantify the angular orientation distribution if multiple aligned fiber families are present in the image. For example, the OI vanishes in case of two highly aligned fiber families, which are perpendicular to each other.

To account for an arbitrary number of fiber families, the alignment index (AI) is introduced:

$$\mathrm{AI} = \sum_{1}^{N} a_i \cdot b_i' \qquad b_i' = (b_i - b_{\min})/(b_{\max} - b_{\min}), \tag{4.4}$$

which represents the weighted sum over the dispersion parameters of each fiber family identified by the FINE algorithm. The dispersion parameters b_i are normalized by means of $b_{\max}$ and $b_{\min}$, defining the scale of the AI. $b_{\max}$ defines the upper limit of the AI and represents a fully aligned fiber family. It is chosen as $b_{\max} = 0.26$, which is equal to $k = 20$. In contrast, $b_{\min} = 0.016\,(k \to 0)$ is introduced as lower limit of the AI indicating an isotropic fiber family.

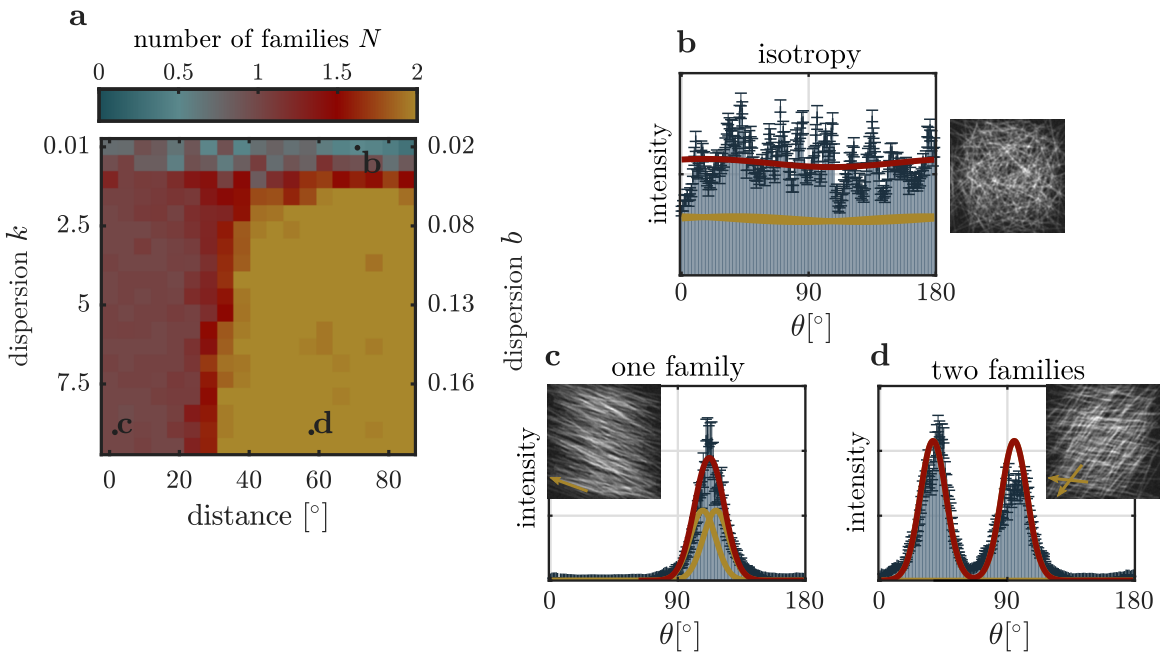

Figure 4.6: Effect of the overlap of two fiber families on the number of fiber families identified by the FINE algorithm. (**a**) Number of fiber families identified by the FINE algorithm as a function of the dispersion and the angular distance of two fiber families. (**b**) Example of two isotropic fiber families (yellow) that are overlapping to a single, isotropic fiber family (red). (**c**) Example of two aligned fiber families (yellow) that are overlapping to a single, aligned fiber family (red). (**d**) Example of two properly spaced (60°), highly aligned fiber families.

For a better understanding of the OI and AI, both quantities are calculated as a function of the dispersion and angular spacing of two fiber families in Monte-Carlo simulated images. A total of 10^4 images are created. The mean number of fiber families identified by the FINE algorithm is shown in figure 4.6 (a) as a function of dispersion and angular spacing. If the dispersion parameter of both fiber families is small, as exemplary shown in figure 4.6 (b), the angular orientation distribution appears as a single, isotropic fiber family. Similarly, a small angular spacing, like in figure 4.6 (c), effectively results in a single fiber family. If both fiber families are properly spaced, the FINE algorithm is able to discriminate both fiber families, like in figure 4.6 (d). The calculated AI, which is shown in figure 4.7 (a), is generally independent from the angular spacing between both fiber families. However, if the angular orientation distributions of both fiber families overlap to a single, broadened distribution, the AI is decreased. In contrast, the OI in figure 4.7 (b) is highest, if a single, strongly pronounced orientation is present in the angular orientation distribution.

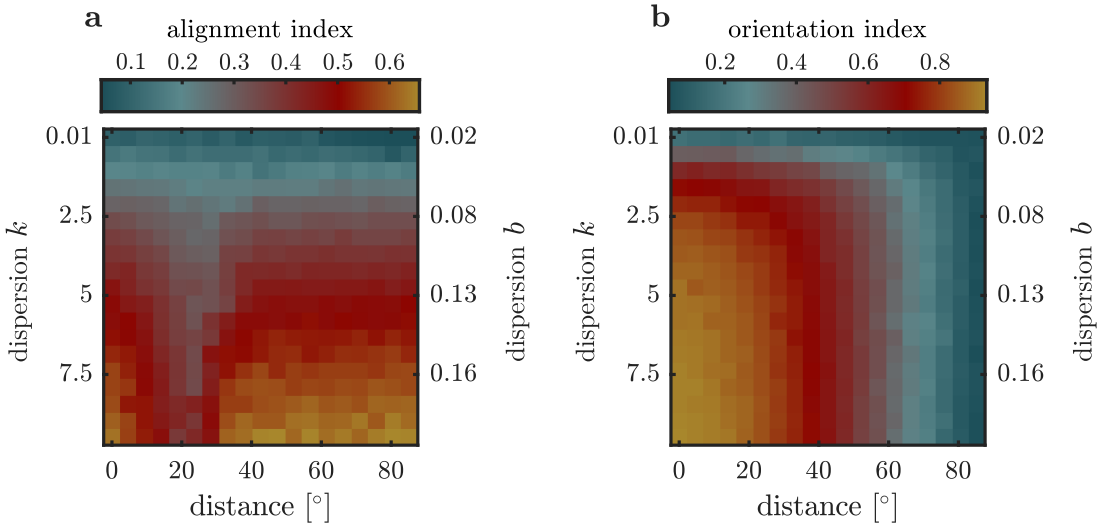

Figure 4.7: Orientation and alignment index as a function of dispersion and angular spacing of two fiber families. (**a**) Orientation index as a function of dispersion and angular spacing of two fiber families. (**b**) Alignment index as a function of dispersion and angular spacing of two fiber families.

4.4 Local Fiber Orientations

In addition to the quantification of the entire fiber network using the FINE algorithm, local orientations give meaningful insights into the angular properties of a fiber network.

4.4.1 Orientation Space

The orientation space for 2D images was introduced by [92] and is used here for calculating local orientation quantities such as main orientation and orientation index. The

orientation space is a discretized space, where the orientation $\theta \in [0, 180°]$ is introduced as third coordinate. The transformation of an image $I(x, y)$ from Cartesian coordinates to the orientation space $I_{\text{loc}}(x, y, \theta)$ is defined as:

$$I_{\text{loc}}(x, y, \theta) = \mathcal{F}^{-1}[\hat{I}(u, v) \cdot w(u, v, \theta)] = \mathcal{F}^{-1}[\mathcal{F}[I(x, y)] \cdot w(u, v, \theta)], \tag{4.5}$$

where $w(u, v, \theta)$ denotes a wedge-shaped filter bank, which is for example represented by the weighting factors w_{int}, introduced in equation (3.18). Figure 4.8 illustrates the transformation of a SHG image of dermal collagen in figure 4.8 (a) to the orientation space using w_{int} as wedge filters. The first step is to transform the image to the Fourier domain, as shown in figure 4.8 (b). Next, according to equation 4.5, a wedge filter bank is applied by pixel-wise multiplication, as shown in figure 4.8 (c). The orientation space $I_{\text{loc}}(x, y, \theta)$ is then achieved by applying an inverse discrete Fourier transformation on each wedge-filtered Fourier transform (figure 4.8).
The local main orientation $I_{\bar{\theta}}(x, y)$ then results from evaluating the angular location of maximum intensity at each pixel (x, y):

$$I_{\bar{\theta}}(x, y) = \max_{\theta}[I_{\text{loc}}(x, y, \theta)]. \tag{4.6}$$

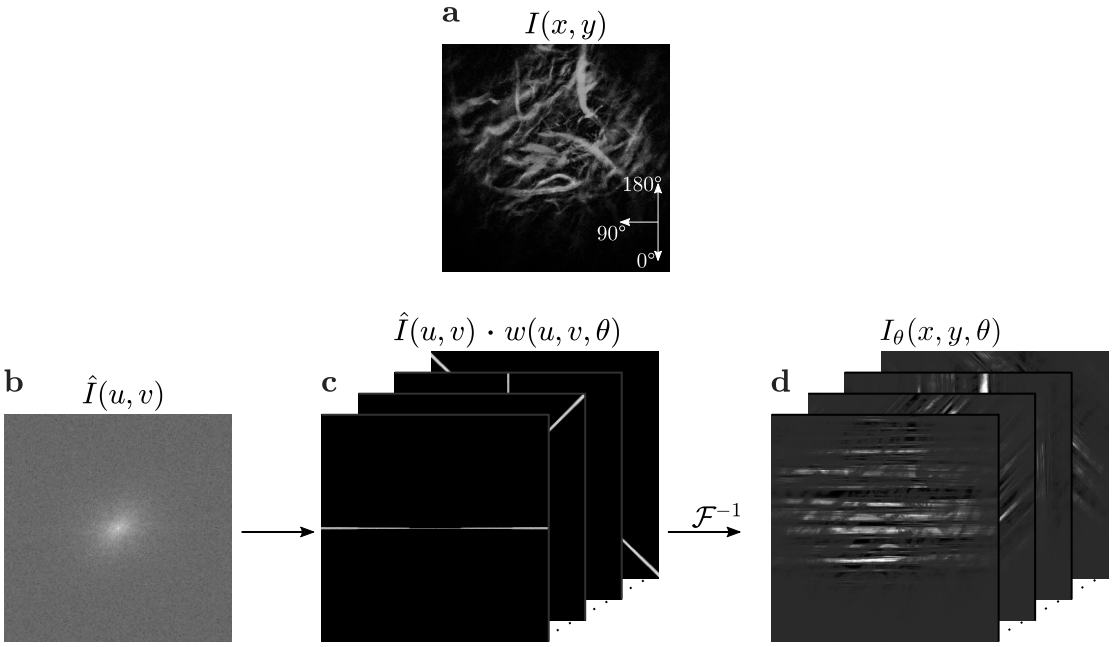

Figure 4.8: Computation of local orientation spectra. (**a**) Input in-vivo, preprocessed SHG image $I(x, y)$ of dermal collagen. (**b**) Fourier transform $\hat{I}(x, y) = \mathcal{F}[I(x, y)]$. Note that only the real part of $\hat{I}(x, y)$ is shown in logarithmic greyscale for a better visibility. (**c**) Wedge filter bank $w_{\text{int}}(u, v, \theta)$ applied on $\hat{I}(x, y)$. (**d**) Inverse transformation of every wedge filtered image to achieve local orientation spectra $I(x, y, \theta)$.

4.4.2 Wedge Filter Banks

The shape of the wedge filter bank $w(x, y, \theta)$ influences the accuracy of local orientation spectra. McLean *et al.* used a wedge filter bank which consists of pixels in the frequency domain that are included in an angular interval $[\theta - \delta\theta, \theta + \delta\theta]$ [93]:

$$w_w(u, v, \theta) = \begin{cases} 1 & \text{if } \tan^{-1}\left(\frac{v}{u}\right), \\ 0 & \text{else.} \end{cases} \tag{4.7}$$

In addition, McLean *et al.* [93] used a Gaussian kernel for a convolution in the Fourier domain to remove sharp edges of the wedge filter bank, which reduces the effect of Gibbs artifacts:

$$w_g(u, v, \theta) = w_w(u, v, \theta) * g(u, v), \tag{4.8}$$

where the operator $*$ denotes the convolution. In the following the filter bank w_g is referred to as *gaussian-wedge*. Exemplary gaussian-wedge filters are shown in figure 4.9 (a). For comparison, the true-intersection filter bank w_{int} with an angular span of $\delta\theta = 0.5°$ is shown in figure 4.9 (b).

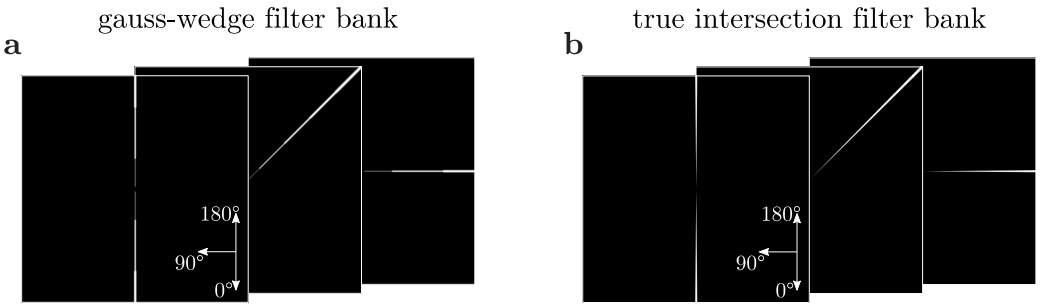

Figure 4.9: Directional filter banks $w(u, v, \theta)$**.** (**a**) Wedge filter bank that was smoothed using a Gaussian convolution kernel with $\sigma = 0.9$ according to [93]. (**b**) True intersection wedge filter bank. Note that in (**a**) and (**b**) solely orientations $\theta \in [0°, 45°, 90°]$ are displayed.

In order to quantitatively compare both wedge filter banks, the main local fiber orientation of Monte-Carlo images are simulated using one fiber family. A total of 500 images are generated using the input parameters listed in table 4.1. Here, the noise factor is set to zero to allow for an accurate pixel-wise calculation of the local main orientation.

Table 4.1: Input parameters of the Monte-Carlo simulation for the comparison of wedge filter banks.

input parameter	values
dispersion k	$[0.01, 10]$
mean orientation $\bar{\theta}$	$[0°, 180°]$
fiber width	$[3, 10]$
aspect ratio	$[20, 45]$
noise factor	0

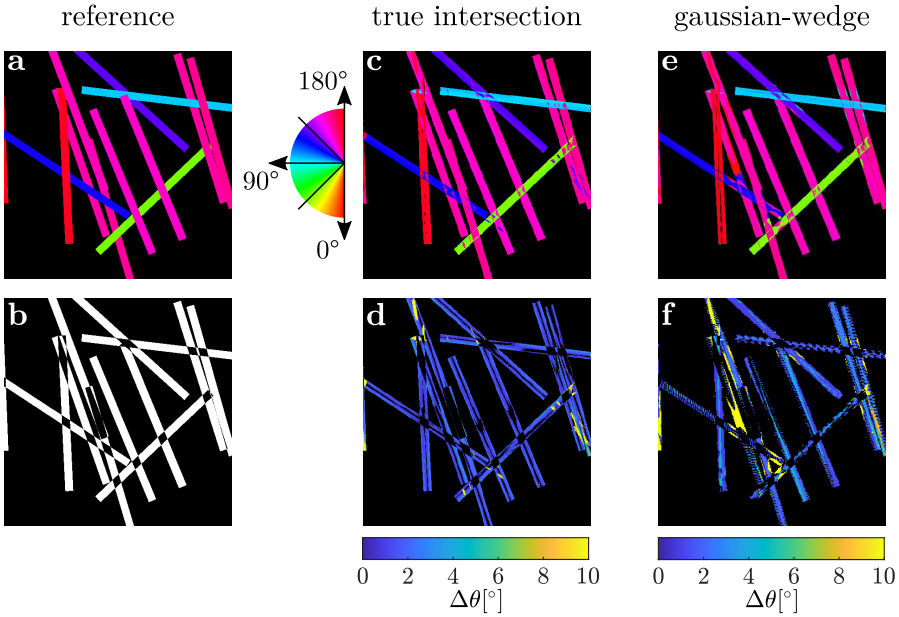

Figure 4.10: Comparison of the local main fiber orientation using different wedge filters. (**a**) Reference fiber orientation of the exemplary Monte-Carlo image. (**b**) Evaluation mask that is used for excluding areas of overlapping fibers where the local main orientation is not unique. (**c**) Main fiber orientation using the true intersection wedge filter bank. (**d**) Absolute difference between reference (**a**) and computed local main fiber orientation using true intersection wedges (**c**). (**e**) Main fiber orientation using the gaussian-convoluted wedge filter bank. (**f**) Absolute difference between reference (**a**) and computed local main fiber orientation using gaussian-convoluted wedges (**c**).

The respective local main orientation (equation (4.6)) in false colors of an exemplary, Monte-Carlo generated fiber image is shown in figure 4.10 (a). Since the main orientation at overlaps of crossing fibers is ambiguous, an evaluation mask is created to exclude overlaps from statistical evaluation. An exemplary evaluation mask is shown in figure 4.10 (b). White areas are indicating locations where the local main orientations are compared to the reference. The calculated local main orientation using the true-intersection wedge filter bank with an angular span of $\Delta\theta = 0.5°$ is shown in figure 4.10 (c).

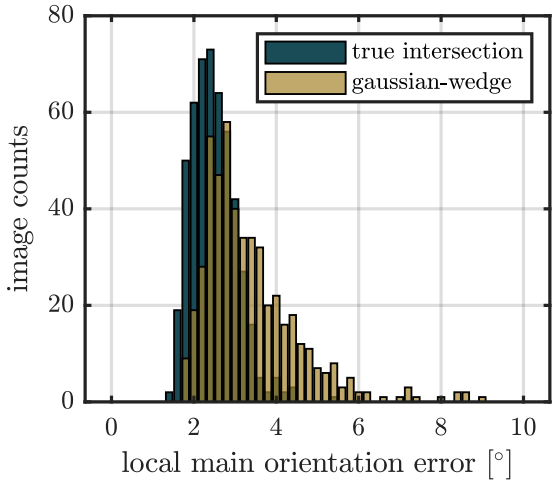

Figure 4.11: Error distribution of different wedge filter banks. The local main orientation error indicates the mean error of each pixel averaged over each image. $N = 1000$ images are used in total.

The local absolute angular deviation to the reference in figure 4.10 (d) shows that the computed local main orientation is most accurate in the center of each fiber. The error slightly increases to $\sim 3°$ towards the fiber edges. Larger errors are occurring where the imaginary interpolation of a fiber strongly contributes to the local orientation spectrum, such that the main orientation is wrongly determined. The corresponding local main fiber orientation using gaussian-convoluted wedge filter bank in figure 4.10 (e) is more sensitive to surrounding fibers. The local deviation to the reference in figure 4.10 (f) indicates that in areas of a high fiber density the computation of the local fiber orientation is unstable. In order to quantitatively compare the usage of true-intersection wedges to gaussian-convoluted wedges in terms of the local fiber orientation the local error is averaged for each image. The resulting error distributions of the Monte-Carlo simulated images are shown in figure 4.11. The error distribution using gaussian-convoluted wedges is broadened and shifted towards higher averaged errors. The mean local main orientation error amounts to $(2.5 \pm 0.5)°$ and $(3.4 \pm 1.2)°$ using true-intersection and gaussian-convoluted wedges, respectively.

4.4.3 Local Orientation Index

In addition to the local main orientation of equation (4.6) the local orientation index, $\mathrm{OI}(x, y)$ is introduced as a pixel-wise version of equation (4.3):

$$\mathrm{OI}(x,y) = 2\frac{\sum_{\theta=0°}^{180°} I_{\mathrm{loc}}(x,y,\theta)\cos^2(\theta-\bar{\theta})}{\sum_{\theta=0°}^{180°} I_{\mathrm{loc}}(x,y,\theta)} - 1. \tag{4.9}$$

Figure 4.8 shows an exemplary SHG image of dermal collagen, for which local quantities are calculated. Local orientation spectra in figure 4.8 (a)-(d) indicate the presence of either one main orientation like in figure 4.8 (b) and figure 4.8 (c), or the presence

of two main orientations at intersections of fibers like in figure 4.8 (d). In the latter case, the local main orientation in figure 4.8 (e) is ambiguous. Intersecting fibers can be identified by a vanishing orientation index, which is shown in figure 4.8 (f) in false colors. Note that for the false color representations of figure 4.8 (e) and figure 4.8 (f), the local main orientation (equation (4.6)) and the local orientation index (equation (4.9)), are scaled by the relative intensity $I(x, y)/\max[I(x, y)]$ to suppress areas of low intensity.

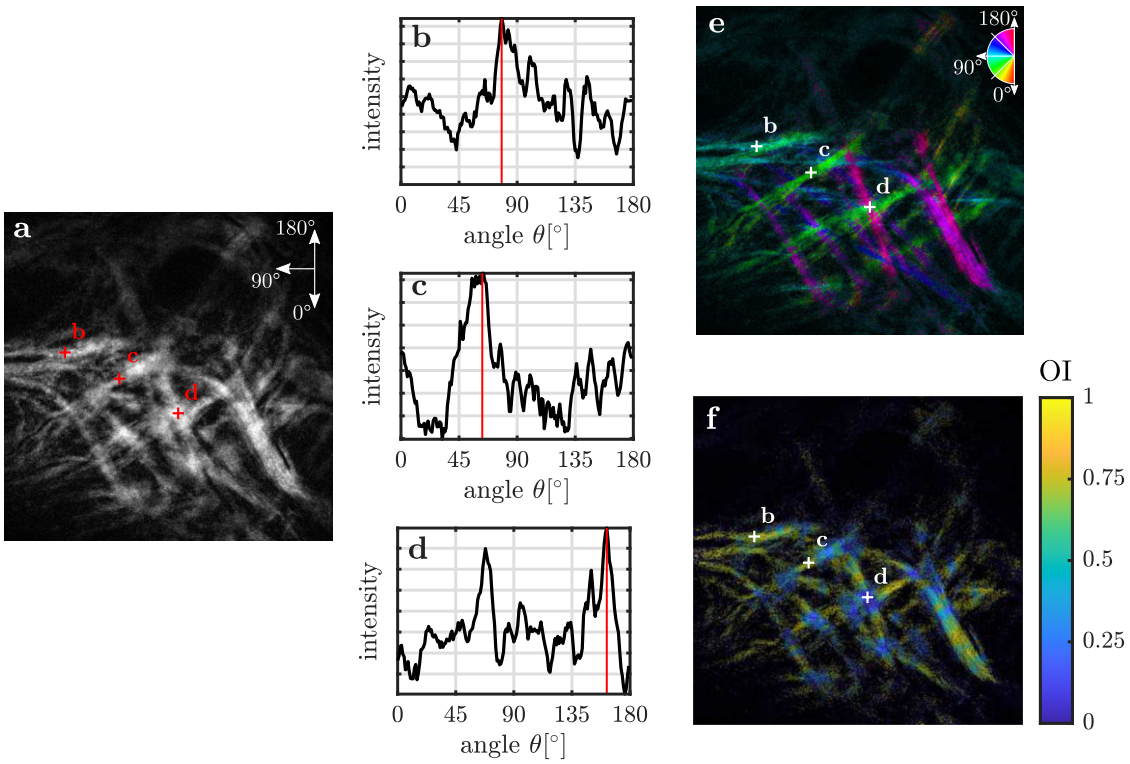

Figure 4.12: Computation of the local main orientation and the local orientation index. (**a**) Input in-vivo SHG image $I(x, y)$ of dermal collagen. The image was preprocessed by means of a background subtraction using the function *Subtract Background* of the software ImageJ (Fiji)[94] with a rolling ball radius of 50 pixels to enhance the contrast of fibers. (**b**) Local orientation spectrum with a main orientation of 80°. (**c**) Local orientation spectrum with a main orientation of 60°. (**d**) Local orientation spectrum at an intersection of two collagen fibers. (**e**) Local main orientations shown in false colors. (**f**) Local orientation index shown in false colors. Note that local orientation spectra that feature a clear main orientation like in (**b**) and (**c**) exhibit a high orientation index. Contrary, the OI vanishes at perpendicular fiber intersections like in (**d**).

4.5 Monte-Carlo Simulations

Similar to section 3.6, Monte-Carlo simulated fiber images are used to compare calculated quantities of the FINE algorithm against their reference values. Here, the Monte-Carlo procedure described in 4.1 is used to simulate multiple fiber families.
The anisotropic mechanical behavior of fiber-reinforced materials is strongly determined by the alignment of fibers [10, 86, 95]. To simulate the degree of anisotropy, the anisotropic ratio of fibers (ARF) is varied in a controlled fashion. This is realized by the simulation of an isotropic family with $N_f = 200$ fibers in addition to an anisotropic family with a variable number of fibers, $N_f = [0, 200]$. Exemplary images are shown in figure 4.1 (a-d). The FINE algorithm is then examined for its ability to differentiate between the isotropic fiber family and the anisotropic fiber family.
The second Monte-Carlo simulation tests the performance of the FINE algorithm to identify multiple, aligned fiber families. Images are allowed to contain up to five fiber families with a sufficient angular separation of the mean orientation of adjacent families. Figure 4.6 (a) reveals that a clear separation of highly aligned fiber families is ensured for an angular spacing of $> 30°$. Monte-Carlo input parameters of both simulations are given in table 4.2.

Table 4.2: Input parameters of the Monte-Carlo simulations to benchmark the FINE algorithm. *Anisotropic ratio* and *multiple fiber families* denote different simulations.

input parameter	anisotropic ratio	multiple fiber families
number of fiber families N	1	$[1, 5]$
ARF	$[0, 0.5]$	1
dispersion k	10	10
mean orientation $\bar{\theta}$	$[0°, 180°]$	$[0°, 180°]$
fiber width	$[3, 10]$	$[3, 10]$
aspect ratio	$[20, 45]$	$[20, 45]$
noise factor	$[0, 1]$	$[0, 1]$

4.6 Application to In-Vivo Data

The FINE algorithm is applied to in-vivo SHG images of dermal collagen. By using a depth-stack of images, differences of the fiber network across the skin depth are investigated. Images are recorded using the multiphoton microscope DermaInspect (section 2.2.3) at a constant mean illumination power of 50 mW and a scan time of 7 s. The 40× magnification objective lens images a $220 \times 220\,\mu$m field of view on 512×512 pixels. The depth relative to the skin surface is achieved by normalizing the depth of collagen skin layers to the measured depth of the skin surface. The skin surface is recorded by capturing the TPF signal with a broad band-pass filter of (548 ± 150) nm at an excitation wavelength of 750 nm.

4.7 Results and Discussion

The FINE algorithm, the results of the Monte-Carlo simulations, and the application to in-vivo data are presented and discussed in a paper published in *Scientific Reports* [96]. The publication is shown in section 4.8. However, a brief summary of the main findings is given here.

Monte-Carlo simulations. The FINE algorithm exhibits an accuracy of $\geq 90\,\%$ to distinguish the isotropic fiber family from the anisotropic fiber family for a minimum ARF of 0.163. The amplitude of the identified, anisotropic fiber family is found to slightly overestimate the defined ARF. For example, an amplitude of 0.6 is measured at a maximum ARF of 0.5. This is related to fibers of the isotropic fiber family that are by chance aligned in the direction of the anisotropic family. The mean orientation of the anisotropic fiber family is accurately estimated with a mean absolute error of $(2.4 \pm 2.5)^\circ$.
In addition, the FINE algorithm is able to identify up to four fiber families with an accuracy of $\geq 98.1\,\%$. Calculated amplitudes closely match the expected values, which are equal to the reciprocal number of defined fiber families. In case of five defined fiber families, the accuracy to detect five fiber families slightly decreases to $87.0\,\%$. Simultaneously, the variance of the amplitude of the first fiber family is increased in this case. This indicates that some networks consisting of five highly aligned fiber families are considered as a single, isotropic fiber family.

Application to in-vivo data. Parameters of the fiber families and the AI and OI determined by the FINE algorithm, show an evolution of the angular properties of the dermal collagen fiber network with increasing dermal depth. Upper layers of the papillary dermis exhibit one isotropic fiber family in addition to a highly aligned fiber family. Up to a depth of $85\,\mu$m the amplitude of the isotropic fiber family dominates the aligned fiber family. With increasing depth two aligned fiber families emerge with perpendicular mean orientations around the Langer lines. This is visually validated by local main orientations. Furthermore, the decrease of the OI with a concurrent increase of the AI between $85\,\mu$m and $90\,\mu$m strongly suggests a transition from the papillary dermis to the reticular dermis. This is in line with Neerken *et al.* [97], who measured the onset of the reticular dermis at a depth of $(95 \pm 10)\,\mu$m at the temple using optical coherence tomography (OCT).

4.8 Publication

www.nature.com/scientificreports

SCIENTIFIC REPORTS
nature research

OPEN

General method for classification of fiber families in fiber-reinforced materials: application to in-vivo human skin images

Maximilian Witte[1,2], Sören Jaspers[2], Horst Wenck[2], Michael Rübhausen[1] & Frank Fischer[2]✉

Fiber structures play a major role for the function of fiber-reinforced materials such as biological tissue. An objective classification of the fiber orientations into fiber families is crucial to understand its mechanical properties. We introduce the Fiber Image Network Evaluation Algorithm (FINE algorithm) to classify and quantify the number of fiber families in scientific images. Each fiber family is characterized by an amplitude, a mean orientation, and a dispersion. A new alignment index giving the averaged fraction of aligned fibers is defined. The FINE algorithm is validated by realistic grayscale Monte-Carlo fiber images. We apply the algorithm to an in-vivo depth scan of second harmonic generation images of dermal collagen in human skin. The derived alignment index exhibits a crossover at a critical depth where two fiber families with a perpendicular orientation around the main tension line arise. This strongly suggests the presence of a transition from the papillary to the reticular dermis. Hence, the FINE algorithm provides a valuable tool for a reliable classification and a meaningful interpretation of in-vivo collagen fiber networks and general fiber reinforced materials.

Biological tissue such as articular cartilage[1], myocardium[2], aortic valve[3], arterial walls[4], and skin[5] exhibit a stress strain behavior that strongly depends on the collagen fiber distribution. Fiber reinforced materials are classified by the underlying fiber network which is characterized by its anisotropy and the fiber orientation[6–8]. Upon stretching, tensile forces are applied to biological specimens and collagen fibers align in the stretching direction[9–14]. The characterization of the collagen network is typically determined by quantities like the orientation index, mean fiber orientation, and the fiber dispersion. These parameters are obtained from the angular orientation distribution which is commonly modeled by a pi-periodic von-Mises function[15–21]. However, this approach assumes that all fibers are part of a single fiber family. Gasser et al. introduced a mechanical model for arterial walls which assumes the existence of two opposing collagen fiber families, which are oriented around a main direction[4]. Parameters for this model are achieved by modeling the fiber orientation distribution using two pi-periodic von-Mises functions[22]. Skin is of major relevance as it represents the largest organ of the human body. It is subject to diverse environmental stress conditions and also large mechanical strains. Langer lines, also known as cleavage lines, are reported to indicate the main orientation of collagen fibers in skin[16].

We introduce the Fiber Image Networks Evaluation algorithm (FINE algorithm), which is based on the cumulative orientation distribution (COD), to classify and quantify the fiber network by means of fiber families. The FINE algorithm uses an iterative approach to identify the number of fiber families and their angular properties. The variance of the COD that is obtained by the adaptive Fourier filtering method, proposed in[23], is used to estimate the significance of each fiber family. To benchmark the FINE algorithm, realistic grayscale Monte-Carlo simulated fiber images containing multiple fiber families are used. We derive the minimum fraction of anisotropic fibers as well as the maximum number of highly aligned fiber families that the FINE algorithm is able to discriminate. In addition to the orientation index (OI), we introduce and validate the alignment index (AI) which quantifies the average alignment degree of different fiber families. We apply the FINE algorithm to in-vivo, three-dimensional images of collagen fibers in human skin. Indeed, at a depth of 85–90 µm we find an increase of the derived alignment index with a concurrent decrease of the orientation index. Furthermore, two

[1]Center for Free-Electron Laser Science (CFEL), University of Hamburg, 22607 Hamburg, Germany. [2]Beiersdorf AG, 20245 Hamburg, Germany. ✉email: Frank.Fischer@Beiersdorf.com

www.nature.com/scientificreports/

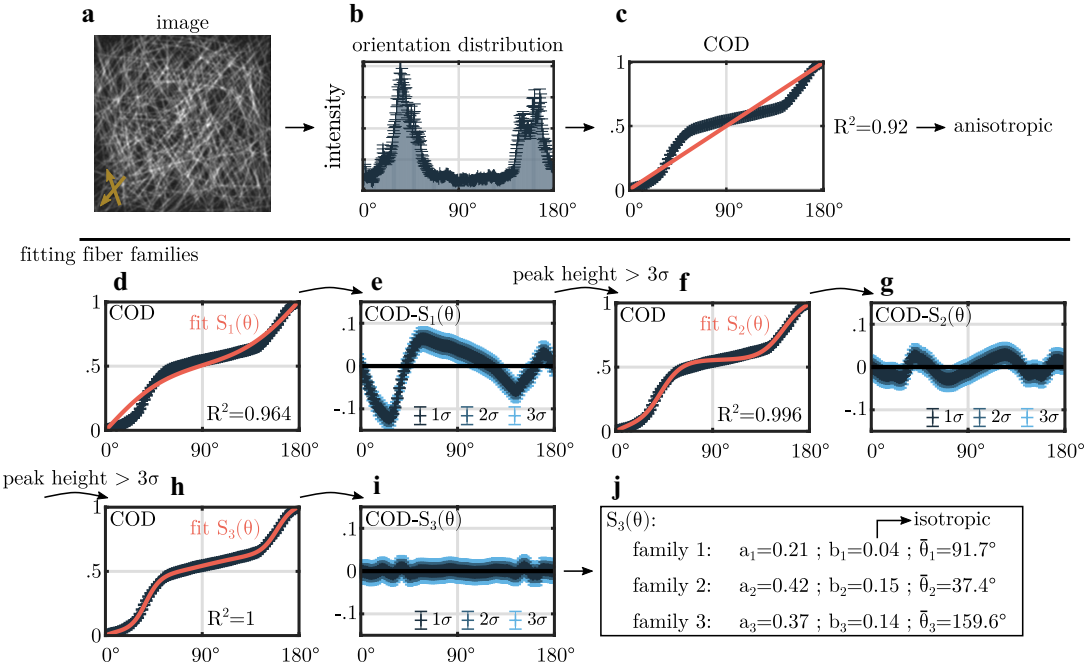

Figure 1. Schematic representation of the FINE algorithm. (**a**) Exemplary Monte-Carlo simulated fiber image with 300 isotropically distributed fibers and two aligned fiber families, each containing 175 fibers ($\bar{\theta}_2 = 40°$ and $\bar{\theta}_2 = 160°$; $b_2 = b_3 = 0.18$). (**b**) The angular orientation distribution $I(\theta)$ is achieved according to Witte *et al.*[23]. (**c**) As a first step the cumulative orientation distribution (COD) is checked for isotropy as the R^2 value of a straight line with slope 1/180° is examined. (**d**) Fit of a single step function to model one fiber family (S_1 Eq. (8)) to the COD. (**e**) Difference between the COD and S_1 with subsequent peak finding. (**f**) Fit of two fiber families using a series of two sigmoid functions (S_2). (**g**) Difference between the signal COD and S_2 with subsequent peak finding. (**h**) Final fit of three fiber families using a series of three sigmoid functions S_3. (**i**) Final difference between the COD and S_3. Since no significant residuals are present, the algorithm terminates. (**j**) Summary of the fit parameters of the three fiber family fit S_3. Two highly aligned fiber families in addition to one isotropic fiber family are identified.

intersecting fiber families with a perpendicular orientation around the Langer line arise. This strongly suggests the presence of a transition from the papillary to the reticular dermis.

Results and discussion

Fiber image network evaluation algorithm (FINE algorithm). We develop a general method for classification of fiber families in fiber-reinforced materials, Fiber Image Network Evaluation Algorithm (FINE algorithm). In order to explain the algorithm, we use an artificial fiber image, shown in Fig. 1(a). Artificial, grayscale fiber images are created using a Monte-Carlo procedure that allows us to control the number of fiber families, their amplitudes and their fiber distributions.

In the FINE algorithm, the number N, the mean orientations $\bar{\theta}_i$, the amplitudes a_i and the dispersion b_i of fiber families, based on the cumulative orientation distribution (COD) of an input fiber image, are identified. We obtain the COD by applying the adaptive Fourier filter method (AF method), as proposed by Witte *et al.*[23], to a fiber image. Exemplary, this is shown for an artificial, grayscale Monte-Carlo fiber image in Fig. 1(b). The proposed AF method provides the variance σ of the COD, which we use in the FINE algorithm as termination criterion.

We use the sigmoid function of Eq. (5) to model the COD of one fiber family. This sigmoid function has a step at the mean orientation angle $\bar{\theta}$, a steepness given by the dispersion b of the fibers around its mean orientation and a height given by the amplitude a. Furthermore, the analysis of N fiber families in the fiber image is realized by modeling the COD as a sum of N sigmoid functions [Eq. (8)]. The number N of fiber families is iteratively determined by the FINE algorithm. The FINE algorithm starts with the most trivial assumption of a completely isotropic fiber distribution. Such a distribution is described by a straight line with slope 1°/180° in the COD. Thus, the first step in the algorithm is to check for an isotropic distribution by evaluating the R^2 value of the straight line. Exemplary, this is shown in Fig. 1(c) for the artificial Monte Carlo generated fiber image of Fig. 1(a). In Fig. 1(c), the ideal isotropic fiber distribution is represented by a red, straight line. In the FINE algorithm, a fiber distribution is considered as isotropic for a fit quality better than $R^2 = 0.9916$. In our example, $R^2 = 0.92$

indicates the presence of at least one fiber family, and the first sigmoid function (Eq. (8) with $N=1$) is fitted to the COD. The resulting fit of a single fiber family is shown in Fig. 1(d). The quality of the fit increases to $R^2 = 0.964$. However, the difference between the single sigmoid fit and the COD, shown in Fig. 1(e), is larger than 3σ. For the FINE algorithm, this is the criterion to consider an additional fiber family. Now, the angular location of the largest deviation between COD and fit is considered as new starting value for the additional fiber family. The corresponding fit of a series of two sigmoid functions ($N = 2$) is shown in Fig. 1(f). Although a better goodness of the fit with $R^2 = 0.996$ is reached, the corresponding residual, as shown in Fig. 1(g) indicates the existence of another significant amplitude. Again, we employ the location of the highest deviation between fit and COD as initial location for a third sigmoid function ($N = 3$). In our fiber image simulation example the COD and the fit are presented in Fig. 1(h). We now obtain $R^2 = 1$, and the residual between fit and COD is within the 3σ criterion (Fig. 1(i)). This terminates the FINE algorithm.

The fit parameters received from the FINE algorithm, shown for our example in Fig. 1(j), are now used to evaluate the structure of the fiber network. In our fiber image, a small dispersion coefficient of $b_1 = 0.04$ indicates that this fraction of fibers is isotropically distributed. Fiber families 2 and 3 are highly aligned with $b_2 = 0.15$ and $b_3 = 0.14$. The amplitudes a_i are a measure for the fraction of each fiber family with respect to the whole fiber network. The amplitudes show that the aligned fiber families 2 and 3 exhibit a similar fiber fraction within the network ($a_2 = 0.42$ and $a_3 = 0.37$). In contrast, the isotropic fiber family 1 contributes less with $a_1 = 0.21$. Since we used a Monte-Carlo generated fiber image as input in our example, the determined parameters found by FINE algorithm can be compared to the preset values of the Monte Carlo simulation. For our example, we find that the dispersion coefficients of fiber families 2 and 3 calculated by the FINE algorithm underestimate the Monte-Carlo input value of $b = 0.18$, indicating a broadening of the distribution of aligned fibers. Predefined mean orientations of the highly aligned fiber families with $\bar{\theta}_2 = 40°$ and $\bar{\theta}_3 = 160°$ are reproduced with $\bar{\theta}_2 = 37.4°$ and $\bar{\theta}_3 = 159.6°$.

In order to evaluate the FINE algorithm, we generate Monte-Carlo fiber images with systematically modified properties and compare preset fiber network parameters with the network parameters calculated by the FINE algorithm.

FINE evaluation using Monte-Carlo images. Our general expectation to a fiber distribution includes isotropic as well as aligned parts. The quantification of both parts is crucial in order to identify an anisotropic material behavior. Since the FINE algorithm calculates the dispersion as well as the amplitude of each fiber family, we are analyzing its ability to discriminate the aligned part from the isotropic part. In order to control the aligned part of our Monte-Carlo images, we define the anisotropic ratio of fibers (ARF) of our Monte-Carlo simulated images. The ARF measures the number of fibers contributing to an aligned fiber family relative to the total number of sampled fibers.

Anisotropic ratio of fibers. Monte-Carlo images with two fiber families, one isotropic and one highly aligned family are created. In the process, we use a constant number of 200 isotropically distributed fibers, together with a variable number of highly aligned fibers as anisotropic part. The maximum number of aligned fibers is limited to 200 (ARF = 0.5), whilst zero aligned fibers ensure a pure isotropic distribution (ARF = 0). A total of 10^4 images are generated to guarantee a high statistical accuracy of the result. Exemplary Monte-Carlo images with a different ARF are shown in Fig. 2(a). Figure 2(b) shows the calculated local fiber orientation in false colors. Color-coded fiber angles visually coincide well with the expected angles.

For quantitative evaluation, we measure different parameters of the FINE algorithm as a function of the ARF. The mean number of total fiber families N_{tot}, the mean number of anisotropic fiber families N_{align} and the mean number of isotropic fiber families N_{iso} identified by the algorithm are shown in Fig. 2(c). As expected, the mean number of isotropic fiber families constantly remains at a mean value of $N_{\text{iso}} = 1$. Contrary, its standard deviation first increases to maximum of 0.25 at a ratio of ARF = 0.12 and then decreases to a constant value of ~ 0.05 for a fraction larger than ARF > 0.35. The mean number of identified aligned fiber families increases from near zero at a vanishing anisotropic part to a value of $N_{\text{align}} = 1$ for a ratio of ARF ≥ 0.163. The determined mean orientation $\bar{\theta}$ of the aligned fiber family exhibits an absolute deviation to the reference angle of $\Delta\bar{\theta} = (2.4 \pm 2.5)°$. Next, we determine the probability that the FINE algorithm identifies exactly one isotropic and one highly aligned fiber family, which is shown in Fig. 2(d). The accuracy rapidly increases with the number of aligned fibers. At a ratio of ARF = 0.163, a 90% accuracy for the identification for one isotropic and one aligned fiber family is reached. For ARF ≥ 0.163, the error of the calculated mean orientation $\bar{\theta}$ of the aligned fiber family decreases to $\Delta\bar{\theta} = (2.0 \pm 1.9)°$. The mean amplitude of the aligned fiber family increases from near zero at a vanishing ARF to 0.6 at ARF = 0.5 (Supplementary Fig. 1(a)). Remarkably, the calculated amplitudes are overestimating the anisotropic ratio. Since grayscale images are created, where fiber intensities are added to the image, the overlay of multiple fibers causes an artifact in the angular orientation distribution[18]. Additionally, isotropic fibers that are by chance oriented in the direction of the aligned fiber family might further raise the intensity of the aligned fiber family.

Furthermore, the dispersion of the aligned fiber family constantly increases with the ARF but remains underneath the predefined value of $b = 0.18$ (Supplementary Fig. 1(b)). This indicates a broadened angular width of the aligned fiber family with respect to its defined value. The deviation to the reference most likely originates from the significant angular overlap between both fiber families, such that fibers either contribute to the anisotropic or the isotropic part. A very high mean goodness of the fit of $R^2 = 0.999 \pm 0.001$ indicates a very good representation of the COD by the FINE algorithm.

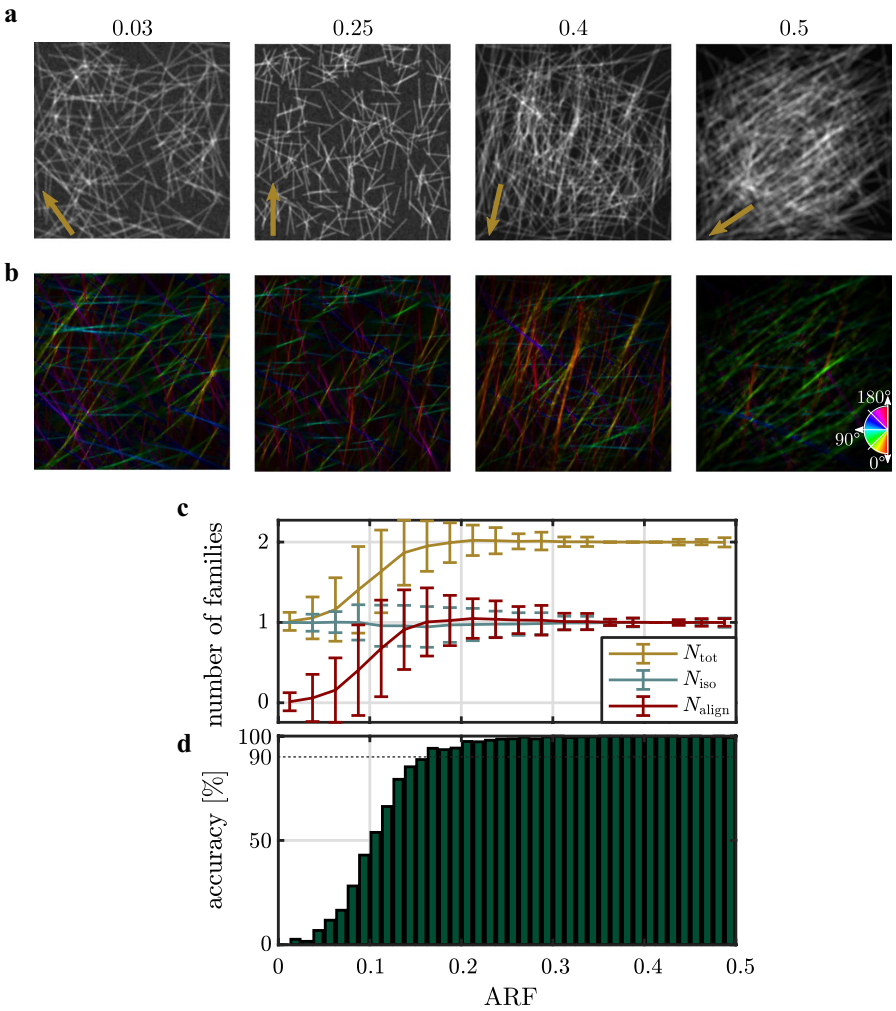

Figure 2. Result of the FINE algorithm as a function of the anisotropic ratio of fibers (ARF) of Monte-Carlo simulated fiber images. (**a**) Representative Monte-Carlo images with a different ARF. Mean orientations of the aligned fiber families are indicated by arrows in the bottom, left corner. (**b**) Calculated local main orientation in false colors. (**c**) Mean number of fiber families N_{align} (aligned), N_{iso} (isotropic) and N_{total} (total) that were identified by the algorithm. Error bars represent the standard deviation. (**d**) Accuracy of the algorithm to identify exactly one aligned and one isotropic fiber family.

Multiple aligned fiber families. Another important evaluation aims to capture the performance of the FINE algorithm to identify multiple non-overlapping highly aligned fiber families. To ensure a clear angular separation of each created fiber family, a minimum angular distance between adjacent families has to be enforced. In order to find a good estimate for the minimum angular distance, the ability of the algorithm to separate two equally dispersed families from each other is investigated. Supplementary Fig. 2(a) shows the mean number of identified fiber families for Monte-Carlo images with two equally dispersed fiber families as a function of their alignment and their angular distance. If the angular distributions of both fiber families are exceeding a critical angular overlap, as exemplary shown in Supplementary Fig. 2(b) and (c) the FINE algorithm identifies a single fiber family. A clear separation of both families can be accomplished by a vanishing angular overlap, which is ensured for a minimum angular distance of 30° and a high alignment of $b > 0.16$ (Supplementary Fig. 2(d)).

We generate Monte-Carlo images containing up to five highly aligned fiber families, that are exemplary shown in Fig. 3(a). The number of fibers contributing to one fiber family as well as their dispersion are held constant. The calculated local fiber orientations are shown in false colors in Fig. 3(b). The COD is modeled with $R^2 = 0.999 \pm 0.002$. Mean orientation angles of each aligned fiber family are found with a high accuracy as the absolute deviation to the reference mean orientations amounts to $\Delta\bar{\theta} = (0.7 \pm 0.5)°$. The ratio of images where

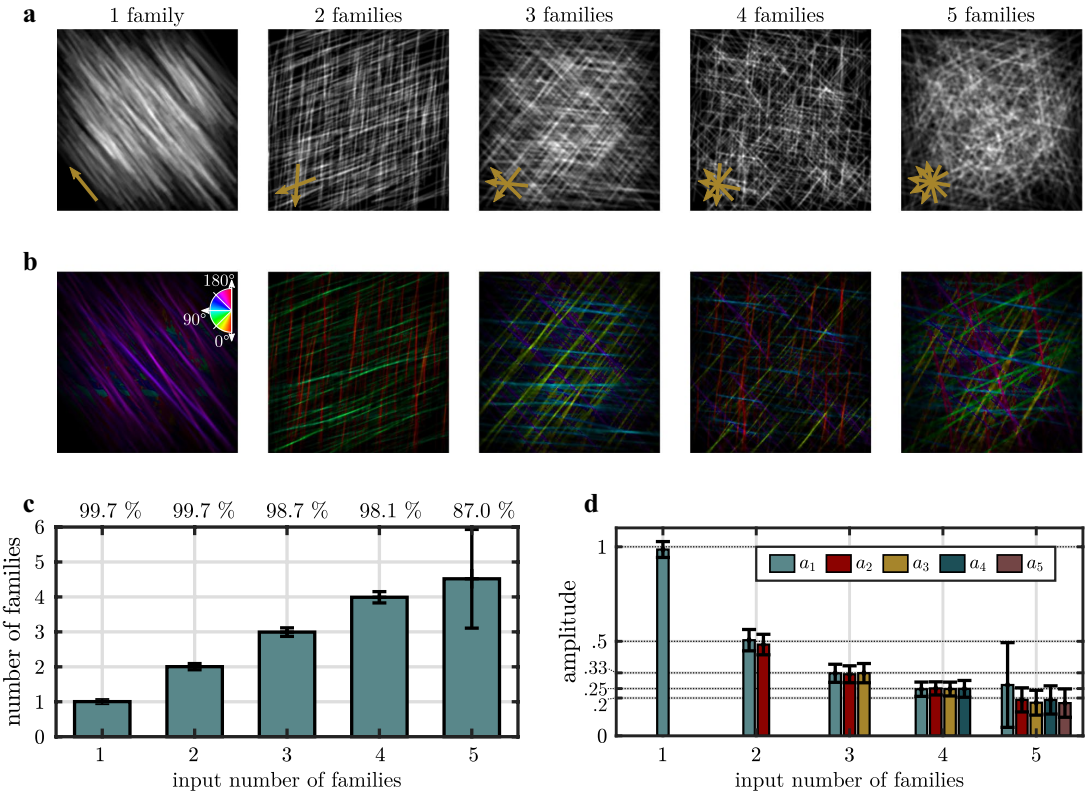

Figure 3. Result of the FINE algorithm applied to Monte-Carlo simulated grayscale fiber images containing one to five fiber families. (**a**) Representative images with one to five fiber families. Mean fiber orientations are indicated by arrows in the bottom, left corner. (**b**) Calculated local main orientation in false colors. (**c**) The mean number of fiber families estimated by the algorithm. Error bars represent the standard deviation. The percentage of images for which the number of estimated fiber families matches the number of defined fiber families is specified at the top. (**d**) The amplitudes of each identified fiber family. Error bars represent the standard deviation. Expected amplitude levels at 1, 0.5, 0.33, 0.2 are marked with dotted lines. Note that amplitudes below a value of 0.01 are removed for the sake of clarity.

the predefined number of fiber families is identified, decreases from 99.7% in case of one and two predefined fiber families down to 87.0% in case of five predefined fiber families (Fig. 3(c)). The mean number of identified fiber families matches the number of predefined fiber families for Monte-Carlo images with up to four fiber families. With an increase of fiber families, the probability to wrongfully identify the network as an isotropic network increases, since an infinite number of fiber families yields an isotropic network. The amplitude of each identified fiber family as well as expected amplitudes 1, 0.5, 0.33, 0.2 are shown in Fig. 3(d). Mean amplitudes are found to closely match the expected values.

Dermal collagen fiber network. Collagen fibers represent the major load-bearing component of connective tissue such as the dermal skin layer[16,24,25]. Contrary to the straight fibers that are sampled in our artificial Monte-Carlo images, collagen fibers are wavy and bended[17] Compared to the angular orientation distribution of a network of straight fibers, the angular orientation distribution of a wavy and bended fiber network is broadened. Since the FINE algorithm processes the entire angular orientation distribution of an image, the waviness of fibers does not influence the algorithms accuracy. We capture the second harmonic generation (SHG) signal of dermal collagen fibers by using multi-photon microscopy, which is a common tool to visualize collagen fibers of human skin in-vivo[26,27]. We apply the FINE algorithm to an in-vivo depth scan of the SHG signal of dermal collagen in human skin. Depths from 60 µm up to 105 µm relative to the skin surface are measured. Mean orientation angles, amplitudes and dispersions of identified fiber families are evaluated. Additionally, derived parameters, which quantify the entire orientation distribution are calculated. The orientation index (OI) describes the global alignment of the fibers with respect to their main orientation based on the angular orientation distribution[28]. Contrary, we define the alignment index (AI) as a measure of the global alignment of the fibers, independent

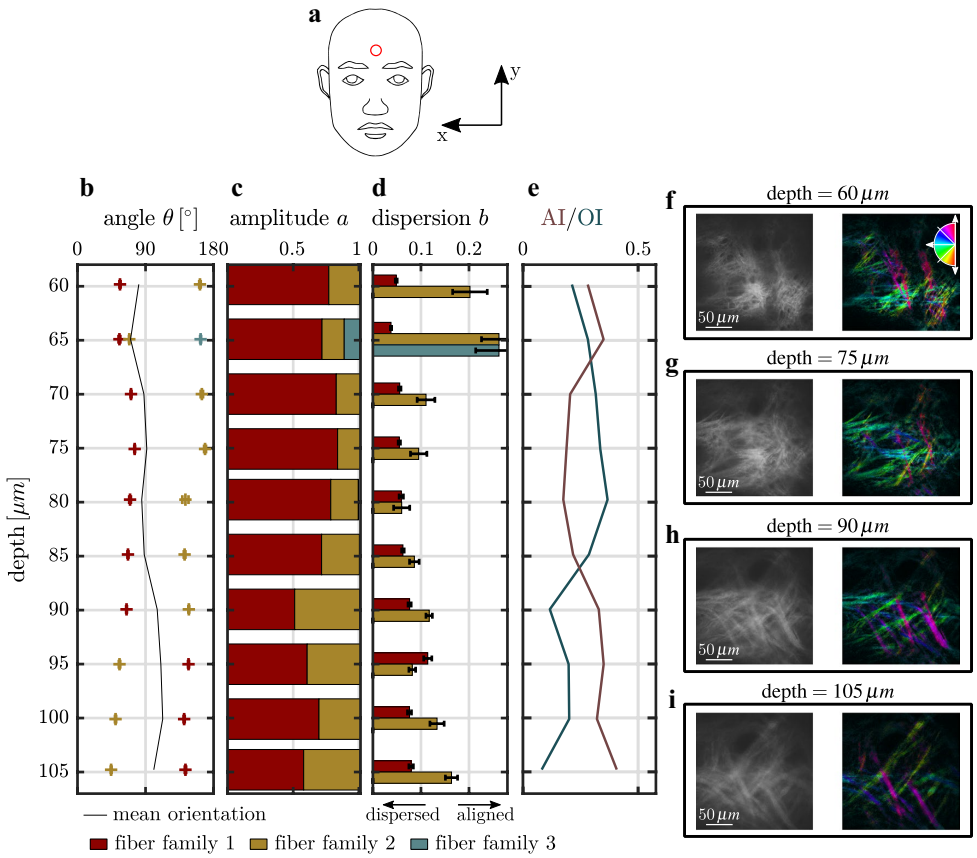

Figure 4. Results of the FINE algorithm of in-vivo multi-photon SHG images as a function of skin depth. (**a**) Location of the measurement and origin of the coordinate system. (**b**) Mean orientation angles $\bar{\theta}_i$ of the identified fiber families. (**c**) Amplitudes a_i of each identified fiber family. (**d**) Dispersion parameter b_i of each identified fiber family. Error bars represent the 95% confidence intervals. (**e**) Derived parameter AI (alignment index) and OI (orientation index) as a function of depth. (**f–i**) Exemplary SHG images (left) and the local fiber orientation shown in false colors (right). The color wheel shows the assignment of each color.

from their main orientation. Assume N identified fiber families with amplitudes a_i and dispersion parameter b_i. The AI then reads as:

$$\mathrm{AI} = \sum_{1}^{N} a_i \cdot b_i' \quad \text{with} \quad b_i' = \frac{b_i - b_{\min}}{b_{\max} - b_{\min}}. \tag{1}$$

b_i' represents the normalized dispersion coefficient with normalization quantities $b_{\min}$ and $b_{\max}$. For example, a fiber network of two highly aligned fiber families that are arranged perpendicular to each other exhibit an OI of zero and an AI of one. We further illustrate the difference between the OI and the AI in the Supplementary Fig. 3.

Figure 4 summarizes the result of the FINE algorithm as well as the corresponding parameters as a function of dermal depth. In general, two fiber families are identified. The weighted mean orientation of both fiber families, shown in Fig. 4(b), fluctuates around 90°, which coincides with the direction of the so called Langer lines[29]. Langer lines are the main tension lines of human skin, that were correlated to a preferred orientation of collagen in ex-vivo experiments[30–32]. At a depth of 60 µm, fiber family 1 dominates the fiber distribution with an amplitude that is 3.2 times stronger as compared to fiber family 2, shown in Fig. 4(c). With increasing depth, the amplitudes of both fiber families evolve to similar values. The measured dispersions, that are shown in Fig. 4(d), reveal a different degree of alignment between both families at 60–80 µm of depth. Note that, at a depth of 60 µm and 65 µm, high dispersion values, $b_{2,3} \geq 0.2$, are measured. This is favored by a low fraction of fibers, $a \leq 0.2$, contributing to fiber families 2 and 3. Below a depth of 80 µm, the dispersion of both fiber families is identical. The mean alignment of the fiber network, measured by the AI, continuously increases with depth (Fig. 4(e)). Contrary, the OI first increases until a depth of 75–80 µm and then decreases to a value of nearly zero at 105 µm. This is visually expressed by local fiber orientations covering almost the full angular half space (Fig. 4(e) and

(f)). Below a depth of 80 µm, the color variety of local orientations reduces (Fig. 4(h)). At a depth of 105 µm, the large majority of fibers is visualized in green and blue/purple representing fiber orientations fluctuating around mean values of $\bar{\theta}_1 = 44.4°$ and $\bar{\theta}_2 = 142.8°$.

The collagen fiber network of soft tissue is in general not isotropic and expresses a preferred orientation[5,33,34]. In human skin, the preferred orientation is supposed to coincide with the main tension lines of skin, e.g. the Langer lines, which was confirmed ex-vivo[16,30]. However, scanning electron microscopy (SEM) and SHG ex-vivo experiments failed to support this model[35–38].

Our results show that with the newly introduced FINE algorithm a direct analysis of a collagen network in-vivo is possible. The quantification algorithm allows to determine the number of fiber families without any previous assumptions about the underlying tissue. With increasing depth, mean fiber family orientations align perpendicular to each other such that no main orientation is expressed. The transition of the fiber network from overall dispersed fibers to aligned fibers at a depth of 80 µm is expressed by all parameters describing the collagen network. We associate this transition with the crossover from the papillary dermis to the reticular dermis, which is in line with Neerken et al., who measured the onset of the reticular dermis at a depth of (95 ± 10) µm at the temple[39]. The transition is additionally characterized by loose, thin collagen fibers in the papillary dermis that form a resilient network of thicker fibers in the reticular dermis[40]. The fiber status of the papillary dermis has been shown to be of main importance in skin aging[27,41].

Furthermore, the FINE algorithm might be suitable for the classification of pathological deficiencies that impact the collagen fiber network like the Ehlers–Danlos syndrome[42]. It should be noted that our presented measurement serves as a proof of principle study and does not allow for a general conclusion, which would require a higher number of samples.

In conclusion, the FINE algorithm was found to be able to reliably quantify the fiber network by determining the number of fiber families, their mean orientations, amplitudes, dispersions as well as the orientation index, and the alignment index. The newly derived alignment index captures fiber family dependent information about the fiber network independently from the widely used averaged orientation index. Combined with in-vivo SHG microscopy of dermal collagen, we demonstrate a fully non-invasive and reliable algorithm to obtain meaningful insights into the composition of the dermal collagen fiber network. In general, the presented FINE algorithm is not limited to the application of dermal collagen. Potential applications might reach from different soft tissues to the quantification of any kind of fiber-reinforced material.

Methods

Image processing, Monte-Carlo image generation and curve fitting was realized by using MATLAB[43] in conjunction with the image processing toolbox and the curve fitting toolbox.

Monte-Carlo fiber images. The generation of artificial, grayscale fiber images is described in detail by Witte *et al.*[23]. The orientation angles of fibers, which contribute to a certain fiber family are sampled from a semi-circular von-Mises distribution with mean orientation $\bar{\theta}$:

$$P(\theta; \bar{\theta}, k) = \frac{1}{\pi I_0(k)} e^{k\cos(2(\theta-\bar{\theta}))}, \tag{2}$$

where the dispersion parameter k defines the width of the distribution. A large value of k describes a narrow angular distribution, which corresponds to a high degree of fiber alignment. The Monte-Carlo sampling is repeated for each defined fiber family. To achieve a true isotropic fiber distribution, fiber angles are equally distributed across the entire angular range $[0°, 180°]$. In addition, every fiber features a width and an aspect ratio, which defines its length. As fibers with a very small width were found to produce large errors[23], we choose a minimum fiber width of 3 pixels. Similar to[20,23] we set the maximum fiber width to 10 pixels. The aspect ratio is constrained to the interval[20,45]. Note that uniform fiber geometries (width, length) are used for each Monte-Carlo image. To account for different image qualities, we use a random noise factor which defines the amplitude of added speckle noise.

Angular orientation distribution. We use a Fourier-based method (AF method), as proposed by Witte *et al.*[23], to obtain the angular orientation distribution $I(\theta)$ of an image $I_p(x, y)$. Using the method, the power spectrum $P(u, v)$, which is defined as the square of the absolute value of the 2D discrete Fourier transform, is computed. First, coordinates are shifted such that low frequencies are located in the center of the power spectrum. In addition, the adaptive filter, which is based on the relative variance of the signal, is applied to the power spectrum. As shown by Witte *et al.*[23], most accurate results are obtained by allowing relative variances smaller than 2.1%. To extract the angular orientation information, the signal of the filtered power spectrum is radially summed and normalized. The variance of the angular orientation distribution, $\Delta I(\theta)$, is obtained by propagating the variance of the image $\Delta I_p(x, y) = \sqrt{I_p(x, y)}$ to the Fourier domain[23].

Similar to Witte *et al.*[23], we employ the cumulative orientation distribution $C(\theta)$ (COD):

$$C(\theta) = \sum_{\theta'=0°}^{\theta} I(\theta') \tag{3}$$

Note that the angular orientation distribution is normalized with $\sum_{\theta=0}^{180°} I(\theta) = 1$. The variance of the COD, $\Delta C(\theta)$, follows from propagating Eq. (3):

$$\Delta C(\theta) = \sqrt{\sum_{\theta'=0^\circ}^{\theta} \Delta I(\theta')^2} \tag{4}$$

Since the choice of the starting angle of computing the COD [Eq. (3)] is arbitrary, the variance of the COD, $\Delta C(\theta)$, has to be independent from θ. Thus, we employ the variance as $\sigma = \max(\Delta C(\theta))$. Note that within the FINE algorithm, σ is crucial for identifying additional, significant fiber families. For further information on the calculation of $\Delta C(\theta)$, please refer to[23].

Fit model. We model the COD by using a sigmoid function:

$$S_{\text{circ}}(\theta) = A \cdot \left[S(\theta) + S\left(\theta + 180^\circ\right) - S\left(180^\circ\right) + S\left(\theta - 180^\circ\right) - S\left(-180^\circ\right) - S\left(0^\circ\right)\right] \tag{5}$$

$$\text{with} \quad S(\theta) = \frac{1}{1 + e^{-b(\theta - \bar{\theta})}}, \tag{6}$$

where $\bar{\theta}$ denotes the mean orientation and b the steepness of the step, which is a measure of the fiber dispersion. The added terms take care of the semi-circularity of the angular orientation distribution and its characteristic in the cumulative orientation distribution. The factor A is chosen such that the employed sigmoid function [Eq. (5)] fulfills $S_{\text{circ}}(180^\circ) = 1$ for all parameter $\bar{\theta}$ and b. This is given for:

$$A = \frac{1}{S(360^\circ) - S(-180^\circ)}. \tag{7}$$

To account for the contribution of multiple fiber families, a series of sigmoid functions is applied:

$$S_N(\theta) = \begin{cases} S_{\text{circ}}, & N = 1 \\ \sum_{i=1}^{N} a_i S_{\text{circ}}\left(\theta; b_i, \bar{\theta}_i\right), & N > 1, \end{cases} \tag{8}$$

where N denotes the number of fiber families. The i-th fiber family which exhibits a dispersion b_i and a mean orientation $\bar{\theta}_i$ contributes with an amplitude of a_i. We relate the von-Mises dispersion parameter k to the sigmoidal dispersion b using a numerical transfer function $b(k)$, which is shown in Supplementary Fig. 4. For each value of k, we sample 10^4 values from the respective von-Mises function. After calculating the cumulative distribution, we fit the sigmoid [Eq. (5)] to obtain the dispersion parameter b. Each datapoint of Supplementary Fig. 4 is calculated from averaging over 100 values. Best results are obtained by splitting the dataset into $k < 2$ and $k \geq 2$. We fit both datasets using a power function $c_1 \cdot k^{c_2} + c_3$ with coefficients c_1, c_2 and c_3.

Note that in Witte et al.[23], a sigmoid model was proven to provide a more accurate representation of the mean orientation and dispersion of one fiber family compared to the classical von-Mises approach[12,22]. Especially the calculation of the dispersion parameter can be significantly improved using the sigmoidal approach. Further details on the comparison of both methods can be found in Witte *et al.*[23].

Isotropy criterion. In order to classify an unknown cumulative distribution function as isotropic prior to fit potential fiber families, a criterion similar to the approach of Schriefl *et al.*[22] is used. Since an ideal cumulative distribution function of an isotropic distribution is a straight line with a slope of 1/180°, the initial fit of the FINE algorithm (Fig. 1) is used to evaluate the isotropy of the distribution. R^2 is used as parameter to measure the goodness of the fit. In total 10^4 images with an isotropic fiber orientation distribution were created using the implemented Monte-Carlo method. 95% of the images were considered as isotropic for a threshold value of $R^2 \geq 0.9916$. Even if an isotropic distribution fails the initial isotropy criterion, the fitted fiber family can be classified as isotropic retrospectively. We emphasize, that the isotropy criterion is not used to evaluate the significance of additional fiber families. Instead, the variance $\sigma = \Delta C(\theta)$ of the COD is evaluated and used in terms of a 3σ criterion in the FINE algorithm.

Level of significance. The level of significance is controlled by multiplying the variance of the cumulative distribution function, $\Delta C(\theta)$, with a factor n. The right choice of n is crucial in order to not over-interpret small fluctuations and still capture significant fiber families of the cumulative distribution. To find the factor which maximizes the accuracy to determine the number of identified fiber families, Monte-Carlo images that feature multiple fiber families (up to three) as well as images with a single, aligned family together with an isotropic family were included. To ensure an unambiguous differentiation of neighbored fiber families in the orientation distribution, a von-Mises dispersion of $k = 10$ ($b = 0.18$) with a minimum distance of 30° between neighbored families was chosen. Subsequently, the limits n_{min} and n_{max} defining the range of significance, in which the calculated number matches the defined number of fiber families, were determined. Each limit was calculated by repeatedly applying the implemented fit procedure on the cumulative distribution function while adapting the level of significance using a bisection algorithm. The algorithm was terminated as the difference between subsequent iterations was smaller than 10^{-4}. The maximum accuracy of the algorithm was found at $n = 3$.

Orientation index. In order to characterize the entire orientation distribution, we evaluate the orientation index (OI)[28] and the novel alignment index (AI). The orientation index is based on the angular orientation distribution $I(\theta)$:

$$\mathrm{OI} = 2\frac{\int_{0°}^{180°} I(\theta)\cos^2\left(\theta - \bar{\theta}_{\mathrm{mean}}\right)\mathrm{d}\theta}{\int_{0°}^{180°} I(\theta)\,\mathrm{d}\theta} - 1 \tag{9}$$

A fully isotropic distribution results in a vanishing orientation index, whereas a full alignment of the fibers yields an OI of one. $\bar{\theta}_{\mathrm{mean}}$ describes the overall mean orientation, which is determined from fitting a single sigmoid (S_1) to the COD.

Alignment index. The alignment index (AI) is defined in Eq. (1). Normalization constants b_{min} and b_{max} define the scale of the AI. The lower limit of the dispersion parameter is defined as $b_{\mathrm{min}} = 0.016$, which results from the transfer function $b(k)$ for $k \to 0$. b_{max} corresponds to the maximum dispersion parameter at which the AI has a value of one. We consider a family as fully aligned if its dispersion parameter b is equal to 0.26 ($k = 20$). We therefore choose a value of $b_{\mathrm{max}} = 0.26$. The defined scale is found to cover a large majority of the measured distributions without a saturation.

Local fiber orientation. The local fiber orientation is achieved similarly to the fan-filter method proposed by McLean *et al.*[44]. In each pixel the angular distribution contributes to an orientation spectrum. The contribution of one specific angle θ' results from applying the inverse Fourier transform to the fan-filtered discrete Fourier transform of the image. The fan-filter is a wedge-shaped filter, that covers $\theta \in [\theta' - \delta\theta, \theta' + \delta\theta]$. Contrary to McLean et al., we define the fan-filter by computing the fraction of each pixel in the Fourier domain that is covered by the angle interval. Hence, we do not need to apply a Gaussian convolution to remove sharp filter edges that induce Gibbs artifacts. We use the fan-filter in the frequency domain with a subsequent inverse Fourier transformation for every angle $\theta \in [0°, 180°]$ in 1° steps with $\delta\theta = 0.5°$ to obtain local orientation spectra $I(x, y, \theta)$. Spectra are smoothed using a moving average filter with an angular span of 7°. We assign a color to each pixel based on the angle at maximum spectral intensity. In agreement with McLean *et al.*[44], in non-fibrous areas of the image the amplitude of the RGB color is reduced using the relative intensity of the background-subtracted pixel. For background subtraction, the Fiji (ImageJ) build-in function subtract background with a rolling ball radius of 40 pixels is used[45].

Multi-photon microscopy. For collagen measurements we use a multi-photon microscope which was developed in collaboration with Jenlab GmbH (Jena, Germany)[46]. To measure the collagen-specific second-harmonic generation (SHG) signal, a femtosecond ti:sapphire laser (Mai Tai, Spectra-Physics, California, USA) adjusted to a wavelength of 820 nm is used in combination with a 410 nm band-pass filter (AQ 410/20 m-2P, Chroma Technology Corp., Bellows Falls, VT). The microscope was used at a scan time of 7 s, a constant mean illumination power of 50 mW, and a field of view that covers a 220×220 µm area at an image dimension of 512×512 pixels.

In order to measure the three-dimensional distribution of collagen, a 3D-stack of in total 10 SHG images is recorded at the forehead of a 53 years old male Caucasian. An image slice spacing of 5 µm was chosen. The initial depth of the stack resulted from the onset of visible collagen fibers which was at a depth of 60 µm. The maximum depth of 105 µm was limited by the decreasing image quality. Depth is measured relative to the skin surface which was recorded by measuring the two-photon autofluorescence signal of the uppermost skin layer using an excitation wavelength of 750 nm with a (548 ± 150) nm band pass filter (HQ 548/305 m-2P, Schott AG, Mainz, Germany).

This study was conducted according to the recommendations of the current version of the Declaration of Helsinki and the Guideline of the International Conference on Harmonization Good Clinical Practice, (ICH GCP). In addition, this study was approved and cleared by the institutional ethics review board (Beiersdorf AG, Hamburg, Germany). Written informed consent was obtained from the volunteer.

Received: 22 January 2020; Accepted: 4 June 2020
Published online: 02 July 2020

References

1. Ateshian, G. A., Rajan, V., Chahine, N. O., Canal, C. E. & Hung, C. T. Modeling the matrix of articular cartilage using a continuous fiber angular distribution predicts many observed phenomena. *J. Biomech. Eng.* https://doi.org/10.1115/1.3118773 (2009).
2. Eriksson, T. S. E., Prassl, A. J., Plank, G. & Holzapfel, G. A. Modeling the dispersion in electromechanically coupled myocardium. *Int. J. Numer. Method Biomed. Eng.* https://doi.org/10.1002/cnm.2575 (2013).
3. Billiar, K. L. & Sacks, M. S. Biaxial mechanical properties of the natural and glutaraldehyde treated aortic valve cusp—part I: experimental results. *J. Biomech. Eng.* https://doi.org/10.1115/1.429624 (2000).
4. Gasser, T. C., Ogden, R. W. & Holzapfel, G. A. Hyperelastic modelling of arterial layers with distributed collagen fibre orientations. *J. R. Soc. Interface* **3**, 15–35 (2006).
5. Annaidh, A. N., Bruyere, K., Destrade, M., Gilchrist, M. D. & Ottenio, M. Characterising the anisotropic mechanical properties of excised human skin. *J. Mech. Behav. Biomed. Mater.* **5**, 139–148. https://doi.org/10.1016/j.jmbbm.2011.08.016 (2013).
6. Hashin, Z. & Rotem, A. A fatigue failure criterion for fiber reinforced materials. *J. Compos. Mater.* **7**, 448–464 (1973).
7. Limbert, G. Mathematical and computational modelling of skin biophysics: a review. *Proc. R. Soc. A Math. Phys. Eng. Sci.* **473**, 1–20 (2017).
8. Holzapfel, G. A., Ogden, R. W. & Sherifova, S. On fibre dispersion modelling of soft biological tissues: a review. *Proc. R. Soc. A Math. Phys. Eng. Sci.* **475**, 20180736 (2019).
9. Timmins, L. H., Wu, Q., Yeh, A. T., Moore, J. E. & Greenwald, S. E. Structural inhomogeneity and fiber orientation in the inner arterial media. *AJP Heart Circ. Physiol.* **298**, H1537–H1545 (2010).
10. Alavi, S. H., Ruiz, V., Krasieva, T., Botvinick, E. L. & Kheradvar, A. Characterizing the collagen fiber orientation in pericardial leaflets under mechanical loading conditions. *Ann. Biomed. Eng.* **41**, 547–561 (2013).

11. Chow, M. J., Turcotte, R., Lin, C. P. & Zhang, Y. Arterial extracellular matrix: A mechanobiological study of the contributions and interactions of elastin and collagen. *Biophys. J.* **106**, 2684–2692 (2014).
12. Bancelin, S. *et al.* Ex vivo multiscale quantitation of skin biomechanics in wild-type and genetically-modified mice using multiphoton microscopy. *Sci. Rep.* **5**, 1–14 (2015).
13. Nesbitt, S., Scott, W., Macione, J. & Kotha, S. Collagen fibrils in skin orient in the direction of applied uniaxial load in proportion to stress while exhibiting differential strains around hair follicles. *Materials (Basel).* **8**, 1841–1857 (2015).
14. Yang, W. *et al.* On the tear resistance of skin. *Nat. Commun.* **6**, 6649 (2015).
15. Pandolfi, A. & Holzapfel, G. A. Three-dimensional modeling and computational analysis of the human cornea considering distributed collagen fibril orientations. *J. Biomech. Eng.* **130**, 061006 (2008).
16. Annaidh, A. N. *et al.* Automated estimation of collagen fibre dispersion in the dermis and its contribution to the anisotropic behaviour of skin. *Ann. Biomed. Eng.* **40**, 1666–1678 (2012).
17. Rezakhaniha, R. *et al.* Experimental investigation of collagen waviness and orientation in the arterial adventitia using confocal laser scanning microscopy. *Biomech. Model. Mechanobiol.* **11**, 461–473 (2012).
18. Polzer, S. *et al.* Automatic identification and validation of planar collagen organization in the aorta wall with application to abdominal aortic aneurysm. *Microsc. Microanal.* **19**, 1395–1404 (2013).
19. Gizzi, A., Pandolfi, A. & Vasta, M. Statistical characterization of the anisotropic strain energy in soft materials with distributed fibers. *Mech. Mater.* **92**, 119–138 (2016).
20. Morrill, E. E. & Stender, C. J. A validated software application to measure fiber organization in soft tissue. *Biomech. Model. Mechanobiol.* **15**, 1467–1478 (2017).
21. Stender, C. J. *et al.* Modeling the effect of collagen fibril alignment on ligament mechanical behavior. *Biomech. Model. Mechanobiol.* **17**, 543–557 (2018).
22. Schriefl, A. J., Wolinski, H., Regitnig, P., Kohlwein, S. D. & Holzapfel, G. A. An automated approach for three-dimensional quantification of fibrillar structures in optically cleared soft biological tissues. *J. R. Soc. Interface* https://doi.org/10.1098/rsif.2012.0760 (2012).
23. Witte, M., Jaspers, S., Wenck, H., Rübhausen, M. & Fischer, F. Noise reduction and quantification of fiber orientations in greyscale images. *PLoS ONE* https://doi.org/10.1371/journal.pone.0227534 (2020).
24. Comninou, M. & Yannas, I. V. Dependence of stress-strain nonlinearity of connective tissues on the geometry of collagen fibres. *J. Biomech.* https://doi.org/10.1016/0021-9290(76)90084-1 (1976).
25. Levillain, A., Orhant, M., Turquier, F. & Hoc, T. Contribution of collagen and elastin fibers to the mechanical behavior of an abdominal connective tissue. *J. Mech. Behav. Biomed. Mater.* **61**, 308–317 (2016).
26. Lutz, V. *et al.* Characterization of fibrillar collagen types using multi-dimensional multiphoton laser scanning microscopy. *Int. J. Cosmet. Sci.* **34**, 209–215 (2012).
27. Puschmann, S., Rahn, C.-D., Wenck, H., Gallinat, S. & Fischer, F. Approach to quantify human dermal skin aging using multiphoton laser scanning microscopy. *J. Biomed. Opt.* **17**, 036005 (2012).
28. Bayan, C., Levitt, J. M., Miller, E., Kaplan, D. & Georgakoudi, I. Fully automated, quantitative, noninvasive assessment of collagen fiber content and organization in thick collagen gels. *J. Appl. Phys.* **105**, 1–11 (2009).
29. Langer, K. On the anatomy and physiology of the skin: II. Skin Tension. *Br. J. Plast. Surg.* **31**, 93–106 (1978).
30. Ridge, M. D. & Wright, V. The directional effects of skin. A bio-engineering study of skin with particular reference to Langer's lines. *J. Investig. Dermatol.* **46**, 341–346 (1966).
31. Gibson, T., Kenedi, R. M. & Craik, J. E. The mobile micro-architecture of dermal collagen: A bio-engineering study. *Br. J. Surg.* https://doi.org/10.1002/bjs.1800521017 (1965).
32. Stark, H. L. Directional variations in the extensibility of human skin. *Br. J. Plast. Surg.* https://doi.org/10.1016/0007-1226(77)90001-7 (1977).
33. Vilarta, R. & De Campos Vidal, B. Anisotropic and biomechanical properties of tendons modified by exercise and denervation: aggregation and macromolecular order in collagen bundles. *Matrix* https://doi.org/10.1016/S0934-8832(89)80019-8 (1989).
34. Schriefl, A. J., Zeindlinger, G., Pierce, D. M., Regitnig, P. & Holzapfel, G. A. Determination of the layer-specific distributed collagen fibre orientations in human thoracic and abdominal aortas and common iliac arteries. *J. R. Soc. Interface* https://doi.org/10.1098/rsif.2011.0727 (2012).
35. Brown, I. A. Scanning electron microscopy of human dermal fibrous tissue. *Ups. J. Med. Sci.* **77**, 3–7 (1972).
36. Lavker, R. M., Zheng, P. & Dong, G. Aged skin: A study by light, transmission electron, and scanning electron microscopy. *J. Investig. Dermatol.* **88**, 44–51 (1987).
37. Pierard, G. E. & Lapiere, C. M. Microanatomy of the dermis in relation to relaxed skin tension lines and Langer's lines. *Am. J. Dermatopathol.* https://doi.org/10.1097/00000372-198706000-00007 (1987).
38. Ueda, M. *et al.* Combined multiphoton imaging and biaxial tissue extension for quantitative analysis of geometric fiber organization in human reticular dermis. *Sci. Rep.* **9**, 1–12 (2019).
39. Neerken, S., Lucassen, G. W., Bisschop, M. A., Lenderink, E. & Nuijs, T. Characterization of age-related effects in human skin: a comparative study that applies confocal laser scanning microscopy and optical coherence tomography. *J. Biomed. Opt.* **9**, 274 (2004).
40. Humbert, P., Maibach, H., Fanian, F. & Agache, P. *Measuring the skin*, Vol. 49 (Springer, New York, 2004).
41. Varani, J. *et al.* Decreased collagen production in chronologically aged skin: roles of age-dependent alteration in fibroblast function and defective mechanical stimulation. *Am. J. Pathol.* **168**, 1861–1868 (2006).
42. Malfait, F. *et al.* The 2017 international classification of the Ehlers-Danlos syndromes. *Am. J. Med. Genet. C Semin. Med. Genet.* **175**, 8–26 (2017).
43. MATLAB. *MATLAB Version 9.4.0.813654 (R2018a)* (The MathWorks Inc., Natick, 2018).
44. McLean, J. P. *et al.* High-speed collagen fiber modeling and orientation quantification for optical coherence tomography imaging. *Opt. Express* **27**, 14457 (2019).
45. Schindelin, J. *et al.* Fiji: an open-source platform for biological-image analysis. *Nat. Methods* https://doi.org/10.1038/nmeth.2019 (2012).
46. Bückle, R. *et al.* 5D-intravital tomography as a novel tool for non-invasive in-vivo analysis of human skin. In *Advanced Biomedical and Clinical Diagnostic Systems VIII* (eds Vo-Dinh, T. *et al.*) (SPIE, Bellingham, 2010). https://doi.org/10.1117/12.841861.

Acknowledgements
We acknowledge financial support from Beiersdorf AG.

Author contributions
S.J. and H.W. supervised the research. M.W., F.F. and M.R. conceived the experiment. M.W. conducted the experiment and implemented the algorithm. M.W., F.F. and M.R. analyzed the results. M.W., F.F. and M.R. wrote the manuscript. S.J. and H.W. reviewed the manuscript.

Competing interests
The authors declare no competing interests.

Additional information
Supplementary information is available for this paper at https://doi.org/10.1038/s41598-020-67632-z.

Correspondence and requests for materials should be addressed to F.F.

Reprints and permissions information is available at www.nature.com/reprints.

Publisher's note Springer Nature remains neutral with regard to jurisdictional claims in published maps and institutional affiliations.

Chapter 5

Behavior of the Collagen Network under Load

Biological tissue like skin exhibits a complex material behavior, which is believed to be related to the collagen network [6, 98, 99]. However, a clear micro-structural interpretation of mechanical properties such as strain-history-dependence, stress-relaxation and creep is still missing [27, 98]. In this section, methods for analyzing the mechanical behavior of skin in relation to changes of the collagen fiber network are introduced and applied to pig skin.

5.1 Stretching Device

To deform skin in a controlled fashion, a custom stretching device is developed. The stretching device, which is shown schematically in figure 5.1, is designed for use at the DermaInspect multiphoton microscope. The entire stretching unit is mounted onto a lifting stage allowing for a precise adjustment of the setup under the objective of the microscope. A minimum working distance between objective and sample of 2 mm is ensured by means of a 3D-printed, cylindrical spacer (*Form 2, standard black resin*, Formlabs, Somerville, USA), which is mounted to the microscope. At the same time, the spacer keeps a constant level of water between sample and objective ensuring its immersion. The sample is clamped between two opposing linear rigs (*RK Compact 30*, RK Rose+Krieger GmbH, Minden, Germany) that are controlled by two stepper motors (*ST4209S1006-B*, Nanotec Electronic GmbH & Co. KG, Feldkirchen, Germany) to enable a controlled, bidirectional stretching. To prevent the sample from slippage, the gripping strength of each clamp is reinforced with two screws. Encoders (*WEDS5541-A14*, Nanotec Electronic GmbH & Co. KG, Feldkirchen, Germany) mounted to the stepper motors are used to establish a feedback loop for the position of the stepper motors. This ensures that the exact number of predefined steps is executed by the stepper motors. In addition, any variations of the motor position are monitored. Encoders and

stepper motors are controlled by two motor control units (*C5-E*, Nanotec Electronic GmbH & Co. KG, Feldkirchen, Germany). Force is measured using two independent force sensors (*SML-45N*, Interfaceforce e.K., Tegernsee, Germany) in combination with a 4-channel amplifier (*IFFDM4*, Interfaceforce e.K., Germany).

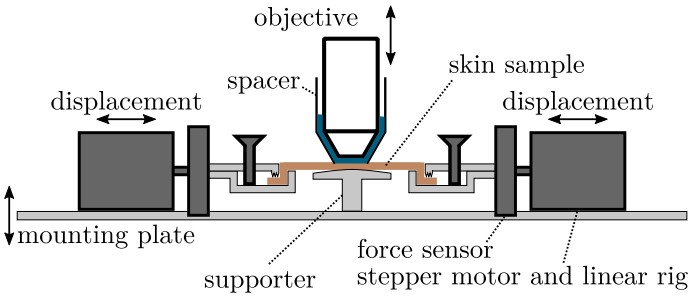

Figure 5.1: Schematic setup of the stretching device at the multiphoton microscope. The multiphoton microscope is represented by the objective lens, which is enclosed by a 3D printed spacer.

In order to control the stretching setup, a graphical user interface (GUI) was written in *visual basic* using the .NET framework. The GUI is shown in appendix figure C.3 and allows the user to perform diverse displacement-controlled mechanical tests such as simple stress-strain, cyclic stress-strain, stress-relaxation and creep tests. The communication of the computer with the stepper motors is separated from the communication with the force amplifier, as shown in figure 5.2. A CANopen protocol is used for communicating with the motor control units (*C5-E*, Nanotec Electronic GmbH & Co. KG, Feldkirchen, Germany) [100]. A CAN-interface (*Ixxat, USB-to-CAN v2*, HMS Industrial Networks, Halmstad, Sweden) is used together with an application programming interface (*CANopen Master API*, HMS Industrial Networks, Halmstad, Sweden).

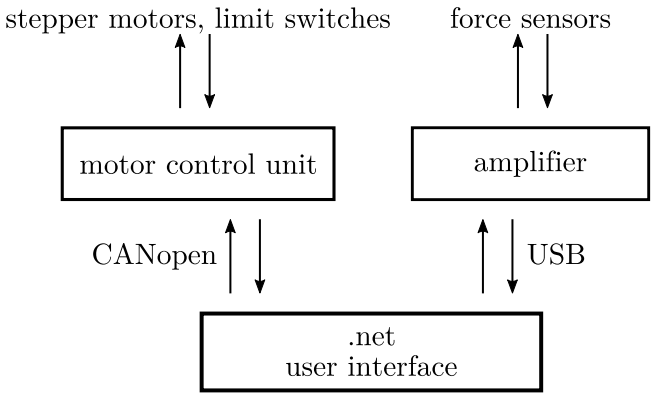

Figure 5.2: Communication of the user interface with the stretching device.

5.1.1 Stretching of Skin

Skin samples used in this work, were punched from a back skin of a female pig acquired from a local commercial butcher. Figure 5.3 shows an example of the force measured during stretching of a rectangular 80 mm × 6 mm sample of pig skin. It expresses the classic non-linear behavior of soft tissue, which was studied extensively in the past [6, 27, 101]. This mechanical behavior is called hyperelasticity. Several studies, e.g. including Small Angle X-ray Scattering (SAXS) [10, 102, 103] and SHG imaging [12, 31] investigated the change of the collagen fiber network due to stretching. Upon stretching, collagen fibers were found to straighten, then align in the direction of stretching and, at high strains, slide against each other. However, there is a discussion about the onset of fiber alignment [12]. Diverse hyperelastic material models to simulate soft biological tissue like skin using the finite element method (FEM) have been developed in the past [3, 34]. The orientation of the collagen fiber network for predicting the material behavior of soft tissue was incorporated into so-called structural models [8, 104] (see appendix A). Besides its hyperelastic properties, however, biological tissue exhibits additional, viscoelastic properties, for which there is neither a micro-structural interpretation nor a material model considering the collagen fiber network [3].

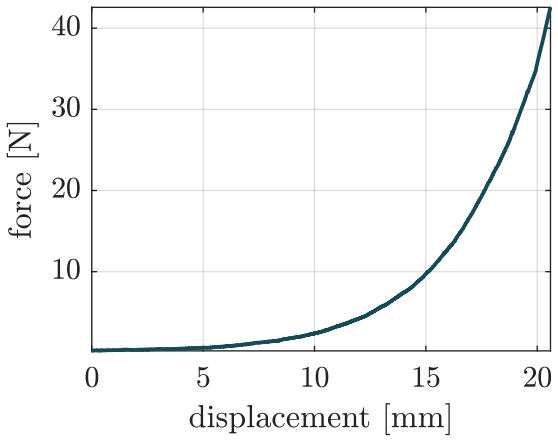

Figure 5.3: Measured force acting on skin due to stretching. The sample was stretched with a strain rate of 60 μm/s using the stretching device of figure 5.1.

5.1.2 Cyclic Deformation of Skin

Cyclic sequences of stretching and relaxation of biological samples reveal its history-dependent mechanical behavior. Using the stretching device, a sample of skin is periodically deformed according to the protocol shown in figure 5.4 (a). The measured force as a function of stretched distance is shown in figure 5.4 (b). The force expresses a hysteretic behavior. This is accompanied by a reduction of the measured force with every deformation cycle, which is referred to as preconditioning effect [27, 105].

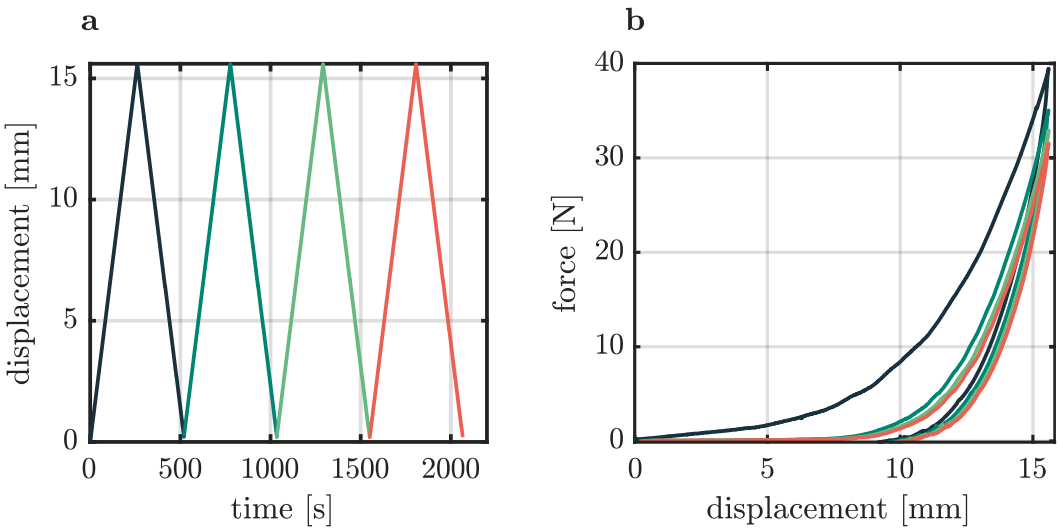

Figure 5.4: Cyclic stretching and relaxation of a pig skin sample. (**a**) Deformation protocol consisting of four repeated cycles of stretching and relaxation at a deformation rate of 60 μm/s. (**b**) Measured force of each deformation cycle acting onto the sample. Curves are plotted in false colors according to their deformation cycle.

5.2 Stretching of Skin with Simultaneous Imaging of Collagen Fibers

In order to relate the micro-structural changes of the collagen network to the macroscopic mechanical behavior of skin, stretching experiments are combined with the DermaInspect multiphoton microscope. Tensile, strain-controlled, mechanical tests with four consecutive cycles of repeated stretch and relaxation are performed according to the protocol in figure 5.3 (a). Images at a resolution of 512 $\times$ 512 pixels are recorded with a mean scan-time of (2.63$\pm$0.06) s every 3 s to ensure a reliable sequence of consecutive image acquisition and data storage. The water-immersion objective with a 20$\times$ magnification (*XLUMPlanFl 20x/0.95*, Olympus, Tokio, Japan) is used to capture a 440 $\times$ 440 μm field of view. Due to scanning-mirror induced artifacts, 100 pixels are excluded from the left boundary of the image. To keep the image quadratic, the upper 100 pixels are excluded as well, resulting in a 354 $\times$ 354 μm field of view. During measurement, the piezo element of the microscope is used to adjust residual displacements in the direction of the optical axis. Distorted images are omitted from quantitative analysis.

As reported in literature, collagen fibers orient in the direction force [10, 12]. To measure the fraction of fibers that are oriented along the direction of force, the OI (equation (4.3)) is redefined by replacing the mean orientation $\bar{I}(\theta)$ with the direction of force

(90°):

$$\mathrm{OI} = 2\frac{\sum_{\theta=0^\circ}^{180^\circ} I(\theta)\cos^2(\theta - 90^\circ)}{\sum_{\theta=0^\circ}^{180^\circ} I(\theta)} - 1. \tag{5.1}$$

5.3 Results and Discussion

The results are presented and discussed in detail in a paper submitted to *Scientific Reports*. The submitted version is shown in section 5.4. The main findings of the paper are briefly summarized here.

A maximum alignment of collagen fibers is observed at $16 - 18\,\%$ sample stretch indicated by the AI (equation (4.4)). This is consistent with the literature, where collagen fibers are reported to straighten first before they start to bear load [3]. However, Bancelin *et al.* [12] observed a concurrent increase of the OI with the force uptake. This is verified by an OI (equation (5.1)), which constantly increases with force. Thus, the FINE algorithm is able to separate the fibers alignment within their fiber families from their orientation into the direction of force. The maximum orientation of the collagen network is found to be determined by the largest strain, and does not increase with additional stretching cycles.

Repeated deformation reveals a different behavior of an isotropic and an anisotropic skin sample. The isotropic and the anisotropic sample are identified due to their initial collagen fiber network prior the first stretching cycle. The alignment of the collagen network of the isotropic sample increases continuously in the relaxed state with each deformation cycle. After two deformation cycles, its AI and OI fluctuate around values of 0.3 and 0.5, respectively. In contrast, the collagen network of the anisotropic sample has an AI fluctuating around the value of 0.3 throughout the entire deformation procedure. The approximation of the AI between both samples is found to be correlated with the relative force reduction at maximum stretches between consecutive deformation cycles.

In conclusion, the permanent orientation of the collagen fiber network is related to the presence of an isotropic fiber family. Once fibers of the isotropic sample are aligned after two deformation cycles, both samples exhibit a similar microscopic and macroscopic behavior. This proof of principle study reveals that the multiphoton stretching device in combination with the FINE algorithm allows for a detailed micro-structural interpretation of the mechanical properties of biological tissue or any kind of fiber-reinforced material.

5.4 Publication (submitted)

Influence of repeated mechanical strain on isotropic and anisotropic dermal collagen morphologies

Maximilian Witte[1,2], Michael Rübhausen[1], Sören Jaspers[2], Horst Wenck[2], and Frank Fischer[2,*]

[1]Center for Free-Electron Laser Science (CFEL), University of Hamburg, Hamburg, 22607 ,Germany
[2]Beiersdorf AG, Hamburg, 20245, Germany
[*]Frank.Fischer@Beiersdorf.com

ABSTRACT

Complex tissue morphologies as found in dermal collagen were studied by second harmonic generation imaging and by applying the Fiber Image Network Evaluation (FINE) algorithm to characterize the tissue fiber network. The change of the dermal collagen fiber orientation in skin due to cyclic stretching and relaxation sequences was investigated with a dedicated multiphoton stretching device. We find that the alignment index maximizes at $16-18\,\%$ sample stretch. Families of collagen fibers are found to form a partially aligned collagen network under strain. We find that the relative force uptake is accomplished in two steps. Firstly, fibers align within their fiber families and, secondly, fiber families orient in the direction of force. The maximum alignment of the collagen fiber network is found to be determined by the largest strain. Repeated deformation of skin reveals a different micro-structural behavior of isotropic and anisotropic samples leading to similar force uptakes after two stretching cycles. Our method enables the possibility to study the correlation between mechanical properties and morphologies in collagen fiber networks.

Introduction

Skin is the largest organ of the human body and it is responsible for the bodys protection towards external factors. In our daily life skin is able to undergo large strains of up to $30\,\%$[1]. Collagen fibers are known to determine the mechanical properties of skin and are also one of its main constituents[2–5]. Upon stretching of skin, fibers straighten, align in the direction of force and, at high strains, slide against each other[6,7]. There is a discussion about the onset of fiber alignment in the literature[3]. It is assumed that the unstressed orientation distribution of the dermal collagen fiber network defines the anisotropic mechanical behavior of skin[8,9]. Furthermore, diverse viscoelastic properties such as creep, stress relaxation, strain history-dependence, and strain-rate dependence are believed to depend on the collagen fiber network[10–15]. Indeed previous second harmonic generation (SHG) imaging[16] at different stretching states has shown that the fibers orient along the force direction[3,7]. However, a microstructural interpretation of the observed changes of collagen networks requires a suitable approach to measure and characterize complex fiber reinforced materials.

In order to understand the properties of the dermal collagen fiber network under cyclic loads, we use a dedicated multiphoton stretching device and determine the network properties by the Fiber Image Network Evaluation (FINE) algorithm. The FINE algorithm evaluates the number of fiber families, their angular properties, and the alignment index. It is based on the cumulative orientation distribution[17] and was successfully applied to a stack of in-vivo SHG images of human dermal collagen[18]. Here, we present a method allowing for SHG imaging, while simultaneously deforming the sample. On each image representing a specific strain state, the FINE algorithm is applied to obtain detailed information about the orientation of the collagen fiber network[18].

Results and Discussion

Sample Stretching and Imaging

Two rectangular samples originating from the same dorsal pig skin are investigated. The multiphoton stretching device that is used for deforming the skin, while simultaneously capturing the collagen fiber network, is visualized in Fig. 1 (a) and Supplementary Fig. 1. The deformation protocol is shown as an example in Fig. 1 (b). Four consecutive cycles of repeated stretching and relaxation with maximum stretches of $25\,\%$ are applied. This range of strain is reported to represent the physiological situation[1]. To ensure a reliable sequence of image acquisition and storage, images are recorded every $3\,\mathrm{s}$ with a mean scan time of $(2.63\pm0.04)\,\mathrm{s}$. By using a rather low strain rate of $0.075\,\%/\mathrm{s}$, compared to other studies[5,15], the variation of

strain during image acquisition is assumed to be negligible.

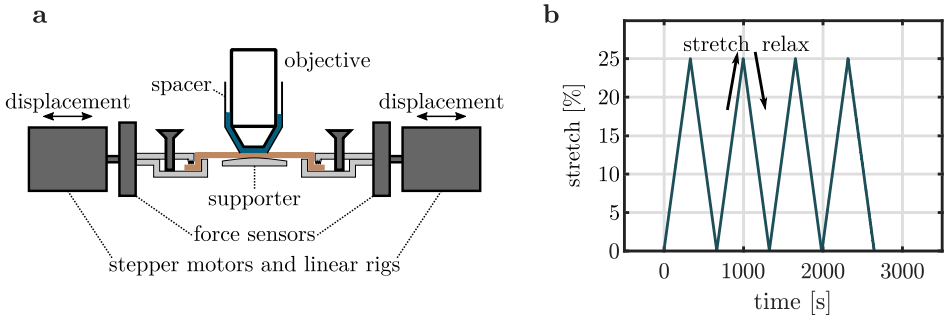

Figure 1. Experimental set-up and deformation protocol. (**a**) Schematic illustration of the multiphoton microscope stretching device. (**b**) Deformation protocol consisting of four repeated cycles with successive stretching and relaxation.

The collagen fiber network at minimum and maximum strain is shown for an exemplary sample in Fig. 2 (a)-(i) as a function of the deformation cycle number. The measured averaged force acting onto the sample is shown in Fig. 2 (j). SHG images in Fig. 2 (a)-(i) are processed to visualize the local orientation of collagen fibers in false colors.
As shown in Fig. 2 (a), the orientation of the collagen fibers initially occupies the entire angular range from 0° to 180°. At maximum stretch of the first cycle, the fibers in Fig. 2 (b) orient along the direction of force (90°) with a variation of ±45°. After complete relaxation of the sample, the thick fiber bundle originally oriented along the 110° direction have disappeared (Fig. 2 (c)). Compared to the initial state in Fig. 2 (a), the fraction of fibers that are aligned along the force direction has strongly increased as visible by the enhanced amount of blue colors. At maximum stretch of the second deformation cycle (Fig. 2 (d)), the fraction of oriented fibers is further increased compared to Fig. 2 (b). The fraction of oriented fibers further increases after the second deformation cycle in Fig. 2 (e), compared to Fig. 2 (c). This trend continues after the third and the fourth deformation cycle in Fig. 2 (g) and (i), respectively. Repeated stretching of the sample seems to have little effect on the local fiber orientation at maximum stretch, as seen in Fig. 2 (f) and (h).

Adaptation of the FINE algorithm to stretching

We use the FINE algorithm to obtain detailed, quantitative information about the collagen fiber network at each state of the deformation protocol.
The FINE algorithm determines the number of fiber families N and their angular properties in terms of their mean orientations $\bar{\theta}_i$, their amplitudes a_i and their dispersion parameters b_i. The dispersion parameter b describes the spread of fiber angles around their main orientation and increases with fiber alignment. To measure the overall alignment of the fiber network, we evaluate the alignment index (AI)[18]:

$$\mathrm{AI} = \sum_{1}^{N} a_i \cdot b_i' \qquad b_i' = (b_i - b_{\min})/(b_{\max} - b_{\min}), \tag{1}$$

where $b_{\min} = 0.016$ and $b_{\max} = 0.26$ define the scale of the AI[18]. In addition, we make use of the orientation index (OI) to quantify the fraction of fibers that is oriented along the force direction of 90°:

$$\mathrm{OI} = 2\frac{\sum_{\theta=0^\circ}^{180^\circ} I(\theta)\cos^2(\theta - 90^\circ)}{\sum_{\theta=0^\circ}^{180^\circ} I(\theta)} - 1, \tag{2}$$

where $I(\theta)$ denotes the angular orientation distribution, which is achieved by a Fourier-based method[17]. Note that the common definition of the OI uses the main orientation $\bar{I}(\theta)$ of the fiber network[19]. We are analyzing two different samples of skin. In the process, we compare FINE parameters of an isotropic collagen fiber network to which refer as isotropic sample and a skin sample exhibiting an aligned fiber network to which we refer as the anisotropic sample. With this labelling we describe the initial collagen fiber network prior to the first stretching cycle. Note that Fig. 2 shows the isotropic skin sample.

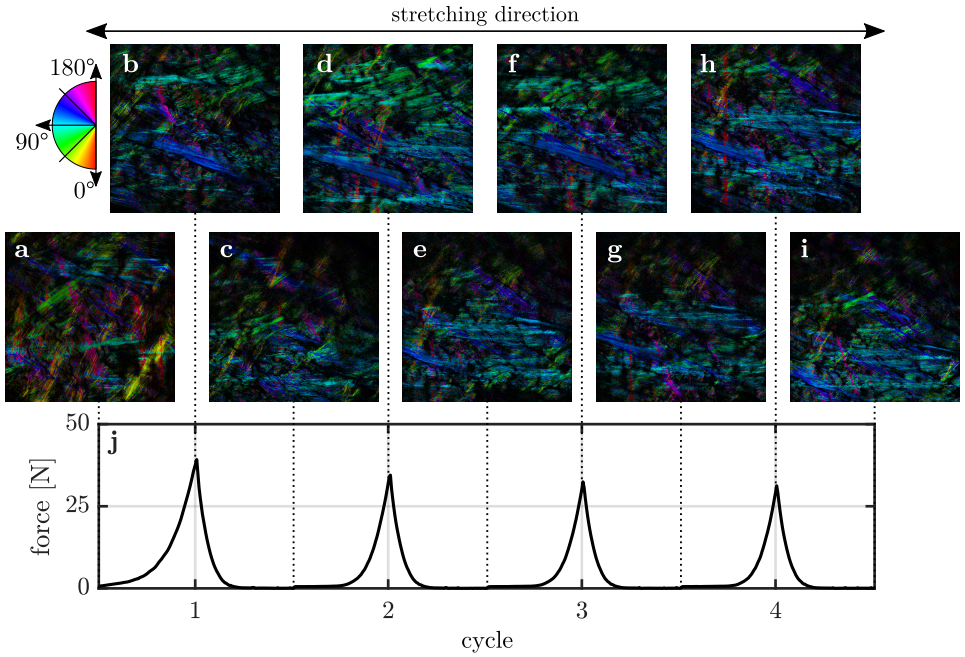

Figure 2. Evolution of the local collagen fiber orientation of a skin sample due to repeated stretching and relaxation. (**a**) Local fiber orientation prior deformation of the sample shown in false colors. The sample is stretched in the 90° direction as indicated by the arrow. (**b**) Local fiber orientation at maximum stretch of the first deformation cycle. (**c**) Local fiber orientation at maximum relaxation of the first deformation cycle. (**d**) Local fiber orientation at maximum stretch of the second deformation cycle. (**e**) Local fiber orientation at maximum relaxation of the second deformation cycle. (**f**) Local fiber orientation at maximum stretch of the third deformation cycle. (**g**) Local fiber orientation at maximum relaxation of the third deformation cycle. (**h**) Local fiber orientation at maximum stretch of the fourth deformation cycle. (**i**) Local fiber orientation at maximum relaxation of the fourth deformation cycle. (**j**) Averaged force acting on the sample, measured by the force sensors as a function of the deformation cycle.

Collagen Fiber Network upon Stretching

The OI and the AI of the isotropic sample are shown in Fig. 3 (a) as a function of the deformation cycle number. The measured force is displayed in Fig. 3 (b). The isotropic sample is characterized by an initial OI of 0.05 and an AI of 0.16. This indicates an isotropic fiber network, where a negligible fraction of fibers is oriented along the direction of force. Upon stretching, both quantities increase until the OI reaches a maximum value of 0.50 at maximum sample stretch. This agrees with the local fiber orientation of Fig. 2 (b), where aligned fibers still express a considerable angular range. The AI reaches its highest value of 0.32 at 16 % of maximum stretch. Compared to their initial values, the OI and the AI are significantly increased after relaxation as they amount to 0.31 and 0.15, respectively. This trend continues throughout the additional deformation cycles until the OI and the AI fluctuate permanently around values of 0.48 and 0.30, respectively. This is visually in line with the local collagen fiber orientation of Fig. 2 (e)-(i), which hardly differ from each other after two deformation cycles. This suggests that collagen fibers of the isotropic sample are not relaxing to their initial orientation.

The OI and the AI of the anisotropic sample are shown in Fig. 3 (c) as a function of the deformation number. The corresponding measured force is displayed in Fig. 3 (d). The aligned network is characterized by an OI of 0.31 and an AI of 0.32 in the initial state. This OI additionally indicates that a non-vanishing fraction of fibers aligned along the direction of force before the initial stretching cycle. Stretching the anisotropic sample increases the AI to a local maximum of 0.44 at 18 % sample stretch. The OI first decreases, but then maximizes locally to 0.40 at maximum stretch. Similar to the isotropic sample, the collagen fibers first align themselves and then orient into the direction of stretch during the first deformation cycle.

This is in line with the literature, where collagen fibers are reported to first orient themselves into the direction of stretch and then start to bear load[20,21]. The observations of Bancelin *et al.*, who measured a simultaneous increase of the OI with sample

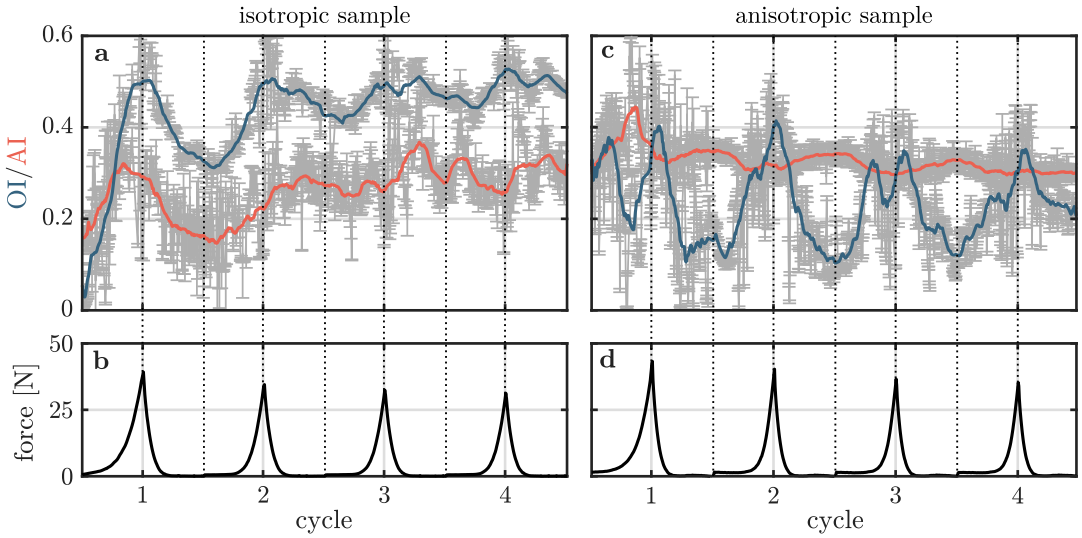

Figure 3. Derived parameters of the FINE algorithm applied to the collagen fiber network of the isotropic and the anisotropic sample under repeated stretching and relaxation. (**a**) Orientation index (OI) and alignment index (AI) of the collagen network of the isotropic sample as a function of the deformation cycle number. Data points with error bars indicating the 95 % confidence intervals are shown in grey. Solid lines represent smoothed data points. (**b**) Averaged force acting on the isotropic sample measured by the force sensors as a function of the deformation cycle number. (**c**) OI and AI of the collagen network of the anisotropic sample as a function of the deformation cycle number. (**d**) Averaged force acting on the anisotropic sample measured by the force sensors as a function of the deformation cycle number.

stretch, are also verified[3]. Repeated stretching and relaxation is found to decrease the ability of the collagen network to orient along the direction of force. This is indicated by a continuously decreasing amplitude of the OI for both samples.

To analyze the micro-structural differences between both samples in detail, we track the amplitudes and dispersions of fiber families which are identified by the FINE algorithm. These are shown for both samples in Fig. 4.
The measured force of the isotropic sample is shown in Fig. 4 (a). Amplitudes and dispersion parameters of the identified fiber families are plotted in 4 (b) and 4 (c), respectively. Throughout the entire deformation protocol, the isotropic sample is characterized by two collagen fiber families. The dispersion parameter of fiber family 1 falls below the threshold of an isotropic distribution except for a few data points located at maximum relaxation of the first deformation cycle. Fiber family 2, however, strongly fluctuates within the domain of a high alignment up to dispersion parameter values of 0.3. In the initial, unstressed state, 70 % of the fibers are contained in the isotropic fiber family 1. The corresponding measured force of the anisotropic sample is shown in 4 (d). Amplitudes and dispersion parameters of the identified fiber families are plotted in 4 (e) and 4 (f), respectively. The collagen network of the anisotropic sample is characterized by two aligned fiber families. In the initial state before the first stretching cycle both fiber families have equal amplitudes and equal dispersion parameter values of 0.10 and 0.09. Upon stretching, we find a similar behavior for both samples. Fibers migrate from fiber family 1 to fiber family 2 with an periodically oscillating amplitude maximizing to $\sim 60\,\%$. One fiber family is oriented along the force direction as indicated by the OI of Fig.s 3 (a) and (c) increasing upon stretching. Furthermore, the dispersion parameter of fiber family 2 of the isotropic sample increases continuously in the relaxed state being responsible for its permanently increased AI.

Morphological Changes and Mechanical behavior upon Stretching

The AI of both skin samples is related to their respective mechanical behaviors in Fig. 5. The AI of both samples is shown in Fig. 5 (a). As pointed out before, the AI of the anisotropic sample constantly fluctuates around a value of 0.3, while the collagen network of the isotropic sample approaches this value after two deformation cycles. As shown in Fig. 5 (b) and in Supplementary Fig. 2, the force at maximum stretches decreases for samples with each deformation cycle, which is in line with stress strain curves measured in literature[4,5,15]. This altered mechanical response of soft tissue due to repeated deformation cycles is referred to as preconditioning effect[22]. In capsular ligaments Quinn et al.[23] correlated this effect with

a permanent alignment of collagen fibers along the direction of force. Here, we note that for both samples, the degree of maximum orientation of the collagen network is only determined by the maximum stretch, since the maximum of the OI of the first deformation cycle is not exceeded by performing additional deformation cycles. A permanent increase of the OI and the AI of collagen fibers in the relaxed state can be observed in case of the isotropic sample. The alignment of the collagen networks of both samples becomes identical after two deformation cycles. This is microscopically reflected by the relative change of the maximum force between each deformation cycle, shown in Fig. 5 (c). The large relative difference of $-12\,\%$ between maximum forces of the first two cycles of the isotropic sample correlates with the permanent alignment of fibers. Once fibers align to an AI of 0.3, the relative difference of maximum forces between consecutive deformation cycles becomes identical for both samples.
In conclusion, we are able to resolve different micro-structural variations of the collagen fiber network of skin, that are related

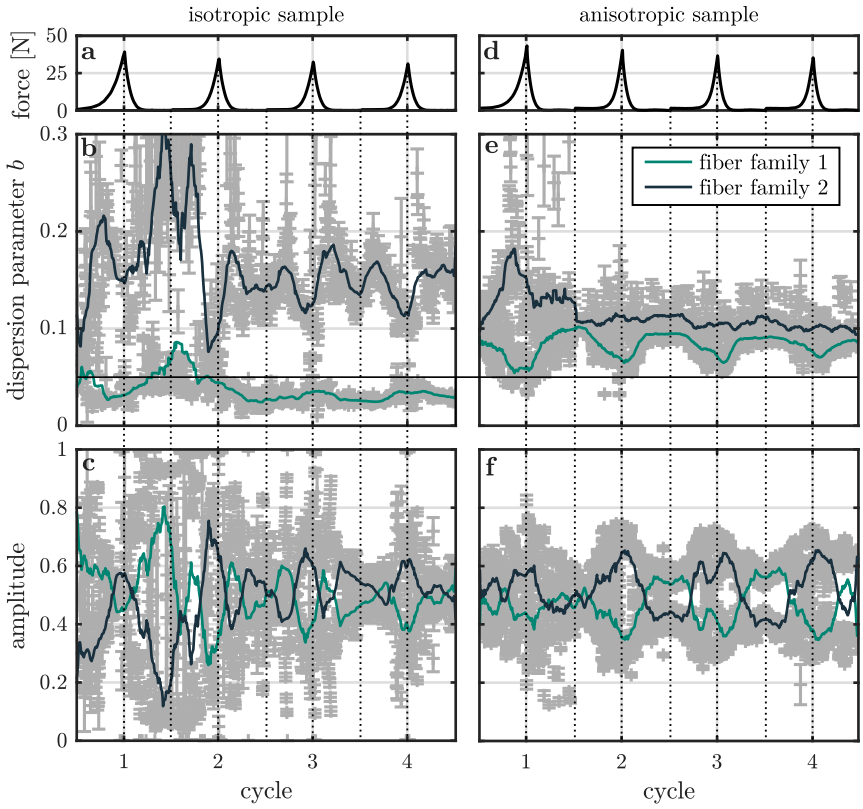

Figure 4. FINE algorithm parameters of the collagen fiber families of the isotropic and the anisotropic sample under repeated stretching and relaxation. (**a**) Averaged force acting on the isotropic sample, measured by the force sensors as a function of the deformation cycle number. (**b**) Dispersion parameter b of each fiber family identified by the FINE algorithm in the isotropic sample as a function of the deformation cycle number. Data points with error bars indicating the 95 % confidence intervals are shown in grey. Solid lines represent smoothed data points. Note that, a third fiber family is identified in a negligible fraction of images ($\leq 1\,\%$). For the sake of clarity, parameters of this fiber family are not shown. The line at $b = 0.05$ indicates the threshold value below which a fiber family is considered as isotropic. (**c**) Amplitude of each fiber family identified by the FINE algorithm in the isotropic sample as a function of the deformation cycle number. (**d**) Averaged force acting on the anisotropic sample, measured by the force sensors as a function of the deformation cycle number. (**e**) Dispersion parameter b of each fiber family identified by the FINE algorithm in the anisotropic sample as a function of the deformation cycle number. (**f**) Amplitude of each fiber family identified by the FINE algorithm in the anisotropic sample as a function of the deformation cycle number.

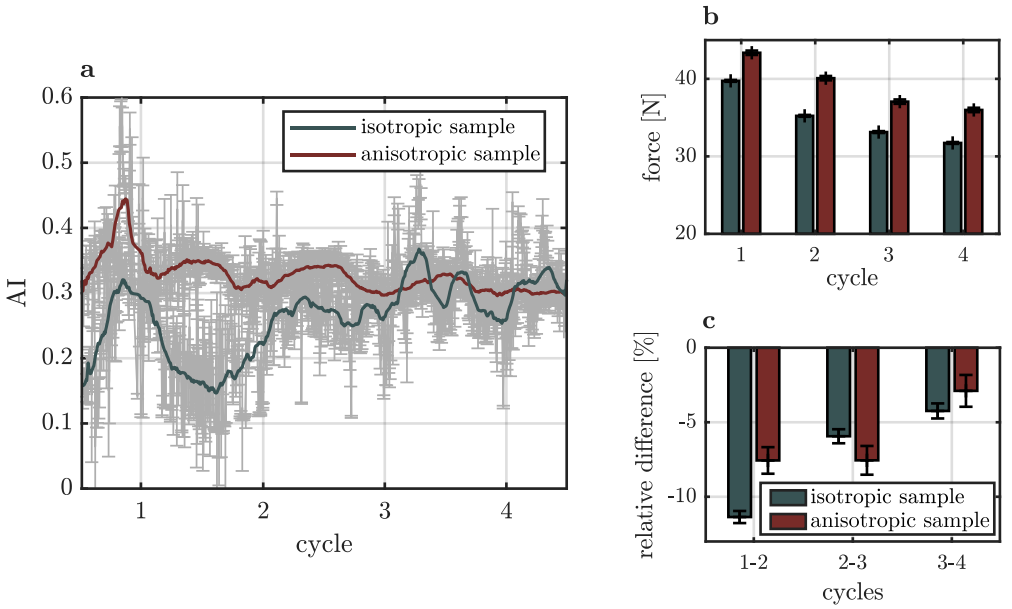

Figure 5. Relation between measured force and orientation of the collagen fiber network. (**a**) Alignment index of the isotropic sample and the anisotropic sample as a function of the deformation cycle number. (**b**) Relative maximum force applied to the isotropic and the anisotropic sample as a function of the deformation cycle number. (**c**) Relative difference of the maximum force of each deformation cycle of the isotropic and the anisotropic sample.

to the interplay of its fiber families. Permanent as well as periodic processes of the collagen fiber network due to cyclic deformations are identified. Furthermore, differences across the samples in terms of their mechanical response are successfully correlated with their individual collagen fiber networks and thus to skin morphologies. Our proof of principle study opens a new avenue to investigate biological fiber-reinforced tissue upon mechanical strain. The FINE algorithm in combination with the multiphoton stretching device represents a sophisticated method to relate micro-structural properties to the macroscopic mechanical behavior.

Methods

Sample Preparation

A back skin of a female pig was acquired from a local, commercial butcher. Rectangular skin samples were punched with an orientation parallel to the spine and stored in the freezer at $-24°$ until usage. Directly before the experiment, the subcutaneous fat is cautiously removed using a surgical blade. The skin samples were still frozen to avoid any pre-stress of the collagen fibers. Additionally, samples are cut to dimensions of $(80 \times 6)\,\mathrm{mm}^2$. Thawed sample were placed between the two clamps with the dermis pointing towards the multiphoton microscope to image deep dermal layers. Constant hydration of the skin sample during the experiment was ensured by constantly moistening the samples with water.

Multiphoton Microscope Stretching Device

Multiphoton Microscopy

For second harmonic generation (SHG) measurements we used a multiphoton microscope (DermaInspect) which was developed in collaboration with Jenlab GmbH (Jena, Germany)[24]. To measure the collagen-specific second-harmonic generation (SHG) signal, a femtosecond titanium:sapphire laser (*Mai Tai*, Spectra-Physics, California, USA) at a wavelength of 820 nm was used together with a 410 ± 10 nm band-pass filter (*AQ 410/20m-2P*, Chroma Technology Corp., Bellows Falls, VT). A water-immersion objective with a 20*x* magnification (*XLUMPlanFl 20x/0.95*, Olympus) captured a $440 \times 440\,\mu$m field of view with a resolution of (512×512) pixels. Images were cropped by 100 pixels since the left border was found to suffer from motion artefacts induced by the scanning mirrors of the microscope.

Stretching Device

As shown in Fig. 1 (a), samples were clamped into a custom made traction device, which consists of two opposing linear guide units (*RK Compact 30*, RK Rose+Krieger GmbH, Minden, Germany) with equipped stepper motors and 45 N load cells (*SML-45*, Interfaceforce e.K., Germany). The stepper motors (*ST4209S1006-B*, Nanotec Electronic GmbH & Co. KG, Feldkirchen, Germany) with encoder (*WEDS5541-A14*, Nanotec Electronic GmbH & Co. KG, Feldkirchen, Germany) allow for a minimum step size of 1 μm. The whole set-up was mounted onto a lifting stage to allow for a precise placement under the object lens of the microscope. To minimize displacements of the imaging plane, the skin samples were constrained in both directions along the optical axis. The minimum distance to the objective was ensured by a 3D-printed cylindrical spacer (*Form 2, standard black resin*, Formlabs, Somerville, USA) that was mounted to the microscope. The spacer further guaranteed a constant immersion of the objective, since a certain level of water between objective, spacer and the sample was kept. To avoid a potential sagging of the sample, a 3D-printed supporter was attached to the mounting plate underneath the sample. The stretching device was checked for sample slippage in preliminary tests.

Tensile Tests with Simultaneous Imaging

We performed tensile, strain-controlled, mechanical tests with four consecutive cycles of repeated stretch and relaxation. For a simultaneous deformation and imaging of the sample, tensile tests were performed at low strain rate of 0.075 %/s. Images were recorded with a mean scan-time of (2.63 ± 0.06) s every 3 s to ensure reliable sequences of consecutive image acquisition and data storage. Prior deformation, samples were slightly pre-stretched to a force of 0.2 N to ensure a uniform starting point. Although stretching and relaxation were performed bidirectional, a shift of the field of view in the tensile direction could ultimately not be prevented. We took advantage of the piezo element to adjust residual displacements in the direction of the optical axis. Distorted images were omitted from quantitative analysis. However, a sufficient number of images was captured at every point of the deformation curve ensuring a continuous tracking of the dermal collagen fiber network throughout the entire measurement.

Image Processing

Angular Orientation Distribution

We used a Fourier-based method[17] to obtain the angular orientation distribution $I(\theta)$ of the unprocessed SHG images. Fourier-based methods make use of the power spectrum, defined as the absolute square of the Fourier transform of the image, to calculate $I(\theta)$ by means of a radial sum. Within the method, Poissonian photonic noise of the measured SHG image is assumed[17]. Measurement uncertainties are then propagated to the Fourier domain. These uncertainties are used to define a filter by means of a relative error constrain on the power spectrum. In addition, the uncertainty of the angular orientation spectrum, $\Delta I(\theta)$ is achieved. $I(\theta)$ is used for the computation of the orientation index (OI) (equation 2). Since the FINE algorithm[18] is based on the cumulative orientation distribution $C(\theta)$ and its uncertainty, $\Delta C(\theta)$, both quantities were calculated and passed to the algorithm.

FINE algorithm

The FINE algorithm[18] determines the number of fiber families N, their mean orientations θ_i, amplitudes a_i and dispersion parameters b_i. The dispersion parameter b quantifies the spread of angles around their mean orientation. It can be understood as reciprocal standard deviation, meaning that a large value of b indicates a small spread of angles, i.e. an aligned fiber family, and vice versa. Within the FINE algorithm, a single fiber family is modelled with a sigmoid function that respects the semi-circularity of the angular orientation distribution. Fiber families are iteratively added until the deviation between cumulative orientation distribution, $C(\theta)$, and the fitted model is smaller than $3\sigma = 3\Delta C(\theta)$[18].

Local fiber orientation

The local fiber orientation was calculated as described previously[18]. First, the local angular orientation spectra of an image $I_p(x,y)$ were calculated, denoted as $I_p(x,y,\theta)$. Local orientation spectra were achieved from applying the inverse Fourier transformation to the wedge-filtered Fourier transform of the image. The main local orientation in each pixel indicates the angle at which the local orientation spectrum reaches its maximum intensity. The color-coded local main orientation was scaled by the relative intensity of each pixel. To enhance the contrast of fibers, the background signal was removed from the image by using the function *Subtract Background* of the open-source platform Fiji[25] with a rolling ball radius of 50 pixels.

References

1. Maiti, R. *et al.* In vivo measurement of skin surface strain and sub-surface layer deformation induced by natural tissue stretching. *J. Mech. Behav. Biomed. Mater.* **62**, 556–569, DOI: 10.1016/j.jmbbm.2016.05.035 (2016).

2. Ní Annaidh, A., Bruyère, K., Destrade, M., Gilchrist, M. D. & Otténio, M. Characterization of the anisotropic mechanical properties of excised human skin. *J. Mech. Behav. Biomed. Mater.* **5**, 139–148, DOI: 10.1016/j.jmbbm.2011.08.016 (2012). 1302.3022.

3. Bancelin, S. *et al.* Ex vivo multiscale quantitation of skin biomechanics in wild-type and genetically-modified mice using multiphoton microscopy. *Sci. Rep.* **5**, 1–14, DOI: 10.1038/srep17635 (2015).

4. Lynch, B. *et al.* A novel microstructural interpretation for the biomechanics of mouse skin derived from multiscale characterization. *Acta Biomater.* **50**, 302–311, DOI: 10.1016/j.actbio.2016.12.051 (2017).

5. Pissarenko, A. *et al.* Tensile behavior and structural characterization of pig dermis. *Acta Biomater.* **86**, 77–95, DOI: 10.1016/j.actbio.2019.01.023 (2019).

6. Yang, W. *et al.* On the tear resistance of skin. *Nat. Commun.* **6**, 6649, DOI: 10.1038/ncomms7649 (2015).

7. Nesbitt, S., Scott, W., Macione, J. & Kotha, S. Collagen Fibrils in Skin Orient in the Direction of Applied Uniaxial Load in Proportion to Stress while Exhibiting Differential Strains around Hair Follicles. *Mater. (Basel).* **8**, 1841–1857, DOI: 10.3390/ma8041841 (2015).

8. Ridge, M. D. & Wright, V. The directional effects of skin. A bio-engineering study of skin with particular reference to Langer's lines. *J. Invest. Dermatol.* **46**, 341–346, DOI: 10.1038/jid.1966.54 (1966).

9. Annaidh, A. N. *et al.* Automated estimation of collagen fibre dispersion in the dermis and its contribution to the anisotropic behaviour of skin. *Ann. Biomed. Eng.* **40**, 1666–1678, DOI: 10.1007/s10439-012-0542-3 (2012). 1203.4733.

10. Arumugam, V., Naresh, M. D. & Sanjeevi, R. Effect of strain rate on the fracture behaviour of skin. *J. Biosci.* DOI: 10.1007/BF02716820 (1994).

11. Purslow, P. P., Wess, T. J. & Hukins, D. W. Collagen orientation and molecular spacing during creep and stress-relaxation in soft connective tissues. *J. Exp. Biol.* **201**, 135–142 (1998).

12. Crichton, M. L. *et al.* The viscoelastic, hyperelastic and scale dependent behaviour of freshly excised individual skin layers. *Biomaterials* **32**, 4670–4681, DOI: 10.1016/j.biomaterials.2011.03.012 (2011).

13. Wong, W. L., Joyce, T. J. & Goh, K. L. Resolving the viscoelasticity and anisotropy dependence of the mechanical properties of skin from a porcine model. *Biomech. Model. Mechanobiol.* **15**, 433–446, DOI: 10.1007/s10237-015-0700-2 (2016).

14. Oftadeh, R., Connizzo, B. K., Nia, H. T., Ortiz, C. & Grodzinsky, A. J. Biological connective tissues exhibit viscoelastic and poroelastic behavior at different frequency regimes: Application to tendon and skin biophysics. *Acta Biomater.* **70**, 249–259, DOI: 10.1016/j.actbio.2018.01.041 (2018).

15. Remache, D., Caliez, M., Gratton, M. & Dos Santos, S. The effects of cyclic tensile and stress-relaxation tests on porcine skin. *J. Mech. Behav. Biomed. Mater.* **77**, 242–249, DOI: 10.1016/j.jmbbm.2017.09.009 (2018).

16. Zipfel, W. R. *et al.* Live tissue intrinsic emission microscopy using multiphoton-excited native fluorescence and second harmonic generation. *Proc. Natl. Acad. Sci. U. S. A.* **100**, 7075–7080, DOI: 10.1073/pnas.0832308100 (2003).

17. Witte, M., Jaspers, S., Wenck, H., Rübhausen, M. & Fischer, F. Noise reduction and quantification of fiber orientations in greyscale images. *PLoS One* 1–21, DOI: 10.1371/journal.pone.0227534 (2020).

18. Witte, M., Jaspers, S., Wenck, H., Rübhausen, M. & Fischer, F. General method for classification of fiber families in fiber - reinforced materials : application to in - vivo human skin images. *Sci. Rep.* 1–11, DOI: 10.1038/s41598-020-67632-z (2020).

19. Bayan, C., Levitt, J. M., Miller, E., Kaplan, D. & Georgakoudi, I. Fully automated, quantitative, noninvasive assessment of collagen fiber content and organization in thick collagen gels. *J. Appl. Phys.* **105**, 1–11, DOI: 10.1063/1.3116626 (2009).

20. Daly, C. H. Biomechanical properties of dermis. *J. Invest. Dermatol.* **79**, 17–20, DOI: 10.1038/jid.1982.4 (1982).

21. Benítez, J. M. & Montáns, F. J. The mechanical behavior of skin: Structures and models for the finite element analysis. *Comput. Struct.* **190**, 75–107, DOI: 10.1016/j.compstruc.2017.05.003 (2017).

22. Fung, Y. C. & Skalak, R. Biomechanics: Mechanical Properties of Living Tissues. *J. Biomech. Eng.* DOI: 10.1115/1.3138285 (1981).

23. Quinn, K. P. & Winkelstein, B. A. Preconditioning is Correlated With Altered Collagen Fiber Alignment in Ligament. *J. Biomech. Eng.* **133**, 064506, DOI: 10.1115/1.4004205 (2011).

24. Bückle, R. *et al.* 5D-intravital tomography as a novel tool for non-invasive in-vivo analysis of human skin. In *Adv. Biomed. Clin. Diagnostic Syst. VIII*, DOI: 10.1117/12.841861 (2010).

25. Schindelin, J. *et al.* Fiji: An open-source platform for biological-image analysis, DOI: 10.1038/nmeth.2019 (2012).

Acknowledgements

We acknowledge financial support from Beiersdorf AG.

Author contributions

M.W., F.F. and M.R. conceived the experiment. M.W. established the setup, wrote the software, and conducted the experiments. M.W., F.F. and M.R. analyzed the results. M.W., F.F. and M.R. wrote the manuscript. S.J. and H.W. reviewed the manuscript.

Competing interests

The authors declare no competing interests.

Chapter 6

Fiber Orientations in Ag:NW Composites

The AF method and the FINE algorithm were introduced to provide an accurate quantification of the angular orientation distribution of fibrous images without any assumptions on the underlying material. Thus, the method is suitable for the application to any type of scientific image, where the orientation distribution of fibers is of special interest.

The functional printing of conductive silver-nanowire (Ag-NW) photopolymer composites was introduced recently [4]. Such composites are advantageous in comparison to other 3D printed composites aiming for electrical conductivity since a high optical transmittance is ensured. Spherical nanoparticles, for example, which are embedded in a polymer matrix suffer from agglomeration together with a strong photon absorption [106, 107]. Spray-coated Ag-NW layers were found to circumvent these problems as sheet resistances between $10\,\Omega/sq$ and $30\,\Omega/sq$ at transparencies of around $90\,\%$ were measured [108, 109].

The functional printing of Ag-NW covers a large field of potential applications in electronics such as a top contact for solar cells or a flexible capacitor [4]. Imaging Ag-NW with light microscopy reveals a fibrous network containing fibers with a high aspect ratio of AR = 1000.

The electrical line resistance of Ag-NW composites increases by several orders of magnitude upon mechanical stretching of the material. A relation to its micro-structure is investigated by using the FINE algorithm of chapter 4 to resolve the properties of the nanowire network.

6.1 Stretching of Ag:NW Photopolymer Composites

6.1.1 Image Pre-Processing

Light microscopy is applied to capture the nanowire network. The source images are pre-processed to allow for a reasonable and reproducible evaluation using the FINE algorithm. As shown in figure 6.1 (a) source images suffer from a fluctuating intensity of the present fibers as well as fluctuations of the background signal. Fourier-based methods are sensitive to the intensity contrast of fibers with respect to the surrounding background signal [68]. In a first step, microscopy images are converted to greyscale and cropped to quadratic dimensions. To account for local variations of the background signal, the local background correction of the Fiji (ImageJ) build-in function *subtract background* with a rolling ball radius of 50 pixels is used [94]. The completely pre-processed image is shown in figure 6.1 (b). The corresponding orientation distribution as calculated by the AF method (chapter 3) is shown in figure 6.1 (c). The FINE algorithm identified one isotropic fiber family with a dispersion parameter of $b = 0.029 \pm 0.001$, shown in figure 6.1 (d).

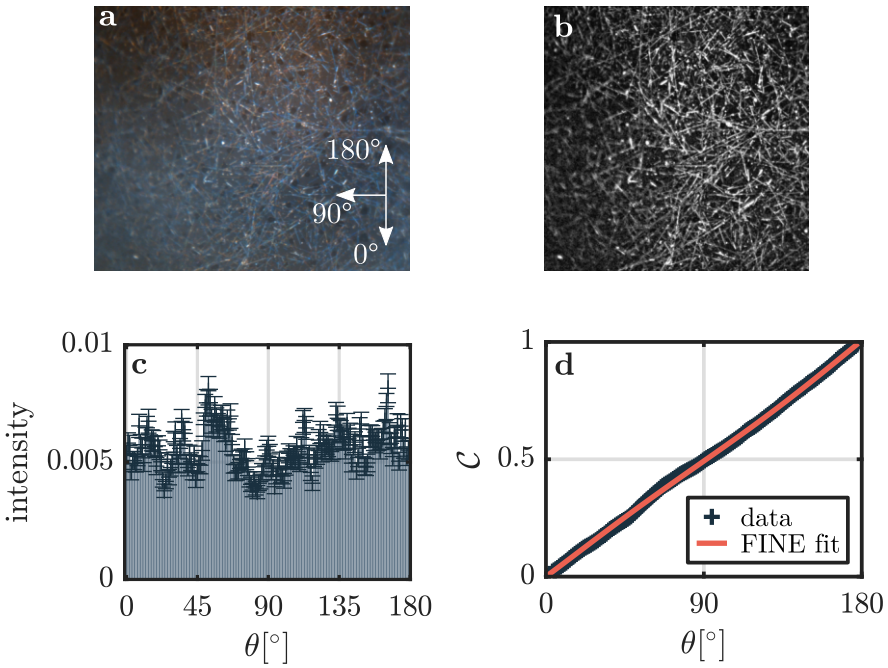

Figure 6.1: Pre-processing of microscopy images of silver-nanowires composites. (**a**) Source image of silver-nanowire composites. (**b**) Pre-processed image that is used as input for the FINE algorithm. (**d**) Orientation distribution calculated by the AF method. (**e**) Cumulative orientation distribution with the corresponding FINE fit. One isotropic fiber family is found with a dispersion of $b = 0.015 \pm 0.001$.

6.1.2 Stretching Experiments

Ag-NW composites with nanowire concentrations of $40\,\mu g/cm^2$, $80\,\mu g/cm^2$ and $120\,\mu g/cm^2$ are stretched up to 23 %. A total of eight light microscopy images are recorded for each sample representing stretch states from 3 % to 23 %. The FINE algorithm is applied to each pre-processed nanowire image to investigate changes of the nanowire network.

6.2 Results and Discussion

The results are presented and discussed in detail in a paper submitted to *Small*. The submitted version is shown in section 6.3. The main findings of the submission are briefly summarized here.

The FINE algorithm identifies one fiber family in each Ag-NW image. Dispersion parameters indicate that the nanowires are isotropically distributed at any stretch state for any concentration. At a concentration of $40\,\mu g/cm^2$, fibers slightly align in the direction of stretch, increasing the OI by a factor of 4.5 at a maximum stretch of 23 %. In contrast, samples with high concentrations ($80\,\mu g/cm^2$ and $120\,\mu g/cm^2$) keep a constant OI upon stretching. The line resistance, however, strongly increases upon stretching by factors of 2000, 1000, and 225 at 23 % elongation of the $40\,\mu g/cm^2$, $80\,\mu g/cm^2$ and $120\,\mu g/cm^2$, respectively. Thus, the drastic change of line resistance is not explained by an alignment of nanowires. Instead, Monte-Carlo simulations reveal that the line resistance is very sensitive to a decreasing number of nanowire junctions, which break upon exceeding critical forces.

6.3 Publication (submitted)

WILEY-VCH

Electrical and Network Properties of Flexible Silver-Nanowire Composite Electrodes under Mechanical Strain

Tomke E. Glier, Marie Betker, Maximilian Witte, Toru Matsuyama, Lea Westphal, Benjamin Grimm-Lebsanft, Florian Biebl, Lewis O. Akinsinde, Frank Fischer, Michael Rübhausen**

T. E. Glier, M. Betker, M. Witte, L. Westphal, Dr. B. Grimm-Lebsanft, F. Biebl, L. O. Akinsinde, Prof. M. Rübhausen
Institut für Nanostruktur- und Festkörperphysik, Center for Free Electron Laser Science (CFEL), Universität Hamburg, Luruper Chaussee 149, 22761, Hamburg, Germany.
E-mail: tglier@physnet.uni-hamburg.de, ruebhausen@physnet.uni-hamburg.de

M. Witte, Dr. F. Fischer
Beiersdorf AG, Unnastraße 48, 20245, Hamburg, Germany.

Dr. T. Matsuyama
Max-Planck Institute for the Structure and Dynamics of Matter, Luruper Chaussee 149, 22761, Hamburg, Germany.

Keywords: flexible electronics, silver nanowire polymer composites, stretching, electrical conductivity, Monte-Carlo simulation, resistor networks, fiber orientation

Flexible and conductive silver nanowire photopolymer composites are fabricated and studied under mechanical strain. The initial resistances of the unstretched flexible composites are between 0.27 Ω mm^{-1} and 1.2 Ω mm^{-1} for silver-nanowire concentrations between 120 µg cm^{-2} and 40 µg cm^{-2}. Stretching of the samples leads to an increased resistance by a factor of between 225 for 120 µg cm^{-2} and 2000 for 40 µg cm^{-2} at elongations of 23 %. In order to correlate network morphology and electrical properties, micrographs are recorded during stretching. On these images the Fiber Image Network Evaluation (FINE) algorithm is employed to determine morphological properties of the silver nanowire networks under stretching. For unstretched and stretched samples, an isotropic nanowire network is found with only small changes in fiber orientation upon stretching. Monte-Carlo simulations on 2D percolation networks of 1D conductive wires and the corresponding network resistance confirm that the elastic polymer matrix under strain exhibit forces acting on the nanowire junctions in agreement with Hooke's law. By variation of a critical force distribution the experimental data are accurately reproduced. This results in a model explaining the electrical

behavior and sensitivity of nanowire-composites with different filler concentrations under mechanical strain.

1. Introduction

Functional polymer composites have caught the attention of materials science and industry due to their enormous versatility for applications in e.g. medicine, electronics, and functional printing.[1–3] Conductive films are of great interest because of their various electronic and optical applications in solar cells and OLEDs.[4–6] Silver-nanowire-polymer composites are a promising alternative to indium tin oxide. They offer a scalable process for large scale, flexible, conductive materials, as used in integrated photovoltaics, touch screens, and flexible electronics.[7–11] Furthermore, the embedding of metal nanoparticles in a printable polymer matrix enables a fabrication process with a high design flexibility and allows rapid prototyping. Additive manufacturing of components has developed over the last 25 years to be an important and innovative part of the industrial process.[12–14] As a matrix material, photopolymers have tunable viscosities, are curable by illumination with UV-light, and are well suited to create three dimensional structures via layer by layer additive manufacturing. For example, a flexible silver nanowire composite capacitor was built and demonstrated recently.[15] Due to the fact, that the matrix material of the composite is exchangeable and tunable in e.g. color, optical, and mechanical properties, the composites can easily be tailored to their respective application.[15] Bending and stretching of silver nanowire composite electrodes have been investigated from many different perspectives.[16–22] Flexible electrodes as used in foldable touch displays are some of the most demanding applications of these materials.

We have investigated flexible electrodes, which are based on silver nanowires embedded in a flexible and photocurable polymer matrix. In order to test their deformation and durability, we

performed mechanical strain tests, in situ conductivity, and light microscopy measurements. The conductivity measurements monitor the functionality of the films. By light microscopy, the nanowire network morphology was observed. In order to obtain quantitative information on the network structure change upon stretching, the Fiber Image Network Evaluation (FINE) algorithm was employed.[23,24] Based on the micrographs, the FINE algorithm determines the number of fiber families, their amplitudes, mean orientation and dispersion, based on the cumulative angular orientation distribution. Monte-Carlo simulations on the nanowire networks and the corresponding network resistance confirm that the elastic polymer matrix under strain exhibit forces acting on the nanowire junctions in agreement with Hooke's law. The experimental data were reproduced by variation of a critical force distribution leading to a model explaining the electrical behavior of nanowire-composites with different concentrations under mechanical strain.

2. Results and Discussion

Figure 1(a) shows the experiment. Flexible silver-nanowire (Ag-NW) composite films were clamped in a stretching setup, which is based on two linear translation stages motorized with two stepper motors. Two isolating polyether ether ketone (PEEK) base plates were mounted on top of the linear translation stages. The composite samples, behaving like thin rubber like foils, are placed on the PEEK plates and clamped on each site with a small polyimide plate, which contains two gold electrodes. By doing so, the electrical conductivity of the samples can be measured in a four-point geometry. More details on the setup are given in the experimental section.

The samples consist of Ag-NW networks, which were embedded in a flexible photopolymer matrix as described in the experimental section. The samples have a size of 12 mm x 12 mm and a total thickness of 150 µm. The embedded nanowires extend up to 1 µm into the polymer

matrix, resulting in a conductive composite layer at the top site of the sample, which is shown in Figure 1(b). In Figure 1(c) a SEM image of Ag NWs drop-casted on a bare silicon wafer is shown. One can see how the nanowire networks are formed and how the thinner wires are flexibly above and below other wires. Nanoparticles (spheres, triangles and plates) arise as marginal side products during the synthesis. The Ag NWs were synthesized by a polyol route and have a pentagonal cross section as discussed in detail in [15]. The Ag-NW networks are produced by drop-casting of a Ag-NW suspension on a clean and smooth substrate like silicon or glass. Homogeneous networks of randomly orientated nanowires are formed, which show high conductivities even at small amounts of silver.[15] This is a consequence of a percolative process, which is determined by the high aspect ratio of the used wires. Compared to composites of spherical fillers, anisotropic sticklike fillers reach the percolation threshold at a lower amount of the filler material, decreasing with increasing aspect ratio (length/diameter).[25–28] Furthermore, by using one-dimensional (1D) structures, conductive pathways with a minimum number of terminations can be obtained, which minimizes the influence of the tunneling resistance on the total resistance of the system. Therefore, 1D nanostructures with high aspect ratio are highly desirable for the formation of conductive 2D films. In addition, the small amount of necessary conductive filler material facilitates the fabrication of transparent and conductive composites.[15] In order to fabricate the composites, the drop-casted networks were coated with a photocurable resin. After curing the polymer layer with UV-light, the composite film can be detached from the substrate and subsequently investigated in our stretching setup. Figure 1(d) shows three micrographs of a Ag-NW composite film during stretching at different elongations. The stretching direction is horizontal and the width of the images corresponds to the relative lengthening of the film during stretching.

In **Figure 2**(a) the line resistance of three samples with nanowire concentrations of 40 µg cm^{-2}, 80 µg cm^{-2}, and 120 µg cm^{-2} are shown. The line resistance was measured along the stretching direction and the measured values were divided by the length of the sample, respectively. The initial resistances of the unstretched flexible composites are (0.269 ± 0.002) Ω mm^{-1} for the 120 µg cm^{-2} sample, (0.387 ± 0.001) Ω mm^{-1} for the 80 µg cm^{-2} sample, and (1.193 ± 0.002) Ω mm^{-1} for the 40 µg cm^{-2} sample. The samples were stretched stepwise. Each stretching step corresponds to a relative elongation of 3.3 %. One can observe an increase in line resistance for samples with lower Ag-NW concentrations. The increase in resistance during stretching follows a sigmoidal shape with a higher relative increase for lower nanowire concentrations. All curves are saturated after 20 % stretching. For the 120 µg cm^{-2} sample, an increase by a factor of 225 after stretching by 23 % elongation was observed. A sample with a Ag-NW concentration of 80 µg cm^{-2} shows an increase by a factor of 1000 and the resistance of the 40 µg cm^{-2} sample was increased by a factor of 2000. Since optical measurements require flat sample surfaces, pre-stretching of the samples by 3.3 % elongation was necessary. In the following, we, therefore, analyze all our data normalized to the pre-stretched value at 3.3 % elongation. The line resistance upon stretching for the samples shown in Figure 2(a) normalized to the resistance value at 3.3 % are shown in Figure 2(b).

For each stretching step, a light microscopy image was recorded as shown in Figure 1(d)-(f). These images were analyzed using an algorithm that determines the number of fiber families, their amplitudes, mean orientation and dispersion, based on the cumulative angular orientation distribution, the FINE algorithm.[23] The analysis clearly shows that the nanowire networks consist of one isotropic fiber family (see Supporting Information SI 1 for details). Upon stretching, changes in the overall network morphology are observed by the orientation index as shown in Figure 2(c).[29] The orientation index represents the degree of fiber orientation in the angular distribution function. A completely isotropic distribution leads to a vanishing

orientation index, while a full alignment of the fibers yields an orientation index of one.[23,29] Samples with high concentrations (80 µg cm^{-2} and 120 µg cm^{-2}) show no remarkable changes in orientation, whereas for the 40 µg cm^{-2} sample a change in orientation index by a factor of 4.5 was observed. However, no emerging anisotropic fiber family could be found by the FINE algorithm (see Supporting Information). The lower the concentration, the greater the impact of individual changes and alignments within the network. Overall, the orientation indices for all samples and all stretching conditions are small (≤ 0.1) and in the isotropic region. From these results, it becomes clear that changes in network morphology and mean fiber orientation are not the primary effect leading to the observed drastic resistance changes of several orders of magnitude depending on the Ag-NW concentration.

When considering a percolation of randomly orientated 1D wires, the position of the wires, their length, number and orientation, as well as their length distribution are critical parameters. The behavior of a percolation network during stretching conditions can be calculated by a Monte-Carlo simulation on the resistor network formed by overlapping wires in a 2D network. In **Figure 3**(a), a sample (350 µm x 350 µm) with a typical length distribution corresponding to the synthesized nanowires and a concentration of 10 µg cm^{-2} is shown. The orientation of the wires was chosen randomly between $-90° \leq \theta_i \leq 90°$, which results in an isotropic sample. Intersections of the wires were found by using two criteria: If the distance between the centers of two wires *i* and *j* is larger than the sum of half the length of wire *i* and wire *j* (Equation (1)), an intersection can be excluded. If Equation (1) is fulfilled, the distances A_i and A_j were calculated (see Equation (2) and Figure 3(b)).[25,26] If $A_i \leq L_i/2$ and $A_j \leq L_j/2$, an intersection is found.

$$d_{ij} = [(x_i - x_j)^2 + (y_i - y_j)^2]^{1/2}$$
$$d_{ij} < \frac{L_i}{2} + \frac{L_j}{2} \quad (1)$$

$$A_i = d_{ij}\left|\cos(\theta_j + \gamma)/\sin(\theta_j - \theta_i)\right|$$
$$A_j = d_{ij}\left|\cos(\theta_i + \gamma)/\sin(\theta_j - \theta_i)\right| \quad (2)$$
$$\gamma = \arctan[(y_i - y_j)/(x_i - x_j)]$$

Due to the fact, that the Ag NW itself is an excellent conductor, the junctions between the wires determine the total resistance of the network. A sample consisting of *N* wires (see Figure 3(c)) can be considered as a resistor network with *N* nodes and the tunneling resistance r_{ij} of the resistor connecting nodes *i* and *j* (see Figure 3(d)).[30–33] For the simulation all tunneling resistances r_{ij} of intersecting wires were assumed to be equal to 1, resulting in a conductance of $c_{ij} = r_{ij}^{-1} = 1$. The resistance between wires, which are not intersecting, is infinity resulting in a conductance of 0. With V_i being the electric potential at the *i*-th node and I_i being the current flowing in the system at the *i*-th node, Kirchhoff's Law can be written as

$$\boldsymbol{L}\vec{V} = \vec{I} \quad (3)$$

where $\boldsymbol{L}$ is the Laplace matrix as given in Equation (4)[30]

$$\boldsymbol{L} = \begin{pmatrix} c_1 & -c_{12} & \cdots & -c_{1N} \\ -c_{21} & c_2 & \cdots & -c_{2N} \\ \vdots & \vdots & \ddots & \vdots \\ -c_{N1} & -c_{N2} & \cdots & -c_N \end{pmatrix}. \quad (4)$$

According to the method presented by Wu et al.[30] the resistance of a resistor network between two nodes can be calculated by Equation (5), where ψ_i are the eigenvectors and λ_i are the eigenvalues of $\boldsymbol{L}$.[30]

$$R_{\alpha\beta} = \sum_{i=1}^{N} \frac{1}{\lambda_i} \left| \psi_{i\alpha} - \psi_{i\beta} \right|^2 \quad (5)$$

Wires representing the contacts at the left and the right side of the sample were assumed spanning the whole length of the simulated width. Figure 3(e) shows the resistance as a function of Ag-NW concentration. The concentration was determined by calculating the silver mass per square centimeter using a mean wire diameter of 200 nm and a silver density of 10.49 g cm^{-3}. The resistance shows an exponential dependence on the concentration, as discussed in previous simulations and experimental studies.[15,16,34] The red solid line depicts an exponential curve as guide to the eye. For an experimental realization of a Ag-NW network, Ag-NW concentrations of 40 µg cm^{-2} – 120 µg cm^{-2} were used. These experimental concentrations are by a factor of about 4 higher than the corresponding effective concentrations used for the simulation. We have benchmarked the nominal concentration against the silver nanowire concentration observed in the experimental micrographs. The effective concentration of silver that contributes to a conductive percolation network of nanowires is lower due to side products (particles and rods, see Figure 1(c)) in the Ag-NW suspension used for the experiments and its effective distribution in the composite.

In order to simulate the fiber morphology during stretching of a composite material, one has to consider that the distances between the filler particles in the stretching direction become larger, based on the assumption that the particles follow the matrix. This aspect was simulated by changing the positions of the wires according to the respective elongation. Thus, an increase in resistance by a factor of between 2 and 2.5 was reproducibly observed at an elongation of 23 %, see Figure 3(f) for an exemplary sample with an effective concentration of 20 µg cm^{-2}. In a second step, the impact of wire alignment during stretching was investigated. For this purpose, the x-component d*x* of the vector that describes a wire was

adapted in accordance with the respective elongation to $d\tilde{x} = dx * (1 + E_{[\%]}/100)$. The orientation angle of the wire θ_i was then adapted by $\cos(\theta_i) = d\tilde{x}/L_i$, where L_i is the fixed length of a wire *i*. With these assumptions, the simulation results, in contrast to the experiment, in the formation of an anisotropic fiber family upon stretching as analyzed by the FINE algorithm (see Supporting Information SI 2). The initial, unstretched samples consist of a single isotropic fiber family and have an orientation index of smaller than 0.05. After stretching, an anisotropic fiber family with orientation in stretching direction is formed, resulting in an orientation index of around 0.5. Both, the isotropic and the anisotropic fiber families co-exist with equal amplitudes. The red curve in Figure 3(f) represents a sample for which the stretching conditions were simulated by the described changes in terms of position and alignment. We can conclude, that an alignment of the wires in stretching direction does not lead to the drastic resistance changes observed in the experiment. Furthermore, the findings obtained from the microscopy images clearly show, that the simulated alignments are much higher than the observed alignments in the experiment.

The force *F* used to stretch an elastic polymer matrix can be described by Hooke's law $F = k \cdot \Delta x$, where *k* is a constant factor characteristic for the elastic polymer matrix and Δx is the elongation. This force acts on the nanowire junctions. In order to explain the drastic increase in resistance during stretching observed in the experiments, a critical force at which the individual junctions break and disconnect was introduced. Considering two wires with the x-positions (*x* is stretching direction) x_i^0 and x_j^0 before stretching and the positions after stretching x_i^1 and x_j^1, the acting force *F* is proportional to the relative movement of the wires, or rather the distance change $F \propto \Delta x_{ij} = \left|x_i^1 - x_j^1\right| - \left|x_i^0 - x_j^0\right|$. The critical force for each nanowire junction should depend on the embedding polymer matrix of the two intersecting nanowires. The top nanowires at the surface of the sample are not completely covered with

polymer resulting in a weaker connection to the matrix and the wires embedded in it. The simulated results together with the experimental data for different concentrations are shown in Figure 3(g). For the simulation shown in Figure 3 (g), a critical distance Δx_{ij} from four junction classes A, B, C, and D with the frequencies p_A, p_B, p_C, and p_D was assigned to each wire-wire junction. They represent the critical forces required to break the respective junction. The qualitative behavior of the experimental data such as the increase in resistance and the shape of the curves was successfully simulated with $\Delta x_{ij}(A) = 0.2$ µm, $\Delta x_{ij}(B) = 0.3$ µm, $\Delta x_{ij}(C) = 0.7$ µm, $\Delta x_{ij}(D) = 50$ µm, and $p_A = 75$ %, $p_B = 14$ %, $p_C = 4$ %, and $p_D = 7$ % (see Figure 3(g)). We can not only describe the shape of the resistance curves upon stretching but also its change upon concentration and stretching. The simulated networks consist of a total number of wires between 4400 wires for the lowest concentration and 7350 wires for the highest concentration, resulting in an effective concentration between 18 µg cm^{-2} and 30 µg cm^{-2} and a number of junctions of the wires between 21700 and 60500. The number of undamaged junctions as well as the normalized number of completely disconnected wires (wires that no longer have undamaged connections to other wires) for the simulations in Figure 3(g) are shown in Figure 3(h). The number of junctions was fitted by $y = y_0 + Ax^{-1.3}$ with the same decay constant of -1.3 for all nanowire concentrations. The variable x is the elongation. The lower the nanowire concentration, the lower is the number of junctions in the network resulting in a respective change in offset y_0 and amplitude A. The number of detached wires was fitted by $y = y_0 + B\exp(-\alpha x)$, where y_0 is a constant background of 0.5 and x is the elongation. The amplitude B changes gradually from -0.6 for the lowest concentration to -0.55 for the highest concentration. The decay constant α is also changing from 0.055 for the lowest concentration to 0.025 for the highest concentration.

These results demonstrate and explain the strong concentration dependence and sensitivity of the investigated nanocomposite material under stretching conditions. The decrease of the number of junctions in the network results in an enhanced sensitivity towards mechanical

strain. Even small changes in the number of connections at high elongations lead to large changes in resistance. The observed saturation in the resistance curves can be explained by the existence of a class of junctions with a high critical force ($\Delta x_{ij}(D) = 50$ µm), representing wire-wire connections, which are well embedded in the polymer matrix and highly durable. The lower the concentration, the lower is the number of junctions of an individual wire to other wires, which is a measure for the connectivity of the network. By looking at the relative number of wires without undamaged junctions to the nanowire network after 23 % stretching, we found a linear decrease of this number with increasing concentration. This linear decrease in connectivity leads to drastic changes in the resistivity as shown in Figure 3(g) and (e).

3. Conclusion

In Conclusion, we have shown that the electrical behavior of Ag-NW networks in flexible polymer composites can be controlled by the Ag-NW concentration and lead to resistance changes of up to three orders of magnitude upon stretching. The samples were investigated by an integrated light microscopy setup, that allows to image the Ag-NW composite during stretching. Furthermore, we were able to model the composite conductance as a function of concentration and stretching by a Monte-Carlo simulation that considers a resistor network consisting of the tunneling resistances between the wires. Moreover, we model and quantitively reproduce the experimentally observed resistance changes upon stretching by means of the interaction between the nanowire network and the polymer matrix by means of Hooke's Law and a critical force distribution of the nanowire junctions within the composite.

4. Experimental Part

4.1 Sample Preparation

Ag NWs were synthesized as described in [15]. After the synthesis, the Ag-NW suspension was washed successively twice with isopropanol, twice with acetone and twice with isopropanol. After each washing step, the suspension was centrifuged at 2000 rpm for 10 min. The supernatant was removed and replaced with fresh solvent. The resulting Ag-NW isopropanol suspension was drop-casted on a solvent-cleaned glass substrate using a 3 cm^2 template. The dried Ag-NW networks were coated with the liquid polymer resin Flexible (Formlabs, USA) by using a doctor blade, which was moved over the sample in a defined distance to the glass substrate. The polymer layer with a thickness of around 150 µm was cross-linked with a laser driven UV light source EQ-99X (Energetiq, USA) for 100 s. Remaining resin was removed after the curing process with isopropanol and acetone. Finally, the samples were removed from the substrate.

4.2 Characterization and Stretching

For scanning electron microscopy measurements, a commercial field emission scanning electron microscope (FE-SEM Zeiss, Germany) was used. For conductivity measurements a DC voltage/current source GS200 (Yokogawa, Japan) and the 34401A 6 ½ Digit Multimeter (Keysight, USA) were used. A constant current of 0.6 mA was applied to the nanowire composite samples and the voltage drop across the sample in stretching direction was measured. This measurement mode allows the measurement of line- and sheet resistances without the influence of the contact resistance. The resistance measurements were carried out after each stretching step (3.3 % relative elongation). The time between each stretching step was 10 min. Light microscopy was carried out using a custom-made microscope with a magnification of 50X consisting of the infinity corrected 50X objective Plan Apo NA = 0.55

(Mitutoyo, Japan) in combination with the MT-40 accessory tube lens (Mitutoyo, Japan), a color industrial camera DFK 37AUX264 (The Imaging Source, Germany), and a LED lamp QTH10/M (Thorlabs, USA). The stretching-setup consists of an aluminum base plate on which two single-axis translation stages PT1/M (Thorlabs, USA) are mounted. Both have a travel range of 25 mm with a translation of 0.5 mm per revolution. Each stage is driven by a stepping motor 0.9-NEMA 17 (Nanotec, Germany). The stepping motors are controlled by a closed-loop-stepping motor-controller SMCI33-2 (Nanotec, Germany) with an encoder controlled guaranteed resolution of 2 µm.

Supporting Information
Supporting Information is available from the Wiley Online Library or from the author.

Acknowledgements
The authors thank Birger Höhling and Boris Fiedler for making the circuits boards. We thank Sarah Scheitz, Nils Huse and Robert Frömter for supporting the SEM measurements. This work is funded by the DFG (Deutsche Forschungs-Gesellschaft) RU773/8-1, by the Helmholtz Society through DESY and by BMBF (Bundesministerium für Bildung und Forschung) 05K19GU5.

Conflict of Interest
We have no conflict of interest to declare.

Received: ((will be filled in by the editorial staff))
Revised: ((will be filled in by the editorial staff))
Published online: ((will be filled in by the editorial staff))

References

[1] R. Dermanaki Farahani, M. Dubé, *Adv. Eng. Mater.* **2018**, *20*, 1700539.

[2] J. F. Tressler, S. Alkoy, A. Dogan, R. E. Newnham, *Compos. Part A Appl. Sci. Manuf.* **1999**, *30*, 477.

[3] S.-B. Park, E. Lih, K.-S. Park, Y. K. Joung, D. K. Han, *Prog. Polym. Sci.* **2017**, *68*, 77.

[4] S. Lu, Y. Sun, K. Ren, K. Liu, Z. Wang, S. Qu, *Polymers (Basel).* **2017**, *10*, 5.

[5] Y. Xu, X. Wei, C. Wang, J. Cao, Y. Chen, Z. Ma, Y. You, J. Wan, X. Fang, X. Chen, *Sci. Rep.* **2017**, *7*, 45392.

[6] W. U. Huynh, J. J. Dittmer, A. P. Alivisatos, *Science (80-.).* **2002**, *295*, 2425.

[7] M. S. Miller, J. C. O'Kane, A. Niec, R. S. Carmichael, T. B. Carmichael, *ACS Appl. Mater. Interfaces* **2013**, *5*, 10165.

[8] J. Li, Y. Tao, S. Chen, H. Li, P. Chen, M. Z. Wei, H. Wang, K. Li, M. Mazzeo, Y. Duan, *Sci. Rep.* **2017**, *7*, 1.

[9] X.-Y. Zeng, Q.-K. Zhang, R.-M. Yu, C.-Z. Lu, *Adv. Mater.* **2010**, *22*, 4484.

[10] X. He, F. Duan, J. Liu, Q. Lan, J. Wu, C. Yang, W. Yang, Q. Zeng, H. Wang, *Materials (Basel).* **2017**, *10*, 1362.

[11] T. Sannicolo, M. Lagrange, A. Cabos, C. Celle, J.-P. Simonato, D. Bellet, *Small* **2016**, *12*, 6052.

[12] E. MacDonald, R. Wicker, *Science (80-.).* **2016**, *353*, aaf2093.

[13] M. Hofmann, *ACS Macro Lett.* **2014**, *3*, 382.

[14] A. D. Valentine, T. A. Busbee, J. W. Boley, J. R. Raney, A. Chortos, A. Kotikian, J. D. Berrigan, M. F. Durstock, J. A. Lewis, *Adv. Mater.* **2017**, *29*, 1703817.

[15] T. E. Glier, L. Akinsinde, M. Paufler, F. Otto, M. Hashemi, L. Grote, L. Daams, G. Neuber, B. Grimm-Lebsanft, F. Biebl, D. Rukser, M. Lippmann, W. Ohm, M. Schwartzkopf, C. J. Brett, T. Matsuyama, S. V. Roth, M. Rübhausen, *Sci. Rep.* **2019**, *9*, 6465.

[16] A. R. Madaria, A. Kumar, F. N. Ishikawa, C. Zhou, *Nano Res.* **2010**, *3*, 564.

[17] W. Hu, X. Niu, L. Li, S. Yun, Z. Yu, Q. Pei, *Nanotechnology* **2012**, *23*, 344002.

[18] R. Wang, H. Zhai, T. Wang, X. Wang, Y. Cheng, L. Shi, J. Sun, *Nano Res.* **2016**, *9*, 2138.

[19] W. Xu, L. Zhong, F. Xu, W. Shen, W. Song, S. Chou, *ACS Appl. Nano Mater.* **2018**, *1*, 3859.

[20] X. Crispin, F. L. E. Jakobsson, A. Crispin, P. C. M. Grim, P. Andersson, A. Volodin, C. van Haesendonck, M. Van der Auweraer, W. R. Salaneck, M. Berggren, *Chem.*

Mater. **2006**, *18*, 4354.

[21] J. Liang, L. Li, K. Tong, Z. Ren, W. Hu, X. Niu, Y. Chen, Q. Pei, *ACS Nano* **2014**, *8*, 1590.

[22] W. Xu, L. Zhong, F. Xu, W. Song, J. Wang, J. Zhu, S. Chou, *Small* **2019**, *15*, 1805094.

[23] M. Witte, S. Jaspers, H. Wenck, M. Rübhausen, F. Fischer, *Sci. Rep.* **2020**, *10*, 10888.

[24] M. Witte, S. Jaspers, H. Wenck, M. Rübhausen, F. Fischer, *PLoS One* **2020**, *15*, e0227534.

[25] I. Balberg, N. Binenbaum, *Phys. Rev. B* **1983**, *28*, 3799.

[26] G. E. Pike, C. H. Seager, *Phys. Rev. B* **1974**, *10*, 1421.

[27] S. H. Munson-McGee, *Phys. Rev. B* **1991**, *43*, 3331.

[28] S. I. White, R. M. Mutiso, P. M. Vora, D. Jahnke, S. Hsu, J. M. Kikkawa, J. Li, J. E. Fischer, K. I. Winey, *Adv. Funct. Mater.* **2010**, *20*, 2709.

[29] C. Bayan, J. M. Levitt, E. Miller, D. Kaplan, I. Georgakoudi, *J. Appl. Phys.* **2009**, *105*, 102042.

[30] F. Y. Wu, *J. Phys. A. Math. Gen.* **2004**, *37*, 6653.

[31] S.-H. Yook, W. Choi, Y. Kim, *J. Korean Phys. Soc.* **2012**, *61*, 1257.

[32] X. Ni, C. Hui, N. Su, W. Jiang, F. Liu, *Nanotechnology* **2018**, *29*, 075401.

[33] I. Balberg, N. Binenbaum, C. H. Anderson, *Phys. Rev. Lett.* **1983**, *51*, 1605.

[34] K. K. Kim, S. Hong, H. M. Cho, J. Lee, Y. D. Suh, J. Ham, S. H. Ko, *Nano Lett.* **2015**, *15*, 5240.

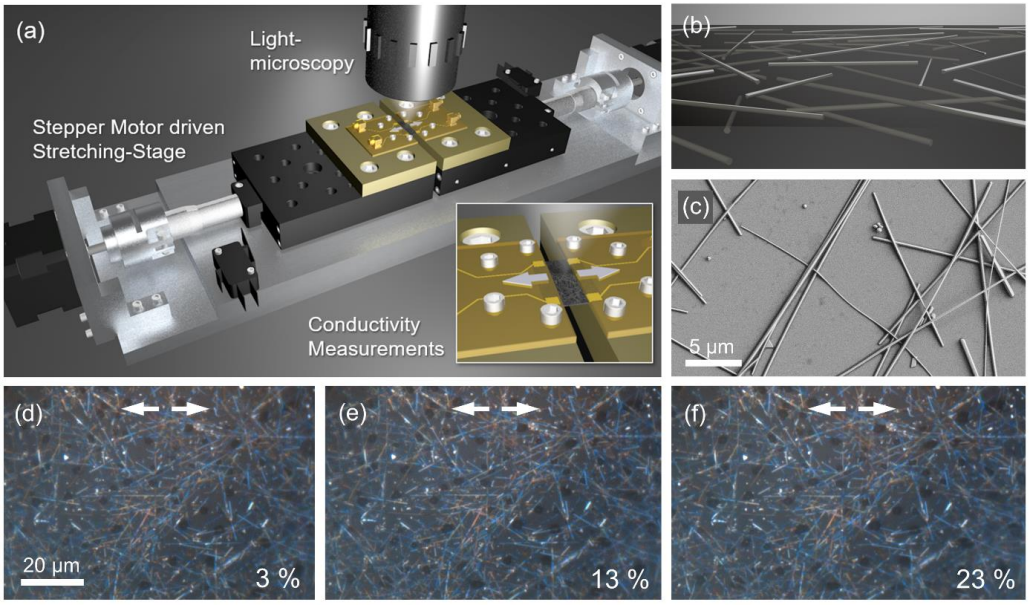

Figure 1. (a) Representation of the experimental setup. The sample is fixed and contacted with two circuit boards and stretched by two motorized linear translation stages. A custom-made light microscope is installed above the sample. The inset shows the clamped sample in stretching mode. Of the 12 mm x 12 mm samples, an area of 3 mm x 12 mm is stretched. (b) Ag NWs, which are embedded in the polymer matrix. (c) SEM image of drop-casted Ag NWs on a silicon wafer without polymer matrix. (d)-(f) Excerpts from light microscopy images of a Ag-NW composite with a Ag-NW concentration of 120 µg cm^{-2} for 3 exemplary stretching steps at 3 %, 13 %, and 23 % elongation, respectively. The elongation is given in relative units (distance of the translation stages after stretching divided by initial distance). The stretching direction is depicted as white arrows.

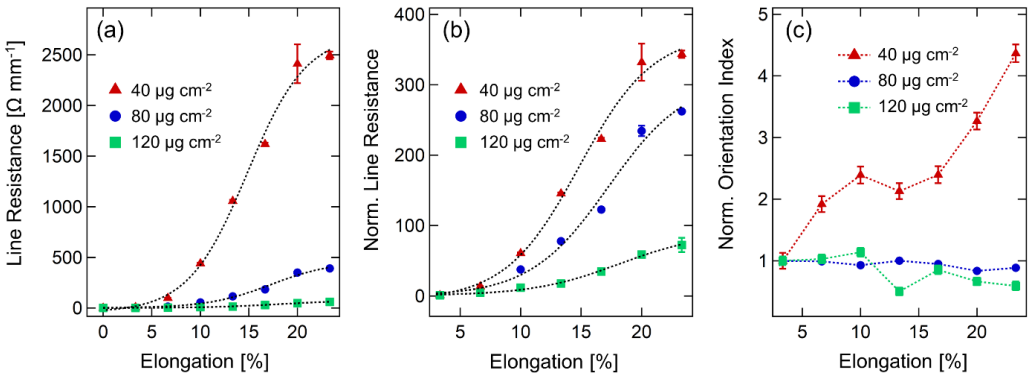

Figure 2. (a) Line resistance in stretching direction as function of elongation of three samples with a Ag-NW concentration of 40 µg cm^{-2} (red), 80 µg cm^{-2} (blue) and 120 µg cm^{-2} (green). The resistance measurements were carried out after each stretching step (3.3 % relative elongation). The dashed line is a sigmoidal guide to the eye. (b) Same experimental data shown in (a) normalized to the value of the pre-stretched sample at 3.3 % elongation. (c) Orientation index of the same samples shown in (a). The data was normalized to the value of the pre-stretched sample at 3.3 % stretching.

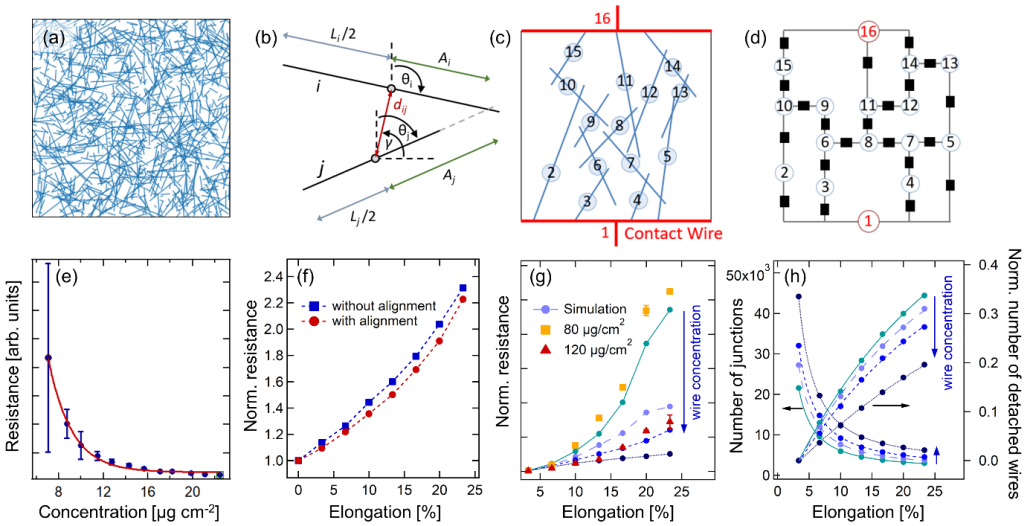

Figure 2. (a) Exemplary two-dimensional nanowire network with a size of 350 µm x 350 µm and a concentration of 10 µg cm^{-2}. The wires have random angles and positions. The lengths of the wires follow the length distributions that was determined by the analysis of SEM images of real samples. (b) Geometrical quantities, which were used in Equation (1) and (2) to check whether two wires *i* and *j* are intersecting. (c) Network of 14 wires and 2 contact wires. The resistance will be calculated between the contact wires 1 and 16. (d) Resistor network corresponding to the network shown in (b). Every node (numbered) represent a wire and every resistor (black squares) depict a wire-to-wire junction with the tunneling resistance r_{ij}. (e) Simulated resistance as a function of nanowire concentration. Each datapoint is the average of 16 simulated samples with a size of 200 µm x 200 µm. (f) Resistance change during simulated stretching conditions based on morphological changes, for elongations between 0 and 23 % and a nanowire concentration of 20 µg cm^{-2}. The wire positions were changed according to the changed sample dimensions during stretching. For the red curve, an alignment of the wires was considered. (g) Simulation of the experimental data together with the experimental data. The curves were normalized to the resistance of the pre-stretched sample at 3.3 % elongation. The simulation parameters for the critical distance distribution were $\Delta x_{ij}(A)$ = 0.2 µm, $\Delta x_{ij}(B)$ = 0.3 µm, $\Delta x_{ij}(C)$ = 0.7 µm, $\Delta x_{ij}(D)$ = 50 µm, and p_A = 75 %, p_B = 14 %, p_C = 4 %, and p_D = 7 %. The simulated effective concentrations are 18 µg cm^{-2}, 20 µg cm^{-2}, 22 µg cm^{-2} and 30 µg cm^{-2}. The blue arrow depicts the direction of increasing concentration. (h) Number of junctions and amount of detached wires (wires without undamaged junctions to other wires) for the simulations shown in (g). The curves were fitted by $y = y_0 + Ax^{-1.3}$ (number of junctions) and $y = y_0 + B\exp(-\alpha x)$ (disconnected wires).

WILEY-VCH

The table of contents entry

Flexible and conductive silver-nanowire polymer composites are studied under stretching. Morphological changes are investigated by light microscopy using the Fiber Image Network Evaluation algorithm. The conductivity of the nanowire composites during stretching is measured and simulated by a Monte-Carlo method. This work provides a model explaining the electrical behavior of nanowire composites depending on the nano-filler concentration under mechanical strain.

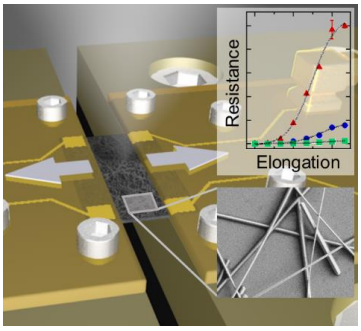

Chapter 7

Summary and Outlook

In this thesis, novel methods have been introduced for characterizing fiber networks in scientific images. These methods were applied to collagen fibers of skin and to silver-nanowires in photopolymer composites to analyze their micro-structure and their contribution to their macroscopic behavior.

The AF method was introduced to obtain the angular orientation distribution. The method is based on an adaptive Fourier filter, which is defined on a relative error constraint. Thus, the method does not require assumptions on the fiber network. Optimal evaluation parameters $\delta_{\text{cut}} = 2.1\,\%$ and $\alpha = 1.5$ were identified by using realistic, Monte-Carlo simulated greyscale fiber images. In combination with a sigmoid model of the cumulative orientation distribution, the method provides an accurate assessment of mean orientation and dispersion of fiber networks in in-vivo SHG images of dermal collagen. Since the AF method does not require assumptions about the fiber geometry it is suitable for application to any type of fiber-reinforced material.

The FINE algorithm was developed to objectively determine the number of fiber families and their properties in terms of amplitude, mean orientation and dispersion in fiber images. The FINE algorithm is able to differentiate between up to four aligned fiber families with an accuracy of 98.1 %. By applying the algorithm to an in-vivo depth-stack of dermal collagen, the transition from the papillary to the reticular dermis could quantitatively be determined by a crossover of the alignment and the orientation index at a skin depth of $85 - 90\,\mu$m. Furthermore, the assumption of collagen fibers aligning around the main tension lines of skin, the Langer lines, was verified.

A stretching device was developed to analyze the collagen fiber network of skin by SHG imaging during mechanical deformation. Stepper motors with attached force sensors allow for controlled deformations, while measuring the applied force. A lifting stage ensures a precise placement of the sample under the DermaInspect multiphoton microscope. 3D-printed components minimize displacements of the field of view due to

stretching and relaxation.
The FINE algorithm was applied to SHG images of collagen fibers of pig skin during cyclic deformation. Upon stretching, collagen fibers were found to first align within their fiber families and then orient in the direction of force. In addition, the maximum alignment of fibers was found to be determined by the maximum strain and does not increase with additional deformation cycles. Furthermore, the macroscopic mechanical behavior was associated with the alignment of collagen fibers. Differences across the samples were identified and related to the initial orientation of collagen fibers. This proof of principle study revealed that the multiphoton stretching device in combination with the FINE algorithm is a sophisticated method to relate changes of the macroscopic material behavior to the micro-structure of fiber-reinforced materials like soft biological tissue.

Silver-nanowire photopolymer composites exhibit a drastic increase in electrical line resistance upon stretching. To investigate changes in the orientation of the silver-nanowire network, light microscopy images were analyzed at every state of stretch using the FINE algorithm. Nanowires were found to be isotropically distributed and, at low concentrations, slightly align along the direction of force. It could be concluded that the alignment of nanowires is not the main factor for the drastic increase of line resistance with material elongation.

In the future, further experiments using the multiphoton stretching device will complete the micro-structural interpretation of different mechanical processes of biological tissue, like creep and strain-rate dependence. Additional in-vivo measurements on the orientation of dermal collagen fibers by the FINE algorithm will reveal its global distribution to identify main tension lines in human skin. By studying different age groups and various locations of the body, a correlation between the alignment of the collagen fiber network and continuous physiological skin deformations could be established. Output parameters of the FINE algorithm can additionally be used as input for finite element models to simulate skin or other soft tissue (see appendix A).

Appendices

A Mechanical Simulation of Skin

The finite element method (FEM) enables the prediction of various physical quantities such as mechanical deformation and stress of materials due to external factors such as mechanical forces [110]. The mechanical investigation of biological tissue is relevant for diverse medical and cosmetic topics such as stent design [111] and wrinkle formation [112]. As a consequence of its complex structure and high deformation capacity, the mechanical description of soft tissue such as skin is a large field of research [3].

A.1 Skin from a Mechanical Point of View

Skin exhibits a hierarchical structure as it is composed of three main layers: the epidermis, the dermis and the subcutis.

A.1.1 The Epidermis

The epidermis has a total thickness of about $200\,\mu$m and consists of four sublayers, which are namely, from the top to the bottom, the *stratum corneum*, *stratum granulosum*, *stratum spinosum* and *stratum basale*. Due to their rather homogeneous composition, the latter three layers are usually combined into a single layer, the *viable epidermis* [113].
The *stratum corneum* is the most outer surface of the skin and forms the main barrier against external mechanical, thermal, chemical, biological and electromagnetic influences. It consists in average of six to 47 layers of corneozytes [114] which are mainly joined by protein links called corneodesmosomes forming a very stiff layer. The Young's modulus of the stratum corneum, which is a measure for stiffness, can exceed the modulus of the underlying dermis by up to six orders of magnitude (see table A.1). Despite its small thickness of only $(8-20)\,\mu$m [115] (except for palms and soles), the stratum corneum plays a major role in the overall mechanics of the skin [113, 116]. The viable epidermis is joined to the underlying dermis through the so-called dermal-epidermal junction (DEJ), which is a 3D finger-like interface [117]. Disregarding its morphology, the viable epidermis is commonly treated as a single isotropic layer with a Young's modulus, which is an order of magnitude lower than the dermis' modulus (table A.1).

A.1.2 The Dermis

The dermis is 15-40 times as thick as the epidermis [28] and is the main load bearing structural component of the skin [34]. In contrast to the stratum corneum and viable epidermis, the dermis contains aligned load bearing fibers, including collagen and elastic fibers, resulting in an anisotropic material behavior. Skin shows a stiffer tensile response, if the direction of tension is parallel to the Langer lines [10, 16]. Lapeer *et al.* measured a ratio of 2.21:1 for the Young's modulus parallel to the Langer lines compared with a perpendicular tension. However, Jacquet *et al.* [118] measured the highest tensile strength with 45° with respect to the Langer lines. In mechanical modeling of skin, it is generally claimed that collagen fibers form two wavy families in biological tissue which are oriented symmetrically around the langer lines [8]. The high contribution of collagen fibers (approximately 70%) to the dry weight of the dermis [119], together with its hierarchical substructure, results in a high tensile strength in the large strain domain (see section 2.1). In the small strain region, the load is mainly carried by elastic fibers, which are much more elastic than collagen fibers and have the ability to fully recover from strains of up to 100% [33].

A.1.3 The Subcutis

The hypodermis (or subscutis) is the intermediate layer between the dermis and underlying muscles or bones. The subcutis contains two physiologically and anatomically different components; the interstitial tissue and the adipose tissue. The interstitial tissue is a fiber-reinforced tissue which resembles the dermis in terms of collagen and elastin fibers. The main difference to upper skin layers is the increased looseness which allows the skin to be moved laterally and axially without excessive distension [62].
Subcutaneous fat, the second component, is found over the entire body except for eyelids, nose, the ear pinna and male genitalia. Its thickness can range from a few millimeters up to several centimeters [62].
Values for the elastic modulus are rarely found in literature. Alkhouli *et al.* subdivided the non-linear stress strain curve of subcutaneous tissue in two regions of a linear stress strain behavior determining an initial Young's modulus of 1.6 ± 0.8 kPa (means $\pm$ SD) and a final of 2.9 ± 1.5 kPa [120]. Compared to the dermis, the subcutaneous tissue is up to three orders of magnitude softer (table A.1). The mechanically important constituents of the skin have been discussed in the previous section; (i) the very thin, but stiff and isotopic stratum corneum (uppermost layer), (ii) the isotropic and rather soft viable epidermis and the mechanically crucial, fibrous and anisotropic dermis.

A.2 Stress-Strain Curves

The principle of a finite element simulation is the numerical computation of differential equations defining the material behavior. The finite element method can be used for

Table A.1: Linear elastic skin parameter for the stratum corneum (SC), viable epidermis (VE), and dermis (D). The table was adopted from [113]. The ratio of the stiffness of the stratum corneum devided by the stiffness of the dermis (E_{SC}/E_D) ranges from 0.08 up to 10^5, E = Young's modulus, ν = Poisson's ratio

Layer	Linear elastic $E[MPa]$	ν	Test	Reference
SC	0.6	0.3	Human skin, *ex vivo* indentation	[121]
	1.2	0.3	Human skin, *ex vivo* indentation	[121]
	6	0.5	FE model	[122]
	8.87	0.3	Murine skin, tensile test	[123]
	10	0.3	FE model	[124]
	12	0.5	FE model	[122]
	13	0.3	Human skin, *in vivo*	[123]
	13.5	0.3	Human skin, *ex vivo* out of plane test	[125]
	57.8	0.3	Human skin, *in vivo* sonic propagation	[123]
	100	0.3	Human skin, *in vivo* indentation	[123]
	175.3	0.3	Human skin, in plane tensile test	[125]
	240	0.48	Porcine skin, rheological test	[126]
	1000	0.3	Human skin, *in vivo* indentation	[123]
VE	0	0.3	Human skin, *in vivo* suction test	[127]
	0.05	0.3	FE model	[124]
	0.05	0.3	FE model	[122]
	0.6	0.3	Human skin, *ex vivo* indentation	[121]
	7.8	0.3	Human skin, *in vivo* indentation	[123]
D	0.01	0.3	Human skin, *in vivo* indentation	[123]
	0.6	0.3	FE model	[124]
	0.6	0.5	FE model	[122]
	0.8	0.3	Human skin, *in vivo* suction test	[127]
	1	0.5	FE model	[122]
	1.6	0.3	Human skin, *in vivo* indentation	[123]

simulating thermal transfer, fluid dynamics, mass transport, electromagnetic potential or, most commonly for structural analysis [110]. Depending on the physical interaction, different material models have to be considered. Modeling the physical deformation due to external forces, like in the case of skin mechanics, requires the definition of a stress-strain $\sigma(\epsilon)$ relationship. This function describes the force, which is needed to achieve a certain relative change in length $\epsilon = \frac{\Delta L}{L}$. Typically, these curves are recorded in a tension experiment by varying the tension force (see chapter 5).

A.3 Linear elasticity

Linear elasticity is the simplest material law and describes a linear correlation between stress and strain:

$$\sigma_{lin} = E \cdot \epsilon \tag{A.1}$$

whereas E is the *Young's modulus*, which describes the stiffness of the material. Materials like rubber and soft biological tissue, which undergo large deformations are described as hyperelastic materials.

A.4 Hyperelasticity

The correlation between stress and strain of hyperelastic materials is derived from a strain-energy function ψ, which measures the amount of stored energy as the material undergoes a certain strain. Strain energy functions are defined using variables which are independent from rotations of the coordinate system. These are called invariants and derived from the Cauchy-Green deformation tensor. A detailed description can be found in [128]. Invariants I_1, I_2 and I_3 are used for describing isotropic materials, whereas higher invariants, such as I_4 are contained in anisotropic constitutive equations. However, the mechanical description of anisotropic materials will be part of future quarterly reports. The strain energy is commonly split into a deviatoric part ψ_{dev} and a volumetric $\psi_{vol}(J = \sqrt{I_3})$ part, which covers the compressibility behavior of hyperelastic materials:

$$\psi = \psi_{dev} + \psi_{vol} \tag{A.2}$$

In literature, basically two different volumetric strain energy formulations are used.

A.4.1 The Volumetric Part

The volumetric part $\psi(J)$ of hyperelastic strain energy materials describes the compressibility of the material and depends only on J. A general formulation of $\psi(J)$ is provided by [129]:

$$\psi(J) = \frac{1}{2}K(\ln(J))^2, \tag{A.3}$$

with K being the bulk modulus. For a fully incompressible solid $J = 1$ holds. For a nearly incompressible solid, $\psi(J)$ is given by a Tylor expansion of (A.3) around $J = 1$:

$$\begin{aligned} \psi(J) &\approx \frac{1}{2}K(\ln(1))^2 + K(\ln(1))(J-1) + \frac{1}{2}\left(\frac{K}{1^2} - \frac{K\ln(1)}{1^2}\right)(J-1)^2 + \mathcal{O}\left(J^3\right) \\ &\approx = \frac{1}{2}K\left(J-1\right)^2 = \frac{1}{D_1}\left(J-1\right)^2, \end{aligned} \tag{A.4}$$

where the latter representation (including D_1 as coefficient) matches the formulation which is used by the finite element software Abaqus (Dassault Systèmes, Vélizy-Villacoublay, France) [130]. An alternative approach of $\psi(J)$ was introduced in [131]:

$$\psi(J) = L_2(J - 1 - \frac{1}{2}\ln(J^2)), \tag{A.5}$$

where $L_2 = (3\mu/(1+\mu))K$ is the second Lamé constant with ν and K being the shear and the bulk modulus.[132]

A.4.2 Neo-Hookean Solids

The deviatoric part of the energy function of a neo-Hookean solid [133] is the simplest hyperelastic constitutive equation:

$$\psi_{dev,NH} = c_{10}(I_1 - 3). \tag{A.6}$$

The nearly incompressible formulation, derivation is given in appendix, using the corresponding invariant $\bar{I}_1$ reads as:

$$\bar{\psi}_{dev,NH} = c_{10}(\bar{I}_1 - 3). \tag{A.7}$$

Equation A.4 and A.7 are used by Abaqus for describing a neo-Hookean solid. Although anisotropic material models are more appropriate for modeling skin, the neo-Hookean solid is a good approximation for studying the compression of skin, since the volumetric part is the same for both formulations. This will be presented in future reports. In addition, numerous values of linear elastic parameters (Young's modulus E and Poisson's ratio ν) of the skin were published (table A.1) and can easily be translated to the neo-Hookean coefficients c_{10} and D_1 using:

$$c_{10} = \frac{E}{4(1+\nu)} \qquad D_1 = \frac{2(1-2\nu)}{E}. \tag{A.8}$$

A.4.3 Holzapfel Model

The most popular structural material model for soft tissue is the Holzapfel model [7], which later was extended for rotationally symmetric distributed fibers [8] and even for non-symmetric distributed fibers [134]. The strain energy function ψ_{HA}reads as:

$$\psi_{\mathrm{HA}}(\mathbf{H}) = \psi_g + \sum_{i=1,2} \psi_{\mathrm{f}i}(\mathbf{H}), \tag{A.9}$$

where ψ_g denotes the strain energy function of the isotropic ground matrix, which is modeled as neo-Hookean material. $\psi_{\mathrm{f}i}(\mathbf{H})$ denotes the strain energy function of the i-th fiber family. $\psi_{\mathrm{f}i}(\mathbf{H})$ is a function of the so-called structure tensor $\mathbf{H}$, which depends on fiber orientation and dispersion:

$$\mathbf{H} = \kappa\mathbf{I} + (1-3\kappa)\mathbf{a}_{0,i} \otimes \mathbf{a}_{0,i}, \tag{A.10}$$

where $\mathbf{I}$ is the identity tensor. κ is a dispersion parameter, which is a measure for the degree of anisotropy. Within this model, fiber families are assumed to exhibit a similar dispersion. $\mathbf{a}_{0,i}$ is a vector which points into the mean referential direction of the fiber family. For example, $\mathbf{a}_{0,i}$ can be determined by the mean orientation $\bar{\theta}_i$ of fiber families determined by the FINE algorithm (chapter 4).
The dispersion parameter κ is determined from the fiber orientation distribution $P(\theta)$:

$$\kappa = \frac{1}{4}\int_0^{\pi} P(\theta)\sin^3(\theta)\mathrm{d}\theta, \tag{A.11}$$

which is modelled by the semi-circular von-Mises distribution $P(\theta) = P_{\mathrm{vm}}(\theta)$:

$$P_{\mathrm{vm}}(\theta) = 4\sqrt{\frac{k}{2\pi}}\frac{1}{\mathrm{erfi}(\sqrt{2k})}\exp\left[k(\cos 2\theta + 1)\right], \tag{A.12}$$

where $\mathrm{erfi}(x)$ denotes the imaginary error function $\mathrm{erfi}(x) = -\mathrm{i}\,\mathrm{erf}(x)$. Note that this definition of the von-Mises function differs from equation (3.1) in the form of their

normalization factor. The relationship between both definitions is given in [8]. So far, three different quantities have been introduced describing the dispersion of the collagen fiber network. These are namely, the von-Mises dispersion parameter k, the sigmoidal dispersion b and the dispersion parameter κ. k and b are related by the transfer function of equation (3.53). In order to derive the relation between κ and k, the integral of equation (A.11) is solved.
First, $P_{\mathrm{vm}}(\theta)$ is expressed as:

$$P_{\mathrm{vm}}(\theta) = \underbrace{4\sqrt{\frac{k}{2\pi}}\frac{1}{\operatorname{erfi}(\sqrt{2k})}}_{\equiv A} \exp\left[k(\cos 2\theta + 1)\right]. \tag{A.13}$$

Using $\cos 2\theta = \cos^2\theta + \sin^2\theta = 2\cos^2\theta - 1$ equation (A.13) follows as:

$$\rho(\theta) = A \cdot \exp\left[2k(\cos^2\theta)\right]. \tag{A.14}$$

the integral (A.11) then reads as:

$$\kappa = \frac{A}{4}\int_0^{\pi} \exp\left[2k(\cos^2\theta)\right] \cdot \sin\theta \underbrace{\sin^2\theta}_{=1-\cos^2\theta} \mathrm{d}\theta \tag{A.15}$$

Substituting $\cos\theta = x$, $\cos^2\theta = x^2$ and $\mathrm{d}\theta = -\frac{\mathrm{d}x}{\sin\theta}$ yields:

$$\kappa = \frac{A}{4}\int_{-1}^{1}\left(1-x^2\right)\exp\left[2kx^2\right]\mathrm{d}x = \frac{A}{4}\left(\underbrace{\int_{-1}^{1}\exp\left[2kx^2\right]\mathrm{d}x}_{\mathrm{I}} - \underbrace{\int_{-1}^{1}x^2\exp\left[2kx^2\right]\mathrm{d}x}_{\mathrm{II}}\right) \tag{A.16}$$

Integral **I** reads as:

$$\int_{-1}^{1}\exp\left[2kx^2\right]\mathrm{d}x = \sqrt{\frac{\pi}{2k}}\cdot\operatorname{erfi}(\sqrt{2k}), \tag{A.17}$$

while Integral **II** follows as:

$$\int_{-1}^{1}\underbrace{x}_{u}\cdot\underbrace{x\exp\left[2kx^2\right]}_{v'}\mathrm{d}x = \frac{x}{4k}\exp\left[2kx^2\right]\Big|_{-1}^{1} - \frac{1}{4k}\int_{-1}^{1}\exp\left[2kx^2\right]\mathrm{d}x \tag{A.18}$$

$$= \frac{1}{4k}\cdot\left(2\exp\left[2k\right] - \sqrt{\frac{\pi}{2k}}\operatorname{erfi}(\sqrt{2k})\right). \tag{A.19}$$

Inserting integrals **I** and **II** in equation (A.16) yields:

$$\kappa = \frac{A}{4}\cdot\left[\sqrt{\frac{\pi}{2k}}\operatorname{erfi}(\sqrt{2k})(1+\frac{1}{4k}) - \frac{2}{4k}\exp\left[2k\right]\right] \tag{A.20}$$

$$= \frac{1}{2} + \frac{1}{8k} - \frac{1}{2k}\sqrt{\frac{k}{2\pi}}\frac{\exp\left[2k\right]}{\operatorname{erfi}(\sqrt{2k})}. \tag{A.21}$$

Using equation (A.21), the dispersion of fiber families together with their mean orientations, determined by the FINE algorithm, can be inserted in the Holzapfel model of equation (A.9) to simulate soft biological tissue like skin.

B Matrix implementation

The performance of code written in MATLAB benefits from using matrices instead of *for*-loops [135]. Thus, the matrix representation of the discrete Fourier transform and its uncertainty propagation is used for an efficient implementation.

B.1 Discrete Fourier Transform

Starting from the discrete Fourier transform $I(x,y) \to \mathcal{F}[I(x,y)] = \hat{I}(u,v)$ of an image $I(x,y)$ with $x \in [0, X-1]$ and $y \in [0, Y-1]$:

$$\hat{I}(u,v) = \sum_{y=0}^{Y-1} \sum_{x=0}^{X-1} I(x,y) \cdot e^{-2\pi i \left(\frac{x}{X}u + \frac{y}{Y}v\right)} \quad , \tag{B.22}$$

The respective matrix representation of the $X \times Y$ image I then reads as:

$$\hat{I} = W(w_x, X) \cdot I \cdot W(w_y, Y) \qquad \text{with} \qquad w_x = e^{-2\pi \mathrm{i}/X},\ w_y = e^{-2\pi \mathrm{i}/Y} \tag{B.23}$$

and where

$$W(w,X) = \begin{bmatrix} 1 & 1 & 1 & \dots & 1 \\ 1 & w^1 & w^2 & \dots & w^{(X-1)} \\ 1 & w^2 & w^4 & \dots & w^{2(X-1)} \\ \vdots & \vdots & \vdots & \ddots & \vdots \\ 1 & w^{(X-1)} & w^{2(X-1)} & \dots & w^{(X-1)(X-1)} \end{bmatrix} \tag{B.24}$$

is a $X \cdot X$ Fourier transform matrix.

B.2 Uncertainty of the Discrete Fourier Transform

The equations of the uncertainty of the discrete Fourier transform were derived in section 3.4.2.1 of chapter 3:

$$\Delta \operatorname{Re}[\hat{I}(u,v)] = \sqrt{\sum_{y=0}^{Y-1} \sum_{x=0}^{X-1} \Delta I^2(x,y) \cos^2\left(2\pi\left(\frac{x}{X}u + \frac{y}{Y}v\right)\right)}, \tag{B.25}$$

$$\Delta \operatorname{Im}[\hat{I}(u,v)] = \sqrt{\sum_{y=0}^{Y-1} \sum_{x=0}^{X-1} \Delta I^2(x,y) \sin^2\left(2\pi\left(\frac{x}{X}u + \frac{y}{Y}v\right)\right)}. \tag{B.26}$$

$$\Delta \hat{I}_{\operatorname{Re}\operatorname{Im}}(u,v) = \sqrt{\sum_{y=0}^{Y-1} \sum_{x=0}^{X-1} \Delta I^2(x,y) \sin\left(2\pi\left(\frac{x}{X}u + \frac{y}{Y}v\right)\right) \cos\left(2\pi\left(\frac{x}{X}u + \frac{y}{Y}v\right)\right)}. \tag{B.27}$$

In order to express equations (B.25 - B.27) as a multiplication of matrices similar to equation (B.23), the summations over both dimensions need to be separated. Hence, the

relations $\cos(A+B) = \cos(A)\cos(B) - \sin(A)\sin(B)$ and $\sin(A+B) = \sin(A)\cos(B) + \cos(A)\sin(B)$ are employed:

$$\Delta \operatorname{Re}[\hat{I}(u,v)]^2 = \sum_{y=0}^{Y-1}\sum_{x=0}^{X-1} \Delta I^2(x,y)\,[c_x c_y - s_x s_y]^2 \tag{B.28}$$

$$= \sum_{y=0}^{Y-1}\sum_{x=0}^{X-1} \Delta I^2(x,y)\left[c_x^2 c_y^2 - 2c_x c_y s_x s_y + s_x^2 s_y^2\right] \tag{B.29}$$

$$\Delta \operatorname{Im}[\hat{I}(u,v)]^2 = \sum_{y=0}^{Y-1}\sum_{x=0}^{X-1} \Delta I^2(x,y)\,[s_x c_y + s_y c_x]^2 \tag{B.30}$$

$$= \sum_{y=0}^{Y-1}\sum_{x=0}^{X-1} \Delta I^2(x,y)\left[s_x^2 c_y^2 + 2s_x c_y s_y c_x + s_y^2 c_x^2\right] \tag{B.31}$$

$$\Delta \hat{I}_{\operatorname{Re}\operatorname{Im}}(u,v)^2 = \sum_{y=0}^{Y-1}\sum_{x=0}^{X-1} \Delta I^2(x,y)\,[c_x c_y - s_x s_y]\cdot[s_x c_y + s_y c_x] \tag{B.32}$$

$$= \sum_{y=0}^{Y-1}\sum_{x=0}^{X-1} \Delta I^2(x,y)\left[c_y^2 c_x s_x + c_x^2 c_y s_y - s_x^2 s_y c_y - s_y^2 s_x c_x\right] \tag{B.33}$$

with $s_x = \sin(2\pi \cdot ux/X)$, $s_y = \sin(2\pi \cdot vy/Y)$, $c_x = \cos(2\pi \cdot ux/X)$ and $c_y = \cos(2\pi \cdot vy/Y)$. The respective matrix representations follow as:

$$\Delta \operatorname{Re}[\hat{I}]^2 = W_c^2(Y)\Delta I^2 W_c^2(X) - 2(W_c(Y)W_s(Y))\Delta I^2(W_c(X)W_s(X)) \tag{B.34}$$
$$+ W_s^2(Y)\Delta I^2 W_s^2(X)$$

$$\Delta \operatorname{Im}[\hat{I}]^2 = W_c^2(Y)\Delta I^2 W_s^2(X) + 2(W_c(Y)\odot W_s(Y))\Delta I^2(W_c(X)\odot W_s(X)) \tag{B.35}$$
$$+ W_s^2(Y)\Delta I^2 W_c^2(X)$$

$$\Delta \hat{I}_{\operatorname{Re}\operatorname{Im}}(u,v)^2 = (W_c(Y)\odot W_s(Y))\Delta I^2(W_c^2(X) - W_s^2(X)) \tag{B.36}$$
$$+ (W_s^2(Y) - W_c^2(Y))\Delta I^2(W_s(X)\odot W_c(X)),$$

where the operator $\odot$ denotes the elementwise multiplication. The corresponding matrices are defined as:

$$W_c(X) = \begin{bmatrix} 1 & 1 & 1 & \dots & 1 \\ 1 & \cos(2\pi/X) & \cos(4\pi/X) & \dots & \cos(2(X-1)\pi/X) \\ 1 & \cos(4\pi/X) & \cos(8\pi/X) & \dots & \cos(4(X-1)\pi/X) \\ \vdots & \vdots & \vdots & \ddots & \vdots \\ 1 & \cos(2(X-1)\pi/X) & \cos(4(X-1)\pi/X) & \dots & \cos(2(X-1)(X-1)\pi/X) \end{bmatrix}$$

and

$$W_s(X) = \begin{bmatrix} 1 & 1 & 1 & \dots & 1 \\ 1 & \sin(2\pi/X) & \sin(4\pi/X) & \dots & \sin(2(X-1)\pi/X) \\ 1 & \sin(4\pi/X) & \sin(8\pi/X) & \dots & \sin(4(X-1)\pi/X) \\ \vdots & \vdots & \vdots & \ddots & \vdots \\ 1 & \sin(2(X-1)\pi/X) & \sin(4(X-1)\pi/X) & \dots & \sin(2(X-1)(X-1)\pi/X) \end{bmatrix}$$

C Programming

C.1 Fiber Orientation Framework

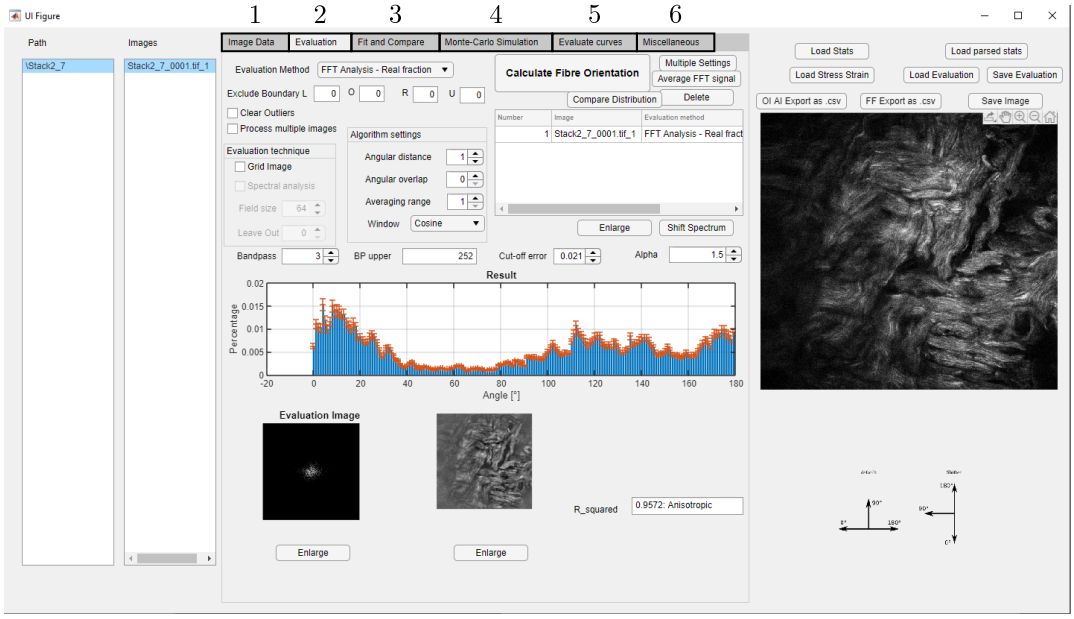

Figure C.1: Screenshot of the graphical user interface of the image processing framework in the field of fiber orientations.

The entire image processing framework is written in MATLAB [136] using the image processing toolbox [137] and the curve fitting toolbox [138]. Methods of chapters 3 and 4 are incorporated in a graphical user interface (GUI), shown in figure C.1. It allows the user to perform multiple tasks in the field of image orientations. The GUI is sectioned into two *ListBoxes* for data handling, an image preview window, where the currently selected image is shown and the main part which covers diverse responsibilities which are organized in different tabs:

1. **Image Data**: Images can be either imported by a manual selection or by an automatic recursive through the specified folder and sub-folders. In order to ensure that datasets are still distinguishable after data import, datasets are sorted depending on their parent folder.

2. **Evaluation**: The evaluation tab covers the settings for different approaches to quantify the angular orientation distribution in terms of angular spacing, image cropping, windowing functions and method-related settings. The methods of Schriefl *et al.* [84], Ní Annaidh *et al.* [6], Morrill *et al.* [21] and Witte *et al.* [54] are implemented. Evaluation images and plots like filtered power spectra, the related inverse Fourier transforms as well as the angular orientation spectra give insights into the results and properties of each method.

3. **Fit and compare**: The fit and compare tab allows for a quantification of the angular orientation distribution and the respective cumulative distribution. The angular orientation can be quantified using a von-Mises function like in [6, 21, 84, 139]. In addition different fit methods based on the cumulative orientation distribution are covered including the fit of a single sigmoid function as proposed in [54] and the FINE algorithm. In addition, derived parameter like the orientation index (OI) and the alignment index (AI) are calculated. Multiple fit results can be combined to a dataset in order to visualize the evolution of parameters, e.g. as a function of measurement depth or material stretch.

4. **Monte-Carlo Simulation**: The Monte-Carlo Simulation tab covers a section to create artificial fiber images using the Monte-Carlo approach of section 4.1. The user can specify the number of fiber families, the number of contributing fibers, their mean orientation, dispersion as well as the fiber width and length.

5. **Evaluate Curves**: The evaluate curves tab is implemented for handling the parameters that have been combined to a dataset. Datasets can be visualized, saved and reloaded. Additionally, datasets can be linked to stress strain curves.

6. **Miscellaneous**: The miscellaneous tab includes other functions like plotting stress-strain curves.

The entire state of the GUI can be saved by *Save Evaluation* and loaded by *Load Evaluation*. Data points that have been combined to a curve can be exported to a *comma separated text file* by *OI AI Export as .csv* (OI and AI export) and *FF Export as .csv* (detailed export of fiber families).

C.2 Fiber Tracing App

A screenshot of the fiber tracing app, written in MATLAB [136], is shown in figure C.2. The purpose of this application is the manual tracing of fibers in greyscale images. After loading an image, the user can trace single fibers by means of multiple straight line segments. The application was used in chapter 3 to compare the AF method against a manual segmentation.

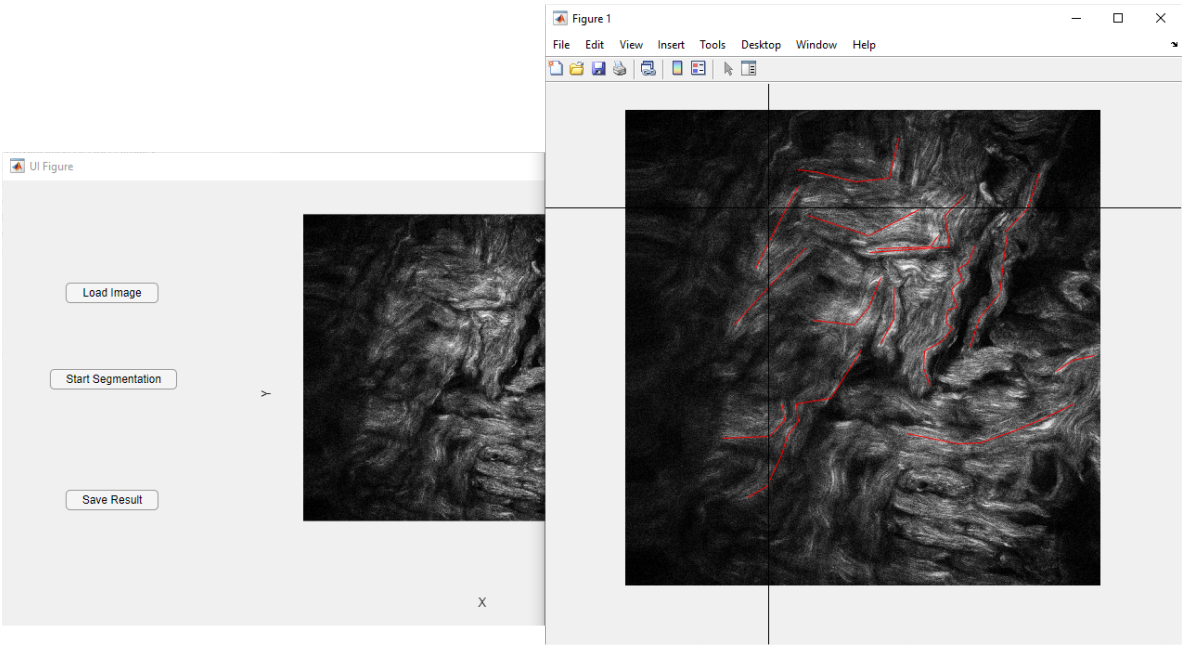

Figure C.2: Screenshot of the graphical user interface for the manual tracing of fibers in images.

C.3 Stretching Device GUI

Figure C.3 shows a screenshot of the GUI to control the stretching device. It is used to perform the stretching experiments of chapter 5. Its main functionalities can be summarized into the following segments:

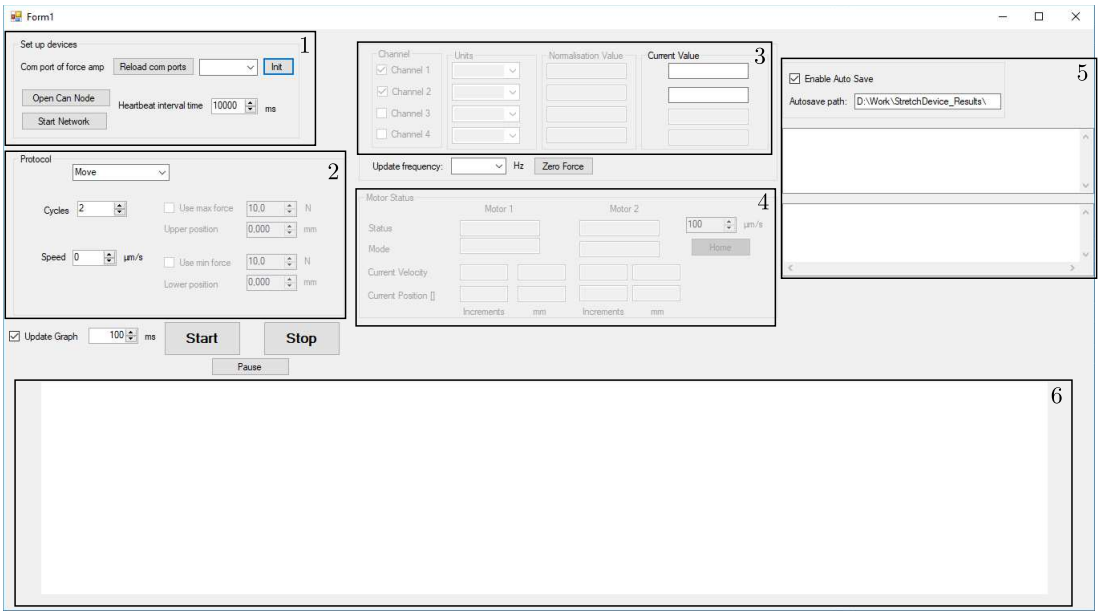

Figure C.3: Screenshot of the user interface of the stretching device.

1. **Set up devices**: Section to specify the COM port of the force amplifier to initialize it. In addition, the communication to the CANopen network of the two motor control units is established. The heartbeat interval time specifies the time spacing of messages from each node signaling their existence.

2. **Measurement protocol**: Section to define the type of protocol including *move* (to a position), *stress-strain*, *cyclic stress-strain*, *custom protocol*. Within the panel, the user can specify the minimum and maximum turning points of the measurement protocol, each either as position of measured force.

3. **Force sensor setup**: The force sensor setup sections allows for calibrating the force sensors as well as zeroing the measured force. Once the amplifier is initialized, force values are displayed according to the specified update frequency. Up to four force sensors are supported.

4. **Motor status**: The motor status section gives information about the current status and the mode of the motors. Current velocity and motor position are displayed as well. A *home* button allows for a reference drive.

5. **Logging section**: The logging section keeps track of the events, which are occurring. Such events can either for example represent a status change of the motors or the start of a measurement. Logged events are automatically saved in the defined directory upon closing the GUI.

6. **Graphical display**: In this section, the measured force is displayed live. The time interval where values are updated can be specified.

Bibliography

1. M. Hassanpour, P. Shafigh, and H. B. Mahmud. Lightweight aggregate concrete fiber reinforcement - A review, 2012. ISSN 09500618.

2. P. W. Manders and M. G. Bader. The strength of hybrid glass/carbon fibre composites - Part 1 Failure strain enhancement and failure mode. *J. Mater. Sci.*, 16(8):2233–2245, 1981. ISSN 00222461. doi: 10.1007/BF00542386.

3. J. M. Benítez and F. J. Montáns. The mechanical behavior of skin: Structures and models for the finite element analysis. *Comput. Struct.*, 190:75–107, 2017. ISSN 00457949. doi: 10.1016/j.compstruc.2017.05.003. URL `http://linkinghub.elsevier.com/retrieve/pii/S0045794916314183`.

4. T. E. Glier, L. Akinsinde, M. Paufler, et al. Functional Printing of Conductive Silver-Nanowire Photopolymer Composites. *Sci. Rep.*, 9(1), dec 2019. ISSN 20452322. doi: 10.1038/s41598-019-42841-3.

5. T. Ackermann, R. Neuhaus, and S. Roth. The effect of rod orientation on electrical anisotropy in silver nanowire networks for ultra-transparent electrodes. *Sci. Rep.*, 2016. ISSN 20452322. doi: 10.1038/srep34289.

6. A. Ní Annaidh, K. Bruyère, M. Destrade, M. D. Gilchrist, and M. Otténio. Characterization of the anisotropic mechanical properties of excised human skin. *J. Mech. Behav. Biomed. Mater.*, 5(1):139–148, 2012. ISSN 17516161. doi: 10.1016/j.jmbbm.2011.08.016. URL `http://dx.doi.org/10.1016/j.jmbbm.2011.08.016`.

7. G. A. Holzapfel, T. G. Gasser, and R. W. Ogden. A new constitutive framework for arterial wall mechanics and a comparative study of material models. *J. Elast.*, 61:1–48, 2000. doi: 10.1023/a:1010835316564.

8. T. C. Gasser, R. W. Ogden, and G. A. Holzapfel. Hyperelastic modelling of arterial layers with distributed collagen fibre orientations. *J. R. Soc. Interface*, 3 (6):15–35, 2006. ISSN 17425662. doi: 10.1098/rsif.2005.0073. URL `http://rsif.royalsocietypublishing.org/cgi/doi/10.1098/rsif.2005.0073`.

9. R. Rezakhaniha, A. Agianniotis, J. T. C. Schrauwen, et al. Experimental investigation of collagen waviness and orientation in the arterial adventitia using confocal

laser scanning microscopy. *Biomech. Model. Mechanobiol.*, 11(3-4):461–473, 2012. ISSN 16177959. doi: 10.1007/s10237-011-0325-z.

10. W. Yang, V. R. Sherman, B. Gludovatz, et al. On the tear resistance of skin. *Nat. Commun.*, 6:6649, 2015. ISSN 2041-1723. doi: 10.1038/ncomms7649. URL `http://www.nature.com/doifinder/10.1038/ncomms7649`.

11. M. Ueda, S. Saito, T. Murata, et al. Combined multiphoton imaging and biaxial tissue extension for quantitative analysis of geometric fiber organization in human reticular dermis. *Sci. Rep.*, 9(1):1–12, 2019. ISSN 2045-2322. doi: 10.1038/s41598-019-47213-5.

12. S. Bancelin, B. Lynch, C. Bonod-Bidaud, et al. Ex vivo multiscale quantitation of skin biomechanics in wild-type and genetically-modified mice using multiphoton microscopy. *Sci. Rep.*, 5(December):1–14, 2015. ISSN 20452322. doi: 10.1038/srep17635. URL `http://dx.doi.org/10.1038/srep17635`.

13. M. D. Ridge and V. Wright. The directional effects of skin. A bio-engineering study of skin with particular reference to Langer's lines. *J. Invest. Dermatol.*, 46(4):341–346, 1966. ISSN 0022202X. doi: 10.1038/jid.1966.54. URL `http://dx.doi.org/10.1038/jid.1966.54`.

14. K. Langer. On the anatomy and physiology of the skin: II. Skin Tension. *Br. J. Plast. Surg.*, 31(2):93–106, 1978. ISSN 00071226. doi: 10.1016/S0007-1226(78)90056-5.

15. R. J. Lapeer, P. D. Gasson, and V. Karri. Simulating plastic surgery: From human skin tensile tests, through hyperelastic finite element models to real-time haptics. *Prog. Biophys. Mol. Biol.*, 103(2-3):208–216, 2010. ISSN 00796107. doi: 10.1016/j.pbiomolbio.2010.09.013. URL `http://dx.doi.org/10.1016/j.pbiomolbio.2010.09.013`.

16. A. N. Annaidh, Karine Bruyère, M. Destrade, et al. Automated estimation of collagen fibre dispersion in the dermis and its contribution to the anisotropic behaviour of skin. *Ann. Biomed. Eng.*, 40(8):1666–1678, 2012. ISSN 00906964. doi: 10.1007/s10439-012-0542-3.

17. I. A. Brown. Scanning electron microscopy of human dermal fibrous tissue. *Ups. J. Med. Sci.*, 77(1):3–7, 1972. ISSN 03009734. doi: 10.1517/03009734000000001.

18. R. M. Lavker, P. Zheng, and G. Dong. Aged skin: A study by light, transmission electron, and scanning electron microscopy. *J. Invest. Dermatol.*, 88(3 SUPPL.):44–51, 1987. ISSN 0022202X. doi: 10.1038/jid.1987.9. URL `http://dx.doi.org/10.1038/jid.1987.9`.

19. G. E. Pierard and C. M. Lapiere. Microanatomy of the dermis in relation to relaxed skin tension lines and Langer's lines. *Am. J. Dermatopathol.*, 1987. ISSN 01931091. doi: 10.1097/00000372-198706000-00007.

20. A. J. Schriefl, A. J. Reinisch, S. Sankaran, D. M. Pierce, and G. A. Holzapfel. Quantitative assessment of collagen fibre orientations from two-dimensional images of soft biological tissues. *J. R. Soc. Interface*, 9(76):3081–3093, 2012. ISSN 1742-5689. doi: 10.1098/rsif.2012.0339. URL `http://rsif.royalsocietypublishing.org/cgi/doi/10.1098/rsif.2012.0339`.

21. E. E. Morrill, A. N. Tulepbergenov, C. J. Stender, et al. A validated software application to measure fiber organization in soft tissue. *Biomech. Model. Mechanobiol.*, 15(6):1467–1478, 2016. ISSN 16177940. doi: 10.1007/s10237-016-0776-3.

22. V. Arumugam, M. D. Naresh, and R. Sanjeevi. Effect of strain rate on the fracture behaviour of skin. *J. Biosci.*, 1994. ISSN 02505991. doi: 10.1007/BF02716820.

23. P. P. Purslow, T. J. Wess, and D. W. Hukins. Collagen orientation and molecular spacing during creep and stress-relaxation in soft connective tissues. *J. Exp. Biol.*, 201(1):135–142, 1998. ISSN 00220949.

24. M. L. Crichton, B. C. Donose, X. Chen, et al. The viscoelastic, hyperelastic and scale dependent behaviour of freshly excised individual skin layers. *Biomaterials*, 32(20):4670–4681, 2011. ISSN 01429612. doi: 10.1016/j.biomaterials.2011.03.012. URL `http://dx.doi.org/10.1016/j.biomaterials.2011.03.012`.

25. W. L. Wong, T. J. Joyce, and K. L. Goh. Resolving the viscoelasticity and anisotropy dependence of the mechanical properties of skin from a porcine model. *Biomech. Model. Mechanobiol.*, 15(2):433–446, 2016. ISSN 16177940. doi: 10.1007/s10237-015-0700-2.

26. R. Oftadeh, B. K. Connizzo, H. T. Nia, C. Ortiz, and A. J. Grodzinsky. Biological connective tissues exhibit viscoelastic and poroelastic behavior at different frequency regimes: Application to tendon and skin biophysics. *Acta Biomater.*, 70 (March):249–259, 2018. ISSN 18787568. doi: 10.1016/j.actbio.2018.01.041. URL `https://doi.org/10.1016/j.actbio.2018.01.041`.

27. D. Remache, M. Caliez, M. Gratton, and S. Dos Santos. The effects of cyclic tensile and stress-relaxation tests on porcine skin. *J. Mech. Behav. Biomed. Mater.*, 77 (August 2017):242–249, 2018. ISSN 18780180. doi: 10.1016/j.jmbbm.2017.09.009. URL `https://doi.org/10.1016/j.jmbbm.2017.09.009`.

28. H. Shimizu. Shimizu's Textbook of Dermatology. *Nursing (Lond).*, 2007.

29. J. Sandby-Møller, T. Poulsen, and H. C. Wulf. Epidermal Thickness at Different Body Sites: Relationship to Age, Gender, Pigmentation, Blood Content, Skin Type and Smoking Habits. *Acta Derm. Venereol.*, 83(6):410–413, 2003. ISSN 00015555. doi: 10.1080/00015550310015419.

30. C. Griffiths, J. Barker, T. Bleiker, R. Chalmers, and D. Creamer. *Rook's Textbook of Dermatology*. Wiley-Blackwell, 9 edition, 2016. ISBN 978-1-118-44119-0.

31. S. Nesbitt, W. Scott, J. Macione, and S. Kotha. Collagen Fibrils in Skin Orient in the Direction of Applied Uniaxial Load in Proportion to Stress while Exhibiting Differential Strains around Hair Follicles. *Materials (Basel).*, 8(4): 1841–1857, 2015. ISSN 1996-1944. doi: 10.3390/ma8041841. URL `http://www.mdpi.com/1996-1944/8/4/1841/`.

32. S. Ricard-Blum. The Collagen Family. *Cold Spring Harb. Perspect. Biol.*, 2011. ISSN 19430264. doi: 10.1101/cshperspect.a004978.

33. J. Gosline, M. Lillie, E. Carrington, et al. Elastic proteins: biological roles and mechanical properties. *Philos. Trans. R. Soc. Lond. B. Biol. Sci.*, 357(1418):121–32, feb 2002. ISSN 0962-8436. doi: 10.1098/rstb.2001.1022. URL `http://www.ncbi.nlm.nih.gov/pubmed/11911769http://www.pubmedcentral.nih.gov/articlerender.fcgi?artid=PMC1692928`.

34. G. Limbert. Mathematical and computational modelling of skin biophysics: A review. *Proc. R. Soc. A Math. Phys. Eng. Sci.*, 473(2203):1–20, 2017. ISSN 14712946. doi: 10.1098/rspa.2017.0257.

35. T. Yasui, Y. Takahashi, M. Ito, S. Fukushima, and T. Araki. Ex vivo and in vivo second-harmonic-generation imaging of dermal collagen fiber in skin: comparison of imaging characteristics between mode-locked Cr:forsterite and Ti:sapphire lasers. *Appl. Opt.*, 48(180):D88–D95, 2009. ISSN 0003-6935. doi: 10.1364/AO.48.000D88.

36. X. Jiang, J. Zhong, Y. Liu, et al. Two-photon fluorescence and second-harmonic generation imaging of collagen in human tissue based on multiphoton microscopy. *Scanning*, 2011. ISSN 01610457. doi: 10.1002/sca.20219.

37. S. Wu, H. Li, H. Yang, et al. Quantitative analysis on collagen morphology in aging skin based on multiphoton microscopy. *J. Biomed. Opt.*, 2011. ISSN 10833668. doi: 10.1117/1.3565439.

38. X. Chen, O. Nadiarynkh, S. Plotnikov, and P. J. Campagnola. Second harmonic generation microscopy for quantitative analysis of collagen fibrillar structure. *Nat. Protoc.*, 7(4):654–669, 2012. ISSN 1754-2189. doi: 10.1038/nprot.2012.009. URL `http://www.nature.com/doifinder/10.1038/nprot.2012.009`.

39. T. Yasui, M. Yonetsu, R. Tanaka, et al. ¡i¿In vivo¡/i¿ observation of age-related structural changes of dermal collagen in human facial skin using collagen-sensitive second harmonic generation microscope equipped with 1250-nm mode-locked Cr:Forsterite laser. *J. Biomed. Opt.*, 2012. ISSN 1083-3668. doi: 10.1117/1.JBO.18.3.031108.

40. Y. Mega, M. Robitaille, R. Zareian, et al. Quantification of lamellar orientation in corneal collagen using second harmonic generation images. *Opt. Lett.*, 37(16):3312–4, aug 2012. ISSN 1539-4794. URL `http://www.ncbi.nlm.nih.gov/pubmed/23381241http://www.pubmedcentral.nih.gov/articlerender.fcgi?artid=PMC3784649`.

41. S. Puschmann, C.-D. Rahn, H. Wenck, S. Gallinat, and F. Fischer. Approach to quantify human dermal skin aging using multiphoton laser scanning microscopy. *J. Biomed. Opt.*, 17(3):036005, 2012. ISSN 10833668. doi: 10.1117/1.JBO.17.3.036005. URL `http://biomedicaloptics.spiedigitallibrary.org/article.aspx?doi=10.1117/1.JBO.17.3.036005`.

42. R. Tanaka, S.-i. Fukushima, K. Sasaki, et al. ¡i¿In vivo¡/i¿ visualization of dermal collagen fiber in skin burn by collagen-sensitive second-harmonic-generation microscopy. *J. Biomed. Opt.*, 2013. ISSN 1083-3668. doi: 10.1117/1.JBO.18.6.061231.

43. Y.-H. Liao, W.-C. Kuo, S.-Y. Chou, et al. Quantitative analysis of intrinsic skin aging in dermal papillae by in vivo harmonic generation microscopy. *Biomed. Opt. Express*, 5(9):3266, 2014. ISSN 2156-7085. doi: 10.1364/BOE.5.003266. URL `https://www.osapublishing.org/boe/abstract.cfm?uri=boe-5-9-3266`.

44. J.-C. Pittet, O. Freis, M.-D. Vazquez-Duchêne, G. Périé, and G. Pauly. Evaluation of Elastin/Collagen Content in Human Dermis in-Vivo by Multiphoton Tomography—Variation with Depth and Correlation with Aging. *Cosmetics*, 2014. ISSN 2079-9284. doi: 10.3390/cosmetics1030211.

45. L. V. Johnson, M. L. Walsh, B. J. Bockus, and L. B. Chen. Monitoring of relative mitochondrial membrane potential in living cells by fluorescence microscopy. *J. Cell Biol.*, 88(3):526–535, 1981. ISSN 00219525. doi: 10.1083/jcb.88.3.526.

46. D. Taylor and Y. Wang. Fluorescence microscopy of living cells in culture. Part B. Quantitative fluorescence microscopy–imaging and spectroscopy. *Methods Cell Biol.*, 30:1–498, 1989. ISSN 0091679X.

47. J. W. Lichtman and J. A. Conchello. Fluorescence microscopy, 2005. ISSN 15487091.

48. B. R. Masters and P. T. C. So. Confocal microscopy and multi-photon excitation microscopy of human skin in vivo. *Opt. Express*, 8(1):2, 2001. ISSN 1094-4087. doi: 10.1364/oe.8.000002.

49. R. Bückle, K. König, I. Riemann, et al. 5D-intravital tomography as a novel tool for non-invasive in-vivo analysis of human skin. In *Adv. Biomed. Clin. Diagnostic Syst. VIII*, 2010. doi: 10.1117/12.841861.

50. V. Lutz, M. Sattler, S. Gallinat, et al. Characterization of fibrillar collagen types using multi-dimensional multiphoton laser scanning microscopy. *Int. J. Cosmet. Sci.*, 34(2):209–215, 2012. ISSN 01425463. doi: 10.1111/j.1468-2494.2012.00705.x.

51. S. Puschmann, C.-D. Rahn, H. Wenck, S. Gallinat, and F. Fischer. Approach to quantify human dermal skin aging using multiphoton laser scanning microscopy. *J. Biomed. Opt.*, 17(3):036005, 2012. ISSN 10833668. doi: 10.1117/1.JBO.17.3.036005. URL `http://biomedicaloptics.spiedigitallibrary.org/article.aspx?doi=10.1117/1.JBO.17.3.036005`.

52. S. Puschmann, C.-D. Rahn, H. Wenck, S. Gallinat, and F. Fischer. In vivo quantification of human dermal skin aging using SHG and autofluorescence. *Multimodal Biomed. Imaging VII*, 8216:821608, 2012. doi: 10.1117/12.906460.

53. D. Mellem, M. Sattler, S. Pagel-Wolff, et al. Fragmentation of the mitochondrial network in skin in vivo. *PLoS One*, 12(6):1–10curation, 2017. ISSN 19326203. doi: 10.1371/journal.pone.0174469.

54. M. Witte, S. Jaspers, H. Wenck, M. Rübhausen, and F. Fischer. Noise reduction and quantification of fiber orientations in greyscale images. *PLoS One*, pages 1–21, 2020. doi: 10.1371/journal.pone.0227534.

55. J. C. Maxwell. A dynamical theory of the electromagnetic field. *Philos. Trans. R. Soc. London*, 119(2986):125–127, 1865. ISSN 00280836. doi: 10.1038/119125a0.

56. R. W. Boyd. *Nonlinear Optics*, volume 53. 2007. ISBN 9788578110796. doi: 10.1017/CBO9781107415324.004.

57. R. Bonifacio. Theory of Optical Maser Amplifiers. *IEEE J. Quantum Electron.*, QE-1(4):169–178, 1965. ISSN 15581713. doi: 10.1109/JQE.1965.1072212.

58. R. LaComb, O. Nadiarnykh, S. S. Townsend, and P. J. Campagnola. Phase matching considerations in second harmonic generation from tissues: Effects on emission directionality, conversion efficiency and observed morphology. *Opt. Commun.*, 281 (7):1823–1832, 2008. ISSN 00304018. doi: 10.1016/j.optcom.2007.10.040.

59. J. Mertz and L. Moreaux. Second-harmonic generation by focused excitation of inhomogeneously distributed scatterers. *Opt. Commun.*, 196(1-6):325–330, 2001. ISSN 00304018. doi: 10.1016/S0030-4018(01)01403-1.

60. L. Moreaux, O. Sandre, and J. Mertz. Membrane imaging by second-harmonic generation microscopy. *J. Opt. Soc. Am. B*, 2000. ISSN 0740-3224. doi: 10.1364/josab.17.001685.

61. R. M. Williams, W. R. Zipfel, and W. W. Webb. Interpreting second-harmonic generation images of collagen I fibrils. *Biophys. J.*, 88(2):1377–1386, 2005. ISSN 00063495. doi: 10.1529/biophysj.104.047308. URL `http://dx.doi.org/10.1529/biophysj.104.047308`.

62. P. Humbert, H. Maibach, F. Fanian, and P. Agache. *Measuring the Skin*, volume 49. 2004. ISBN 3540017712. doi: 10.1007/978-3-319-26594-0_40-1.

63. S. P. Tai, T. H. Tsai, W. J. Lee, et al. Optical biopsy of human skin with backward-collected optical harmonics signals. *Opt. InfoBase Conf. Pap.*, 13(20): 946–952, 2005. ISSN 21622701.

64. M. J. Koehler, K. König, P. Elsner, R. Bückle, and M. Kaatz. In vivo assessment of human skin aging by multiphoton laser scanning tomography. *Opt. Lett.*, 31 (19):2879, 2006. ISSN 0146-9592. doi: 10.1364/ol.31.002879.

65. R. Bückle, K. König, I. Riemann, et al. 5D-intravital tomography as a novel tool for non-invasive in-vivo analysis of human skin. In *Adv. Biomed. Clin. Diagnostic Syst. VIII*, 2010. doi: 10.1117/12.841861.

66. N. P. Galletly, J. McGinty, C. Dunsby, et al. Fluorescence lifetime imaging distinguishes basal cell carcinoma from surrounding uninvolved skin. *Br. J. Dermatol.*, 2008. ISSN 00070963. doi: 10.1111/j.1365-2133.2008.08577.x.

67. F. Fischer, K. Konig, S. Puschmann, et al. Characterization of multiphoton laser scanning device optical parameters for image restoration. *Femtosecond Laser Appl. Biol.*, 5463(September):140, 2004. ISSN 16057422. doi: 10.1117/12.545604.

68. S. Polzer, T. C. Gasser, C. Forsell, et al. Automatic identification and validation of planar collagen organization in the aorta wall with application to abdominal aortic aneurysm. *Microsc. Microanal.*, 19(6):1395–1404, 2013. ISSN 14319276. doi: 10.1017/S1431927613013251.

69. S. Mori and P. C. Van Zijl. Fiber tracking: Principles and strategies - A technical review. *NMR Biomed.*, 15(7-8):468–480, 2002. ISSN 09523480. doi: 10.1002/nbm.781.

70. J. S. Bredfeldt, Y. Liu, C. A. Pehlke, et al. Computational segmentation of collagen fibers from second-harmonic generation images of breast cancer. *J. Biomed. Opt.*, 19(1):016007, 2014. ISSN 1083-3668. doi: 10.1117/1.JBO.19.1.016007. URL `http://biomedicaloptics.spiedigitallibrary.org/article.aspx?doi=10.1117/1.JBO.19.1.016007`.

71. J. Wu, B. Rajwa, D. L. Filmer, et al. Analysis of Orientations of Collagen Fibers by Novel Fiber-Tracking Software. *Microsc. Microanal.*, 9(6):574–580, 2003. ISSN 14319276. doi: 10.1017/S1431927603030277.

72. I. Usov and R. Mezzenga. FiberApp: An open-source software for tracking and analyzing polymers, filaments, biomacromolecules, and fibrous objects. *Macromolecules*, 48(5):1269–1280, 2015. ISSN 15205835. doi: 10.1021/ma502264c.

73. F. Christidi, E. Karavasilis, K. Samiotis, S. Bisdas, and N. Papanikolaou. Fiber tracking: A qualitative and quantitative comparison between four different software tools on the reconstruction of major white matter tracts. *Eur. J. Radiol. Open*, 3:153–161, 2016. ISSN 23520477. doi: 10.1016/j.ejro.2016.06.002. URL `http://dx.doi.org/10.1016/j.ejro.2016.06.002`.

74. J. P. Marquez. Fourier analysis and automated measurement of cell and fiber angular orientation distributions. *Int. J. Solids Struct.*, 43(21):6413–6423, 2006. ISSN 00207683. doi: 10.1016/j.ijsolstr.2005.11.003.

75. R. Bracewell. *The Fourier Transform and its Applications.*, volume 73. 1986.

76. L. Moisan. Periodic plus smooth image decomposition. *J. Math. Imaging Vis.*, 39(2):161–179, 2011. ISSN 09249907. doi: 10.1007/s10851-010-0227-1.

77. University of Wisconsin. Public-Domain Test Images for Homeworks and Projects. URL `https://homepages.cae.wisc.edu/$\sim$ece533/images/`.

78. B. Pourdeyhimi, R. Dent, and H. Davis. Measuring Fiber Orientation in Nonwovens Part III: Fourier Transform. *Text. Res. J.*, 67(2):143–151, 1997. ISSN 0040-5175. doi: 10.1177/004051759706700211. URL `http://journals.sagepub.com/doi/10.1177/004051759706700211`.

79. A. Kim, N. Lakshman, and W. M. Petroll. Quantitative assessment of local collagen matrix remodeling in 3-D Culture: The role of Rho kinase. *Exp. Cell Res.*, 2006. ISSN 00144827. doi: 10.1016/j.yexcr.2006.08.009.

80. S. Chaudhuri, H. Nguyen, R. M. Rangayyan, S. Walsh, and C. B. Frank. A Fourier Domain Directional Filtering Method for Analysis of Collagen Alignment in Ligaments. *IEEE Trans. Biomed. Eng.*, 1987. ISSN 15582531. doi: 10.1109/TBME.1987.325980.

81. E. A. Sander and V. H. Barocas. Comparison of 2D fiber network orientation measurement methods. *J. Biomed. Mater. Res. - Part A*, 88(2):322–331, 2009. ISSN 15493296. doi: 10.1002/jbm.a.31847.

82. R. Becker and N. Morrison. The errors in FFT estimation. *IEEE Trans. Signal Process.*, 44(8):133–135, 2002. doi: 10.1109/eeis.1996.566911.

83. W. Withayachumnankul, B. M. Fischer, H. Lin, and D. Abbott. Uncertainty in terahertz time-domain spectroscopy measurement. *J. Opt. Soc. Am. B*, 25(6): 1059, 2008. ISSN 0740-3224. doi: 10.1364/josab.25.001059.

84. A. J. Schriefl, H. Wolinski, P. Regitnig, S. D. Kohlwein, and G. A. Holzapfel. An automated approach for three-dimensional quantification of fibrillar structures in optically cleared soft biological tissues. *J. R. Soc. Interface*, 2012. ISSN 1742-5689. doi: 10.1098/rsif.2012.0760.

85. R. Rezakhaniha, A. Agianniotis, J. T. C. Schrauwen, et al. Experimental investigation of collagen waviness and orientation in the arterial adventitia using confocal laser scanning microscopy. *Biomech. Model. Mechanobiol.*, 11(3-4):461–473, 2012. ISSN 16177959. doi: 10.1007/s10237-011-0325-z.

86. C. J. Stender, E. Rust, P. T. Martin, et al. Modeling the effect of collagen fibril alignment on ligament mechanical behavior. *Biomech. Model. Mechanobiol.*, 17(2):543–557, 2018. ISSN 16177940. doi: 10.1007/s10237-017-0977-4. URL `https://doi.org/10.1007/s10237-017-0977-4`.

87. J. Lagarias C., J. Reeds A., M. Wright H., and P. Wright E. Convergence Properties of the Nelder-Mead Simplex Method in Low Dimensions. *SIAM J. Optim.*, 9(1):112–147, 1998. URL `http://citeseerx.ist.psu.edu/viewdoc/summary?doi=10.1.1.120.6062`.

88. A. J. Schriefl, G. Zeindlinger, D. M. Pierce, P. Regitnig, and G. A. Holzapfel. Determination of the layer-specific distributed collagen fibre orientations in human thoracic and abdominal aortas and common iliac arteries. *J. R. Soc. Interface*, 2012. ISSN 1742-5689. doi: 10.1098/rsif.2011.0727.

89. H. Kung. The Complexity of Obtaining Starting Points for Solving Operator Equations by Newton's Method. In *Anal. Comput. Complex.*, pages 35–57. Elsevier, 1976. doi: 10.1016/B978-0-12-697560-4.50008-3. URL `https://linkinghub.elsevier.com/retrieve/pii/B9780126975604500083`.

90. M. W. Petroll, D. H. Cavanagh, P. Barry, P. Andrews, and J. V. Jester. Quantitative Analysis of Stress Fiber Orientation During Corneal Wound Contraction. *J. Cell Sci.*, 104:353–63, 1993. ISSN 0021-9533. doi: 10.1016/S0261-5614(03)00031-1.

91. C. Bayan, J. M. Levitt, E. Miller, D. Kaplan, and I. Georgakoudi. Fully automated, quantitative, noninvasive assessment of collagen fiber content and organization in thick collagen gels. *J. Appl. Phys.*, 105(10):1–11, 2009. ISSN 00218979. doi: 10.1063/1.3116626.

92. M. van Ginkel. *Image analysis using orientation space based on steerable filters.* Number october. 2002. ISBN 9075691092.

93. J. P. McLean, Y. Gan, T. H. Lye, et al. High-speed collagen fiber modeling and orientation quantification for optical coherence tomography imaging. *Opt. Express*, 27(10):14457, 2019. ISSN 1094-4087. doi: 10.1364/oe.27.014457.

94. J. Schindelin, I. Arganda-Carreras, E. Frise, et al. Fiji: An open-source platform for biological-image analysis, 2012. ISSN 15487091.

95. X. Qian, X. Zhou, B. Mu, and Z. Li. Fiber alignment and property direction dependency of FRC extrudate. *Cem. Concr. Res.*, 2003. ISSN 00088846. doi: 10.1016/S0008-8846(03)00108-X.

96. M. Witte, S. Jaspers, H. Wenck, M. Rübhausen, and F. Fischer. General method for classification of fiber families in fiber - reinforced materials : application to in - vivo human skin images. *Sci. Rep.*, pages 1–11, 2020. ISSN 2045-2322. doi: 10.1038/s41598-020-67632-z. URL `https://doi.org/10.1038/s41598-020-67632-z`.

97. S. Neerken, G. W. Lucassen, M. A. Bisschop, E. Lenderink, and T. A. M. Nuijs. Characterization of age-related effects in human skin: A comparative study that applies confocal laser scanning microscopy and optical coherence tomography. *J. Biomed. Opt.*, 9(2):274, 2004. ISSN 10833668. doi: 10.1117/1.1645795.

98. A. Pissarenko, W. Yang, H. Quan, et al. Tensile behavior and structural characterization of pig dermis. *Acta Biomater.*, 86:77–95, 2019. ISSN 18787568. doi: 10.1016/j.actbio.2019.01.023. URL `https://doi.org/10.1016/j.actbio.2019.01.023`.

99. S. Mortazavian and A. Fatemi. Effects of fiber orientation and anisotropy on tensile strength and elastic modulus of short fiber reinforced polymer composites. *Compos. Part B Eng.*, 2015. ISSN 13598368. doi: 10.1016/j.compositesb.2014.11.041.

100. M. Farsi, K. Ratcliff, and M. Barbosa. An introduction to CANonen. *Comput. Control Eng. J.*, 1999. ISSN 09563385. doi: 10.1049/cce:19990405.

101. R. W. Ogden, G. Saccomandi, and I. Sgura. Fitting hyperelastic models to experimental data. *Comput. Mech.*, 34(6):484–502, 2004. ISSN 01787675. doi: 10.1007/s00466-004-0593-y.

102. H. C. Wells, K. H. Sizeland, N. Kirby, et al. Collagen Fibril Structure and Strength in Acellular Dermal Matrix Materials of Bovine, Porcine, and Human Origin. *ACS Biomater. Sci. Eng.*, 1(10):1026–1038, 2015. ISSN 2373-

9878. doi: 10.1021/acsbiomaterials.5b00310. URL http://pubs.acs.org/doi/10.1021/acsbiomaterials.5b00310.

103. V. R. Sherman, Y. Tang, S. Zhao, W. Yang, and M. A. Meyers. Structural characterization and viscoelastic constitutive modeling of skin. *Acta Biomater.*, 53:460–469, 2017. ISSN 18787568. doi: 10.1016/j.actbio.2017.02.011. URL http://dx.doi.org/10.1016/j.actbio.2017.02.011.

104. R. Fan and M. Sacks. Structural Constitutive Model : Finite Element. 47(9): 2043–2054, 2015. doi: 10.1016/j.jbiomech.2014.03.014.SIMULATION.

105. K. P. Quinn and B. A. Winkelstein. Preconditioning is Correlated With Altered Collagen Fiber Alignment in Ligament. *J. Biomech. Eng.*, 133(6):064506, 2011. ISSN 01480731. doi: 10.1115/1.4004205. URL http://biomechanical.asmedigitalcollection.asme.org/article.aspx?articleid=1406417.

106. P. Gonon and A. Boudefel. Electrical properties of epoxy/silver nanocomposites. *J. Appl. Phys.*, 2006. ISSN 00218979. doi: 10.1063/1.2163978.

107. S. Nam, H. Woo Cho, T. Kim, et al. Effects of silica particles on the electrical percolation threshold and thermomechanical properties of epoxy/silver nanocomposites. *Appl. Phys. Lett.*, 99(4):043104, jul 2011. ISSN 0003-6951. doi: 10.1063/1.3615690. URL http://aip.scitation.org/doi/10.1063/1.3615690.

108. S. M. Bergin, Y. H. Chen, A. R. Rathmell, et al. The effect of nanowire length and diameter on the properties of transparent, conducting nanowire films. *Nanoscale*, 2012. ISSN 20403372. doi: 10.1039/c2nr30126a.

109. Z. Ding, V. Stoichkov, M. Horie, E. Brousseau, and J. Kettle. Spray coated silver nanowires as transparent electrodes in OPVs for Building Integrated Photovoltaics applications. *Sol. Energy Mater. Sol. Cells*, 2016. ISSN 09270248. doi: 10.1016/j.solmat.2016.05.053.

110. T. Hughes. *The Finite Element Method. Linear Static and Dynamic Finite Element Analysis*. 1987.

111. P. Mortier, G. A. Holzapfel, M. De Beule, et al. A novel simulation strategy for stent insertion and deployment in curved coronary bifurcations: Comparison of three drug-eluting stents. *Ann. Biomed. Eng.*, 38(1):88–99, 2010. ISSN 00906964. doi: 10.1007/s10439-009-9836-5.

112. G. Limbert and E. Kuhl. On skin microrelief and the emergence of expression micro-wrinkles. *Soft Matter*, (January), 2018. ISSN 1744-683X. doi: 10.1039/C7SM01969F. URL http://pubs.rsc.org/en/Content/ArticleLanding/2018/SM/C7SM01969F.

113. M. F. Leyva-Mendivil, A. Page, N. W. Bressloff, and G. Limbert. A mechanistic insight into the mechanical role of the stratum corneum during stretching and compression of the skin. *J. Mech. Behav. Biomed. Mater.*, 49:197–219, 2015. ISSN 18780180. doi: 10.1016/j.jmbbm.2015.05.010. URL http://dx.doi.org/10.1016/j.jmbbm.2015.05.010.

114. Z. Ya-Xian, T. Suetake, and H. Tagami. Number of cell layers of the stratum corneum in normal skin - relationship to the anatomical location on the body, age, sex and physical parameters. *Arch. Dermatol. Res.*, 291(10):555–9, oct 1999. ISSN 0340-3696. URL http://www.ncbi.nlm.nih.gov/pubmed/10552214.

115. K. A. Holbrook and G. F. Odland. Regional differences in the thickness (cell layers) of the human stratum corneum: an ultrastructural analysis. *J. Invest. Dermatol.*, 62(4):415–22, apr 1974. ISSN 0022-202X. URL http://www.ncbi.nlm.nih.gov/pubmed/4820685.

116. J. L. Lévêque and B. Audoly. Influence of Stratum Corneum on the entire skin mechanical properties, as predicted by a computational skin model. *Ski. Res. Technol.*, 19(1):42–46, 2013. ISSN 0909752X. doi: 10.1111/j.1600-0846.2012.00664.x.

117. R. A. Briggaman and C. E. Wheeler. The epidermal-dermal junction. *J. Invest. Dermatol.*, 65(1):71–84, jul 1975. ISSN 0022-202X. URL http://www.ncbi.nlm.nih.gov/pubmed/1097542.

118. E. Jacquet, J. Chambert, J. Pauchot, and P. Sandoz. Intra- and inter-individual variability in the mechanical properties of the human skin from in vivo measurements on 20 volunteers. *Ski. Res. Technol.*, 00:1–9, 2017. doi: 10.1111/srt.12361.

119. M. D. Ridge and V. Wright. A Bio-Engineering Study of the Mechanical Properties of Human Skin in Relation to Its Structure. *Br. J. Dermatol.*, 77(12):639–649, dec 1965. ISSN 0007-0963. doi: 10.1111/j.1365-2133.1965.tb14595.x. URL http://doi.wiley.com/10.1111/j.1365-2133.1965.tb14595.x.

120. N. Alkhouli, J. Mansfield, E. Green, et al. The mechanical properties of human adipose tissues and their relationships to the structure and composition of the extracellular matrix. *Am. J. Physiol. Endocrinol. Metab.*, 305(12):E1427–35, dec 2013. ISSN 1522-1555. doi: 10.1152/ajpendo.00111.2013. URL http://www.ncbi.nlm.nih.gov/pubmed/24105412.

121. M. Geerligs, C. Oomens, P. Ackermans, F. Baaijens, and G. Peters. Linear shear response of the upper skin layers. *Biorheology*, 48(3-4):229–45, 2011. ISSN 1878-5034. doi: 10.3233/BIR-2011-0590. URL http://www.ncbi.nlm.nih.gov/pubmed/22156036.

122. N. Magnenat-Thalmann, P. Kalra, J. L. Lévêque, et al. A computational skin model: Fold and wrinkle formation. *IEEE Trans. Inf. Technol. Biomed.*, 6(4): 317–323, 2002. ISSN 10897771. doi: 10.1109/TITB.2002.806097.

123. A. Delalleau, G. Josse, J.-M. Lagarde, H. Zahouani, and J.-M. Bergheau. A nonlinear elastic behavior to identify the mechanical parameters of human skin in vivo. *Ski. Res. Technol.*, 14(2):152–164, may 2008. ISSN 0909-752X. doi: 10.1111/j.1600-0846.2007.00269.x. URL `http://doi.wiley.com/10.1111/j.1600-0846.2007.00269.x`.

124. J. L. Lévêque and B. Audoly. Influence of Stratum Corneum on the entire skin mechanical properties, as predicted by a computational skin model. *Skin Res. Technol.*, 19(1):42–6, feb 2013. ISSN 1600-0846. doi: 10.1111/j.1600-0846.2012.00664.x. URL `http://www.ncbi.nlm.nih.gov/pubmed/22925192`.

125. K. S. Wu, W. W. van Osdol, and R. H. Dauskardt. Mechanical properties of human stratum corneum: Effects of temperature, hydration, and chemical treatment. *Biomaterials*, 27(5):785–795, feb 2006. ISSN 01429612. doi: 10.1016/j.biomaterials.2005.06.019. URL `http://linkinghub.elsevier.com/retrieve/pii/S0142961205005867`.

126. C. O. Flynn and B. A. McCormack. A three-layer model of skin and its application in simulating wrinkling. *Comput. Methods Biomech. Biomed. Engin.*, 12(2):125–134, apr 2009. ISSN 1025-5842. doi: 10.1080/10255840802529933. URL `http://www.tandfonline.com/doi/abs/10.1080/10255840802529933`.

127. F. M. Hendriks, D. Brokken, C. W. J. Oomens, D. L. Bader, and F. P. T. Baaijens. The relative contributions of different skin layers to the mechanical behavior of human skin in vivo using suction experiments. *Med. Eng. Phys.*, 28(3):259–266, 2006. ISSN 13504533. doi: 10.1016/j.medengphy.2005.07.001.

128. O. Zienkiewicz, R. L. Taylor, and D. Fox. The Finite Element Method for Solid and Structural Mechanics. In *Finite Elem. Method Solid Struct. Mech.*, page iii. 2014. doi: 10.1016/b978-1-85617-634-7.00018-1.

129. J. Simo and R. Taylor. Penalty function formulations for incompressible nonlinear elastostatics. *Comput. Methods Appl. Mech. Eng.*, 35(1):107–118, oct 1982. ISSN 00457825. doi: 10.1016/0045-7825(82)90035-4. URL `http://linkinghub.elsevier.com/retrieve/pii/0045782582900354`.

130. A. Mirmiran, Y. Shao, M. Shahawy, et al. ABAQUS Theory manual. *ABAQUS, Inc. Dassault Systèmes*, 2007.

131. J. T. Fong and R. W. Penn. Construction of a Strain-Energy Function for an Isotropic Elastic Material. *Trans. Soc. Rheol.*, 19(1):

99–113, mar 1975. ISSN 0038-0032. doi: 10.1122/1.549389. URL http://linkinghub.elsevier.com/retrieve/pii/S0020768309001723http://sor.scitation.org/doi/10.1122/1.549389.

132. T. Belytschko, W. K. Liu, B. Moran, and K. Elkhodary. *Nonlinear Finite Elements for Continua and Structures, Second Edition*, volume 38. mar 2014. ISBN 9781909507227. doi: 10.1088/1751-8113/44/8/085201. URL https://www.wiley.com/en-us/Nonlinear+Finite+Elements+for+Continua+and+Structures%2C+2nd+Edition-p-9781118632703.

133. R. W. Ogden. Non-linear elastic deformations. 1984.

134. G. A. Holzapfel, J. A. Niestrawska, R. W. Ogden, A. J. Reinisch, and A. J. Schriefl. Modelling non-symmetric collagen fibre dispersion in arterial walls. *J. R. Soc. Interface*, 12(106):20150188–20150188, 2015. ISSN 1742-5689. doi: 10.1098/rsif.2015.0188. URL http://rsif.royalsocietypublishing.org/cgi/doi/10.1098/rsif.2015.0188.

135. N. Birkbeck, J. Lévesque, and J. N. Amaral. A dimension abstraction approach to vectorization in matlab. *Int. Symp. Code Gener. Optim. CGO 2007*, pages 115–127, 2007. doi: 10.1109/CGO.2007.11.

136. MATLAB. *version 9.4.0.813654 (R2018a)*. The MathWorks Inc., 2018.

137. MATLAB. *Image Processing Toolbox (version 10.2)*. The MathWorks Inc., 2018.

138. MATLAB. Curve fitting toolbox. *MATLAB Man.*, 2011.

139. A. Pandolfi and M. Vasta. Fiber distributed hyperelastic modeling of biological tissues. *Mech. Mater.*, 44:151–162, 2012. ISSN 01676636. doi: 10.1016/j.mechmat.2011.06.004. URL http://dx.doi.org/10.1016/j.mechmat.2011.06.004.

List of Publications

- **M. Witte**, S. Jaspers, H. Wenck, M. Rübhausen, and F. Fischer. Noise reduction and quantification of fiber orientations in greyscale images. *PLoS One* 1–21, DOI: 10.1371/journal.pone.0227534 (2020).
- **M. Witte**, S. Jaspers, H. Wenck, M. Rübhausen, and F. Fischer. General method for classification of fiber families in fiber-reinforced materials: application to in-vivo human skin images. *Scientific Reports* 1–11, DOI: 10.1038/s41598-020-67632-z (2020).
- **M. Witte**, M. Rübhausen, S. Jaspers, H. Wenck, and F. Fischer. Influence of repeated mechanical strain on isotropic and anisotropic dermal collagen morphologies. Submitted to *Scientific Reports* (2020).
- T.E. Glier, M. Betker, **M. Witte**, T. Matsuyama, L. Westphal, B. Grimm-Lebsanft, F. Biebl, L. Akinsinde, F. Fischer, and M. Rübhausen. Electrical and Network Properties of Flexible Silver-Nanowire Composite Electrodes under Mechanical Strain. Submitted to *Scientific Reports* (2020).

Acknowledgements

Mein besonderer Dank gilt:

- Dr. Frank Fischer für die erstklassige Betreuung meiner Doktorarbeit und die zahlreichen, spannenden Gespräche und Diskussionen,
- Prof. Michael Rübhausen für die Übernahme des Erstgutachtens und die konstruktiven Treffen, die mich sehr motiviert haben,
- Sören Jaspers und Dr. Horst Wenck für die Möglichkeit, meine Doktorarbeit bei der Beiersdorf AG zu absolvieren,
- allen Mitarbeitern der Applied Biophysics für das angenehme Arbeitsumfeld und die interessanten Gespräche,
- meiner Familie, insbesondere meinen Eltern, für den Rückhalt und die immerwährende Unterstützung,
- meinen Freunden, für alles, was außerhalb der Doktorarbeit stattfindet.